Spin-dependent Transport and Recombination in Solar Cells studied by Pulsed Electrically Detected Magnetic Resonance

Im Fachbereich Physik der Freien Universität Berlin
zur Erlangung der Würde eines
Doktors der Naturwissenschaften (Dr. rer. nat.)
eingereichte Dissertation

vorgelegt von

Jan Behrends

aus Hannover

Institut für Experimentalphysik der Freien Universität Berlin
2009

1. Gutachter: Prof. Dr. Robert Bittl
2. Gutachter: Prof. Dr. Bernd Rech
3. Gutachter: Prof. Dr. Martin Stutzmann

Tag der Disputation: 11. November 2009

Summary

This thesis deals with spin-dependent transport and recombination of charge carriers in solar cells. A systematic study on the influence of localized paramagnetic states which act as trapping and recombination centres for photogenerated charge carriers, is presented for three different types of solar cells. The central technique used in this thesis is electrically detected magnetic resonance (EDMR). The capabilities of pulsed (p) EDMR were extended with regard to the detection sensitivity. These improvements allowed pEDMR measurements on fully processed devices from cryogenic to room temperature. The instrumental upgrades also set the stage for pEDMR measurements at different resonance frequencies.

In high-efficiency solar cells based on the heterojunction between hydrogenated amorphous silicon (a-Si:H) and crystalline silicon (c-Si), recombination via performance-limiting interface states could directly be measured electrically for the first time. The identification of these defects could be achieved by exploiting their orientation with regard to the surface.

In thin-film solar cells based on hydrogenated microcrystalline silicon (µc-Si:H) the situation is more complex due to the heterogeneous and disordered structure of the material itself. In addition, these cells are multilayer-systems comprising three different silicon layers with different doping levels and microstructures. By combining a systematic alteration of the sample structure with the information extracted from deconvoluting spectrally overlapping signals in the time domain, it was possible to assign the spin-dependent signals to defects in the individual layers of the solar cells. Benefiting from the instrumental improvements, recombination via dangling bond states in silicon-based solar cells could be investigated by pEDMR at room temperature for the first time.

In organic bulk heterojunction solar cells based on MEH-PPV and PCBM two different spin-dependent mechanisms coexist. Both processes, namely polaron pair recombination and bipolaron formation, can be involved in loss mechanisms in solar cell operation. In previous studies these two processes were investigated by continuous wave (cw) EDMR, but the assignment of the underlying microscopic process based on cwEDMR alone remained speculative. In this work it is demonstrated that by electrically measuring spin-Rabi nutations in the spin-locking regime and performing comparative simulations of coherent spin motion, it is possible to discriminate between both processes which lead to indistinguishable cwEDMR spectra.

Zusammenfassung

Die vorliegende Arbeit behandelt spinabhängige Transport- und Rekombinationsprozesse in Solarzellen. Im Rahmen dieser Studie zum Einfluss von paramagnetischen Defektzuständen, die als Einfang- und Rekombinationszentren für optisch erzeugte Ladungsträger wirken, wurden drei unterschiedliche Arten von Solarzellen untersucht. Hierzu wurde die Messmethode der elektrisch detektierten magnetischen Resonanz (EDMR) verwendet. Insbesondere wurde die gepulste (p) EDMR bezüglich ihrer Detektionsempfindlichkeit optimiert, wodurch pEDMR-Messungen an vollständig prozessierten Bauelementen im Temperaturbereich von 10 K bis Raumtemperatur ermöglicht wurden. Darüber hinaus wurden instrumentelle Erweiterungen mit dem Ziel vorgenommen, pEDMR-Messungen bei unterschiedlichen Resonanzfrequenzen durchführen zu können.

In Hocheffizienz-Solarzellen aus mit Wasserstoff versetztem amorphen Silizium (a-Si:H) und kristallinem Silizium (c-Si) konnten Rekombinationsprozesse über Defektzustände an der a-Si:H/c-Si Grenzfläche erstmalig direkt elektrisch detektiert werden. Die Identifikation der Defekte erfolgte anhand ihrer Orientierung bezüglich der c-Si Oberfläche.

In Dünnschicht-Solarzellen aus mit Wasserstoff versetztem mikrokristallinen Silizium (μc-Si:H) ist die Situation komplexer. Zum einen ist das Material selbst heterogen und ungeordnet. Zum anderen bestehen die Solarzellen aus mehreren Silizium-Schichten mit unterschiedlicher Dotierung und Mikrostruktur. Zur Identifikation der spinabhängigen Signale sowie deren Zuordnung zu den einzelnen Schichten wurde die Struktur der Solarzelle systematisch verändert. Darüber hinaus wurden spektral überlappende Signale anhand ihrer unterschiedlichen Zeitstruktur voneinander getrennt. Infolge der instrumentellen Optimierungen konnten erstmalig pEDMR-Messungen an siliziumbasierten Solarzellen bei Raumtemperatur durchgeführt werden.

In organischen Heterostruktur-Solarzellen basierend auf einer Mischung aus MEH-PPV und PCBM existieren zwei unterschiedliche spinabhängige Prozesse, die an Verlustmechanismen im Solarzellenbetrieb beteiligt sind. Beide Prozesse, nämlich die Rekombination von Polaronen-Paaren sowie die Bildung von Bipolaronen, wurden zuvor mit Hilfe der “continuous wave” (cw) EDMR untersucht. Eine eindeutige Zuordnung der gefundenen cwEDMR-Signale zu den zugrunde liegenden Prozessen war jedoch bisher nicht möglich, weil beide genannten Mechanismen zu nicht unterscheidbaren cwEDMR-Spektren führen. Im Rahmen dieser Arbeit konnte gezeigt werden, dass durch die elektrische Detektion von Rabi-Oszillationen im “spin-locking”-Regime in Verbindung mit Simulationen eine Trennung von beiden Prozessen möglich ist.

Contents

1. Introduction

After the first report of a crystalline silicon-based solar cell with an energy conversion efficiency of $\eta = 6\%$ by Chapin, Fuller and Pearson in 1954 [1], a lot of progress has been made in further improving the device performance. Since then, various sophisticated process steps were developed resulting in laboratory-type crystalline silicon (c-Si) solar cells with an efficiency of 25% [2, 3]. Even higher efficiencies were achieved by multi-junction concepts based on stacking several optimized III-V compound semiconductor solar cells on top of each other. Very recently, these cells yielded a world record efficiency of 41.1% utilizing highly concentrated light [2].

Despite dramatic progress in the past decades, the costs for solar energy conversion are still significantly higher than for most other ways of electricity production based on renewable energy sources like hydropower or wind and conventional gas- or coal-fired power stations or nuclear power plants. Hence it follows that bringing down the costs of solar energy conversion is the key issue in world-wide photovoltaics research and development.

Several strategies are pursued in order to achieve higher efficiencies and lower production costs. Thin-film solar cells made from various semiconductor materials comprise the potential for low production cost, allow a variety of new products — e.g. flexible and light-weight solar modules — and require only a small amount of energy for their fabrication. These emerging technologies rely on rather imperfect semiconductor materials, are to a large extent empirically optimized and show conversion efficiencies being far below the physical limits. Thus, fundamental science and new analytical tools are required to provide an in-depth scientific understanding which may serve as a basis for further improvements of these technologies. In this context this thesis addresses spin physics to gain a deeper understanding of the working principles of three new thin-film systems, i.e. solar cells based on hydrogenated microcrystalline silicon (µc-Si:H), organic solar cells and the model system consisting of hydrogenated amorphous silicon (a-Si:H) and c-Si — the latter one bridging the world of thin-film solar cells with the established and well-understood c-Si. Common to all these device structures is that the maximum efficiencies achieved today are still below the theoretical limit. This is mainly due to defects which act as trapping and recombination centres for photogenerated charge carriers. Consequently, detailed insight into these trapping and recombination processes is necessary for improving the solar cell performance.

Due to the fact that defects in semiconductors are often paramagnetic or can be made paramagnetic by adjusting the experimental conditions, the spins of the charge carriers can be used as probes for studying charge transport in solar cells. This renders electron paramagnetic resonance (EPR) the method of choice to elucidate charge transport mechanisms as well as to determine defect structures and material properties (e.g. defect densities, hydrogen networks or strain) [4]. However, the application of EPR to completely processed solar cells remains a challenge because conventional EPR suffers from its poor sensitivity which is usually not sufficient to detect defects in state-of-the-art solar cells. Moreover, it is often impossible to discriminate between signals from the cell structure and background signals from the substrate. To circumvent these limitations, EPR measurements are usually performed on powder samples. Although a correlation between the material quality as determined by EPR and the efficiency of resulting solar cells is well established, it still remains questionable if the defect properties of the thin films in the device and in powder samples are identical, because the boundary conditions for the layer growth are different.

The sensitivity limit of EPR can be overcome by applying electrically detected magnetic resonance (EDMR) to study paramagnetic centres in semiconductors. This technique combines the microscopic selectivity of EPR with the sensitivity of a current measurement and thus provides a tool to directly study the influence of paramagnetic defects on the conductivity. EDMR was demonstrated in 1966 by Maxwell and Honig [5, 6] as well as Schmidt and Solomon [7] who measured the influence of EPR on the photoconductivity in silicon. The underlying mechanism was spin-dependent scattering of charge carriers at impurities. In 1972 Lepine utilized EDMR for the detection of charge carrier recombination via defect states at a silicon surface [8]. Since then, EDMR was applied to a large variety of inorganic and organic semiconductors. In particular, this technique proved beneficial to elucidate spin-dependent transport and recombination pathways in a-Si:H and µc-Si:H thin films and devices (for a review see [9] and references therein). Until recently, EDMR experiments were performed similar like continuous wave (cw) EPR experiments, i.e. the sample was continuously subjected to microwave radiation while sweeping an external magnetic field and detecting the photoconductivity. Thus, spectroscopic information about the current-influencing paramagnetic states could be extracted. Towards the beginning of this century, the field of EDMR got a new impetus when Boehme and Lips demonstrated the first pulsed (p) EDMR measurement employing short microwave pulses [10]. By the use of pEDMR, it is not only possible to study the time behaviour of spin-dependent transport and recombination processes, but also to harness coherent spin effects [11] in a similar way like in pulsed EPR. Recent years witnessed an increasing number of pEDMR studies on model systems related to solar energy conversion. Based on these improvements, the present work constitutes for the first time a systematic study on different fully processed state-of-the-art solar cells applying pEDMR.

1.1. a-Si:H/c-Si heterojunction solar cells

Heterojunction solar cells comprising a-Si:H and crystalline silicon (c-Si) represent a promising concept on the way towards reaching the thermodynamic solar conversion limit for silicon of about 29% [12] because a-Si:H effectively prevents recombination of photogenerated charge carriers at the contacts [13]. Solar cells based on this concept with an efficiency of 23% on 100 cm^2 have been reported recently [2, 14]. Since the defect concentrations in high-quality c-Si wafers that are used as absorbers in a-Si:H/c-Si solar cells are usually so low that the charge carrier diffusion length exceeds the wafer thickness, the influence of c-Si bulk defects on the efficiency is only marginal. As a result, the device performance critically depends on the defect concentration at the heterointerface which, in turn, is highly dependent on pre-treatment of the c-Si wafer [15], a-Si:H deposition conditions [16] and post-treatment [17, 18]. Thus, experimental techniques that provide insight into the crucial role of interface states for charge transport in the device are of particular interest. Previously, characterization methods were developed to measure the energetic distribution and concentrations of defects in ultrathin a-Si:H layers on c-Si [19, 20]. In addition, by the use of capacitance-voltage based methods, the influence of defects on the electric properties of a-Si:H/c-Si interfaces may be analysed [21, 22]. However, the discrimination between defects at the interface and in the ‘bulk’ a-Si:H is complicated if not impossible because all standard characterization methods lack the microscopic selectivity. The questions that are addressed in this thesis are: Is it possible to directly detect recombination via a-Si:H/c-Si interface states by measuring the conductivity? What is the structural identity of the recombination centre at the a-Si:H/c-Si interface?

1.2. μc-Si:H thin-film solar cells

The high efficiencies that can be reached with wafer-based technologies come along with the energy and cost intensive wafer production process. Silicon-based thin-film solar cells offer the potential for a significant cost reduction because they can be deposited at low temperatures [23]. In addition, they are superior with regard to material consumption as compared to wafer-based cells. Although photovoltaic modules based on a-Si:H are commercially available since several years, they suffer from relatively low efficiencies. This can mainly be attributed to defect states in the band gap and tail states near the band edges which are inherently present in the material [24]. Moreover, light-induced defect creation — known as the Staebler-Wronski effect (SWE) [25] — causes a further reduction of the efficiency with illumination time. Microcrystalline silicon consisting of small crystallites surrounded by amorphous silicon, has proven to be less affected by light-induced degradation [26]. High-quality μc-Si:H can be grown using plasma enhanced chemical vapour deposition (PECVD) and is thus compatible with the a-Si:H technology [27]. Therefore, a-Si:H and μc-Si:H can be combined in tandem solar cells, benefiting from the different optical properties of both materials which leads to a more efficient use of the solar spectrum [28]. Since very recently, solar modules consisting of a-Si:H/μc-Si:H tandem structures are being successfully produced by several companies. Still, significant scientific challenges remain with regard to the relationship between the solar cell performance and defect properties of μc-Si:H. The questions that are addressed in this regard are: Which paramagnetic states in the individual layers of the multilayer-system lead to current loss processes? What are the underlying microscopic mechanisms? In order to take advantage of the increased signal-to-noise ratio at low temperatures, the EDMR measurements were performed at 10 K. Thus, a third question remains: Are these processes the same that prevail at room temperature?

1.3. Organic bulk heterojunction solar cells

The application of pEDMR is not exclusively restricted to inorganic solar cells. In recent years, organic solar cells based on conjugated polymers have attracted much attention because they can easily be processed from solution on inexpensive substrates [29]. Among various concepts, organic bulk heterojunction solar cells comprising phase-separated blends of conjugated polymers and fullerene derivatives proved successful for reaching efficiencies of up to 5% [30]. Although the primary excitation process (the creation of an exciton by an absorbed photon) leads to separated charge carriers with almost 100% quantum efficiency, the extraction of these charge carriers remains a challenge and limits the cell efficiency. Similar to the case of solar cells based on silicon materials, recombination of photogenerated charge carriers constitutes a loss mechanism in organic solar cells. Previously, continuous wave (cw) EDMR was employed to study spin-dependent recombination and transport in devices based on conjugated polymers [31, 32]. Although it is possible to extract the EPR signatures of the species that are involved in a spin-dependent process, the assignment of the underlying microscopic mechanisms based on the cwEDMR spectrum alone is always plagued with ambiguity. We applied pEDMR to bulk heterojunction solar cells consisting of MEH-PPV and PCBM in order to address the following questions: Which paramagnetic states are involved? What is the reaction pathway of this process? Apart from the fact that organic solar cells are important and promising devices, they can additionally be considered a testbed for checking the applicability of existing pEDMR models that were originally developed for inorganic materials.

1.4. Thesis structure

The remainder of this thesis is organized as follows:

Chapter 2 provides an introduction into the theoretical concepts of pEDMR which are essential for the interpretation of the experimental results. After a general description of spin-dependent recombination and hopping, the 'bath model' for spin-dependent recombination is developed which — in contrast to the existing models — accounts for the impact of free charge carrier generation (by light absorption) on the dynamics of the resulting pEDMR signals. In addition, we suggest an alternative EDMR mechanism involving three charge carriers which is capable of consistently explaining several experimental observations which are at variance with EDMR models based on the spin-pair mechanism. Subsequently, we address the phenomenon of coherent spin motion with particular emphasis on the role of intersystem crossing for electrically detected spin-Rabi oscillations. Further on, a theoretical description of spin-Rabi oscillations is given, which will be used in Chapter 6 to disentangle spectrally overlapping pEDMR signals. We present simulations of Rabi oscillations taking into account disorder-related effects that are present in all samples which were subject to this study. The consideration of disorder is indispensable for extracting quantitative information from a comparison between simulations and the experiments that were performed within the framework of this thesis.

Chapter 3 gives an overview on the pEDMR setup. Particular emphasis is put on the current detection electronics which were upgraded during the work described in this thesis. On the one hand, the detection sensitivity was improved by suppressing interfering signals with the aim to achieve a sufficient signal-to-noise ratio for pEDMR measurements on silicon-based solar cells at room temperature. In addition, these improvements are beneficial for the extension of pEDMR towards higher microwave frequencies. On the other hand, the time resolution was enhanced. In this work the gain in temporal resolution was exploited to deconvolute overlapping pEDMR signals in the time domain and thereby effectively increase the spectral resolution. Furthermore, this chapter contains a comparative study of continuous wave and pulsed EDMR with regard to detection sensitivity and spectral resolution. Finally, the influence of potential defects that might occur during the sample processing on the pEDMR signals is evaluated. This is a prerequisite for the systematic study on µc-Si:H based solar cells in Chapter 5.

Chapter 4 presents pEDMR results obtained on a-Si:H/c-Si heterojunction solar cells. At first, we study spin-dependent processes at the interface between isotopically purified ^{28}Si and SiO$_2$ which serves as a model system for the a-Si:H/c-Si interface and — due to the reduced superhyperfine interaction to ^{29}Si — provides reference spectra with high resolution. In the second step, we directly study the influence of recombination via defects at the a-Si:H/c-Si interface on the charge transport in the device. In particular, we determine the principal values of the g tensor for the interface defects from a measurement of the EDMR spectrum as a function of the sample orientation in the magnetic field.

Chapter 5 is devoted to spin-dependent transport and recombination in µc-Si:H based thin-film solar cells at low temperature ($T = 10$ K) as well as at room temperature. Here, the situation is more complicated than in Chapter 4 because the structure of µc-Si:H itself is quite complex. It contains small crystallites surrounded by amorphous regions and can thus be considered to consist of many disordered a-Si:H/c-Si interfaces. In addition, the solar cell structures comprise three differently doped thin-film silicon layers. To evaluate the influence of the respective n- and p-doped layers on the pEDMR spectra, the morphology of these layers was systematically varied from amorphous to microcrystalline. The samples were provided by the Forschungszentrum Jülich. For each cell structure we combine the information obtained from pEDMR spectra and from the deconvoluted time evolution of spectrally overlapping resonances in order to identify the spin-dependent processes and the contributing paramagnetic states in the individual layers of the cell structure. We performed pEDMR measurements at different microwave frequencies to improve the spectral resolution as well as to distinguish between field-dependent and field-independent spectral contributions. Moreover, we present results of pEDMR measurements performed on µc-Si:H based solar cells at room temperature and compare the results to findings extracted from the low-temperature measurements.

Chapter 6 is concerned with the application of pEDMR to organic bulk heterojunction solar cells. We investigate the influence of spin-dependent processes on charge transport in the device. For this purpose we make use of Rabi oscillation measurements and comparative simulations with the aim to distinguish between polaron pair recombination and bipolaron hopping. Additionally, we utilize the close analogy between polaron pairs in polymers and spin-correlated radical pairs to further improve our understanding of EDMR in organic and inorganic devices.

Chapter 7 summarizes the results obtained on the different solar cells structures and puts them into a more general perspective. In addition, a strategy for future work is outlined.

2. Theory of EDMR

This chapter provides an introduction into the theoretical concepts of EDMR which are essential for the interpretation of the experimental results presented in Chapters 4, 5 and 6. These concepts constitute the basis for extensions to the body of EDMR theory made in the PhD thesis of Christoph Böhme [33]. The extension of the concepts therein was mandatory to relate the observed EDMR signatures with the underlying material properties in the solar cells under investigation and adjust the experimental design to the respective material properties. The given theoretical background is ordered in the following way:

After a qualitative explanation of spin-dependent recombination and hopping transport in Section 2.1, we will briefly describe the basic principle of electron paramagnetic resonance — the technique EDMR is based on — in Section 2.2. The following section is concerned with the physics of spin pairs consisting of two spin $1/2$ particles and describes how these pairs may influence the conductivity of a sample. The theory of spin-dependent recombination is based on the approach by Boehme and Lips [33, 34]. Since all spin-dependent processes investigated here involve spin pairs with weak spin-spin coupling (exchange or dipolar), we will restrict our description to such weakly coupled pairs. In particular, we will — analogous to the procedure used in [33, 34] — derive an expression for the transient conductivity change induced by a resonant microwave pulse. The measurement of the resulting (photo-)current transient constitutes the basis for all EDMR experiments. We will take advantage of the current transient dynamics in order to distinguish between spectrally overlapping signals in Chapter 5.

In order to improve the information content extractable from EDMR experiments it is essential to understand the relationship between localized electrons and free charge carriers in the conduction and valence bands. For the theoretical description of this relationship, we present an extension of existing pEDMR models which is able to realistically reflect the interaction between the spin pair ensemble and free charge carriers in the bands.

Besides spin-dependent recombination, hopping of charge carriers among localized states can equally be spin-dependent and thus evoke EDMR signals. Especially at low temperatures, spin-dependent hopping may dominate the EDMR spectra of devices based on disordered materials as can be seen in the thin-film solar cells investigated in Chapter 5. The theoretical description of spin-dependent hopping in Section 2.3.1.3 follows the conceptual idea presented in Ref. [35].

The fact that several experimental observations cannot be explained by common EDMR models raises the question whether different mechanisms might give rise to EDMR signals as well. In particular, the fact that EDMR spectra frequently exhibit only one resonance line while a ‘partner spin’ signal is missing, remains puzzling. In Section 2.4 we will present an EDMR mechanism based on a three particle process which can explain several experimental results that are at variance with existing EDMR models based on the spin-pair mechanism.

The possibility to coherently manipulate spins by pEDMR paved the way for EDMR sequences which allow the assignment of overlapping EDMR signals. Thereby, pEDMR measurements can provide highly desired additional information about the spin-dependent charge transport pathways in silicon as well as in organic solar cells. In order to apply this approach to disordered materials, the morphology of the material has to be considered theoretically. In Section 2.5 we will describe the coherent evolution of spin pairs during the microwave excitation for two different cases, namely the manipulation of only one spin partner (selective excitation) and simultaneous excitation of both spin pair constituents (spin-locking). Both situations lead to different nutation-frequencies in electrically detected Rabi oscillations which may be utilized to discriminate between different microscopic processes. This is of particular importance for the interpretation of experimental results on polaron pairs in organic solar cells (see Chapter 6).

Section 2.6 is devoted to numerical simulations of Rabi oscillations. Different from previous studies [36, 37], we will account for disorder-related effects by considering g value distributions for the contributing paramagnetic centres. We will systematically study the influence of the distribution width on the Rabi oscillations using a software that effectively calculates the evolution of several spin pairs in parallel.

2.1. Spin-dependent charge transport

Although each charge carrier in all types of solar cells carries a spin, this spin degree of freedom does usually not influence the operation of the device. This results from the fact

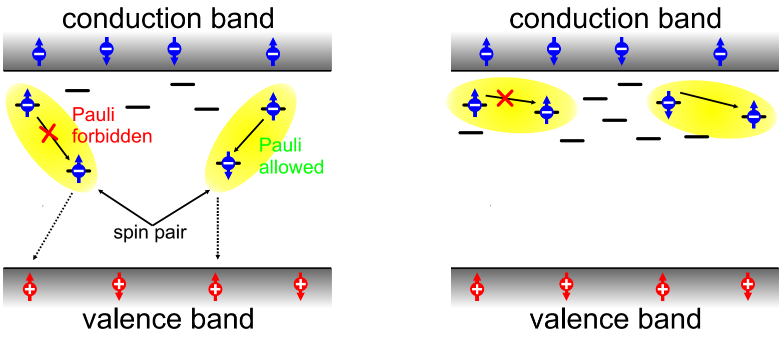

Figure 2.1.: Spin-dependent processes involving localized states in the band gap as observed in thin-film silicon. Left: spin-dependent recombination. Right: spin-dependent hopping transport. The arrows indicate the orientation of the electron and hole spins.

that charge transport is mainly governed by band transport, and the spins of delocalized conduction electrons and holes in semiconductors strongly interact with each other, so that the spin orientation of one specific charge carrier is not conserved for long times, except at very low temperature and/or high magnetic fields when a significant spin polarization is present. This situation is dramatically different for charge carriers trapped in localized defect states in the band gap of a semiconductor. Such defect states can be involved in recombination or transport processes and thus limit the solar cell performance. In the case of paramagnetic defect states, the spin of a trapped charge carrier can be manipulated by means of Electron Paramagnetic Resonance (EPR). This may influence the charge transport in the device in many different ways and can be utilized to study loss mechanisms in solar cells. Thus, the spin of the defect electron may be regarded as a probe which is capable of elucidating the influence of the defect state on the charge transport.

The most important 'spin-to-charge' mechanisms[1] for the effects studied in this thesis are spin-dependent recombination [8] and spin-dependent hopping transport [38]. Both processes are frequently encountered in thin films [39, 40, 41] and devices [42, 43] based on amorphous or microcrystalline silicon and are illustrated schematically in Fig. 2.1. Common to both processes is that they rely on the spin-pair mechanism developed by Kaplan, Solomon and Mott [44] which is referred to as the *KSM model*. Two electrons occupy two localized states in close proximity and constitute a spin pair. In the case of a

---

[1] In EDMR the observable is the conductivity which is determined experimentally by measuring a current signal. Thus, a process which establishes a connection between the spins which are manipulated by the microwave and the charge carriers which contribute to the current, i.e. a 'spin-to-charge' mechanism, is crucial to exist for EDMR.

recombination process as shown on the left side of Fig. 2.1, the spin pair consists of two states with different energy. Although it would be energetically favourable if both electrons occupied the lower-lying state, owing to the Pauli-principle this transition is only allowed when both spins are aligned antiparallel. Thus, invoking that the spin state is conserved during the transition process, the transition is blocked in the case of parallel spins. The application of microwave (mw) radiation, which is resonant with either of the two spin pair constituents, alters the respective spin state and the initially forbidden transition becomes allowed. The recombination process is then completed by the capture of a hole from the valence band. In addition, an electron from the conduction band can be trapped at unoccupied defect state. All in all, one electron from the conduction band and one hole from the valence band are annihilated, resulting in a decrease of the sample conductivity.

In the case of hopping transport as shown on the right side of Fig. 2.1, the spin pair consists of two states having similar energy. Analogous to the recombination process described before, the transition between adjacent singly occupied states can be blocked by the relative spin orientation. Again, resonant mw radiation can flip one spin and enable an initially forbidden transition. The enhancement of the hopping rate can be considered to enhance the mobility in the hopping transport path.

The two mechanisms shown in Fig. 2.1 are explained in more detail in Section 2.3. Since both processes rely on EPR, the following section gives a brief introduction into EPR taking the simplest model, a single spin $1/2$, as an example.

2.2. Basic principles of Electron Paramagnetic Resonance

In an external magnetic field the degeneracy of the spin energy levels is lifted due to the Zeeman-interaction between the magnetic field $\mathbf{B_0}$ and the magnetic moment associated with the spin. The size of this energy splitting is given by the Zeeman term of the spin Hamiltonian which takes the form

$$\hat{H}_Z = \gamma \hat{\mathbf{S}} \cdot \mathbf{B_0} \, , \tag{2.1}$$

where $\hat{\mathbf{S}}$ is the spin operator and $\gamma = \frac{g_e \mu_B}{\hbar}$ the gyromagnetic ratio. Here, $g_e \approx 2.0023$ denotes the g value of the free electron and μ_B represents the Bohr magneton. The g value of a paramagnetic centre in a solid differs from g_e due to spin-orbit interactions as well as the crystal field caused by the host lattice [45, 4]. The variation from g_e is characteristic for the type of defect and can thus be considered as its EPR fingerprint. In general, g is a matrix[2], meaning that the Zeeman energy is a function of the relative orientation of the paramagnetic centre with respect to B_0. For one specific orientation, however, the g matrix can be replaced by a scalar g value. In disordered systems such as amorphous or microcrystalline silicon or polymers, usually many replica of the same paramagnetic defect with statistically distributed orientations coexist in one sample, so that the measurement is a result of the superposition of all these possible orientations referred to as the *powder pattern*. The anisotropy of the g matrix is then reflected in the resulting line shape.

When the magnetic field is oriented along the z-direction, i.e. $\mathbf{B_0} = B_0 \cdot \mathbf{e_z}$, the energy splitting ΔE for a spin $1/2$ with the expectation values of the spin operator $S_z = \pm\hbar/2$ is given by

$$\Delta E = g\mu_B B_0 = \hbar\omega_L \,, \tag{2.2}$$

where ω_L is the *Larmor frequency* describing the spin precession around the magnetic field axis. As it is evident from (2.2), its value is proportional to the magnetic field amplitude B_0. This can be expressed via the relation

$$\frac{\omega_L}{2\pi B_0} = \frac{ge}{4\pi m_e} = \frac{\gamma}{2\pi} \approx 2.80 \text{ MHz/Gauss} = 28 \text{ MHz/ mT} \tag{2.3}$$

with e being the charge and m_e the mass of the electron. The energy difference between the *spin up* and *spin down* states leads to an imbalance between their respective populations. For $\Delta E \ll kT$ the populations of the upper Zeeman state, $N_\uparrow$, and the lower Zeeman state, $N_\downarrow$, are both determined by the Boltzmann distribution, yielding the imbalance

$$\frac{N_\uparrow}{N_\downarrow} = \exp\left[-\frac{\Delta E}{kT}\right] = \exp\left[-\frac{\hbar\omega_L}{kT}\right] \tag{2.4}$$

in thermal equilibrium. This results in a macroscopic spin polarization which amounts to ≈ 5 % at 10 K for $\omega_L/2\pi = 10$ GHz.

In a conventional cwEPR experiment the sample is continuously subjected to mw radiation with fixed frequency ω which induces transitions between the Zeeman levels and equalizes the difference between $N_\uparrow$ and $N_\downarrow$ when the resonance condition is met. The mw absorption is detected as a function of B_0, resulting in an absorption peak when the mw frequency matches the Larmor frequency, i.e. $\omega = \omega_L$. From the centre of the resonance line

---

[2] Although g is no tensor in the strict sense [46], we will use the terms 'g matrix' as well as 'g tensor' interchangeably to refer to the g matrix throughout this thesis.

the g value of the respective paramagnetic centre can be determined, whereas the width of the resonance depends on the g anisotropy (*powder pattern*), the distribution of g values (*g strain*) as well as the spin relaxation times. The intensity of the signal depends on the number of paramagnetic centres in the sample and can thus be used to determine defect concentrations. The sensitivity threshold of cwEPR at X-band (10 GHz) is approximately 10^{11} spins/Gauss [9,4] and is fundamentally limited by the macroscopic spin polarization.

2.3. The spin pair model

Most EDMR measurements can be explained within the framework of the spin pair model [44] that was originally developed for recombination processes and later extended to also describe spin-dependent hopping transport [35]. An earlier model by Lepine [8], in which spin-dependent recombination depends on the thermal polarization of charge carriers, was not able to quantitatively describe the experimental results. In contrast, in all EDMR models based on the spin-pair mechanism, the probability for a transition depends on the symmetry of the spin pair. The time evolution of such a pair is governed by its spin Hamiltonian which consists of a time-independent part, $\hat{H}_0$, and a time-dependent contribution, $\hat{H}_1$. While $\hat{H}_0$ describes the interaction between either of the spins with the external magnetic field as well as mutual spin-spin interactions, $\hat{H}_1$ specifies the interaction between the spin pair and the microwave radiation. The static part can be written as

$$\hat{H}_0 = \frac{g_a \mu_B}{\hbar} \hat{\mathbf{S}}_\mathbf{a} \cdot \mathbf{B_0} + \frac{g_b \mu_B}{\hbar} \hat{\mathbf{S}}_\mathbf{b} \cdot \mathbf{B_0} - \frac{J}{\hbar^2} \hat{\mathbf{S}}_\mathbf{a} \cdot \hat{\mathbf{S}}_\mathbf{b} - \frac{D}{\hbar^2} \left(3 S_a^z S_b^z - \hat{\mathbf{S}}_\mathbf{a} \cdot \hat{\mathbf{S}}_\mathbf{b} \right) \tag{2.5}$$

with g_a and g_b being the g values of spins a and b. The coefficients J and D represent the exchange coupling strength and the electron-electron dipolar coupling strength (for the high field approximation $D \ll |g_i \mu_B B_0|$). The hyperfine interaction with nuclear spins in the vicinity of the spin pair is neglected in (2.5). Note that the Hamiltonian does not exclusively describe spin pairs in semiconductors, but does also apply to spin-correlated radical pairs in organic matter [47, 48, 49, 50]. Consequently, many fundamental effects studied extensively in the field of radical pairs in photo chemistry — often by means of reaction yield detected magnetic resonance (RYDMR) [51] — equally hold true for spin pairs in inorganic and organic semiconductors [52].

The Hamiltonian (2.5) is non-diagonal in the product base $\{|\uparrow\uparrow\rangle, |\uparrow\downarrow\rangle, |\downarrow\uparrow\rangle, |\downarrow\downarrow\rangle\}$ when exchange or dipolar couplings are present. However, it can be diagonalized by a unitary transformation which yields the eigenstates and their respective energies [53, 54, 34]

$$\begin{aligned}
|T_+\rangle &= |\uparrow\uparrow\rangle & E_{T_+} &= \frac{\hbar\omega_0}{2} - \frac{J}{4} - \frac{D}{2} \\
|2\rangle &= \cos(\phi)\,|\uparrow\downarrow\rangle - \sin(\phi)\,|\downarrow\uparrow\rangle & E_2 &= \frac{\hbar\omega_\Delta}{2} + \frac{J}{4} + \frac{D}{2} \\
|3\rangle &= \sin(\phi)\,|\uparrow\downarrow\rangle + \cos(\phi)\,|\downarrow\uparrow\rangle & E_3 &= -\frac{\hbar\omega_\Delta}{2} + \frac{J}{4} + \frac{D}{2} \\
|T_-\rangle &= |\downarrow\downarrow\rangle & E_{T_-} &= -\frac{\hbar\omega_0}{2} - \frac{J}{4} - \frac{D}{2}\,,
\end{aligned} \tag{2.6}$$

which depend on B_0 as well as on J and D. Here, we used the abbreviations

$$\phi = \frac{1}{2}\arctan\left(\frac{J-D}{\hbar\Delta\omega}\right) \qquad \text{and} \qquad \omega_\Delta = \sqrt{\frac{(J-D)^2}{\hbar^2} + \Delta\omega^2} \tag{2.7}$$

with $\omega_0 = \omega_a + \omega_b$ and $\Delta\omega = \omega_a - \omega_b$, where ω_a and ω_b are the Larmor frequencies of both spin pair constituents. It is obvious from (2.6) that the eigenstates of the spin pair generally depend on the ratio between the spin-spin interaction ($J - D$) and the Larmor separation ($\Delta\omega$). However, the product states $|\uparrow\uparrow\rangle = |T_+\rangle$ and $|\downarrow\downarrow\rangle = |T_-\rangle$ are independent of J and D and will thus be referred to as *triplet states* throughout this thesis, even when spin-spin couplings are completely absent. With increasing coupling strength the eigenstates $|2\rangle$ and $|3\rangle$ go over from the product states $|\uparrow\downarrow\rangle$ and $|\downarrow\uparrow\rangle$ with mixed symmetry (for $\phi = 0$) towards the antisymmetric singlet state $|S\rangle = 1/\sqrt{2}(|\uparrow\downarrow\rangle - |\downarrow\uparrow\rangle)$ and the symmetric triplet state $|T_0\rangle = 1/\sqrt{2}(|\uparrow\downarrow\rangle + |\downarrow\uparrow\rangle)$ (for $\phi = \pi/4$). It is worthwhile noting that the combined population of the states $|2\rangle$ and $|3\rangle$ is independent of the basis. This is helpful in the case when the states $|2\rangle$ and $|3\rangle$ can be considered to be equivalent (e.g. when recombination rate coefficients are identical for the states $|2\rangle$ and $|3\rangle$) and calculations are carried out in the product basis. In other words, the combined population of the non-eigenstates $|\uparrow\downarrow\rangle$ and $|\downarrow\uparrow\rangle$ is identical to the combined population of the eigenstates $|2\rangle$ and $|3\rangle$.

2.3.1. From spin pair to current change

The basic principle of EDMR relies on the assumption that the conductivity

$$\sigma = e[n_e\mu_e + n_h\mu_h]\,, \tag{2.8}$$

of a sample changes upon reaching the resonance condition for the spin pair[3]. Here, e is the elementary charge and n_e and n_h represent the concentrations of electrons and holes with their respective mobilities μ_e and μ_h. The resonant excitation can either affect the charge carrier concentrations — as it is the case for a recombination process which annihilates one electron and one hole — or the mobility of electrons and holes by enabling a hopping transition between adjacent singly occupied localized states that is initially forbidden. In both cases the underlying transition depends on the spin pair symmetry. Therefore, the respective transition rate coefficient for the spin pair state $|i\rangle$ becomes [35]

$$r_i = r_S |\langle i|S\rangle|^2 + r_T |\langle i|T_0\rangle|^2 \tag{2.9}$$

with the rate coefficients r_S and r_T for the pure singlet and triplet states, respectively. Together with (2.6) the rate coefficients for the eigenstates of the spin pair can be calculated.

2.3.1.1. Spin-dependent recombination

In a spin-dependent recombination process the charge carrier concentrations are affected by recombining spin pairs. The change in conductivity induced by EPR is thus given by

$$\Delta\sigma_{\mathrm{ph}} = e\left[\Delta n_e(t)\mu_e + \Delta n_h(t)\mu_h\right] \,, \tag{2.10}$$

where Δn_e and Δn_h denote the deviations of the electron and hole concentrations from their respective steady-state values.

Following the description by Boehme [33,35] we will derive the transient current change resulting from a resonant mw pulse. Since the experimental part of this thesis mostly deals with weakly coupled spin pairs, this treatment is also restricted to pairs with negligible spin-spin couplings. Consequently, J and D are assumed to be 0, and the only contribution to the spin pair Hamiltonian (2.5) is the electron Zeeman interaction. Furthermore, the rate coefficients in (2.9), which describe the recombination out of the eigenstates, become identical for the states $|2\rangle$ and $|3\rangle$, so that in total two different rate coefficients are present:

$$r_{1,4} = r_T \qquad \text{and} \qquad r_{2,3} = \frac{1}{2}(r_S + r_T) \,. \tag{2.11}$$

---

[3] Note that this expression is only valid for an ideal semiconductor. In reality, the relationship between charge carrier concentrations, mobilities and conductivity may be more complex — especially when space charge regions are present or when transport over energy barriers at contacts occurs.

We neglect any coherent processes and assume that new spin pairs are created at the same generation rate $G/4$ in all four eigenstates. We further assume a spin-independent dissociation rate coefficient d and omit spin relaxation (T_1 and T_2). Spin-spin relaxation (T_2) influences the current transient signal only in the case of non-vanishing spin-spin interactions as shown in [34].

The time evolution of the spin pair ensemble can conveniently be described within the framework of the density operator formalism [45]. For pairs comprising two $S = 1/2$ particles, the matrix representation of the density operator, $\hat{\rho}$, is given by a 4×4 matrix. Its diagonal elements, ρ_{ii}, represent the populations, i.e. the probability of finding the ensemble in the ith eigenstate as given in (2.6). The non-diagonal elements denote the coherences that describe coherent superpositions of the eigenstates which become important when studying coherent spin effects (see Section 2.5). When coherent effects may be neglected, the time evolution of the spin pair ensemble is given by the time behaviour of the eigenstate populations according to

$$\frac{d}{dt}\begin{pmatrix}\rho_{11}\\ \rho_{22}\\ \rho_{33}\\ \rho_{44}\end{pmatrix} = \frac{G}{4}\begin{pmatrix}1\\1\\1\\1\end{pmatrix} + \begin{pmatrix}-r_T-d & 0 & 0 & 0\\ 0 & -\frac{r_S+r_T}{2}-d & 0 & 0\\ 0 & 0 & -\frac{r_S+r_T}{2}-d & 0\\ 0 & 0 & 0 & -r_T-d\end{pmatrix}\begin{pmatrix}\rho_{11}\\ \rho_{22}\\ \rho_{33}\\ \rho_{44}\end{pmatrix} . \tag{2.12}$$

The density matrix elements influence charge carrier recombination and dissociation and thus affect the concentration of free electrons and holes. The respective rates are given by

$$R(t) = \sum_{i=1}^{4} r_i \rho_{ii}(t) \qquad \text{and} \qquad D(t) = \sum_{i=1}^{4} d\rho_{ii}(t) \, . \tag{2.13}$$

Accordingly, the spin-dependent changes of electron and hole concentrations take the form

$$\Delta n_e = \tau_L \left[D(t) - D^0\right] \qquad \text{and} \qquad \Delta n_h = -\tau_L \left[R(t) - R^0\right] \tag{2.14}$$

with the charge carrier lifetime τ_L which is assumed to be identical for electrons and holes[4]. The superscript 0 denotes the steady-state values of the respective rates. Hence, an increase of the recombination rate reduces the concentration of free holes, and enhanced dissociation of spin pairs leads to a surplus of electrons in the conduction band. Note that the spin

---

[4] In realistic systems the lifetimes of electrons and holes may differ significantly. However, for the sake of simplicity we assume here that both lifetimes are the same.

pair generation rate, which may experimentally be influenced by changing the illumination level, does not enter the description at this point[5].

Together with (2.10) the change in photoconductivity can be written as

$$\Delta\sigma_{\mathrm{ph}}(t) = e\tau_L\mu_e d \sum_{i=1}^{4} \left[\rho_{ii}(t) - \rho_{ii}^0\right] \left(1 - \frac{r_i}{d}\frac{\mu_h}{\mu_e}\right) . \tag{2.15}$$

Combining this result with the solution of the differential equation (2.12) for the density operator yields the transient relaxation of the photoconductivity into the steady-state,

$$\begin{aligned} \Delta\sigma_{\mathrm{ph}}(t) = e\tau_L\mu_e d \bigg[&(\Delta_{11} + \Delta_{44}) \left(1 - \frac{r_T}{d}\frac{\mu_h}{\mu_e}\right) e^{-(r_T+d)t} \\ &+ (\Delta_{22} + \Delta_{33}) \left(1 - \frac{r_2}{d}\frac{\mu_h}{\mu_e}\right) e^{-(r_2+d)t} \bigg] . \end{aligned} \tag{2.16}$$

Here, $\Delta_{ii} := \rho_{ii}(t=0) - \rho_{ii}^0$ represents the difference between the the population of the eigenstate i directly after the pulse and in the steady state (without mw excitation). Note that $\Delta_{22} = -\Delta_{11}$ holds true for weakly coupled spin pairs. It becomes apparent that the photocurrent relaxation following a mw pulse is determined by two exponential functions with different time constants and opposite signs of their amplitudes.

2.3.1.2. Spin-dependent recombination — The bath model

To the best of the author's knowledge, all present models which quantitatively describe pEDMR transients are based on the original approach presented by Boehme *et al.* [33, 34, 35]. In this model, rate equations as given in (2.12) are formulated for the diagonal elements of $\hat{\rho}$, and the change of the photoconductivity is subsequently calculated according to (2.13), (2.14) and (2.10). Initially, generation of spin pairs was assumed to be independent of $\hat{\rho}$. Recently, this model was extended to include a $\hat{\rho}$-dependent generation rate [56, 55]. However, there is one major drawback of this approach: Since the concentration of electrons and holes in the bands, which determine the photoconductivity, are not included in the rate equations, it is impossible to directly express an interrelationship between n_e, n_h and $\hat{\rho}$. To circumvent this limitation, we present a simple model in which

---

[5] The fact that the total concentration of pairs may affect the spin pair generation rate can partly be accounted for by considering a generation rate that depends on $\hat{\rho}$ [55, 56]. However, to correctly incorporate the interaction between free charge carriers and $\hat{\rho}$ via spin pair generation, we suggest to directly include $n_e(t)$ and $n_h(t)$ in (2.12). This approach is presented in Section 2.3.1.2.

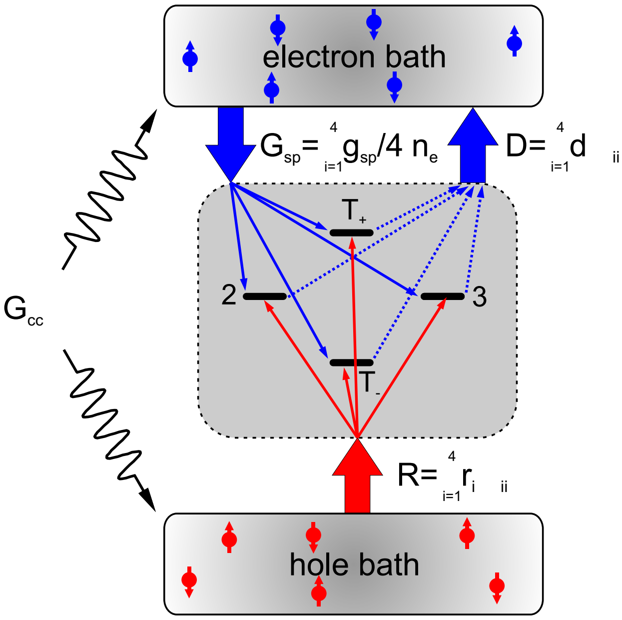

Figure 2.2.: Illustration of the rate equations (2.17) that describe the dynamics of the spin pairs and the free charge carrier concentrations. Free electrons and holes are created by light absorption (at the rate G_{cc}) and act as reservoirs which are connected to the spin pair ensemble via generation (G_{sp}), recombination (R) and dissociation (D). Details are given in the text.

the dynamics of n_e and n_h are calculated explicitly by accounting for the interactions between the spin pair ensemble and the *electrons bath* as well as the *hole bath*. For this purpose, the charge carrier concentrations are included as variables in the rate equations. Note that similar approaches have proven to be successful in modelling cwEDMR results in the past [57, 58, 59, 60, 61].

In the preceding section we assumed that we can derive the time dependence of the photoconductivity by calculating the dynamics of the spin pair density matrix. Spin pair recombination and dissociation — which both solely depend on the spin pair populations and the respective rate coefficients — influence n_e and n_h and thus affect the conductivity. Spin pair generation was taken account of by a constant generation rate G which does not directly depend on n_e and n_h. However, in reality the rate at which electrons from the conduction band are trapped at localized defect states and form spin pairs is certainly affected by n_e.

Consequently, the concentration of free electrons contributes to the spin pair generation rate. In order to account for this fact, a different approach is pursued which is illustrated in Fig. 2.2. Note that we use capital letters for rates (unit $\mathrm{s}^{-1}\ \mathrm{cm}^{-3}$), whereas for rate coefficients (unit s^{-1}) small letters are used throughout this section.

Light absorption leads to the generation of charge carriers in the bands at the rate G_{cc}. Electrons in the conduction band (concentration n_e) and holes in the valence band (concentration n_h) are considered as reservoirs which are connected to the spin pair states via generation, dissociation and recombination. The influence of spin-independent recombination on n_e and n_h is taken into account by introducing a charge carrier lifetime, τ_L, which is assumed to be the same for electrons and holes. Spin pairs are created by trapping of electrons from the conduction band into sites in close proximity to an already singly occupied recombination centre. The rate for this process is denoted by G_{sp} and is proportional to n_e. Note that all spin pair states are populated equally. Dissociation of spin pairs at the rate D, which is equally assumed to be spin-independent, results in an increase of n_e. On the contrary, spin-dependent recombination directly reduces n_h and indirectly leads to a decrease of n_e due to reduced dissociation.

Following the arguments given above, the basis-independent spin pair states $|T_+\rangle$ and $|T_-\rangle$ are equivalent and their combined population can thus be described by $2\rho_{11}$. In the same way one may characterize the population of the mixed states $|2\rangle$ and $|3\rangle$ by $2\rho_{22}$ in the case of negligible spin-spin coupling. The model shown in Fig. 2.2 can easily be described in the form of a system of coupled rate equations

$$\begin{aligned}
\frac{d}{dt}n_e(t) &= G_{cc} + 2d\left[\rho_{11}(t) + \rho_{22}(t)\right] - g_{sp}n_e(t) - \frac{n_e(t)}{\tau_L} \\
\frac{d}{dt}n_h(t) &= G_{cc} - (r_S + r_T)\rho_{22}(t) - 2r_T\rho_{11}(t) - \frac{n_h(t)}{\tau_L} \\
\frac{d}{dt}\rho_{11}(t) &= \frac{g_{sp}}{2}n_e(t) - 2d\rho_{11}(t) - 2r_T\rho_{11}(t) \\
\frac{d}{dt}\rho_{22}(t) &= \frac{g_{sp}}{2}n_e(t) - 2d\rho_{22}(t) - (r_S + r_T)\rho_{22}(t)
\end{aligned} \tag{2.17}$$

with the recombination rates r_S and r_T out of the pure singlet and triplet states, respectively. For the sake of simplicity we omit spin relaxation effects. Since only the diagonal elements of the density matrix (the populations) are taken into account, this approach does not allow us to derive any coherent effects — which is justified for calculation the incoherent current relaxation following a mw pulse. When coherent effects cannot be neglected, all components of the density matrix have to be included in (2.17).

Although it is straightforward to solve the set of linear rate equations in (2.17) analytically, the resulting expressions are lengthy and inconvenient to handle unless we make further assumptions. However, some features which are vital for the measurements are independent of the choice of parameters. First, the amplitude of the photocurrent transient (referred to as *pEDMR transient*) is proportional to the deflection of the diagonal elements

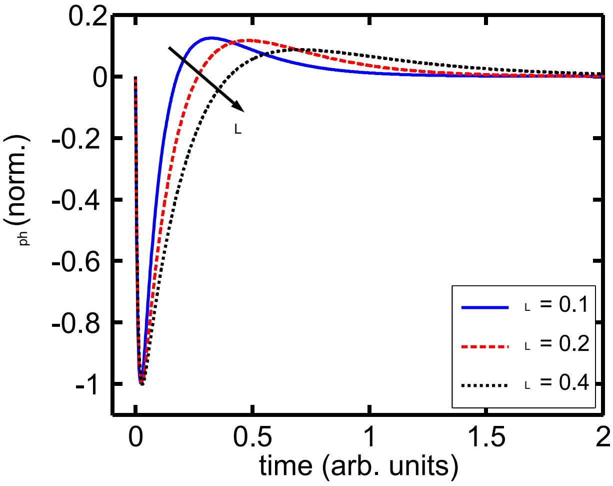

Figure 2.3.: Transient change of the photoconductivity $\Delta\sigma_{\text{ph}}$ following a resonant π mw pulse obtained by solving (2.17) for $G_{cc} = 10$, $d = 0.2$, $g_{sp} = 0.2$, $r_S = 100$ and $r_T = 2$. The plot shows transients for different values of τ_L as indicated in the legend.

of $\hat{\rho}$ from their respective steady-state values, i.e. $\sigma_{\text{ph}}(t=0) \propto \Delta\rho_{ii}(t=0) - \rho_{ii}^0$. Second, the pEDMR transient follows a multiexponential decay, whereas the time constants depend on the choice of the rate coefficients in (2.17). Both facts constitute the basis for pulse length dependent measurements discussed later. A third general point deserves some attention: The time constants of the pEDMR transient do not only depend on the spin-dependent rate constants r_S and r_T, but are also affected by spin-independent properties of the charge carriers in the bands, most importantly by τ_L. Therefore, the time constants of experimentally obtained pEDMR transients originate from a superposition of several effects, and thus it is generally complicated to extract r_S and r_T from a pEDMR transient — even if the current detection had infinite time resolution.

To illustrate the general behaviour of the pEDMR transient and in particular its dependence on the charge carrier lifetime, Fig. 2.3 shows $\Delta\sigma_{\text{ph}} = e\left[\Delta n_e(t)\mu_e + \Delta n_h(t)\mu_h\right]$ for several values of τ_L following a resonant $\pi/2$ pulse assuming identical mobilities for electrons and holes. For this purpose, (2.17) was solved with the initial conditions $\rho_{11}(t=0) = \rho_{22}^0$ and $\rho_{22}(t=0) = \rho_{11}^0$. The parameters used for the simulation are given in the caption of Fig. 2.3 in relative units. It becomes obvious that τ_L can severely affect the time constants of the pEDMR transient. Note that τ_L also influences the amplitude of σ_{ph} which cannot be observed in Fig. 2.3 because the pEDMR transients were normalized to equal amplitudes.

At this point it is important to mention a qualitative difference between EDMR and other magnetic resonance techniques such as ODMR and RYDMR that make a different theoretical description indispensable. In ODMR each radiatively recombining spin pair immediately emits a photon and thus directly contributes to the luminescence (the observable).

Similarly, in RYDMR each reaction product does also directly influence the observable, i.e. the optical absorption or the fluorescence. In contrast to that, in EDMR a recombining spin pair first results in a change of the charge carrier concentrations which in turn influence the conductivity. Hence, spin pair recombination has an indirect influence on the observable. Consequently, it is necessary to include n_e and n_h with their explicit time dependence in the rate equations in order to correctly describe the pEDMR dynamics.

It is worthwhile noting that the effect of spin pair generation, which was assumed to occur at the same rate for all four spin pair states, can be studied experimentally by means of a recently demonstrated pEDMR rotary echo experiment as shown in Appendix C [62].

2.3.1.3. Hopping transport

Hopping transport of charge carriers among paramagnetic localized states can influence the conductivity according to (2.8) in a similar way like spin-dependent recombination. When a ‘hop’ — i.e. the tunnelling process from one localized state to another — occurs between two singly occupied states, spin selection rules govern the transition probability, provided that the spin is conserved throughout the transition. Consequently, EPR can manipulate the spin states and in turn alter transition rates. In contrast to spin-dependent recombination, hopping does not affect the total charge carrier density in a sample. However, the resulting change in conductivity can be treated as a mobility variation of the respective charge carriers. The following description of spin-dependent hopping transport is based on a one-dimensional model which was developed by Boehme and Lips [35].

In disordered semiconductors such as amorphous silicon, localized states exist below the mobility edge for electrons (*conduction band tail states*) and above the mobility edge for holes (*valence band tail states*). At room temperature, these states do not significantly contribute to the transport which is dominated by delocalized charge carriers in the bands. However, upon decreasing the temperature, hopping of charge carriers among band tail states in a range of kT around the Fermi level (or quasi-Fermi level in case of non-equilibrium carrier concentrations) becomes substantial. This can be inferred from temperature-dependent conductivity measurements [24]. Hopping transport can take place in different configurations as illustrated in Fig. 2.4 for two states in spatial and energetic proximity near the electron quasi-Fermi level E_{fn}. The energies of both states are denoted by E_A and E_B. The state for the second electron in a doubly occupied state is higher by the correlation energy U which results from the intrastate interaction energy. Obviously, there

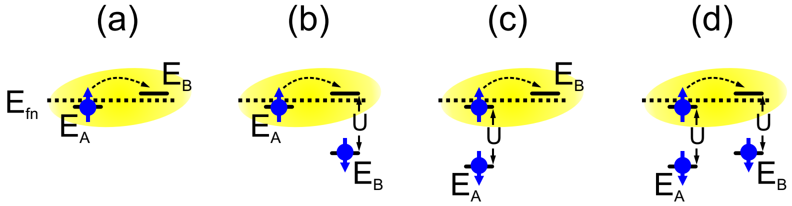

Figure 2.4.: Hopping among localized states in the presence of the correlation energy U. The four depicted processes differ in the occupation of both states prior to the transition (adapted from [63]).

are four different possible hopping processes (a), (b), (c) and (d) which differ in the occupation of both states before the hopping step. While state A can either be singly or doubly occupied, state B can be empty or accommodate one electron prior to the transition. When a state is doubly occupied, i.e. in Fig. 2.4c and d, both spins form a singlet state which cannot be manipulated by EPR. Thus, the hopping transition is not spin-dependent in this case. Note that only process (b) can be spin-dependent and thus evoke effects such as EDMR and magnetoresistance [64,65]. Note further that the size of the correlation energy U plays an important role here. For spin-dependent hopping to occur, U must necessarily be smaller than the width of the distribution function for the energies of the localized states [66, 67, 67]. This is certainly the case for amorphous silicon, where the band tail states extend far into the gap, and the correlation energy is on the order of 10 meV [68].

In the case of two singly occupied states the tunnelling probability depends on the permutation symmetry of the spin pair. In analogy to the description of spin-dependent recombination, the rate coefficients for the hopping transition can be written as

$$p_{1,4} = p_T \qquad \text{and} \qquad p_{2,3} = \frac{1}{2}(p_S + p_T) \tag{2.18}$$

for weakly coupled spin pairs where the spin-spin interaction can be neglected. In this case the rate coefficients for the eigenstates $|2\rangle \approx |\uparrow\downarrow\rangle$ and $|3\rangle \approx |\downarrow\uparrow\rangle$ are identical. The coefficients p_S and p_T in (2.18) refer to the pure singlet and triplet states.

To account for the fact that spin-dependent and spin-independent transport paths coexist, Boehme and Lips [35] suggested to describe the hopping process as illustrated in Fig. 2.5. The figure shows a *pair site* [35] indicated by the shaded region which consists of two energy states A and B. These states are surrounded by two other localized states. When both states of the pair site are singly occupied, they comprise a *spin pair* which is formed

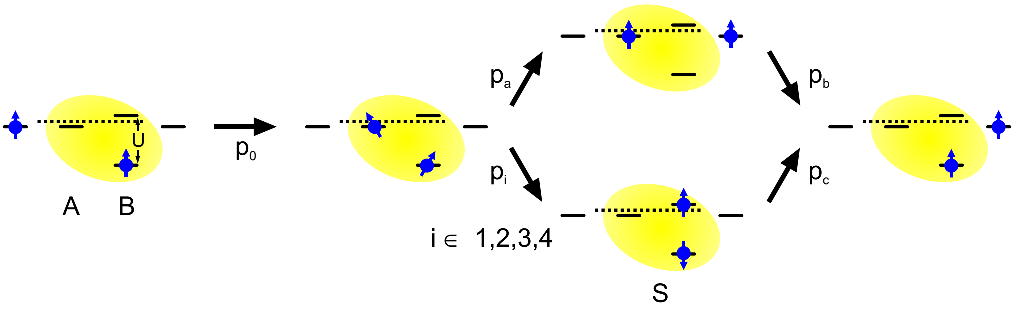

Figure 2.5.: Electron hopping through a pair site based on the spin-dependent hopping model presented in [35]. Note that only the transition from the spin pair state $|\psi\rangle$ into the singlet state $|S\rangle$ is spin-dependent. In addition, there is an alternative hopping path which is spin-independent. Further information is given in the text.

by a tunnelling transition of one electron from a state outside the pair site to the previously unoccupied state A. This process takes place with a probability p_0. The resulting pair is assumed to be in the state $|\psi\rangle$ which can generally be any superposition of the spin pair states given in (2.6). The electron in state A can tunnel into state B, where the ground state of the doubly occupied state B only exists as a singlet. As a result, the probability for this transition depends on the singlet content of the spin pair and is denoted by p_i which is specified in (2.18). One of the electrons may then tunnel into another state and thus leave the pair site with the probability p_c.

The same final state is reached from the spin pair state $|\psi\rangle$ when the electron in state B undergoes a transition to an energy level outside the pair site and a subsequent hop of the remaining electrons from state A to state B. Both processes are assumed to occur with the probability p_a and p_b, respectively. Hence, there is one spin-dependent and one spin-independent pathway for the dissociation of the spin pair from the state $|\psi\rangle$ to the final situation depicted in the rightmost part of Fig. 2.5. Therefore, the situation is similar to the case of spin-dependent recombination as discussed in Section 2.3.1.2 where spin pair recombination is spin-dependent whereas spin pair dissociation is not. As a result, spin-dependent hopping transport may be described in a similar way. The corresponding rate coefficients for the hopping processes can be expressed by the relation

$$d_i = p_a \cdot p_b + p_i \cdot p_c \qquad \text{with} \quad i \in 1,2,3,4 \tag{2.19}$$

with the rate coefficients for the individual steps indicated in Fig. 2.5. It becomes apparent that the spin-dependence of d_i (and thus the signal intensity of the associated EDMR signal) critically depends on the ratio between the probabilities for the spin-dependent and the spin-independent paths [35].

Assuming that spin pairs at pair sites are generated at a constant rate $G/4$ which is equal for all four eigenstates of the spin pair, we can express the time evolution by the rate equations

$$\frac{d}{dt}\begin{pmatrix}\rho_{11}\\ \rho_{22}\\ \rho_{33}\\ \rho_{44}\end{pmatrix} = \frac{G}{4}\begin{pmatrix}1\\1\\1\\1\end{pmatrix} + \begin{pmatrix}-d_1 & 0 & 0 & 0\\ 0 & -d_2 & 0 & 0\\ 0 & 0 & -d_3 & 0\\ 0 & 0 & 0 & -d_4\end{pmatrix}\begin{pmatrix}\rho_{11}\\ \rho_{22}\\ \rho_{33}\\ \rho_{44}\end{pmatrix} . \tag{2.20}$$

in analogy to (2.12). The steady-state solutions are given by

$$\rho^0_{11,44} = \frac{G}{4d_1} \qquad \text{and} \quad \rho^0_{22,33} = \frac{G}{4d_2} , \tag{2.21}$$

indicating a surplus of spin pairs in the triplet states when $d_1 < d_2$.

A spin-resonant excitation alters the spin pair populations according to $\Delta\rho_{ii}(t) = \rho_{ii}(t) - \rho^0_{ii}$ and in turn changes the respective spin-dependent transport rate. This effect can be considered as a variation of the electron mobility μ_e. As long as the resulting deviation of μ_e from its steady-state value μ^0_e is small, the mobility can be expanded in terms of the spin-dependent transport rate R_i. The corresponding change of μ_e then yields $\Delta\mu_e(\Delta R_i) = \mu^0_e + \frac{\partial\mu_e}{R_i}\Delta R_i$. Since the variation of the microscopic transport rate is given by $\Delta R_i = \sum_i \Delta\rho_{ii} d_i$, the resulting change in conductivity according to $\sigma = en_e\mu_e$ takes the form [35]

$$\Delta\sigma(t) = en_e\frac{\partial\mu_e}{\partial R_i}\sum_{i=1}^{4}\left[\rho_{ii}(t) - \rho^0_{ii}\right] d_i . \tag{2.22}$$

Combining this result with the solution of the rate equations given in (2.20) leads to the transient change of the conductivity following a resonant mw pulse ending at $t = 0$

$$\Delta\sigma(t) \propto \left[e^{-d_2 t} - e^{-d_1 t}\right]\Delta \qquad \text{with} \quad \Delta := \rho_{22}(t=0) - \rho^0_{22} = -[\rho_{11}(t=0) - \rho^0_{11}] \tag{2.23}$$

for spin pairs with negligible spin-spin coupling. Here, Δ represents the spin pairs that are shifted form the triplet states towards the states with mixed symmetry by the resonant mw pulse. Steady-state populations are indicated by the superscript 0. Similar to case of recombination, the conductivity transient exhibits a multiexponetial (in this particular case biexponential) relaxation to its steady-state value. It is important to mention that the sign of $\Delta\sigma$ immediately after the mw pulse is always positive, i.e. current enhancing, when the transition probability increases with the singlet content of the spin pair.

In contrast to the recombination process discussed in Section 2.3.1.2, the spin-resonant change of hopping rates *directly* affects the transport and hence the conductivity. Therefore, the concentrations of free electrons and holes are not directly affected here.

Although both spin-dependent processes as described in this section rely on the spin pair model, it is conceivable that other processes equally lead to EDMR signals. In the following Section 2.4 we suggest an alternative EDMR mechanism involving three charge carriers which is capable of consistently explaining several experimental observations which are in contradiction to existing EDMR models based on the spin-pair mechanism. Even though we cannot unambiguously identify this process to be responsible for the signals observed in Chapters 4, 5 and 6, it might particularly be relevant for the correct interpretation of recently reported EDMR measurements at high magnetic fields in the presence of significant thermal electron spin polarization [69, 70, 71].

2.4. The bound exciton model

Lepine was the first to demonstrate spin-dependent recombination of photogenerated charge carriers in silicon at room temperature [8]. To quantitatively explain the experimental results, he developed a model for spin-dependent recombination based on (originally spin-independent) Shockley-Read-Hall (SRH) recombination [72]. According to this model, the optically generated charge carriers in the conduction band recombine via singly occupied states deep in the band gap. The spin polarizations of both recombination partners, i.e. conduction electrons and electrons in the deep defects, were assumed to obey Boltzmann statistics given in (2.4). As a result of this assumption, the model predicts that the EDMR signal is proportional to T^{-2} as well as to B_0^2. However, neither the temperature dependence nor the magnetic field dependence could be confirmed experimentally in proceeding studies on similar specimens. In addition to that, the observed magnitude of the EDMR signals at room temperature exceeded those predicted by Lepine's model by a factor of ≈ 100. These deviations between experimental results and theoretical predictions triggered the development of the Kaplan-Solomon-Mott (KSM) model [44] (cf. Section 2.3) which constitutes the basis for spin-dependent recombination and hopping transport as explained above. The KSM model correctly describes the experimentally observed independence of most EDMR signals with regard to temperature and amplitude of the magnetic field. Since it assumes that two charge carriers are trapped in two localized states in close proximity, the corresponding EDMR spectrum should always exhibit the signature of both charge carriers. However, there are only a few examples where this is the case, e.g. hopping via conduction band tail states and phosphorus donor states in amorphous silicon [73], donor-acceptor recombination in c-Si [74] and recombination from phosphorus ^{31}P donor states to localized states at the c-Si/SiO$_2$ interface (P$_b$ states) [75]. Even in these selected examples there is evidence that the KSM model cannot account for all features, e.g. in the studies on donor-acceptor recombination the acceptor signal is not observed in all cases [4]. Furthermore, for samples where EDMR signals are usually interpreted to arise from recombination between ^{31}P and P$_b$ states — the prime model system for KSM recombination — it was found that the ratio between EDMR signal intensities associated with both centres depends on the experimental conditions like applied voltage and illumination level [76]. It is even possible to completely suppress the spectral feature related to one of the paramagnetic centres and to change the sign of the resonant current change simply by adjusting the applied voltage. These findings clearly reveal that even in systems which are claimed to be well understood with regard to EDMR, the underlying microscopic mechanisms often lack fundamental understanding — a fact that is sometimes not mentioned in regular publications.

Several attempts have been made in the past to modify the KSM model in such a way, that only the EPR signature of one paramagnetic centre appears in the spectrum and the detection of the recombination or hopping partner remains elusive. In the particular example of recombination between e states and db states in a-Si:H only a single line was observed with a g value approximately in the middle between the g values of both individual centres [77]. For this effect to occur, strong exchange coupling between the recombination partners is necessary. Although this would in principle not be in contradiction to the cwEDMR results at that time, more recent pEDMR experiments on similar samples have not revealed any evidence of such strong exchange coupling [78]. Further on, Rong and coworkers developed an EDMR mechanism which is based on SRH recombination but at the same time shares fundamental properties with the KSM model [58]. Similar to the Lepine model, an electron from the conduction band is trapped at singly occupied deep defect state. The EDMR resonance occurs when the electron in the deep defect becomes resonant. Rong *et al.* [58] argue that the trapped electron itself might be invisible to EDMR because it possibly has a broad distribution of g values. Another approach to explain the existence of only one line is based on the *direct capture* process [79, 11]. Here, the spin-manipulation takes place in an excited state consisting of two electrons in a db centre. It is therefore inherently impossible to selectively address one member of the spin pair, which has important consequences for the electrically detected Rabi oscillations as discussed in Section 2.5. In this regard, also the direct capture model frequently fails to correctly describe dangling bond recombination.

All in all, even after almost 40 years of EDMR on samples which did not change considerably during that time, many experimental results cannot consistently be explained within the framework of the existing models. From the arguments stated above it seems that the correct explanation of many EDMR results requires a model that (a) accounts for large signal intensities that cannot be explained by thermal spin polarization (similar like in the KSM model), (b) leads to only one resonance line in the EDMR spectrum, (c) can explain that the coherent spin motion exhibits the behaviour of a single spin $1/2$ and (d) may produce either a current enhancement or current quenching. The necessity for EDMR mechanisms beside the ones incorporated in the existing models is even emphasized by the recently reported results of EDMR performed at low temperatures and high fields where a strong thermal polarization of the electron spins exists [69, 70, 71]. It was found that the spin-dependent processes that govern EDMR low temperature/high field regime are at variance with the experiments carried out in X-band in the absence of strong thermal polarization.

In the following, we will present an EDMR mechanism that involves three charge carriers and which is capable of fulfilling the conditions (a) to (d). Although the addition of a third particle might at first appear to increase the complexity, it turns out that the description becomes even simpler than in the spin pair model. In this regard it is interesting to note that the potential importance of a three-spin process for EDMR was already recognized as early as 1980 by Haberkorn and Dietz [52]. Vranch later suggested a qualitative model based on an electron and a hole trapped at a P_b state also comprising a three-spin system [80] which, however, did not attract much attention. The model presented here follows the approach by Vranch.

We assume that one electron from the conduction band and one hole from the valence band are trapped close to a singly occupied defect state. The defect might either be a

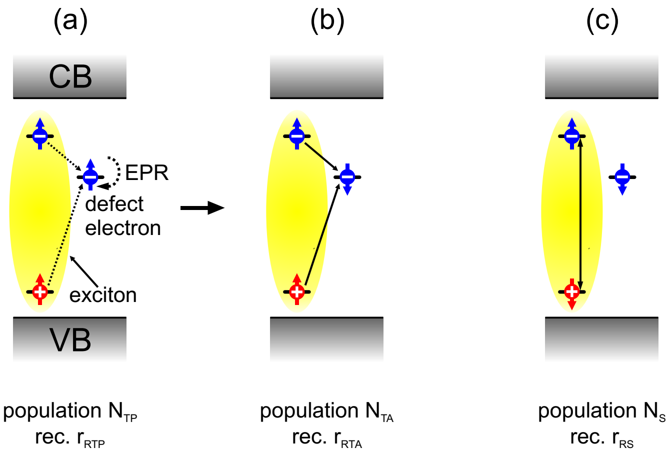

Figure 2.6.: Different configurations of an exciton comprising one electron and one hole trapped at a singly occupied defect state. The representation of the respective states in the product base and its corresponding population is indicated below each schematic band diagram. (a) Triplet exciton bound to defect spin with parallel spin alignment, (b) triplet exciton bound to defect spin with antiparallel spin alignment, (c) singlet exciton. Details are given in the text.

dangling bond in the bulk material or a P_b centre at a Si/SiO_2 interface. The different configurations of this three-spin system are illustrated in Fig. 2.6. When the electron and the hole are in a singlet state, they will recombine almost immediately with a rate coefficient r_{RS}, regardless of the spin state of the defect electron. When they are in a triplet configuration, i.e. when their spins are aligned parallel, the recombination is less probable than in the singlet state. Depending on the spin state of the defect electron, we have to distinguish between two situations: (i) If the spin of the defect electron is parallel to the spin of the exciton electron, i.e. $|\uparrow\Uparrow\uparrow\rangle$ or $|\downarrow\Downarrow\downarrow\rangle$, the recombination path is almost blocked and recombination will take place at the (relatively low) probability r_{RTP}. (ii) In the opposite case, i.e. $|\uparrow\Uparrow\downarrow\rangle$ or $|\downarrow\Downarrow\uparrow\rangle$, we anticipate that the recombination probability r_{RTA} is significantly higher as compared to case (i). In the notation used here the first and the second arrow indicate the spin states of the electron and the hole comprising the exciton, whereas the third arrow denotes the spin of the defect electron. Note that we use the term *exciton* for a correlated electron hole pairs (geminate pairs) which may have different properties than excitons in pure crystals [24]. Nevertheless, as far as amorphous silicon is concerned, there is strong experimental evidence that excitonic effects influence the recombination properties at low temperatures [81, 82, 83, 84, 85].

Table 2.1.: Explanation of the terms used for the description of defect-trapped excitons.

parameter	physical quantity
N_S	population of trapped singlet excitons
N_{TP}	population of trapped triplet excitons with defect electron spin parallel to exciton electron spin
N_{TA}	population of trapped triplet excitons with defect electron spin antiparallel to exciton electron spin
R_{CS}	creation rate for states with population N_S
R_{CTA}	creation rate for states with population N_{TA}
R_{CTP}	creation rate for states with population N_{TP}
r_{RS}	recombination rate coefficient for states with population N_S
r_{RTA}	recombination rate coefficient for states with population N_{TA}
r_{RTP}	recombination rate coefficient for states with population N_{TP}
r_{ISC}	intersystem crossing rate coefficient for transitions between trapped singlet excitons and trapped triplet excitons

We further introduce a rate coefficient r_{ISC} to take account of a finite intersystem crossing probability for the transition between triplet and singlet excitons. The presence of intersystem crossing might strongly depend on the sample structure and the experimental conditions. This process is assumed to be independent of the defect electron spin. The concentrations of the defect-trapped excitons (DTE) are represented by N_S, N_{TP} and N_{TA} with the corresponding creation rates R_{CS}, R_{CTP} and R_{CTA}. The meaning of all parameter is summarized in table 2.1.

Creation of DTE can either take place by the encounter of separately created (by illumination of electrical injection) electrons and holes near a defect site or by trapping of an optically generated exciton consisting of a geminate electron hole pair. While it is reasonable to presume that R_{CTP} and R_{CTA} are equal at room temperature and even at low temperatures (e.g. $T = 10$ K) at X-band frequency, we anticipate an imbalance between both rates when a significant thermal polarization of the defect electrons spin is present in the low temperature/high field regime. This can easily be taken into account by choosing R_{CTP} and R_{CTA} accordingly.

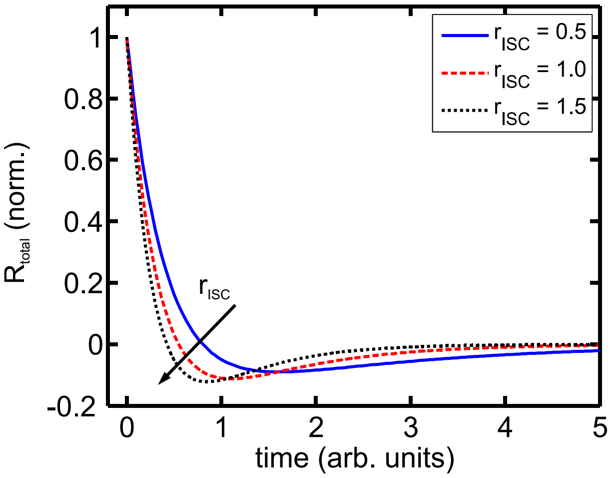

Figure 2.7.: Transient change of the total recombination rate normalized to 1 as defined in (2.25) following a resonant π-pulse according to (2.24) for $R_{CS} = R_{CTA} = R_{CTP} = 10$, $r_{RTA} = 2$, $r_{RTP} = 0$ and $r_{RS} = 100$. The plot shows transients for different values of the intersystem crossing rate as indicated in the legend.

With the definitions given above we can describe the dynamics of the DTE populations by

$$\begin{aligned}
\frac{d}{dt}N_{TA}(t) &= -r_{ISC}N_{TA}(t) + \frac{r_{ISC}}{2}N_S(t) \qquad - r_{RTA}N_{TA}(t) + R_{CTA} \\
\frac{d}{dt}N_{TP}(t) &= -r_{ISC}N_{TP}(t) + \frac{r_{ISC}}{2}N_S(t) \qquad - r_{RTP}N_{TP}(t) + R_{CTP} \\
\frac{d}{dt}N_S(t) &= -r_{ISC}N_S(t) \quad + r_{ISC}\left[N_{TA}(t) + N_{TP}(t)\right] - r_{RS}N_S(t) \quad + R_{CS}\,.
\end{aligned} \tag{2.24}$$

Similar like in the KSM-model of spin-dependent recombination, an excess population of the component with the longest lifetime, i.e. N_{TP}, builds up in the steady-state. When the EPR condition for the defect electron is satisfied, the spin state of the defect electron is manipulated, the population N_{TA} is increased and the concomitant recombination rate of DTE changes abruptly. The relaxation of the DTE populations is given by (2.24). The resulting transient behaviour of the total DTE-related recombination rate change,

$$\Delta R_{\text{total}} = \Delta N_{TA}(t) \cdot r_{RTA} + \Delta N_{TP}(t) \cdot r_{RTP} + \Delta N_S(t) \cdot r_{RS}\,, \tag{2.25}$$

is shown in Fig. 2.7 for a resonant π-pulse on the defect electron spin for different values of the intersystem crossing rate coefficient. The plot shows that the relaxation of the DTE relaxation rate is qualitatively similar like in the KSM-based recombination model presented in Section 2.3.1.2 and indicates that on the one hand certain experimental results previously interpreted in the light of KSM-recombination might in fact originate from recombination of defect trapped excitons. On the other hand, Fig. 2.7 demonstrates that the discrimination between these two different processes based on pEDMR transients alone is impossible and thus the interpretation is always plagued with ambiguity. Furthermore, it is worthwhile noting that to derive the conductivity transient, one has to include the concentrations of free electrons and holes in the rate equations in (2.24) like it was shown in Section 2.3.1.2.

We will now address the question how such a process may affect the conductivity. Excitons generally do not directly contribute to the current because they are electrically neutral. As a result, also the recombination of excitons has no direct effect on the current-carrying free charge carriers. However, the energy that is released during the recombination process may be transferred to the defect electron through an Auger process. The defect electron might thus be emitted to the conduction band and contribute to the conductivity. Auger recombination has indeed been reported for amorphous silicon at low temperatures and light intensities used for EDMR [86, 87, 88, 89]. Also in crystalline silicon — the other important component of the devices investigated in this study — the Auger energy transfer from a recombining donor-bound exciton to the donor electron and its subsequent emission to the conduction band is known to be a very efficient process [90].

Since the spin manipulation is restricted to the defect electron, the EDMR spectrum exhibits only one resonance line with the g value of the defect electron. Accordingly, measurements that probe the coherent spin motion will equally reveal only the EPR signature of the defect electron.

It is important to stress one important point concerning the sign of the EDMR signal which is markedly different for the DTE model and spin-dependent recombination according to the KSM-model: A recombination processes as described in the KSM model annihilates one electron and one hole. Hence, enhanced recombination due to EDMR should effectively reduce the conductivity because the concentrations of both free electrons and free holes are reduced, although the pEDMR transient may exhibit positive as well as negative components[6]. In the DTE model as described above, however, the recombination of an exciton leads to one additional electron in the conduction band and leaves the hole concentration unaffected. Consequently, the sign of the EDMR signal critically depends on the ratio between electron and hole mobilities at the position where the exciton recombines. When electrons are the majority carriers with a high mobility, the additional electron will directly contribute to the current and thus a positive EDMR signal is observed. In contrast

---

[6] For the sake of simplicity, we exclude here devices and experimental conditions where enhanced recombination increases the device current such as pin solar cells in the forward bias regime [91].

to that, when the current is dominated by holes and the electron mobility is low, the released electron will not significantly contribute to the current but rather recombine with a current-carrying hole. As a result, the conductivity is reduced and a negative EDMR signal is expected — a fact which might at first appear to be counterintuitive, because the DTE recombination releases one additional electron. Such an effect was e.g. observed in photocurrent spectroscopy applied to phosphorus-bound excitons in boron-doped crystalline silicon [92] and might also influence EDMR signals in the same way, especially when the experiments are performed at low temperatures. Note that it is generally complicated to ascertain the sign of an EDMR signal from a cwEDMR experiment because the sign of the measurement signal depends on the lock-in phase. Similarly, in a pEDMR experiment overshoots of the transient may obscure the 'real' signal. In contrast to that, the sign of a EDMR signal can unequivocally be determined from a DC-EDMR experiment [93] when the amplitude of the spin-dependent signal is sufficiently strong.

2.5. Coherent spin motion

So far we were concerned with the transient behaviour of a macroscopic variable (i.e. the conductivity) *after* an EPR manipulation. It was assumed that any coherences which might have been created during the mw pulse decay rapidly and can thus be neglected for the description of pEDMR transients. In particular, only the populations of the spin pair eigenstates (the diagonal elements of the density matrix $\hat{\rho}$) given in (2.6) have to be included in the rate equations. In contrast to this incoherent regime, we will now focus on the coherent spin motion *during* the mw pulse sequence which may consist of one or more separate pulses. While the description of the (incoherent) pEDMR transients depends on the underlying recombination or hopping model, the coherent effects described in this section are solely determined by the physics of the spin pair ensemble — which is generally the same for the two microscopic mechanisms.

2.5.1. Rabi oscillations

The coherent spin dynamics is determined by the temporal evolution of the spin pair density matrix. The time dependence of $\hat{\rho}$ is given by the Liouville-von Neumann equation [94]

$$\frac{d\hat{\rho}(t)}{dt} = -\frac{i}{\hbar}\left[\hat{H}(t), \hat{\rho}(t)\right] \tag{2.26}$$

with the spin pair Hamiltonian $\hat{H}(t) = \hat{H}_0 + \hat{H}_1(t)$. The time-independent part $\hat{H}_0$ describes the spin-spin interactions and the interaction of either of the spins with the static magnetic field. The time-dependent part $\hat{H}_1(t)$ specifies the interaction between the spins and the microwave magnetic field and is given in its general form by

$$\hat{H}_1(t) = \frac{g_a \mu_B}{\hbar} \hat{\mathbf{S}}_\mathbf{a} \cdot \mathbf{B_1}(t) + \frac{g_b \mu_B}{\hbar} \hat{\mathbf{S}}_\mathbf{b} \cdot \mathbf{B_1}(t) \tag{2.27}$$

for a pair consisting of two spins a and b with spin operators $\hat{\mathbf{S}}_\mathbf{a}$ and $\hat{\mathbf{S}}_\mathbf{b}$ and g values g_a and g_b, respectively.

The mw field $\mathbf{B_1}(t) = 2B_1 \cdot \mathbf{e_x} \cos(\omega t)$ is assumed to be linearly polarized in x-direction and has the amplitude[7] $2B_1$. The microwave frequency is represented by $\omega/2\pi$, and $\mathbf{e_x}$ denotes the unit vector in x-direction. For analytical calculations and illustrative purposes it is convenient to decompose $\mathbf{B_1}(t)$ into two circularly polarized components according to

$$\mathbf{B_1}(t) = B_1 \begin{pmatrix} \cos \omega t \\ -\sin \omega t \\ 0 \end{pmatrix} + B_1 \begin{pmatrix} \cos \omega t \\ \sin \omega t \\ 0 \end{pmatrix} . \tag{2.28}$$

Only the first term in (2.28) describes the resonant part of the mw field which becomes obvious from the following arguments. Without mw radiation, a single spin $1/2$ (i.e. one constituent of a weakly coupled spin pair) precesses around the axis of the static magnetic field $\mathbf{B_0}$ at the Larmor frequency ω_L given in (2.2). Hence, the spin is at rest when described in a reference frame defined by x', y' and z which equally revolves around the z-axis at the same frequency ω_L. When the mw field is switched on and the mw frequency ω matches ω_L, the first component of (2.28) is stationary[8] in the same *rotating frame*. It thus causes the spin to rotate around the x'-axis at the *Rabi frequency* $\Omega = \gamma B_1$. When ω and ω_L are different, a residual component of $\mathbf{B_0}$ remains in the rotating frame. The Rabi frequency then takes the form

$$\Omega = \sqrt{(\gamma B_1)^2 + (\omega - \omega_L)^2} \, . \tag{2.29}$$

---

[7] The factor 2 appears because the ‘active’ component of $\mathbf{B_1}(t)$ is supposed to have the amplitude B_1.

[8] The second term in (2.28) describes a counterrotating component. Since it has the frequency 2ω, it can be considered as a high-frequency perturbation which can be neglected for the spin motion. This procedure which is frequently used in quantum optics is referred to as *rotating wave approximation* (RWA).

According to (2.26), the population of the spin pair states depends on $\hat{H}_1(t)$ which in turn is influenced by the mw pulse length τ. Therefore, the EDMR signal — in particular the amplitude of the pEDMR transient — is also determined by τ. As demonstrated in detail in Appendix A, we have to distinguish two fundamentally different cases, namely *selective* and *non-selective excitation*.

When the Larmor separation between both spin partners of a pair is larger than the mw field ($\hbar\Delta\omega \gg g\mu_B B_1$), the mw pulse manipulates only one spin (selective excitation, cf. Appendix A.2). In this situations, the occupation of the components of $\hat{\rho}$ oscillates at the Rabi frequency Ω of a single spin $1/2$. This can be demonstrated by considering the dependence of the combined population of the basis-independent spin pair states $|\uparrow\uparrow\rangle$ and $|\downarrow\downarrow\rangle$ as a function of τ. The derivation of the resulting expression for weakly-coupled spin pairs[9],

$$\rho_{11}^{f} + \rho_{44}^{f} = \frac{1}{2} + \frac{1}{2}\cos\Omega\tau\,, \tag{2.30}$$

is described in Appendix A.2.

In the case of non-selective excitation ($\hbar\Delta\omega \ll g\mu_B B_1$) — also referred to as *spin-locking* — the mw pulse is resonant for both members of the spin pair at the same time. Therefore, both spins rotate around the x'-axis simultaneously and lead to a qualitatively different behaviour of the density matrix. In contrast to (2.30), the combined population of the pure triplet states oscillates according to

$$\rho_{11}^{f} + \rho_{44}^{f} = \frac{3}{4} + \frac{1}{4}\cos 2\Omega\tau \tag{2.31}$$

at the frequency 2Ω (see Appendix A.3 for the derivation of this expression). Furthermore, the oscillation is less effective, i.e. the population $\rho_{11}^{f} + \rho_{44}^{f}$ is changed between 0.5 and 1 when spin-locking is present. Especially the different Rabi frequencies allow for an experimental discrimination between selective excitation and spin-locking. Since $g\mu_B B_1$ is proportional to $\sqrt{P_{\mathrm{mw}}}$ (P_{mw} is the microwave power), one can access the spin-locking regime by increasing P_{mw}. Alternatively, it is possible to reduce $\Delta\omega$ by decreasing B_0, which is more complicated to realize experimentally.

---

[9] The superscript ‘f’ denotes the final state of the density matrix, i.e. $\hat{\rho}$ after the application of a resonant pulse.

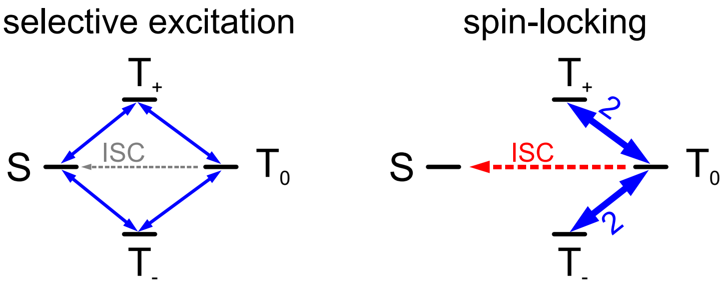

Figure 2.8.: Effect of a resonant mw pulse on the singlet and triplet content of a spin pair. In the case of selective excitation (left), the mw directly ‘connects’ singlet and triplet states (which are not necessarily energy-eigenstates) at the Rabi frequency Ω. In the spin-locking case (right), the singlet state is decoupled from the triplet manifold. Hence, the shift of population is restricted to the three triplet states, and the frequency corresponds to 2Ω. Intersystem crossing (ISC) promotes population transfer from T_0 to S.

2.5.2. The role of intersystem crossing

The observable in EDMR, i.e. the (photo-)current, is often related to the singlet content of spin pairs because the probability for the underlying spin-dependent transition usually depends on the singlet content of the pair. In the previously treated case of selective excitation and spin pairs with negligible spin-spin interactions, a mw pulse which is in resonance with one constituent of a spin pair, induces a transition from the initial pure triplet state to a mixed state with singlet content. Thus, the mw pulse directly leads to an increase of the singlet content and results in an EDMR signal which oscillates at the Rabi frequency Ω. This situation is illustrated on the left side of Fig. 2.8. It is important to note that the states denoted with S and T_0 are not the energy-eigenstates for the weakly-coupled spin pair. The populations of these states can be obtained by applying the respective projection operators to the density matrix.

In contrast, under spin-locking conditions the microwave has no direct effect on the EDMR observable since the total spin remains unchanged and the spin population is only altered between the sublevels (T_+, T_- and T_0) of the triplet manifold [95, 96]. Hence, in this case an EDMR signal can only be observed when a connection between T_0 to S exists. Intersystem crossing (ISC) provides such a pathway: Hyperfine interactions between each spin pair constituent and nuclear spins in the vicinity mixes the states S and T_0. Consequently, population is shifted between both states. This effect is frequently encountered in amorphous hydrocarbons [97, 98], but it is likely to be relevant also for hydrogenated amorphous or microcrystalline silicon because hydrogen is incorporated at high concentrations in this material. In the presence of ISC, microwave-induced shifting of population from T_+ and T_- to T_0, which occurs at the frequency 2Ω as can be seen from (2.31), leads to an oscillations of the singlet population at the same frequency as shown on the right side of Fig. 2.8. Therefore, the oscillation frequency 2Ω is expected to be observed in electrically detected spin-Rabi nutations under spin-locking conditions as will be shown in Chapter 6.

2.6. Numerical simulations

Simulation of spectra and the temporal evolution of spin systems under the influence of mw pulses is often indispensable for the interpretation of experimental data in both conventional EPR and EDMR. While analytical calculations can provide qualitative insight, the quantitatively correct simulation of realistic systems often requires the consideration of disorder. This is generally complicated if not impossible by means of analytical calculations, but can be accomplished by numerical simulations. Disorder manifests itself in distributions of EPR parameters like g values, resonance frequencies and spin-spin interactions. This is especially relevant for highly disordered solid state systems investigated in this study, namely amorphous and microcrystalline silicon or polymers.

EDMR spectra usually exhibit the EPR-signatures of the paramagnetic centres that are involved in the respective spin-dependent process. Therefore, the same simulation tools that are commonly used for simulating conventional EPR spectra may be employed to calculate (cw) EDMR spectra. All spectral simulations presented within this thesis were performed with the EasySpin [99] software package.

For experiments using mw pulses, the analogy between EDMR and EPR does not hold since the observables are distinctively different for both measurement modes. While it is the magnetization that determines the signals in pulsed EPR, most pEDMR experiments probe the permutation symmetry of spin pairs. Still, one might use a simulation tool like EasySpin to model the temporal evolution of a spin pair ensemble and determine the singlet or triplet content of the spin pairs later on. However, this approach turned out to be not fast enough for ‘realistic’ systems when considering disorder effects as explained above for the highly disordered systems investigated here. For this reason we developed a software which is capable of simulating the temporal evolution of spin pair ensembles with or without arbitrary exchange or dipolar couplings. The underlying code is based on the effective Hamiltonian method as described in Appendix B.2 and takes advantage of parallel-computing on multiprocessor-CPUs, which considerably reduces the computation time. All numerical simulations presented in this section have been obtained using this code.

2.6.1. Influence of g value distributions

The distribution of resonance frequencies and the concomitant finite widths of realistic EPR or EDMR resonance lines can have several disorder-related origins. The peak shapes may, for instance, be dominated by unresolved hyperfine interactions between the electron spins and adjacent nuclear spins (e.g. in many polymers [100]) or by g strain (e.g. in amorphous silicon [101]). Both effects can be incorporated into simulations by assuming a Gaussian distributions of g values according to

$$p(g_i) = \exp\left[-4\ln(2)\frac{(g_i-\bar{g}_i)^2}{\Delta g_i^2}\right] \tag{2.32}$$

instead of only two fixed g values. Here, $p(g_i)$ represents the probability of finding a spin with the g value g_i, where i is either a or b for any partner of the spin pair. The mean value of the distribution is given by $\bar{g}_i$, and Δg_i denotes the width (FWHM) of the distribution. Recently, this approach has been used to study the influence of disorder on the different Rabi frequency components [102].

In the following, we study the influence of disorder on the Rabi oscillations in the time domain which is obtained experimentally with a pulse-length-dependent measurement. The degree of disorder in this regard refers to the width Δg_i of the distributions which is assumed to be equal for both spin partners a and b. Accordingly, the absence of disorder corresponds to $\Delta g = 0$. For the sake of simplicity, we imply that $g_a = g_b = 2.0023$ and $\Delta g_a = \Delta g_b$. We choose the combined population of the mixed states $|2\rangle$ and $|3\rangle$ as the observable, which corresponds to the sum of the singlet and the T_0 content of the spin pairs and is calculated by applying the respective projection operators to the density matrix, i.e. $\mathrm{tr}(P_S\hat{\rho}) + \mathrm{tr}(P_{T0}\hat{\rho})$. In the presence of infinitely strong intersystem crossing between $|S\rangle$ and $|T_0\rangle$ (cf. Section 2.5.2) the observable is equal to the singlet content and thus represents the quantity that determines the charge $Q(\tau)$ which is measured in the experiment. In order to separately study the influence of g distributions, we neglect any spin-spin interactions. Fig. 2.9b shows the simulated Rabi oscillations for different values of Δg_i assuming a

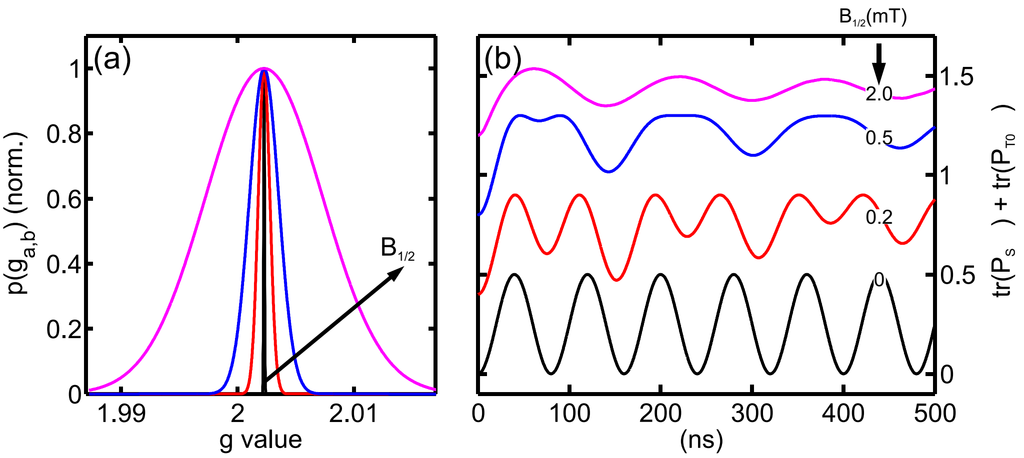

Figure 2.9.: Influence of disorder on spin-Rabi nutations. (a) Gaussian g value distributions as used in the simulation. (b) Rabi oscillations for the distributions given in (a). The line widths that result from $\Delta g_{a,b}$ are indicated by $\Delta B_{1/2}$. The individual curves are offset vertically by 0.4 for clarity.

resonant mw pulse with an equivalent π-pulse length of 80 ns. The line widths (FWHM) of the corresponding EDMR resonances at X-band are indicated for each curve. Fig. 2.9a illustrates these distributions. We included 10^4 spin pairs with varying g values (taken from the distributions $p(g_{a,b})$ consisting of 10^2 points each) in the simulation. For these pairs we calculated the state of the spin pair ensemble at the end of the pulse of length τ under the assumption that all spin pairs start from pure triplet states.

The increase of $\Delta g_{a,b}$ from 0, which essentially corresponds to δ-like g value distributions (lowermost curve in Fig. 2.9b), to $\Delta g_{a,b} = 0.012$ (uppermost curve) has two important consequences for the Rabi oscillations. First, the signal is damped due to the dephasing of the spins, and second, upon increasing $\Delta g_{a,b}$ the ratio between the Ω and 2Ω components changes dramatically. While the lowermost curve exclusively shows spin-locking behaviour, the oscillation for broad g only shows the signature of selective excitation.

This demonstrates an important feature that one should bear in mind when evaluating experimental results: Even when the g values of both spin pair members are identical, the presence of disorder might completely prevent the observation of spin-locking when the available mw power is not sufficient to access the spin-locking regime[10]. Instead, only the frequency component Ω is observed in this case.

---

[10] Note that this conclusion is only valid under the assumption that each spin from the distribution $p(g_a)$ can form a spin pair with each spin from $p(g_b)$.

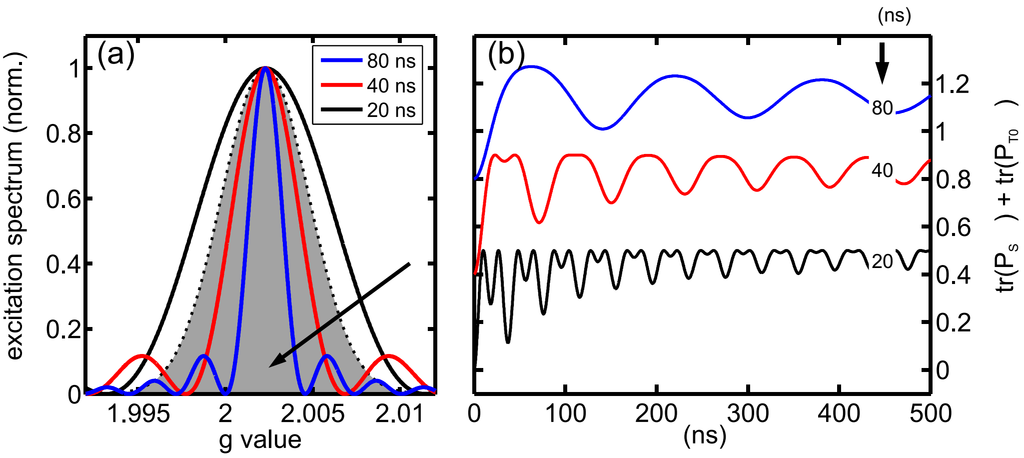

Figure 2.10.: Relationship between mw power and spin-Rabi nutations. (a) Excitation spectra for the chosen values of P_{mw} (solid lines). The corresponding π-pulse lengths, τ_π are given in the legend. The dotted line and the area beneath the curve represent the g distribution. (b) Rabi oscillations illustrating the crossover from spin-locking dominated behaviour (lower part) towards selective excitation (upper part).

This ramification of disorder is particularly important for the correct interpretation of the pEDMR results presented in Chapter 6.

2.6.2. Influence of microwave power

Since the existence of either spin-locking or selective excitation is determined by the ratio between $\Delta\omega$ and γB_1, the appearance of the Ω and 2Ω components can be controlled by adjusting the mw power P_{mw} and, in turn, the associated excitation spectrum. To visualize the influence of P_{mw}, we calculated the Rabi oscillations for several mw power levels which are characterized by the corresponding π-pulse length, τ_π. The simulation parameters are identical to those described in the previous section. We used 1 mT for the width of the g value distribution. Fig. 2.10a shows the excitation spectra for the different values of P_{mw} (solid lines) obtained by solving the Bloch equations along with the g distribution (dotted line and shaded area beneath the curve). It is important to note that the excitation width generally depends on both, the mw power as well as the pulse length, and is thus not constant during the experiment (and equally throughout the simulation). The excitation spectra shown in Fig. 2.10a were calculated assuming a π-pulse. The resulting Rabi oscillations are depicted in Fig. 2.10b. The observable is the combined population of the mixed states as described in Section 2.6.1.

Similar to the previously treated dependence on the g distribution width, the spin-Rabi nutations show a qualitative change from spin-locking dominated behaviour at high mw power (broad excitation width) to selective excitation behaviour (narrow excitation width) at low mw power. Moreover, a comparison between Figs. 2.9 and 2.10 reveals that the damping of the oscillation amplitude is primarily determined by the g distribution whereas the excitation width plays only a minor role for this effect.

2.7. Conclusion

In this chapter we introduced the theoretical concepts of pEDMR and have thus set the stage for the interpretation of the experimental results presented in the following Chapters 4, 5 and 6. On the one hand we described how spin-dependent recombination and hopping processes lead to conductivity changes after a resonant microwave pulse because the resulting pEDMR transients constitute the basis for all pEDMR experiments. On the other hand we addressed the phenomenon of coherent spin motion which can be used to distinguish between different microscopic processes evoking indistinguishable EDMR spectra. In particular, we utilize this effect for the identification of spin-dependent processes that were found in organic solar cells as described in Chapter 6. In order to facilitate the comparison between simulations and experimental results, we studied the influence of disorder-related effects on electrically detected Rabi oscillations.

3. Instrumentation

This chapter describes the experimental setup that was used to measure the effects explained in the previous chapter. In order to spectroscopically assign spin-dependent charge transport pathways by pEDMR, instrumental improvements on the EPR spectrometers at the Helmholtz-Zentrum Berlin für Materialien und Energie (HZB) and the Freie Universität (FU) Berlin (AG Bittl) had to be carried out. Here, the goal was an increase of the detection sensitivity to facilitate pEDMR from cryogenic to room temperatures on solar cells based on silicon as well as on organic materials. Further on, instrumental and methodological developments were necessary to assign defect states with overlapping EDMR signals. The focus of the chapter is the description of the experimental setup that is used for EDMR measurements as described Section 3.1. In particular, we will illustrate how the pEDMR transients — the basis for all pEDMR experiments — are affected by the current detection electronics and present a strategy to reduce these restrictions. Subsequently, we will compare continuous wave and pulsed EDMR with respect to optimum detection sensitivity and spectral resolution. Finally, the proper design of the electrical contacts is described, which turned out to be of major importance since the latter constitute the source of complicated background signals which have to be avoided.

3.1. Principle of a pEDMR experiment

In a pEDMR experiment the current change ΔI following a resonant mw excitation is detected as a function of time. Hence, pEDMR probes the changes of the conductivity which results from the alteration of recombination or hopping rates. Fig. 3.1a shows the pEDMR detection scheme. The corresponding evolution of a spin pair is sketched in Fig. 3.1b. Before the mw is switched on at $t = 0$, the spin pairs predominantly populate the long-living triplet states. The mw pulse manipulates the spin pair states and thus causes their population to oscillate coherently as described in Section 2.5. At the end of the pulse, the spin pair ensemble is no longer in the steady-state. Therefore, spin-dependent recombination or hopping rates also deviate from their respective steady-state values and affect the sample conductivity. While the spin manipulation typically takes place in the range from 10 to a few 100 ns, the detection of the resulting transient current change (referred to as pEDMR transient) is performed for some 100 µs until the current has relaxed to its steady-state value ($\Delta I = 0$). Under the assumption that the coherences have decayed (due to spin-relaxation) when the detection is carried out, the current transient is solely determined by incoherent processes and can be described by rate equations as demonstrated in Sections 2.3 and 2.4. In a typical 2-dimensional experiment, the pEDMR transient is monitored for different values of B_0.

It is impossible to detect conductivity changes during the spin manipulation in EDMR since *RC* time constants of sample and detection electronics are usually larger than typical pEDMR relaxation times. However, since the pEDMR transient depends on the state of the spin pair ensemble at the end of the pulse (cf. Section 2.3.1), different pulse lengths τ lead to different amplitudes of the transients as indicated in Fig. 3.1a. Therefore, the coherent spin motion may be reconstructed by measuring the signal $Q(\tau)$ in a fixed time window as a function of the pulse length. This type of measurement was originally used to study spin nutation in radical pairs in transient RYDMR [103, 95]. Later on, a similar concept was successfully implemented to study Rabi oscillations by means of pEDMR [34].

3.2. EDMR setup

The pEDMR measurements presented in Chapters 4 to 6 were performed at two different setups which are described separately in the following sections. The X-band measurements were carried out at the HZB, whereas a setup for Q-band EDMR was realized at the FU Berlin.

3.2.1. X-band

The X-band pEDMR setup is based on a commercial EPR spectrometer Bruker Elexsys E580 which was upgraded by the equipment for electrical detection. The sample is mounted in a dielectric mw resonator (Bruker ER 4118XMD5 or EN 4118XMD4) and cooled using a continuous flow helium cryostat (Bruker ER 4118CF) with optical access.

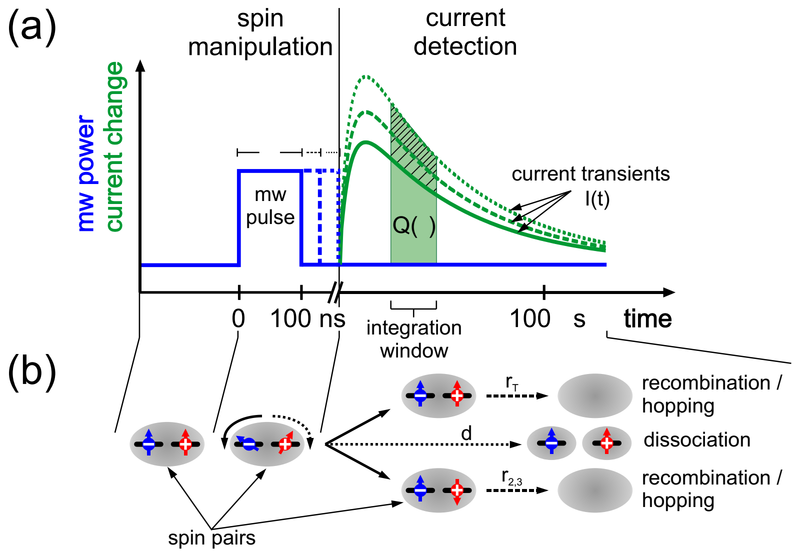

Figure 3.1.: Sketch of a pEDMR measurement. (a) Time-dependence of the mw power (ns time scale) as well as the current relaxation following the mw pulse (µs time scale). In order to investigate the coherent spin motion, the integrated charge Q is detected as a function of the mw pulse length τ. (b) Schematic representation of the spin pair evolution during the experiment. The pairs start from pure triplet states, are manipulated during the mw pulse and are annihilated by recombination or hopping (with rate coefficients r_T, r_2, r_3) or dissociation (with rate coefficient d) according to their singlet or triplet character.

The temperature is adjusted by a temperature controller (Oxford ITC 503) that allows operation in the temperature range between 2.5 and 300 K. Excess charge carriers are generated by a halogen cold light source (Schott KL 2500 LCD), an Argon ion laser (Coherent Innova 90C-A4) or an actively stabilized laser diode ($\lambda = 635$ nm, Elektronik-Manufaktur Mahlsdorf). The sample is illuminated directly through the cryostat window. Alternatively, the light can be fed through a fibre with an attached microprism that allows for illumination conditions which are independent of the sample orientation. For this purpose a special sample holder was developed in the framework of the diploma thesis project of Christoph Meier at the FU Berlin.

3.2.2. Q-band

All Q-band pEDMR experiments were performed at the FU Berlin on a Bruker Elexsys E580 spectrometer with a SuperQ-FT mw bridge. The sample is placed in a laboratory-built Q-band ENDOR resonator with an inner diameter of 3 mm that allows using the same contact design like for X-band (see Section 3.3). In contrast to X-band, small changes of the sample position inside the resonator significantly affect the mw mode and the cavity Q factor. Thus, exact positioning of the sample is mandatory for Q-band EDMR, and it may even be advantageous to fix the sample in a position in which the active device is not centred in the resonator. Consequently, the π-pulse lengths τ_π in pEDMR are longer than the minimum $\tau_\pi = 40$ ns of the resonator in combination with the solid state mw amplifier (maximum output power 0.5 W) used in the experiment. To assure homogeneous illumination under these conditions, the light is fed through a fibre ending in front of the solar cell. For some measurements the above-mentioned sample holder with fibre and microprism was used in order to maximize the light intensity at the solar cell position. The electrical detection setup as described in the following Section 3.2 was identical for X- and Q-band measurements.

3.2.3. Current detection

The transient current changes after a mw pulse excitation are detected by a current/voltage converter — the most critical part in the electrical detection setup. We use a current/voltage converter that was developed within the framework of this thesis in close collaboration with the Elektronik-Manufaktur Mahlsdorf for transient photocurrent detection in pEDMR

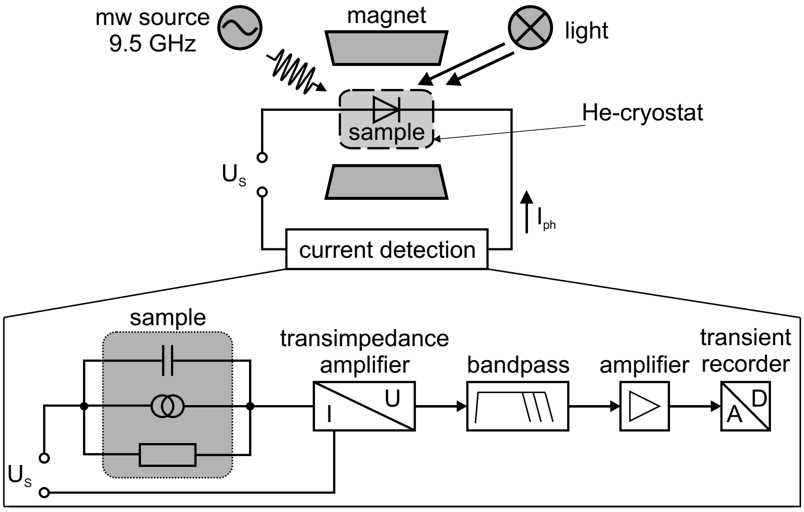

Figure 3.2.: Sketch of the pEDMR setup based on a commercial Bruker Elexsys E580 X-band EPR spectrometer. The sample is located in a microwave resonator which is placed in a He-cryostat with a window for optical access. A constant voltage source is used to apply a voltage U_S to the sample and thus establishing a steady-state (photo-)current I. Changes of the current, $\Delta|I|$, are recorded as a function of time using a current detection unit shown in the lower part. The equivalent circuitry of the solar cell can be considered as a parallel circuit consisting of current source, resistor, and capacitor. Thus, it inherently acts as a lowpass filter for changes of the photocurrent and therefore limits the time resolution. The signal $\Delta|I|$ is converted into a voltage, filtered, and amplified to a level that is sufficient for the transient recorder of the EPR spectrometer.

measurements. This instrument comprises a constant voltage source which is used to apply a fixed voltage, U_S, to the sample[1]. In order to minimize the electrical noise, U_S is split into two voltages, $\pm U_S/2$, which are applied symmetrical to the ground potential. The total current through the sample is determined by subtracting the two currents resulting from $+U_S/2$ and $-U_S/2$. By the use of this symmetrical configuration, the influence of disturbing signals (from outside of the detection setup) on the current can be suppressed to a large extent. Moreover, the current/voltage converter allows for a good trade-off between bandwidth and noise. The EDMR setup is schematically shown in Fig. 3.2. The lower part depicts the principle of the current amplifier. In the transimpedance amplifier the current signal is converted into a voltage which is then filtered by a bandpass with lower cut-off

---

[1] In some measurements (cf. Appendix C) the current/voltage converter is replaced by a constant current source (Keithley 220 PCS) in combination with a conventional current amplifier (Stanford Research SR570) to fix the current instead of the voltage.

frequency of 1 Hz to remove the DC-component of I. The upper cut-off frequency can be varied in order to control the time resolution of the detection setup. This is particularly helpful to evaluate the influence of the current amplifier on the measured time constants under the respective experimental conditions[2]. The resulting signal is then amplified to a level that is suitable for the transient recorder (Bruker SpecJet).

3.2.4. pEDMR transients

The time evolution of the photocurrent after the mw excitation (the pEDMR transient) is determined by the rate coefficients of the spin-dependent microscopic processes as described in Sections 2.3 and 2.4. However, it is generally difficult to determine these coefficients directly from the pEDMR transients since *RC* time constants of the detection electronics or the dielectric relaxation times of the sample dominate the experimentally obtained pEDMR transients. To demonstrate this, Fig. 3.3 shows two pEDMR transients obtained from a µc-Si:H based solar cell (cf. Chapter 5) using two different current/voltage converters under otherwise identical conditions.

The transient labelled with ‘SR570’ was measured using a Stanford Research SR570 current amplifier which is often used for pEDMR. The transient labelled with ‘EMM’ was recorded with the current/voltage converter described above (Elektronik-Manufaktur Mahlsdorf) with the bandwidth set to a value corresponding to a rise time of 2 µs. Both transients clearly exhibit markedly different dynamics, although the experimental conditions were the same. The rise and fall times of the ‘SR570’-transient are slower and the sign reversal of the transient is shifted to longer times. This difference is simply due to the lowpass filtering by the SR570 current amplifier. This can be demonstrated by numerical lowpass filtering of the ‘EMM’ data with the response time of the SR570 amplifier taking into account the *RC* equivalent circuitry as indicated in Fig. 3.2. As shown in Fig. 3.3, the filtered ‘EMM’ data becomes identical with that of ‘SR570’. To elucidate the influence of the sample (not necessarily of the microscopic processes) on the transients, it can be helpful to model the pEDMR transients. Assuming that the transients are determined by two exponential functions with two time constants linked to the spin-dependent process under observation and further taking into account the *RC* time constants induced by the current detection setup and the sample itself, good fits to the experimentally obtained data can be

---

[2] In addition, the current amplifier is capable of determining the capacitance of the sample and the connecting cables by automatically measuring the current response to a voltage pulse right before an EDMR measurement is started.

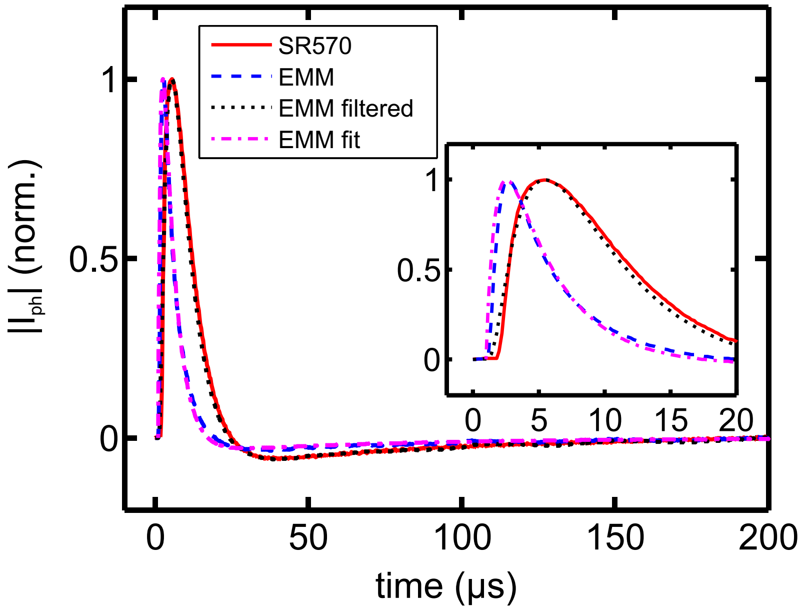

Figure 3.3.: pEDMR transients obtained from a µc-Si:H based solar cell. Two different current amplifiers as described in the text were used in order to demonstrate their influence on the transient dynamics. The curve labelled with 'EMM filtered' was generated by applying a numerical lowpass filter to the data of 'EMM'. The curve 'EMM fit' represents a least square fit of a model function consisting of two exponential functions (time constants τ_1 and τ_2) and taking into account lowpass filtering (time constant τ_{RC}) to the experimental data 'EMM' (fit results: $\tau_1 = 0.75$ µs, $\tau_2 = 65$ µs, $\tau_{RC} = 4$ µs). The inset shows an enlarged view of the first 20 µs of the transients.

achieved. This is demonstrated in Fig. 3.3 for the unfiltered 'EMM'-transient. Regardless of the strong influence of the detection electronics on the pEDMR dynamics, the pEDMR dynamics can be used to deconvolute spectrally overlapping signals as will be shown in Chapter 5.

3.2.5. Continuous wave EDMR

In a continuous wave (cw) EDMR experiment the sample is continuously subjected to mw radiation at a fixed frequency and intensity while the magnetic field B_0 is swept. As in pEDMR, the observable is the current at a fixed applied voltage. When the resonance condition is fulfilled, spin-dependent recombination or hopping rates change and thus alter the conductivity. Therefore, cwEDMR may be used to extract spectroscopic information such as g values and line widths. The main advantage of cwEDMR is its sensitivity which is usually higher than for pEDMR. This fact results from the possibility to employ lock-in detection and benefit from the resulting gain in signal-to-noise ratio. In all cwEDMR measurements presented in this thesis, B_0 was modulated in order to allow for phase-sensitive detection. However, it is equally possible to modulate the mw intensity (by using a pin switch as an equivalent to a mechanical chopper), which is advantageous under certain experimental conditions [104]. Due to the fact that the mw power is usually much lower in cwEDMR[3], power broadening of the resonance lines, which may severely distort pEDMR spectra, is of minor relevance in cwEDMR. To accomplish a high sensitivity in cwEDMR without the necessity of high mw power, the resonator is critically coupled to achieve a high cavity quality factor Q. Conductive parts of the sample, which are indispensable in EDMR samples, are generally detrimental for reaching high Q values. While this is a minor problem for low-temperature measurements on the samples investigated here at X-band frequency, it becomes a serious problem when going to higher mw frequencies (already at Q-band).

The main drawback of cwEDMR is the fact that it does not provide reliable information about the dynamics of the spin-dependent processes because it is a ‘quasi-static’ experiment. Although the high-frequency modulation of B_0 yields a quadrature spectrum, and by adjusting the lock-in phase different processes having different time constants can be separated [77], the extraction of all dynamic information requires to additionally vary the modulation frequency over a wide range. This, however, is critical because the EDMR spectrum is distorted when the modulation frequency approaches the spin-lattice relaxation time T_1 of the spins or the lifetime of the spin pairs that are involved in the recombination or transport process. In particular at low temperatures the respective time constants can be quite long and passage effects [105] have to be considered.

To demonstrate the difference between cw and pulsed EDMR, Fig. 3.4 shows low-temperature pEDMR spectra, i.e. the photocurrent ΔI_{ph} as a function of B_0, at two different times after the mw excitation (lower part) for two different samples[4] (panels a and b). The corresponding in-phase components of the cwEDMR spectra depicted in the lower part of the figure were obtained under identical experimental conditions. For the detection of the cwEDMR spectra, the transimpedance amplifier (cf. Fig. 3.2) was replaced by a current/voltage converter (Femto DLPCA-200) in combination with a battery-based constant voltage source (Stanford Research SIM928). The output of the current/voltage converter

---

[3] The maximum power available in the X-band spectrometer used here is $P_{\mathrm{max}} = 200$ mW for cwEDMR and 1 kW for pEDMR.

[4] Details about the sample structures are given in Chapter 5.

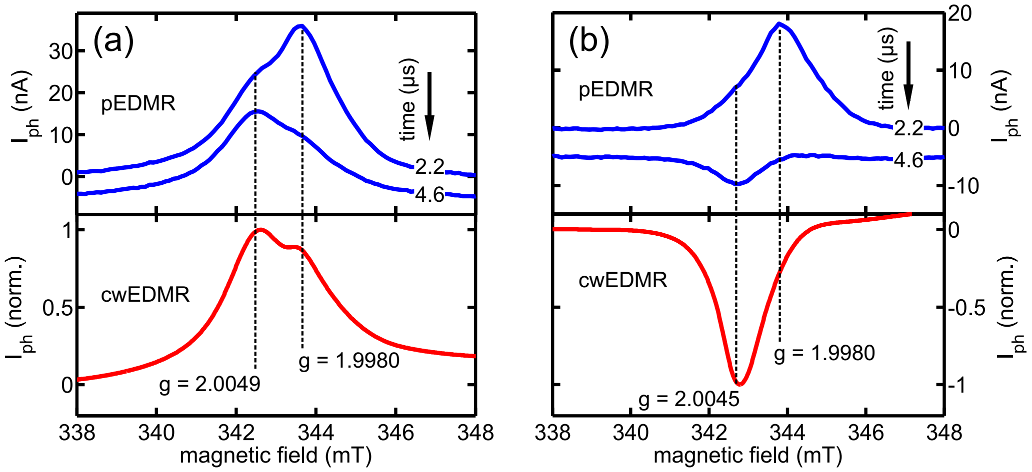

Figure 3.4.: Comparison between pEDMR spectra taken at two different times after the excitation (upper part) as well as the corresponding singly integrated cwEDMR spectra (lower part). (a) Spectra consisting of two resonances with positive amplitudes. (b) Spectra comprising one signal with positive and one signal with negative amplitude. The resonance positions are indicated by vertical dashed lines. Details can be found in the text.

was connected to the internal lock-in amplifier of the EPR spectrometer. The field modulation frequency was set to 10 kHz.

The pEDMR spectra in Fig. 3.4a clearly reveal the presence of two contributions with the same sign (enhancing signals) but different time constants. While the faster component at $g = 1.9980$ dominates the spectrum at 2.2 µs, the slower component at $g = 2.0049$ prevails at 4.6 µs. The in-phase component of the corresponding cwEDMR spectrum exhibits the signatures of both resonances and can thus be used to determine g values and line shapes. The situation depicted in Fig. 3.4b is markedly different. Here, the pEDMR spectra also consist of two resonances with different g values. However, while the line at $g = 1.9980$ shows a similar behaviour like the respective signal in panel a (in fact both signals originate from the same microscopic effect), the resonance at $g = 2.0045$ has a negative sign (quenching signal) and its time dependence is different. In this case the corresponding cwEDMR signal exclusively shows the signature of the slower component. This behaviour can easily be understood when one takes into account that cwEDMR essentially measures the integral over a part of the pEDMR transient. The position and length of this integration window depends on the modulation frequency. In the situation shown in Fig. 3.4b, the slower spectral component dominates the cwEDMR spectrum because it has a stronger time-integrated intensity — although the absolute amplitude of this signal is much smaller as can be inferred from the pEDMR spectra. Under these circumstances, it is obviously impossible to extract any information about the signal at $g = 1.9980$ from the cwEDMR spectrum alone. Here, pEDMR is capable of providing the missing pieces of information.

3.3. EDMR contact schemes

The measurements presented in this thesis were performed on different types of samples which are described in detail in the respective chapters. The explanation in this section is restricted to the part that concerns the electrical contacts. Although each type of sample requires a special contact structure, the design of all these structures is based on the same approach: The electrical contacts of the active device (or layer) are connected to contact pads on the opposite side of the EDMR structure via thin-film strip lines on the substrate. Since conductive material generally distorts the mw modes in the resonator and thus leads to inhomogeneities of B_1, it is essential to keep the thickness of the strip lines below the skin depth for the microwave at the particular frequency (approx. 1 µm for aluminium at 10 GHz [106]). For the same reason the strip lines have to be long enough so that the contact pads and the cables connected to them with silver paste are situated outside of the resonator.

Fig. 3.5 shows sketches of three different contact structures along with micrographs of the active device areas. Structure (a) is used for c-Si:H based solar cells in which the the wafer, which acts as light absorbing layer in the cell, is the substrate itself. This design is e.g. used for the a-Si:H/c-Si heterojunction solar cells described in Chapter 4. The strip line made of aluminium (shown in black) connects the front contacting layer of the cell, whereas the rear side of the substrate is entirely covered with aluminium as back contacting layer. This contacting scheme is realized by standard optical lithography.

The structure shown in Fig. 3.5b is used for thin-film solar cells which are deposited on a foreign substrate (e.g. glass or quartz). Since the (isolating) substrate is not part of the cell, both the front and the rear contact run in parallel on the front side. All necessary structuring steps are carried out by the laser scribing technique [107] without the need for lithography masks. The curved edges of the cell result from the shape of the laser spot used in the ablation process. The preparation of the thin-film samples (cf. Section 5.2) was done at the Forschungszentrum Jülich.

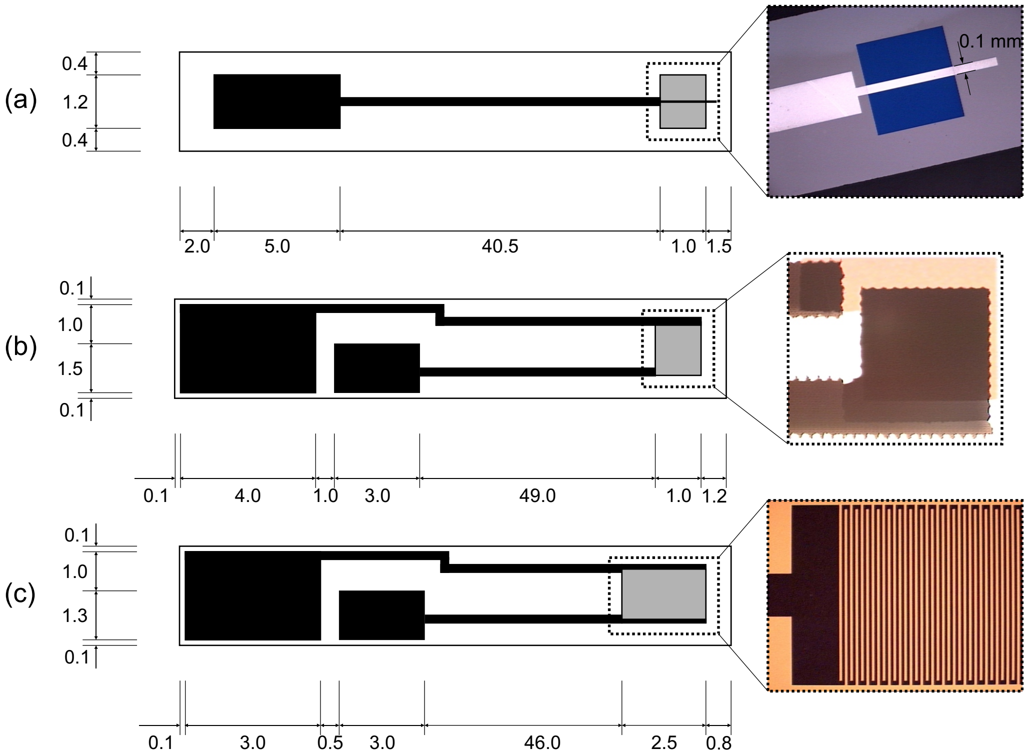

Figure 3.5.: Contact geometries that are used for pEDMR measurements. The black areas indicate the strip lines and contact pads consisting of 100 to 200 nm aluminium, gold or silver. The grey rectangles represent the active area (solar cell or single layer). Micrographs from this part of the samples are shown in the blow-ups on the right side of the figure. (a) and (b) depict vertical contact structures, whereas the meander-like structure shown in (c) comprises lateral contacts. All dimensions are in mm.

The contact geometry (c) is used for investigating single layers. In contrast to the two previously described structures where the current flow is perpendicular to the substrate, in structure (c) the current flows in lateral direction between lithographically defined interdigitated grid contacts. The meander-like contact design provides maximum overlap between both contacts and in this way allows reaching relatively high currents even when the sample resistivity is high. The distance and size of the contact fingers varies between 5 and 10 µm. Note that EDMR measurements performed on this type of structures are particularly sensitive to paramagnetic centres near the surface. This contact design was used for EDMR studies on the Si/SiO$_2$ interface as described in Chapter 4.

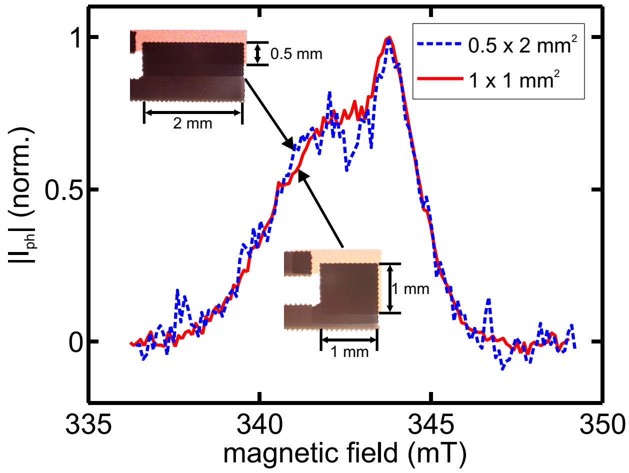

Figure 3.6.: pEDMR spectra ($\Delta|I_{\mathrm{ph}}|$ normalized to 1) recorded at $t = 2.4$ μs for a thin-film solar cell with two different sample geometries as indicated by the two optical micrographs. Note that the difference in the signal-to-noise is attributed to the smaller absolute signal level for the sample with active area of 0.5×2 mm^2. This is a consequence of different illumination conditions.

3.3.1. Sample geometry

The geometry of solar cells to be analysed by pEDMR is inherently limited by the dimensions of the mw resonator which in turn is determined by the wavelength of the microwave. For X-band ($\nu \approx 10$ GHz, wavelength 3 cm), a solar cell area of 1×1 mm^2 has proven to be reasonably small to yield a homogeneous mw amplitude over the whole active area of the solar cell. This is particularly important when studying coherent effects by means of pEDMR. Since the active area of solar cells studied with EDMR is rather small, additional defects induced by the preparation and processing — especially defects located at the edges — can significantly affect the experiments. To exclude that the EDMR spectra are dominated by such defects, we prepared the same solar cell structure with two different geometries with clearly varying edge length as shown by the optical micrographs in Fig. 3.6. The respective low-temperature ($T = 10$ K) pEDMR spectra, i.e. the change of the photocurrent, $\Delta|I_{\mathrm{ph}}|$, as a function of magnetic field, are shown in Fig. 3.6. Within the accuracy of the measurement, the normalized spectra are identical, indicating that the same underlying microscopic processes are involved. It is therefore safe to assume that no new types of defects are introduced by the specific processing of the solar cells for pEDMR measurements. The signal-to-noise ratio is significantly reduced for the 2×0.5 mm^2 sample which is attributed to the smaller photocurrent (and consequently also smaller $\Delta|I_{\mathrm{ph}}|$) resulting from the fact that the illumination condition was optimised for a square-shaped active area. All following experiments on solar cell structures have been carried out on square-shaped samples.

3.4. Conclusion

The instrumental improvements of the detection electronics described in this chapter were particularly beneficial for the pEDMR measurements on µc-Si:H based solar cells presented in Chapter 5. Due to the improved detection sensitivity pEDMR measurements on silicon-based solar cell became feasible. In addition, the enhanced time resolution allowed for a better discrimination between spectrally overlapping resonances by separating the signals in the time domain. Furthermore, the extension of pEDMR to Q-band provided the possibility to perform multi-frequency pEDMR studies which enabled us to distinguish between field-dependent and field-independent interactions.

In the following Chapters 4 to 6 we will take advantage of these improvements with regard to the analysis of charge transport in fully processes solar cells.

4. Electrical detection of a-Si:H/c-Si interface recombination

Heterojunction solar cells based on amorphous and crystalline silicon constitute a promising concept for high-efficiency solar cells in which a-Si:H serves as a passivation layer and simultaneously contributes to the pn junction. Recently, an a-Si:H/c-Si solar cell with an efficiency of 23% and an active area of 100 cm^2 has been reported [2]. Note that solar cells of this type are already being commercially available for several years [108].

The charge carrier diffusion length in high-quality c-Si embodied as absorber in a-Si:H/c-Si heterojunction solar cells usually exceeds the device dimensions. This means that almost all optically generated electrons and holes reach the respective sides of the absorber layer. Thus, defects in the bulk c-Si can be neglected for the charge transport, and the device performance entirely depends on the quality of the interfaces. Especially defects at the interface between the a-Si:H emitter layer and the c-Si absorber play a crucial role because they act as recombination centres for photogenerated charge carriers [109]. The detrimental influence of these interface states on the electronic properties can be studied theoretically by numerical device simulations [110]. This is demonstrated in Fig. 4.1 which shows the simulated solar cell parameters as a function of the interface state density assuming realistic material properties for a-Si:H/c-Si solar cells. The simulation was performed with the AFORS-HET program [110].

Moreover, the impact of interface defects on the electrical properties may be studied experimentally, e.g. by means of capacitance-voltage based methods [21, 22], and photoelectron spectroscopy can be used to obtain the density of defect states in ultrathin a-Si:H layers [111]. However, since standard experimental methods lack the microscopic selectivity and thus simultaneously probe ‘real’ interface states as well as defects in the ‘bulk’ a-Si:H nearby the interface, it is usually not possible to determine the structural identity of the defects without ambiguity. Taking advantage of the ability of EDMR to address spe-

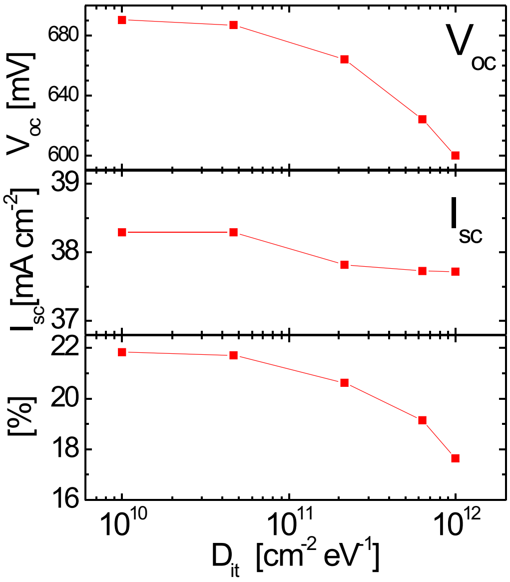

Figure 4.1.: Influence of the interface state density (D_{it}) at the n-a-Si:H/p-c-Si interface on solar cell parameters. Open circuit voltage (V_{oc}), short circuit current density (I_{sc}) and efficiency (η) were simulated for a TCO/n-a-Si:H/p-c-Si/p-a-Si:H/Al solar cell structure with p-a-Si:H back surface field. A recombination velocity of 10^2 cm s^{-1} was assumed for the rear side interface. Other input parameters for the simulation are: electron diffusion length $L_D = 400$ µm, TCO thickness $d_{\mathrm{TCO}} = 80$ nm and emitter thickness $d_{\mathrm{n-a-Si:H}} = 10$ nm [109].

cific defect states, this technique may be utilized to directly study the influence of interface states on charge transport in the device.

To the best of the author's knowledge there are no reports about the investigation of a-Si:H/c-Si interface states by means of conventional EPR or EDMR. However, both techniques were previously applied to the conceptually similar and extensively studied interface between c-Si and SiO_2, which can be considered a model system for the a-Si:H/c-Si heterojunction. In particular, both systems consist of an amorphous material on top of a crystalline Si surface. It is conceivable that the intrinsic defects at the a-Si:H/c-Si interface exhibit similar properties like defects at the Si/SiO_2 interface, but decisive microscopic information from EPR is not available because the concentration of defects at high-quality a-Si:H/c-Si interfaces is relatively low ($\ll 10^{12}$ cm^{-2}) — generally too low for the application of conventional EPR. Nevertheless, there is no doubt about the fact that a-Si:H/c-Si interface defect density is crucial for the efficiency of heterojunction solar cells (cf. Fig. 4.1) [109]. EDMR, however, has a higher sensitivity and can therefore be used to elucidate the role of interface states on the charge transport in both interface systems.

To determine the similarities and differences between spin-dependent recombination at the Si/SiO_2 and the a-Si:H/c-Si interface, we first address EDMR measurements carried out on an oxidized c-Si surface. Many previous EDMR studies [112, 75, 113, 69] focused on the interface between SiO$_2$ and phosphorus-doped c-Si because of its potential relevance for solid-state based quantum computation [114]. To achieve maximum comparability with these studies, we will also investigate P-doped silicon here. We use isotopically purified ^{28}Si which turned out to be advantageous with respect to the spectral resolution due to the reduced EDMR line widths. The EDMR experiments performed on the Si/SiO$_2$ interface, which are described in the following section, provide reference spectra for the measurements carried out on heterostructure solar cells which are presented in Section 4.2.

4.1. The Si/SiO$_2$ interface

The interface between silicon and silicon dioxide is certainly the most intensively studied interface system involving silicon because it plays a key role in microelectronics where SiO$_2$ is e.g. used as gate oxide in field effect transistors. Due to the network-lattice mismatch, coordination defects at the interface are inevitably present [115] and act as trapping or recombination centres for conduction electrons and holes close to the interface. Consequently, these defects have a significant influence on the performance of many silicon-based devices. Several techniques were employed in the past to investigate their implications for the electrical properties of different devices. Especially EPR and related methods proved to be beneficial in identifying the structural defect properties [116, 117, 118, 119]. The most prominent interface defect at the (111) oriented Si surface covered by thermally grown SiO$_2$ as identified by EPR originates from a threefold-coordinated Si atom at the interface. The dangling bond, i.e. the unpaired sp^3 hybrid orbital, was shown to be situated perpendicular to the Si-surface and is referred to as the *P_b centre*. Similar defects exist at the Si/SiO$_2$ systems with different surface orientations, but the microscopic identification of these states is not as unambiguous as in the case of the P$_\mathrm{b}$ centre. It is generally assumed that a 'P$_\mathrm{b}$-like' defect which is oriented along the $\langle 111 \rangle$ directions does equally exist at the Si (100) surface and is chemically equivalent to the P$_\mathrm{b}$ centre [115]. However, its g tensor is slightly different. These types of defects at the (100) surface are usually named *P_{b0} centres* [120, 115].

Besides being technologically relevant itself, the Si/SiO$_2$ system also serves as a well-studied model system for the a-Si:H/c-Si interface which is embedded in high-efficiency heterojunction solar cells.

4.1.1. EDMR in isotopically controlled ^{28}Si

The EPR line width of donors in silicon is dramatically influenced by dipolar broadening induced by hyperfine interactions between the donor electron spins and the nuclear spins $I = 1/2$ of ^{29}Si atoms in the vicinity of the donor atom. Thus, by controlling the isotopic composition of silicon, one can influence the resulting donor EPR line width. This effect was studied theoretically as early as 1957 by Kohn who found that the line width increases with the square root of the fractional abundance of ^{29}Si [121]. His prediction was experimentally confirmed already two years later [122] and more recently verified in a study in which the ^{29}Si content was varied over a wide range [123].

Since the EPR line width depends on the fraction of ^{29}Si atoms, it seems plausible that the line width observed in EDMR does equally decrease when lowering the ^{29}Si content. In the following, we will first provide experimental evidence for the validity of this assumption. In a second step, we will address the question whether this gain in spectral resolution exclusively holds true for donor states or whether it is also valid for (stronger localized) defect states at the Si/SiO$_2$ interface as well as for impurities. For this purpose we fabricated EDMR samples based on the silicon-on-insulator layer sequence[1] shown in Fig. 4.2a. A grid contact structure consisting of 100 nm gold (see Fig. 3.5c) with a grid finger spacing of 5 µm was evaporated on top of the ^{28}Si-layer (purity: 99.85%, (100) surface orientation) which is covered with a thin natural oxide. In the EDMR measurements, the current flows between the contact fingers in lateral direction. In order to evaluate the influence of the reduced ^{28}Si-concentration on the EDMR spectrum, reference measurements were performed on a similar sample comprising an epitaxially grown layer of phosphorus-doped silicon (thickness 15 nm, (100) surface orientation) with natural isotopical composition. Here, also an interdigitated contact-grid was used. Details about the processing of this sample (in the following referred to as the $^{\mathrm{nat}}$Si-sample), which was done at the Walter Schottky Institute, are given in [56].

Fig. 4.2b shows low-temperature ($T = 5$ K) cwEDMR spectra from both samples measured under illumination from a halogen lamp. In the case of the ^{28}Si-sample, a voltage of 80 mV was applied which resulted in a photocurrent of 29 µA. Note that in contrast to $T = 300$ K the contacts do not show ohmic behaviour. Magnetic-field modulation (amplitude: 10 µT, frequency: 1.1 kHz) was employed to obtain the spectrum (solid line). Since the resistivity of the $^{\mathrm{nat}}$Si-sample was lower, the reference spectrum was measured

---

[1] Crystalline silicon wafers with ^{28}Si-layers were supplied by Isonics Corporation.

Figure 4.2.: (a) Structure of the EDMR sample based on a 3.5 µm thick isotopically enriched ^{28}Si layer. (b) Normalized EDMR spectra obtained from two different samples. Solid line: Low-temperature ($T = 5$ K) EDMR spectrum of the sample structure shown in (a). Dashed line: EDMR spectrum from a 15 nm thick epitaxially grown Si layer with natural abundance and a phosphorus-concentration of 10^{17} cm^{-3}. This samples was provided by the Walter Schottky Institute. Details about the structure can be found in [56].

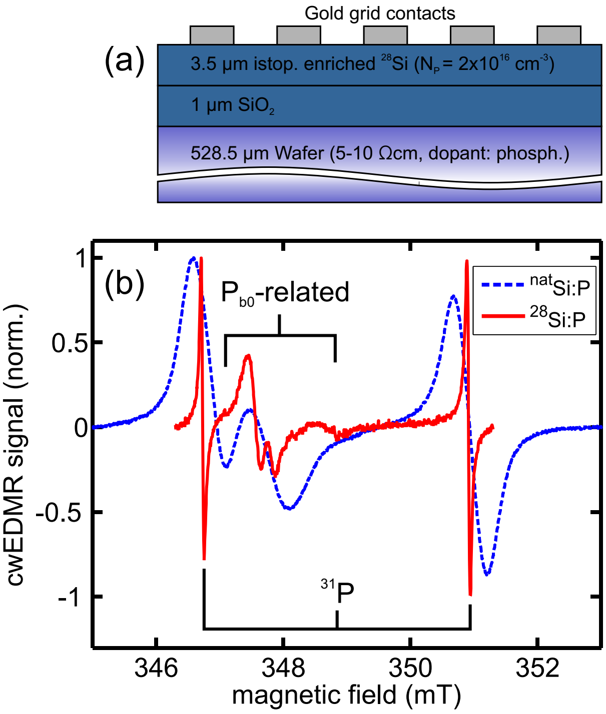

at a lower voltage[2] ($U = 20$ mV, $I_{ph} = 40$ µA). For recording the reference spectrum, the modulation amplitude and frequency were set to 0.5 mT and 10 kHz, respectively[3].

Inspection of both spectra reveals that the EDMR line width of the ^{31}P lines — which can easily be identified by their characteristic hyperfine splitting of 4.2 mT [124] — is significantly reduced for the ^{28}Si-sample. We will quantify this results in Section 4.1.2. Furthermore, the additional spectral features which appear as a structureless line at approximately 348 mT (denoted by 'P$_{b0}$-related') in the ^{nat}Si-spectrum can be better resolved in the spectrum of the ^{28}Si-sample. It thus appears that the gain in spectral resolution also holds true for the defect-related signals. These resonances are generally attributed to differently oriented P$_{b0}$ centres at the SiO$_2$ surface. The EDMR signal is assumed to originate from a spin-dependent transition between electrons in the phosphorus donor states and singly occupied P$_{b0}$ centres [75, 113]. However, a recent systematic study of the relative

---

[2] We verified for both samples that the shape of the spectrum was independent of the voltage in the range from 20 to 80 mV.

[3] The phosphorus line shapes in both spectra shown in Fig. 4.2b are slightly deteriorated by the modulation amplitude and mw power used in the experiments. While the 'true' EDMR line width for the ^{nat}Si-sample is at most 30% smaller (see [55]), the value for the natural line width for the ^{28}Si-sample is at least 50% lower (see Fig. 4.3). Hence, Fig. 4.2b even underestimates the effect of the isotopical purity on the EDMR line width.

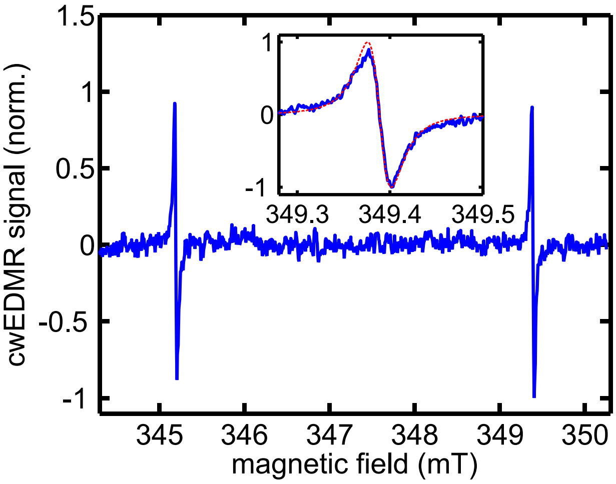

Figure 4.3.: Spectrum obtained from the ^{28}Si-sample. In order to minimize artificial broadening, the mw power was reduced by 12 dB in comparison to the settings used for recording the spectrum shown in Fig. 4.2b. The inset shows a spectrum of the high-field line on a reduced magnetic field range (solid line: experiment; dashed line: fit result assuming a Lorentzian line).

intensities of the individual EDMR resonances indicated that the ^{31}P-P$_{b0}$ transition is not the only spin-dependent transition that contributes to the EDMR spectra [76]. Moreover, the evaluation of the resonance positions as a function of the sample orientation in the magnetic field unambiguously showed that the P$_{b0}$ centre alone cannot account for the spectral feature at 348 mT [125]. In Section 4.1.3 we will also utilize the angular dependence of the EDMR signals to determine the g tensors of the contributing states.

4.1.2. The ^{31}P donor line width

To quantify the gain in spectral resolution, we measured the cwEDMR spectrum of the ^{28}Si-sample with a mw power reduced by 12 dB (0.6 instead of 10 mW as used for obtaining the spectrum shown in Fig. 4.2b) to prevent power-broadening effects. The voltage was set to 100 mV which corresponds to $I_{\text{ph}} = 3$ µA. These settings yielded the spectrum displayed in Fig. 4.3 in which only the ^{31}P hyperfine satellites can be identified, whereas no clear contribution from P$_{b0}$ centres is present. The inset of Fig. 4.3b shows a spectrum of the high-field line which was obtained using the same parameters except for a smaller magnetic field increment. Fitting of a Lorentzian line to the experimental data reveals a peak-to-peak line width[4] of $\Delta B_{pp} = 26(3)$ µT, which is about an order of magnitude lower than in silicon with natural isotopic composition [126]. We will now address the question whether additional features of the cwEDMR spectrum of the ^{28}Si-sample can be identified.

---

[4] Note that the asymmetry of the ^{31}P line can be attributed to the fact that this signal results from a superposition of two resonances. The line shape has previously been investigated in more detail by conventional EPR measurements [56].

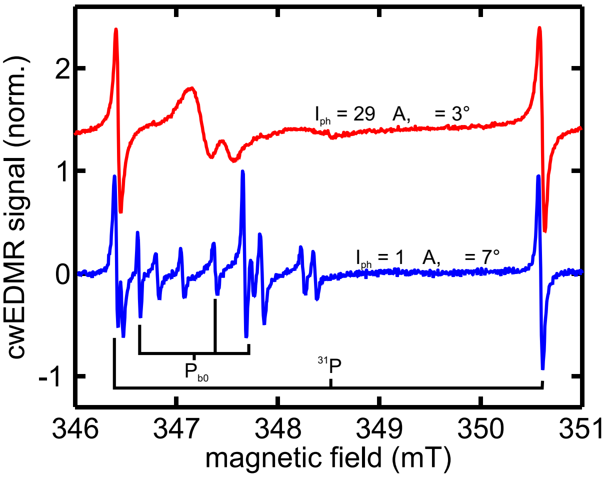

Figure 4.4.: Normalized cwEDMR spectra of the ^{28}Si-sample obtained at two different light intensities. Both measurements were performed with an applied bias voltage of 80 mV. The resulting photocurrents are indicated above the curves. Three lines in the lower spectrum can be attributed to P$_{b0}$ centres as will become clear from the rotation pattern shown in Fig. 4.5. The curves are vertically offset for clarity.

4.1.3. Angular dependence of the EDMR signals

Fig. 4.4 shows two EDMR spectra that were recorded under identical conditions except for slightly different sample orientations and two different light intensities. The latter lead to different photocurrents as indicated in the plot. While the upper trace exhibits the spectral features described above, namely two ^{31}P hyperfine satellites and a broader component consisting of at least two different signals, the spectrum at low light-intensity shows a multitude of lines. This is a clear indication that different types of spin-dependent processes (besides the ^{31}P-P$_{b0}$ transition) coexist in our sample. It is important to note that the width of each line is well below 50 µT and thus significantly lower than the broad features that are present in the upper spectrum. Therefore, we can easily distinguish between the individual signals and determine the resonance positions as function of the sample orientation in the magnetic field. From the resulting rotation pattern we can determine the g tensors of the contributing states. While paramagnetic centres in the ^{28}Si-layer or at the ^{28}Si/SiO$_2$ interface are expected to obey the crystal symmetry, signals from defects in the SiO$_2$ should not show an angular dependence because the resonances result from a superposition of all possible defect orientations (powder pattern).

Fig. 4.5 shows the rotation pattern for the ^{28}Si-sample. The crosses indicate the resonance positions extracted from cwEDMR spectra like the one in Fig. 4.4 (lower curve) that were obtained for several sample orientations. The sample with (100) surface orientation was rotated around the $[011]$ axis with the magnetic field lying in the (011) plane. The angle $\phi = 0°$ defines the orientation in which the external magnetic field points into the $[01\bar{1}]$ direction (i.e. $\mathbf{B_0} \perp [100]$). To facilitate tracking of the resonance positions we added

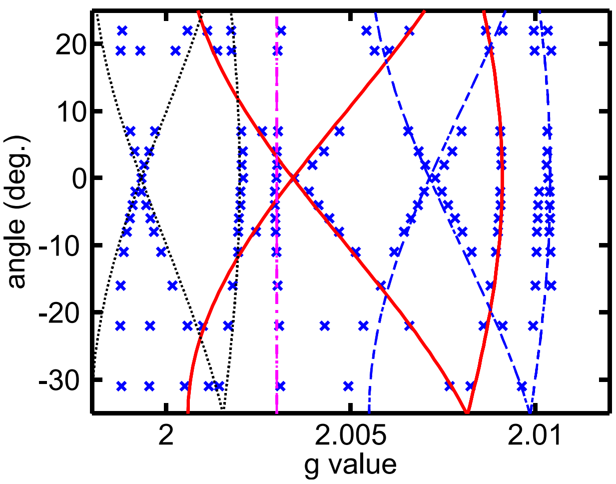

Figure 4.5.: Dependence of the resonance positions on the sample orientation for the spectrum measured at low light intensity (I_{ph} = 1 μA). The lines represent simulated resonance positions assuming three different centres with axially symmetric g tensors (each centre gives rise to three resonances) and one isotropic centre. The solid lines indicate the resonance positions associated with P_{b0} centres. Details are given in the text.

Table 4.1.: Principal g values of the paramagnetic centres that were assumed to simulate the rotation pattern in Fig. 4.5.

paramagnetic centre	linestyle in Fig. 4.5	$g_{\|\|}$	$g_{\perp}$
P_{b0} centre	solid	2.0006	2.0091
centre 2	dashed	2.0055	2.0104
centre 3	dotted	1.9980	2.0020
centre 4	dash-dot	2.0030	2.0030

theoretical curves for three different centres with trigonal symmetry as well as for one isotropic centre. The associated principal g values are given in table 4.1. For the sake of simplicity we will restrict the following analysis to the centre indicated by the solid lines. The other signals could not be assigned to known paramagnetic centres based on literature values for g tensors of bulk or interface defects. Thus, the curves associated with centres 2 to 4 (see table 4.1) should rather be considered as guide-to-the-eye, and it should be noted that some curves do not satisfactorily reproduce the experimental data (see e.g. the dotted lines). In particular, clear discrepancies between the experimental data and the theoretical curves are visible for $|\phi| \gtrsim 20°$.

The solid lines represent the simulated resonance positions for an axially symmetric g tensor with the principal g values $g_{||} = 2.0006(3)$ and $g_{\perp} = 2.0091(3)$. These values are similar to those determined by Langhanki *et al.* [127] for so-called 'P_{ba} centres' at the $^{nat}Si/SiO_2$ interface by means of cwEDMR. They interpreted this centre with the principal values $g_{||} = 2.0008$ and $g_{\perp} = 2.0098$ to be identical to the P_{b0} centre for which, however, the g values obtained by conventional EPR are in the range of $g_{||} = 2.0015 - 2.00185$ and $g_{\perp} = 2.0080 - 2.0087$ [115] — although the values given by different authors scatter significantly (beyond experimental uncertainty). Nevertheless, due to the similarities between the g tensors determined from Fig. 4.5 and the literature values it seems reasonable to assign the resonances to P_{b0} centres at the $^{28}Si/SiO_2$ interface.

In conclusion, we have shown that the gain in spectral resolution, which is known from conventional EPR measurements when reducing the content of ^{28}Si, affects EDMR spectra in a similar way. Moreover, this holds true not only for donor-like states, but also for defects in the ^{28}Si and at the $^{28}Si/SiO_2$ interface. It thus seems conceivable to make use of isotopically purified silicon to systematically study the role of defects at other silicon interfaces at high spectral resolution. In particular, defects at the a-Si:H/c-Si interface, which are highly relevant for the efficiency of heterojunction solar cells, might be investigated in this way. Before doing so, it has to be evaluated whether EDMR is able to detect a-Si:H/c-Si interface recombination at all. This is the subject of the following section.

4.2. Defects at the a-Si:H/c-Si interface

Here, we report on EDMR measurements which were employed to a-Si:H/c-Si heterojunction solar cells with the objective to explore the effect of interface recombination on the charge transport. Although the solar cell preparation for EDMR samples is similar to ‘real’ heterojunction solar cells [128], some important preparation-related aspects have to be considered as described in the following.

4.2.1. a-Si:H/c-Si solar cells for EDMR investigations

Fig. 4.6 shows a sketch of the a-Si:H/c-Si heterostructure. A 380 µm thin single-side polished p-type c-Si wafer ($\rho \approx 1\ \Omega$ cm, dopant: boron) with (111) surface orientation was used as substrate and absorber of the solar cell. Prior to the solar cell preparation, the wafer was treated by a standard RCA cleaning sequence followed by an HF dip to remove the naturally grown oxide and to saturate surface dangling bonds by hydrogen. The emitter layer consisting of 8 nm phosphorus-doped a-Si:H was deposited using PECVD. The optimum a-Si:H thickness for the application as emitter in heterojunction solar cells is between 5 and 10 nm [129]. Furthermore, thicker a-Si:H layers exhibit strong pEDMR signals associated with hopping transport via conduction band tail and phosphorus states which may prevent the observation of interface-related resonances. For a detailed analysis of such layers in

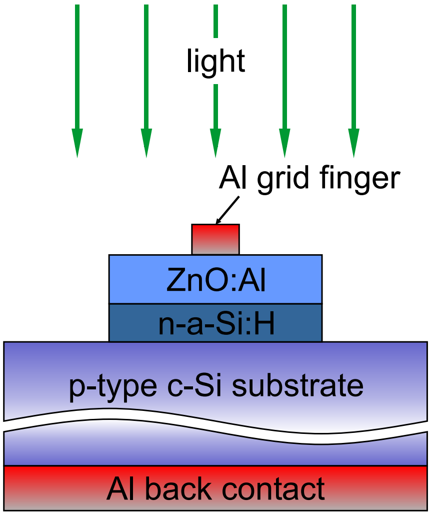

Figure 4.6.: Cross section of the heterostructure solar cell. The sample consists of 2×50 mm^2 of a boron-doped crystalline silicon wafer. The emitter layer (8 nm of phosphorus-doped amorphous silicon) and the ZnO layer (as transparent conducting oxide) cover only a square of 1×1 mm^2. Structuring of the sample was done using standard optical lithography. The solar cell is illuminated through the a-Si:H side.

n-a-Si:H/c-Si heterostructure solar cells we refer to Appendix C and Refs. [130, 131, 132]. This is also discussed in Chapter 5 for n-a-Si:H/µc-Si:H heterostructures.

On top of the a-Si:H an additional layer of 80 nm Al-doped ZnO serves as transparent conducting oxide (TCO). In order to confine the active solar cell to an area which is sufficiently small for X-band EDMR measurements, a-Si:H and ZnO were removed except for a square of 1 mm^2 using standard optical lithography and mesa etching. Subsequently, the front contact system comprising an aluminium thin-film strip line (thickness: 200 nm) and a grid contact finger as well as an Al layer as rear contact were added. Several sample structures were processed on one wafer in parallel. They were cut into the appropriate size after the last processing step (see Fig. 3.5a for details).

Previous investigations on a-Si:H/c-Si solar cells have revealed that this contacting scheme is adequate for EDMR studies [131,35]. However, in the sample structures used so far, a thermally grown SiO_2 layer covering the c-Si substrate accomplished the electrical isolation of the front contact strip line from the c-Si wafer. The a-Si:H and ZnO layers for the solar cell were deposited into a window which was etched into SiO_2 layer. For more details on the device structure see Fig. C.2 in Appendix C.3. This etching process, which is not part of the standard solar cell processing, may deteriorate the c-Si surface morphology. This is strongly implied by minority carrier lifetime measurements on a-Si:H passivated c-Si wafers that have undergone thermal oxidation and successive wet-chemical oxide removal [133]. Therefore, we did not use an isolating SiO_2 layer here. In principle, this leads to shunts at room temperature. However, at low temperatures without illumination

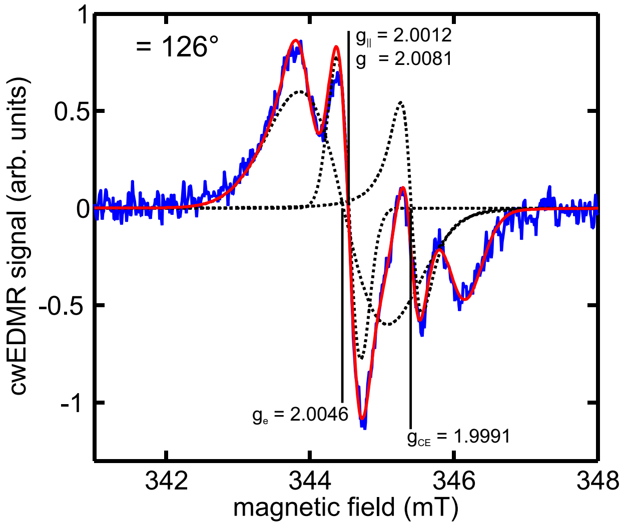

Figure 4.7.: EDMR spectrum of the a-Si:H/c-Si heterostructure solar cell obtained at $T = 18$ K. The solid line represents a fit to the experimental data consisting of five resonance lines. The individual contributions to the fit are shown for three of the signals (dashed curves) along with the respective g values. Note that due to the reverse bias a positive EDMR signal corresponds to a reduction of the current. See text for further details.

the resistivity of the c-Si wafer is high. Thus, when the illuminated region is restricted to the active cell — as it is the case in the measurements — the electrical properties of the EDMR sample are determined by the solar cell. In contrast to high-efficiency a-Si:H/c-Si solar cells [134] we did not use additional a-Si:H layers as back surface field or buffer layers in order to keep the cell structure as simple as possible.

4.2.2. EDMR spectra

For the EDMR measurements the sample was exposed to illumination from a halogen cold light source (cf. Section 3.2.1). To ensure homogeneous illumination independent of the sample orientation, the light was fed through a fibre with an attached microprism in front of the solar cell. All measurements were performed at $T = 18$ K because this temperature resulted in a reasonable signal-to-noise ratio of the interface-related EDMR signals. A bias voltage of -1.0 V (reverse bias regime) was applied to the cell resulting in a photocurrent of -15 µA.

Fig. 4.7 shows a cwEDMR spectrum for a microwave frequency of 9.66 GHz employing magnetic field modulation (modulation amplitude 0.3 mT, modulation frequency 10 kHz). The sample was oriented with its $[10\bar{1}]$ axis parallel to $\mathbf{B_1}$ and the angle $\phi = 126°$ between the $[1\bar{2}1]$ axis and $\mathbf{B_0}$. The spectrum exhibits a multitude of different lines. Best fits to the experimental data could be achieved when assuming four Gaussian lines and one Lorentzian line (resulting fit: solid line in Fig. 4.7). For the sake of clarity, we only included the individual components of the fit for three resonances (dashed lines). While

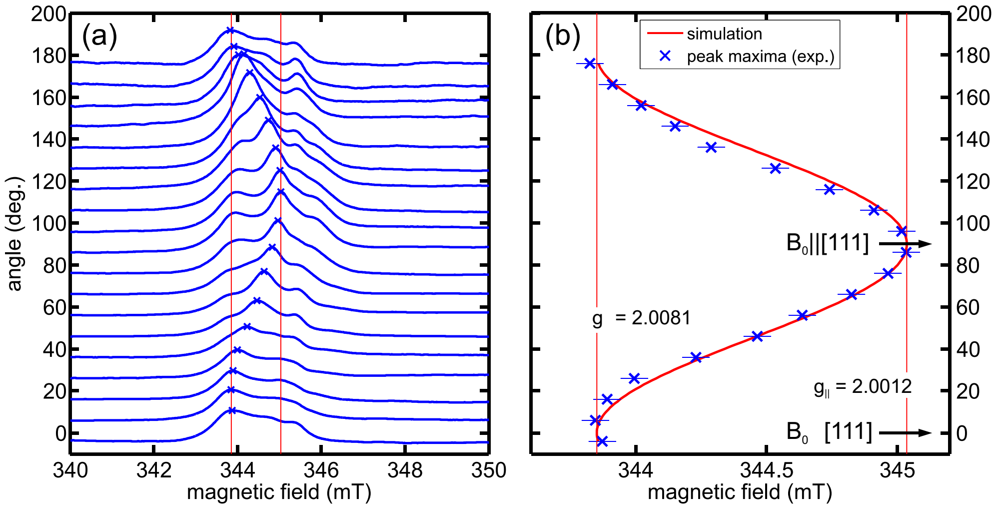

Figure 4.8.: (a) Integrated EDMR spectra for several sample orientations represented by the angle ϕ between the $[1\bar{2}1]$ direction and $\mathbf{B_0}$. The sample was rotated around the $[10\bar{1}]$ axis. The intensity maxima of the spectra are indicated by crosses. (b) Resonance positions of the dominant spectral contribution in (a) (crosses) and simulation (solid line) of the rotation pattern for the P_b centre at the (111) oriented Si/SiO$_2$ interface (g tensor with trigonal symmetry, $g_{||} = 2.0012$, $g_{\perp} = 2.0081$ [117]).

the g values of Gaussian line at $g_e = 2.0046(5)$ and the Lorentzian line at $g_{CE} = 1.9991(5)$ are independent of the sample orientation, the resonance positions of the other resonances contributing to the spectrum change upon sample rotation as will be shown in the following section. Further isotropic contributions due to phosphorus hyperfine split signals stemming from the amorphous silicon layer cannot be observed in Fig. 4.7 because of the limited magnetic field range.

4.2.3. Rotation pattern

In order to evaluate the change of the spectrum when rotating the sample around its $[10\bar{1}]$ axis, we recorded EDMR spectra like the one shown in Fig. 4.7 for several values of ϕ. To be able to better follow the resonance positions, the derivative spectra were singly integrated, so that the resonance positions of the contributing signals correspond to the maxima of the (overlapping) peaks. Fig. 4.8a shows the spectra as a function of the angle ϕ. For the sake of simplicity, we restrict the following analysis to the resonance position of the dominant spectral component (corresponding to the maximum intensity) which is marked by crosses in the individual spectra. Fig. 4.8b shows the resonance positions along with a

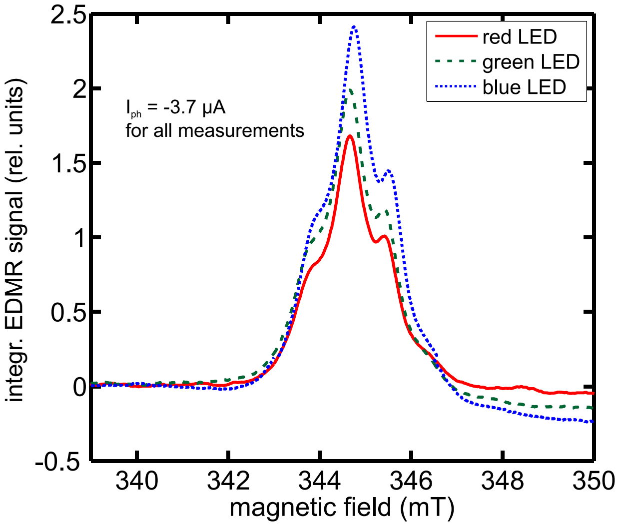

Figure 4.9.: Dependence of the integrated EDMR spectrum obtained at $\phi = 60°$ on the excitation wavelength. The light from three different LEDs (red: $\lambda \approx 620$ nm; green: $\lambda \approx 520$ nm; blue: $\lambda \approx 430$ nm) was fed through a fibre with an attached microprism.

simulation of the resonance position of the P_b centre on a (111) oriented silicon surface based on literature data [117]. The reported principal values for the g tensor having axial symmetry ($g_{||} = 2.0012$, $g_{\perp} = 2.0081$) were obtained by conventional EPR experiments on silicon wafers with thermally grown SiO_2 layers. Inspection of the rotation pattern reveals a good agreement between the experimentally determined resonances positions and the behaviour of the P_b centre, indicating that both signals originate from paramagnetic centres with identical g tensors.

The observation of the rotation pattern unequivocally shows that the dominant signal is related to c-Si and cannot originate from the 'bulk' a-Si:H. Since only the front side of the wafer was polished and the rear side is rough, we can also exclude that the resonance results from recombination at the rear contact. However, to confirm that the assignment of the signal is correct, we took advantage of the fact that the absorption coefficient and the concomitant charge carrier generation profile depend on the photon energy. By replacing the halogen lamp by a blue LED ($\lambda \approx 460$ nm), electrons and holes are predominantly generated near the a-Si:H/c-Si interface, whereas the use of a red LED ($\lambda \approx 620$ nm) results in a more homogeneous generation profile. Fig. 4.9 shows singly integrated EDMR spectra for $\phi = 60°$ and three different excitation wavelengths. For all wavelengths the light intensity[5] was adjusted to yield a photocurrent of -3.7 μA at $U = -1.0$ V. Fig. 4.9 demonstrates that the intensities of all spectral components increase with photon energy.

---

[5] Note that the lower light intensity produced by the LEDs as compared to the intensity of the halogen lamp did not significantly change the shape of the spectra.

4.2.4. Microscopic interpretation

With increasing photon energy the concentration of charge carriers that are generated close to the a-Si:H/c-Si interface also increases. Therefore, the recombination rate of these electrons and holes is enhanced in the same way. Consequently, the dependence of the EDMR spectrum as a function of the photon energy of the incident light strongly indicates that all contributing signals originate from spin-dependent recombination processes occurring at or near the a-Si:H/c-Si interface.

Due to the fact that the spectra comprise a superposition of at least five lines and the determination of the individual resonance positions is not possible without ambiguity for all spectra, we will restrict the discussion to the dominant spectral component with $g_{||} = 2.0012$ and $g_{\perp} = 2.0081$ as well as the two lines at g_{e} and g_{CE} with resonance positions which are independent of ϕ (cf. Fig. 4.7)[6]. According to its g value, the signal at $g_{\mathrm{e}} = 2.0046(5)$ can be attributed to conduction band tail states in the a-Si:H layer [135,136]. Since amorphous silicon is a disordered material, the position of the resonance is independent of the sample orientation in the magnetic field. An EDMR resonance at g_{e} is known to occur for tunnelling transitions between conduction band tail states and neutral dangling bonds in bulk a-Si:H [77]. In analogy to this process, it is conceivable that the spin-dependent recombination at the a-Si:H/c-Si interface equally involves a-Si:H conduction band tail states. However, here the spin partner is not a db state in the a-Si:H, but a singly occupied interface states that gives rise to the dominant EDMR resonance in Fig. 4.8. This spin-dependent recombination process is shown schematically in Fig. 4.10. It is assumed that the recombination step is completed by the capture of a hole from c-Si following the tunnelling transition between the a-Si:H tail state and the paramagnetic centre at the interface. It is important to note that the sign of the EDMR signals (under reverse bias) is in accordance with a recombination process.

Based on the presented results, the resonance at $g_{\mathrm{CE}} = 1.9991(5)$ (see Fig. 4.7) cannot be definitely assigned to a known paramagnetic centre at the a-Si:H/c-Si interface. However, previous pEDMR measurements on similar cell structures with varying emitter layer thicknesses have revealed an EDMR resonance at the same g value [130]. We assume that this signal does not originate from a spin-dependent process involving any of the other resonances that are present in Fig. 4.7 because its temperature dependence is markedly

---

[6] Close inspection of the rotation pattern in Fig. 4.8a reveals the presence of at least two additional signals which are — due to the anisotropy of the corresponding resonance positions — likely to also result from spin-dependent recombination at the a-Si:H/c-Si interface.

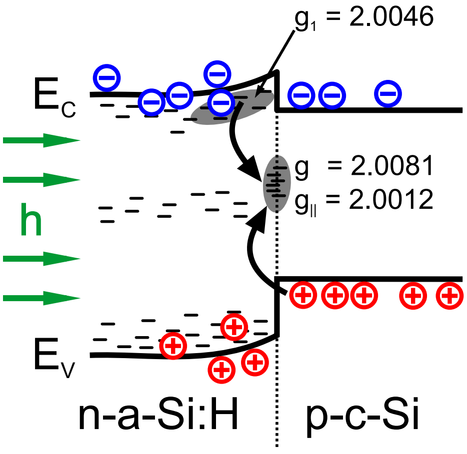

Figure 4.10.: Schematic representation of a tunnelling transition from an a-Si:H conduction band tail state to an a-Si:H/c-Si interface state. The recombination process is completed by the (not spin-dependent) capture of a hole from the c-Si valence band.

different from the behaviour of the other signals. While the interface-related signals show a maximum at ≈ 18 K, the resonance at g_{CE} exhibits maximum intensity at 13 K (data not shown). Within the experimental uncertainty, the g value as well as the line width[7] of approximately 0.15 mT are in accordance with the EPR signature of conduction electrons in crystalline silicon [137]. Based on the presented experimental results it remains unclear to what extent an electron accumulation layer at the a-Si:H/c-Si interface — as was recently suggested to be present in n-a-Si:H/p-c-Si structures based on coplanar conduction and capacitance-voltage measurements [138] — might play role in this regard. Experiments to explore possible EDMR signals originating from such an inversion layer and possible similarities to the CE signal in microcrystalline silicon are currently underway using p-a-Si:H/n-c-Si heterostructures with inverse doping combination.

Besides the important consequences of the P_b-like structure observed at the a-Si:H/c-Si interface for the recombination properties in a-Si:H/c-Si solar cells, the above results also have implications for the much more complex microcrystalline silicon. In μc-Si:H it is believed that c-Si columns are well passivated by amorphous silicon [27, 139, 140]. These columns are oriented along the growth direction, and the surfaces of these crystallites form boundaries to an amorphous silicon region. Hence, we believe that this situation is very similar to the a-Si:H/c-Si interface which we define as a model system for μc-Si:H. Assuming that the g tensor of these defects is identical to the g tensor found for the a-Si:H/c-Si interface defect, the resulting powder-like EDMR spectrum for spin-dependent recombination involving these interface states can easily be calculated. Fig. 4.11a shows a

---

[7] The line width of the signal at g_{CE} in the spectrum shown in Fig. 4.7 is deteriorated by the modulation amplitude of 0.3 mT.

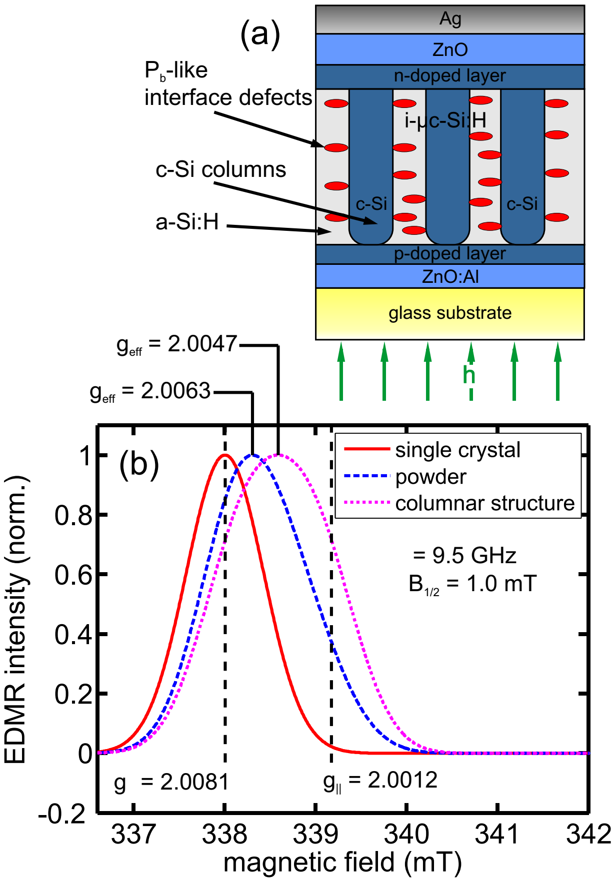

Figure 4.11.: (a) Cross section of a μc-Si:H thin-film solar cell. The columns consist of crystalline silicon and are oriented perpendicular to the substrate. In this simplified sketch it is assumed that all P_b-like interface states are oriented perpendicular to the crystallite surfaces. (b) Simulated EDMR spectra for recombination via defect states for a single crystal (all defects are oriented in the same direction), a randomly oriented μc-Si:H powder and a columnar structure as shown schematically in (a). For all simulations we assumed that the g tensor of the defect states is identical to the g tensor of P_b centres. Details are given in the text.

sketch of the μc-Si:H structure embedded in a thin-film solar cell. Taking into account the direction of the c-Si columns with regard to the magnetic field in the EDMR measurements as presented in Chapter 5 and further assuming that the defects in μc-Si:H have the g tensor as determined in the model system[8], the resulting 'restricted powder pattern' leads to an EDMR resonance at $g_{\text{eff}} = 2.0047$ as shown in Fig. 4.11b. This is markedly different from $g_{\text{eff}} = 2.0063$ which would result from the situation when the defects are located at the surface of randomly oriented c-Si crystals (no columnar structure) or if the defects are only present in the amorphous silicon region. In the latter case, we would expect the typical a-Si:H g value, $g = 2.0055$. An orientation dependence of the g values of dangling bonds was indeed observed in EPR measurements on in μc-Si:H films [141]. Although we neglected that the orientations of the c-Si surfaces deviate from a perfect (111) orientation and thus the principal values of the g tensors will slightly vary [115], the result of the simulation is in agreement with experimental results for dangling bonds in microcrystalline silicon

---

[8] We assumed a line width of 1.0 mT (FWHM) in the simulations.

as will be shown in Chapter 5. Note that deviations from the assumed columnar structure (e.g. close to the substrate, cf. Fig. 4.11a) can lead to further shifts of the g value into the direction of $g = 2.0063$.

In conclusion, we identified a spin-dependent recombination process at the a-Si:H/c-Si interface between a-Si:H band tail states that give rise to an EDMR resonance at $g_e = 2.0046(5)$ and paramagnetic centres at the interface having an axially symmetric g tensor with principal values $g_{||} = 2.0012$ and $g_{\perp} = 2.0081$ and a symmetry axis parallel to the (111) surface normal. The discrimination between interface states and defects in the 'bulk' a-Si:H could be achieved by exploiting the well-defined orientation of the c-Si surface dangling bonds. From the EDMR spectra obtained at different excitation wavelengths, a significant contribution from the back contact can be excluded. Furthermore, the orientation-dependent signals cannot stem from the back surface as it is rough (i.e. not crystallographically defined). The g tensor components extracted from the rotation pattern resemble the signature of the well-studied P_b centre at the interface between c-Si and SiO_2. These findings allow for two different interpretations:

(i) A thin SiO_x interlayer was present at the a-Si:H/c-Si interface and thus the c-Si surface markedly deviates from an ideally hydrogen-terminated surface. This has important implications for the solar cell properties because the defect density at an oxidized silicon surface is significantly higher than the density of interface states at a H-terminated surface. A previous study revealed that the defect density of an initially hydrogen-terminated c-Si surface increases by an order of magnitude upon exposing the sample to clean-room air at room temperature for only 10 minutes [15]. Provided that the oxide is not fully removed during emitter deposition, the impact of this interlayer on the device performance can be quite severe (cf. Fig. 4.1).

(ii) Since there are no literature values available for the g tensor of a-Si:H/c-Si interface states, an alternative explanation in accordance of the observed interface-related EDMR signals is possible: It is conceivable that the g tensor of paramagnetic states at the a-Si:H/c-Si interface is entirely determined by the c-Si surface and that the amorphous layer on top has only a negligible influence. On the one hand this seems very unlikely because the $g_{||}$ and $g_{\perp}$ are sensitive to changes of the surface morphology which can be seen from the different EPR signatures of P_b-like defects at the (100) oriented Si/SiO_2 interface [120, 115]. On the other hand defect states at the interface between silicon and other oxides than

SiO_2, e.g. HfO_2, Al_2O_3 and ZrO_2, exhibit the same [142, 143] or very similar [144] EPR signatures[9] like defects at Si/SiO_2.

In order to unequivocally conclude whether SiO_2 is involved in the recombination process or the g tensor is a generic feature, we suggest to perform an atomic-resolution EDX analysis in a TEM setup[10]. If it turns out that a SiO_2 phase is present at the interface, it is possible that the interface defect density can be further reduced by preparing the heterostructure by depositing a-Si:H on a hydrogen-terminated c-Si surface without bringing the specimen into contact with ambient oxygen prior to the deposition process. This could result in an improved open circuit voltage of the a-Si:H/c-Si solar cell.

4.3. Conclusion

By applying EDMR to heterojunction solar cells we were able to directly detect the influence of recombination via a-Si:H/c-Si interface states on the charge transport in the device for the first time. The discrimination between defect states in the ‘bulk’ a-Si:H and c-Si interface states could be achieved by exploiting the orientation of the dangling bonds at the (111) oriented c-Si surface. The principal values of the g tensor are identical to those of the prominent P_b centre at the Si/SiO_2 interface. This finding indicates that either a thin SiO_x interlayer was present between a-Si:H and c-Si or that the g tensors of the P_b centre and the a-Si:H/c-Si interface defect are identical.

In the following Chapter 5 we employ pEDMR to thin-film solar cells based on µc-Si:H — which can be considered to consist of many disordered a-Si:H/c-Si interfaces — to identify spin-dependent transport and recombination processes and the contributing paramagnetic centres.

---

[9] Note, however, that in contrast to a-Si:H these layers all contain oxygen.

[10] EDX: Energy-Dispersive X-ray spectroscopy, TEM: Transmission Electron Microscopy.

5. pEDMR in µc-Si:H solar cells

Pulsed electrically detected magnetic resonance (pEDMR) was employed to study spin-dependent processes that influence charge transport in microcrystalline silicon (µc-Si:H) pin solar cells. Special emphasis was put on the identification of the signals with respect to the individual layers of the cell structure. For this purpose, we systematically modulated the morphology of the highly doped n- and p-layers from amorphous to microcrystalline. By combining the information obtained from low-temperature ($T = 10$ K) pEDMR spectra and from the deconvoluted time evolution of spectrally overlapping resonances, we found signals from conduction band tail states as well as phosphorus donor states in samples containing an amorphous n-type layer and a resonance associated with valence band tail states in samples with amorphous p-layer. Moreover, signals from the intrinsic microcrystalline absorber layers could be identified. A comparative multifrequency pEDMR study at X- and Q-band further increased the spectral resolution. An additional resonance at $g = 1.9675(5)$ was found, which has not been observed in EDMR before. We assign this signal to shallow donors in the Al-doped ZnO layer which is commonly used as transparent conducting oxide in thin-film solar cells. Room-temperature pEDMR measurements show that in all samples recombination via dangling bonds in the intrinsics absorber layer prevails at 300 K. The experimental findings are discussed in the light of various spin-dependent transport mechanisms known to occur in the respective layers of the pin structure.

5.1. Introduction

The high efficiencies that can be reached with wafer-based technologies, e.g. a-Si:H/c-Si heterojunction solar cells as described in Chapter 4, come along with the energy and cost intensive wafer production process. In contrast to that, solar cells made from hydrogenated amorphous silicon (a-Si:H) and its microcrystalline counterpart (µc-Si:H) can be deposited directly on inexpensive substrates like glass and have the potential to be superior with regard to material consumption and cost effectiveness. Unfortunately, a-Si:H and µc-Si:H suffer from an inferior electronic quality compared to crystalline silicon. This is due to defect states in the band gap of the material resulting from silicon dangling bonds (db) as well as band tail states close to the band edges. In thin-film solar cells, trapping and recombination at localized defects are the main limiting factors for the cell performance. Due to the fact that these defects are often paramagnetic (in the case of db) or can be made paramagnetic by light excitation (in the case of tail states), EPR applied to µc-Si:H powder samples can reveal quantitative as well as structural information (e.g. information on defect concentrations and the local environment of defects) [101, 145, 146].

To overcome the sensitivity limitations of conventional EPR, cwEDMR was applied in the past to study the influence of defects on the charge transport in thin-film solar cells [91]. Though conventional cwEDMR proved to provide valuable information about defect states in the material, a complete picture of the transport mechanisms in the solar cell may only be obtained by pEDMR techniques. Extending the capabilities of EDMR into the time domain, pEDMR allows assigning defect states to complex transport mechanisms.

In this chapter we exploit pEDMR to identify paramagnetic centres in µc-Si:H solar cells. Thin-film solar cells comprising many layers of different materials typically yield overlapping pEDMR signals, which may only be identified by combining appropriate pEDMR techniques with a systematic variation of the sample morphology. While the types of localized defect states that are present in either µc-Si:H or a-Si:H are similar, the fingerprints of their respective EPR signals (most importantly the g value) show significant differences between both morphologies [9]. In a first part, pEDMR measurements were performed at $T = 10$ K in order to benefit from the enhanced signal-to-noise ratio at low temperatures which is indispensable for a thorough analysis of the EDMR signals and the assignment to the respective defect states. In this regard, measurements were carried out at X- and Q-band frequencies to distinguish between field-dependent and field-independent interactions. It is important to note that mechanisms that govern the spin-dependent transport at $T = 10$ K differ significantly from the performance-limiting processes at normal solar cell operating conditions. Thus, in a second part we take advantage of recent instrumental improvements which allowed us to employ pEDMR at room temperature in order to study the mechanisms that prevail at 300 K.

In the following sections we will first describe the sample structures and subsequently focus on measurements employed to a series of thin-film solar cells with a microcrystalline

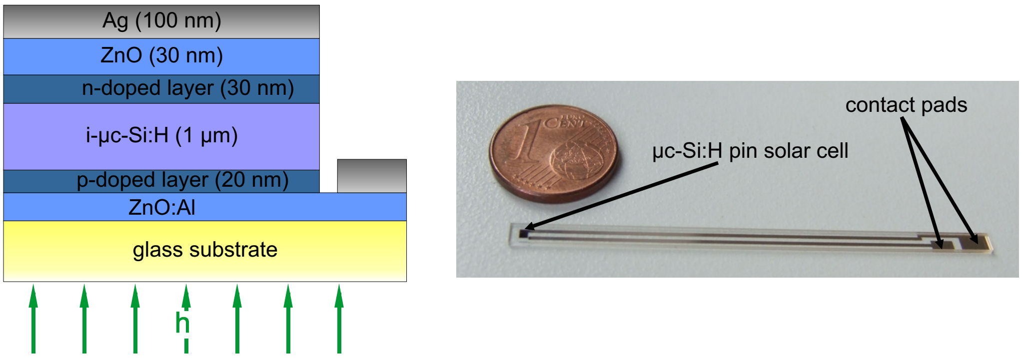

Figure 5.1.: Left: layer structure of the superstrate μc-Si:H pin solar cells. Four different samples which differ in the morphology (amorphous or microcrystalline) of the n- and p-doped layers were investigated. Right: photograph depicting the pEDMR sample geometry. The solar cell (active area of 1 × 1 mm^2) is electrically connected by 5 cm long thin-film wires that extend to contact pads on the opposite side of the substrate.

absorber layer in which the morphology (μc-Si:H or a-Si:H) of the doped layers in the pin structure was systematically altered. The aim of this study is to discriminate between different processes involving various types of defect states in the individual layers of the solar cell. The results will be discussed in the light of information about a-Si:H and μc-Si:H powder samples previously obtained by EPR.

5.2. Samples

All μc-Si:H pin solar cells investigated in this study are based on the layer sequence shown in Fig. 5.1. The samples were deposited on glass substrates (Corning 1737 and Corning Eagle 2000) using plasma enhanced chemical vapour deposition (PECVD) at the Forschungszentrum Jülich with a process that was shown to reach efficiencies above 10% on areas of 1 cm^2 [147]. Four series of solar cells were prepared, where the p- (boron) and n-doped (phosphorus) layers were either composed of amorphous or microcrystalline silicon keeping the deposition conditions for the intrinsic absorber layer unchanged. The solar cells were grown on Al-doped ZnO, always starting with the thin p-doped silicon layer. A ZnO/Al layer stack was used as back reflector and contact. Note that the chosen cell structure was not optimized for high solar cell conversion efficiency but was solely designed for the purpose to reliably study the influence of the various layers on the EDMR behaviour.

Table 5.1.: Structure of the silicon-layers for the μc-Si:H pin solar cells investigated in this study.

	n-layer	i-layer	p-layer
sample A	a-Si:H	μc-Si:H	μc-Si:H
sample B	μc-Si:H	μc-Si:H	μc-Si:H
sample C	a-Si:H	μc-Si:H	a-Si:H
sample D	μc-Si:H	μc-Si:H	a-Si:H

To discriminate between pEDMR signals arising from the intrinsic μc-Si:H absorber or the highly doped layers, four samples with the layer sequence described in table 5.1 were prepared. It should be noted here that different thicknesses of the ZnO layer were used for the four samples. However, we believe that this does not affect the pEDMR signals originating from the silicon pin structures. Throughout this chapter the sample structures will be referred to as sample A, B, C, and D. Schematic energy-band diagrams of all cells neglecting the ZnO as well as metal layers are depicted in Fig. 5.2.

For the pEDMR samples a special contact structure as described in Section 3.3 was used to establish an electrical connection to contact pads that are positioned outside the microwave (mw) resonator. The patterning of the contacts as well as the confinement of the active solar cell area to 1 mm^2 was realized by laser scribing techniques [107] (see Fig. 3.5b). Fig. 5.1 depicts a photograph of a completely processed sample.

5.3. Experimental details

Details about the pEDMR setup are presented in Section 3.2. The EDMR measurements were carried out at $T = 10$ K under illumination through the glass substrate with a cold light source at approximately 50 mW cm^{-2} unless otherwise noted. Fig. 5.3 shows current voltage curves obtained under these experimental conditions. Note that the low-temperature *I*-*V* curves differ significantly from those one would obtain at room temperature. At positive voltages this can primarily be attributed to barriers — in particular the heterobarrier between a-Si:H and μc-Si:H — which hinder the charge transport in the device. This is in line with the observation that the *I*-*V* curve of sample B (μc-Si:H n- and p-layers) varies markedly from the other curves in the forward bias regime.

For the EDMR measurements, a reverse bias voltage of $U = -1$ V was applied to the sample. Due to the different current-voltage-characteristics of the respective sam-

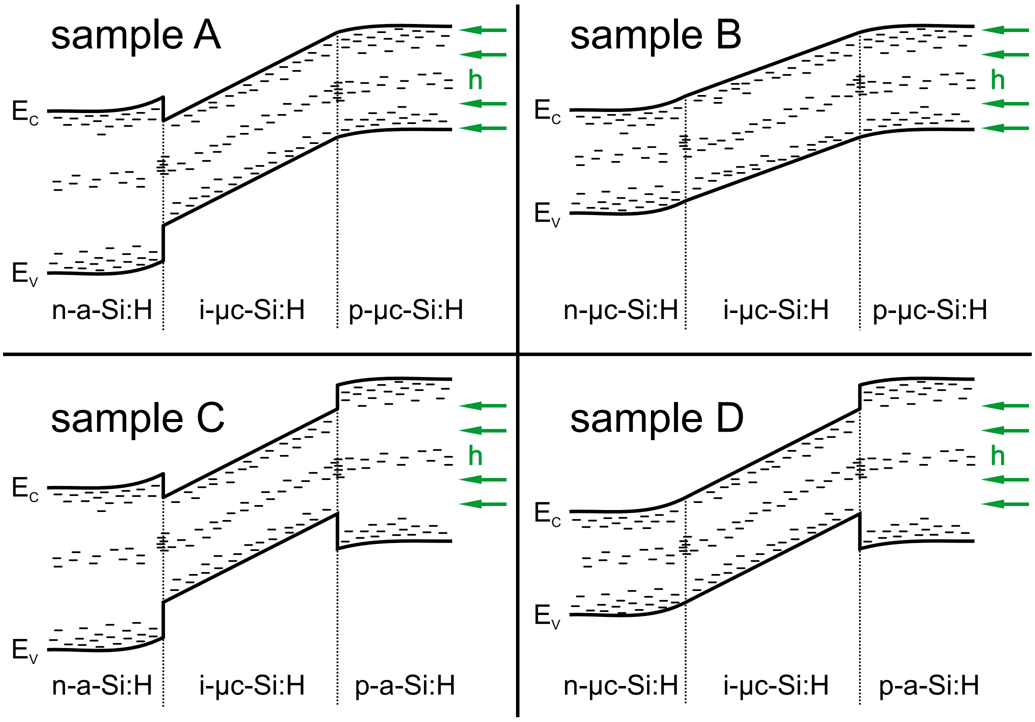

Figure 5.2.: Schematic representation of the energy-band diagrams at room temperature without illumination for samples A to D. The morphology of the doped layers can be identified by the different band gaps. Localized defect states are sketched for all layers without taking into account the difference in their density of states with respect to energy, doping concentration and layer morphology. Note that the ZnO and metal layers have been omitted. Note further that the band bending in the intrinsic layer due to charging of the localized states was neglected. In all measurements presented here, the cells were illuminated through the substrate (p-side of the pin structure).

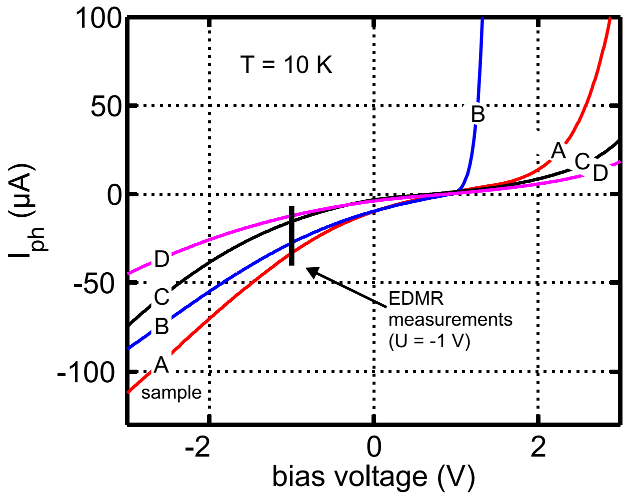

Figure 5.3.: Low-temperature current-voltage characteristics of samples A to D under illumination (50 mW cm^{-2}). All EDMR measurements were carried out at a constant voltage $U = -1$ V (reverse bias regime of the solar cell). This point is indicated in the plot by a vertical line.

ples A to D (cf. Fig. 5.3), this corresponds to photocurrent densities between -1.3 and -3.3 mA cm^{-2}. At this voltage the qualitative behaviour of the illuminated I-V curves was the same for all samples, and in none of the samples the saturation regime of carrier extraction was reached. We believe that at $U = -1$ V the current extraction mechanism is the same for all specimens under study and is dominated by drift currents induced by the electric field of the intrinsic µc-Si:H layer.

For comparative pEDMR measurements at X- and Q-band the sample was illuminated through a fibre with the light from a red laser diode (Elektronik-Manufaktur Mahlsdorf). Details about the Q-band setup are given in Section 3.2.2.

Two-dimensional mappings of the spin-dependent processes were obtained by recording the transient photocurrent changes $\Delta|I_{\mathrm{ph}}|$ following a mw pulse excitation as a function of the external magnetic field. Details about the current detection setup and its influence on the pEDMR transients are given in Section 3.2.4.

5.4. Results and discussion

The pEDMR datasets obtained from samples A to D differ with respect to both their spectral shape as well as their transient behaviour. In the following, we will first identify the defect states by their resonance position in the pEDMR spectra. Combining these pieces of information with the dynamics and Rabi oscillations of the respective spectral components, we will, in a second step, conclude on the underlying transport and recombination mechanisms.

5.4.1. X-band pEDMR spectra

Fig. 5.4 shows the pEDMR spectra of samples A to D recorded at $t = 2.2$ µs after applying the mw pulse. The insets display spectra taken from the same samples on a broader magnetic field range. Common to all spectra is that they contain a narrow component centred around the g value of the free electron and, in addition, a broad (> 20 mT) component with lower intensity. Beside these similarities, further inspection of the spectra unravels that the narrow component as well as the broad line consist of several EDMR signals which, in addition, differ from sample to sample.

For the identification of the defects contributing to the pEDMR spectra, we analysed the resonances by fitting Lorentzian and Gaussian functions to the narrow spectra. The line shapes (Gaussian or Lorentzian) were chosen to achieve best fits to the experimental data. Note that the mw power in pEDMR is considerably higher than in cwEDMR. As a result, mw power broadening of the lines can lead to deviations between line shapes and line widths obtained from cw- and pEDMR experiments. This applies especially to narrow lines. The results of the least square fits can be summarized as follows: Best fits to the experimental spectra can be obtained when assuming a resonance at $g_{\mathrm{CE}} = 1.9975(5)$ for all samples. Additionally, we find a signal at $g_{\mathrm{e}} = 2.0049(5)$ in samples A and C (amorphous n-layer) as well as a line at $g_{\mathrm{h}} = 2.011(1)$ in samples C and D (amorphous p-layer).

The broad spectra reveal an additional pair of lines separated by 25 mT, indicating the presence of hyperfine interaction in samples A and C (amorphous n-layer). Both lines are symmetric to $g_{\mathrm{P}} \approx 2.003$. This feature is absent in samples B and D (microcrystalline n-layer). Instead, in samples B and D an asymmetric broad signal is uncovered. For an unambiguous assignment of the microscopic origin of this line we will discuss its spectral shape in more detail below.

5.4.2. Comparison between X- and Q-band pEDMR spectra

In order to further elucidate the origin of the signals contributing to the spectra we performed pEDMR experiments under different spin resonance conditions (Q-band, $B_0 = 1.2$ T, $\nu = 35$ GHz) but otherwise identical conditions. Since the relative strengths of the signals that were obtained in X-band critically depend on external parameters (such as temperature, applied voltage and spectrum of the illumination [148]) and the pEDMR

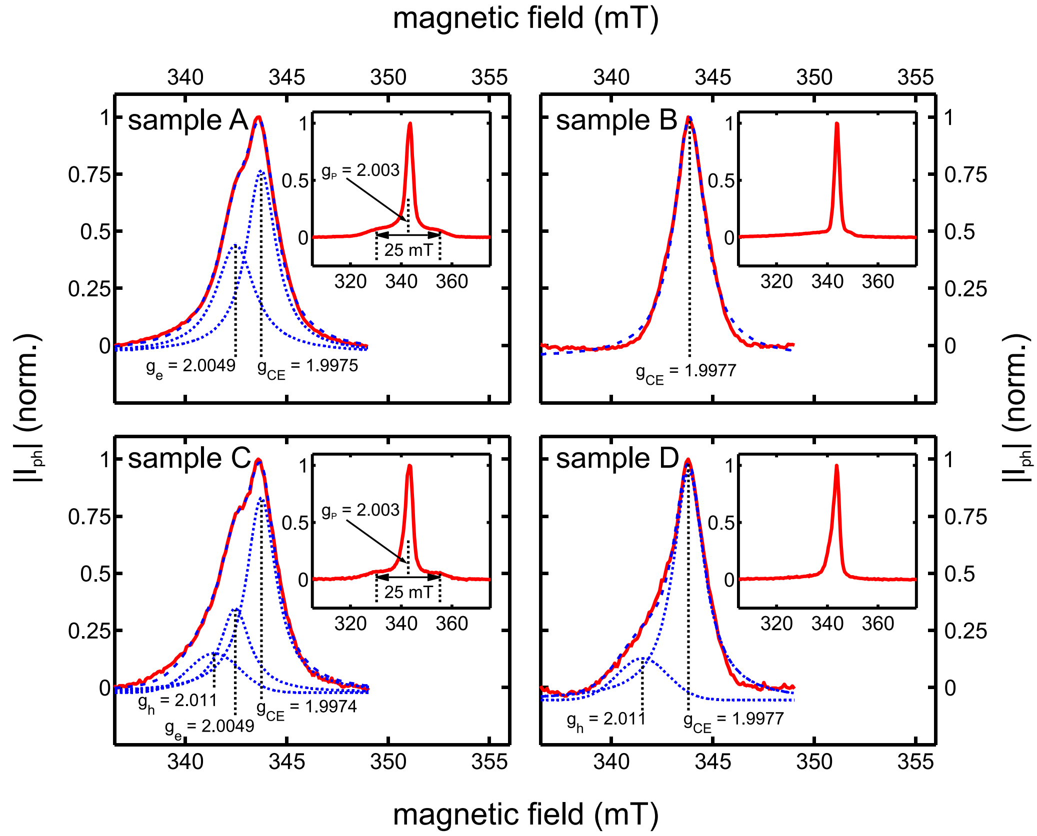

Figure 5.4.: pEDMR spectra ($\Delta|I_{\text{ph}}|$ normalized to 1) of samples A to D taken at t = 2.2 μs after the mw excitation at $T = 10$ K using a pulse length τ of 320 ns (solid line: experiment; dashed line: fit to the experimental data; dotted lines: individual spectral components as obtained from the fit). The resonance positions are indicated by vertical dotted lines. The insets show spectra on a broader magnetic field range measured under the same experimental conditions except for a mw power increased by 9 dB in order to enhance the broad spectral components. In addition, τ was set to values between 50 and 60 ns, which in all cases corresponds to a spin flip angle of $\phi = \Omega \cdot \tau = \pi$, with Ω being the Rabi frequency.

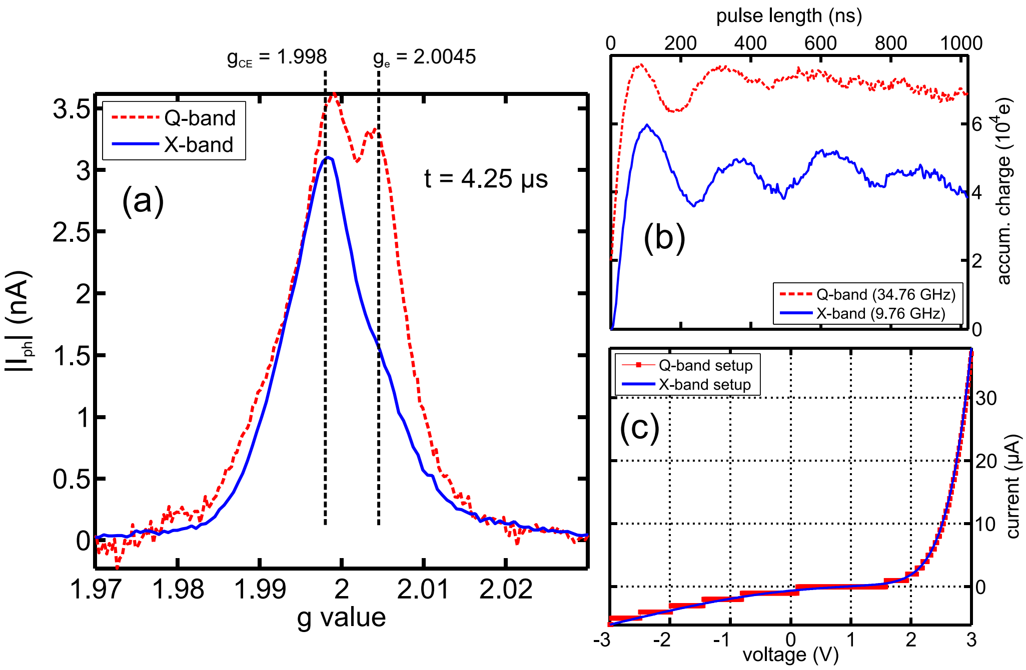

Figure 5.5.: Comparison between X- and Q-band pEDMR spectra obtained under identical experimental conditions. (a) Low-temperature (T = 10 K) pEDMR spectra ($\Delta|I_{\mathrm{ph}}|$ as a function of the g value) taken at $t = 4.25$ μs after a 144 ns long π-pulse for resonance frequencies of 34.76 and 9.76 GHz. (b) Electrically detected spin-Rabi nutations demonstrating that B_1 is similar for both mw frequencies. (c) I-V curves measured prior to the pEDMR measurements in both setups. All measurements were performed under illumination from a laser diode ($\lambda = 635$ nm) and under reverse bias conditions ($U = -1.0$ V, $I_{\mathrm{ph}} = -1.95$ μA).

spectrum may additionally be affected by power broadening effects when strong mw pulses are used, care has to be taken to accomplish identical experimental conditions for X- and Q-band measurements. For this to achieve we verified that the current-voltage characteristics are identical. The I-V curves were measured prior to the pEDMR measurements in X- and Q-band and are shown in Fig. 5.5c. Since the current detection electronics was the same for the measurements at both resonance frequencies, the transient behaviour of the pEDMR signals was identical as well. Furthermore, we adjusted the mw attenuation to yield the same Rabi frequencies in X- and Q-band. The respective spin-Rabi nutations are displayed in Fig. 5.5b, revealing $\tau_\pi \approx 150$ ns in both cases. Moreover, the spin-nutations correspond to the behaviour of spin $1/2$ particles — the signature of weakly coupled spin pairs. No qualitative change between X- and Q-band could be observed.

Fig. 5.5a shows the X- and Q-band pEDMR spectra at $t = 4.25$ μs after a 144 ns long mw pulse for sample A. It is obvious that although the maximum amplitudes of the signals $\Delta|I_{\mathrm{ph}}|$ in X- and Q-band agree within the experimental uncertainty, the ratio between the intensities of the resonances at g_{CE} and g_{e} differs markedly for both spectra[1]. The same tendency, namely a stronger relative intensity of the line at g_{e} in Q-band, is observed when both measurements are carried out under illumination from a halogen lamp[2].

In order to compare the spectral shapes of both contributing signals in X- and Q-band we adjusted the illumination conditions in a way that the ratio between the two signal intensities is identical in X- and Q-band. Fig. 5.6a shows the resulting normalized pEDMR spectra measured at slightly different times after the mw pulse.

From a comparison between the spectra it becomes apparent that the two spectral components are in general dominated by field-dependent broadening (g strain). However, both resonances are affected differently. The width and shape (on a g value scale) of the signal at $g_{\mathrm{CE}} \approx 1.998$ seems to be identical for both frequencies, indicating that already at X-band the signal is entirely determined by g strain. This broadening can only be overcome when going to lower resonance frequencies. In contrast to that, the resonance at $g_{\mathrm{e}} \approx 2.0045$ becomes significantly narrower when going to Q-band. This behaviour indicates that field-independent contributions such as unresolved hyperfine interactions significantly influence the line shape at X-band, resulting in a better spectral resolution in Q-band.

Another point that deserves some attention is the pair of resonances centred at g_{P} which exhibits a splitting of ≈ 25 mT in X-band. If these lines are caused by hyperfine interaction with a nuclear spin, the splitting should remain constant when increasing the mw frequency from X- to Q-band. This is indeed the case as can be seen from the comparison between both spectra shown in Fig. 5.6b. While the width of the central lines increases due to g strain, the satellites are clearly visible in both spectra and exhibit the same splitting. This observation corroborates the interpretation of the signals. Note that the abscissa in the plot (ΔB_0) is the deviation of the magnetic field from the centre of the spectrum. The fact that

---

[1] Note that the pair of resonances centred at g_{P} are not visible in Fig. 5.5 because of the limited magnetic field range.

[2] When white excitation light is used, the relative intensity of the signal at g_{e}, which originates from the n-doped amorphous layer, is more pronounced in both X- and Q-band. This can be attributed to the fact that the excitation spectrum of the halogen lamp extends to ≈ 800 nm and therefore a significant part of the light reaches the n-a-Si:H layer. In the case of the laser diode ($\lambda = 635$ nm), the penetration depth is similar to the cell thickness [149] and so only a small fraction of the light reaches the n-doped layer. This observation is consistent with a systematic study on the influence of the photon energy on the EDMR spectrum [148].

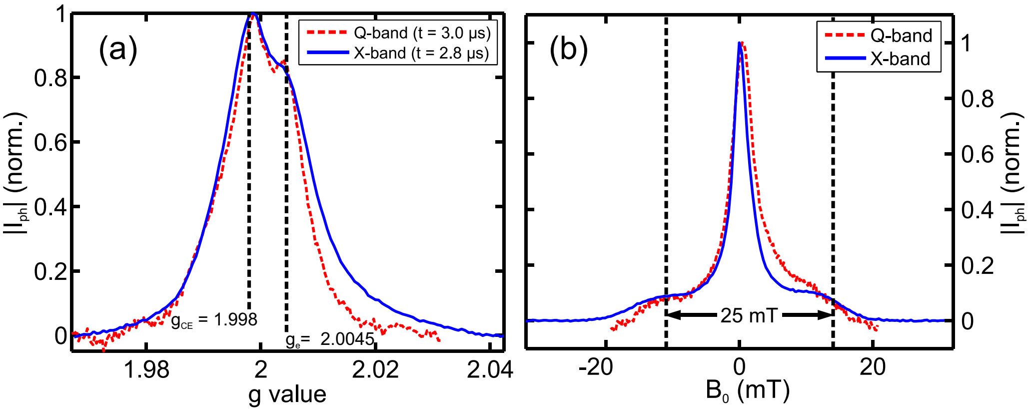

Figure 5.6.: (a) X- and Q-band pEDMR spectra ($\Delta|I_{\mathrm{ph}}|$ normalized to 1 as a function of the g value) from sample A obtained at $T = 10$ K. The Q-band spectrum was measured under the same experimental conditions like the one shown in Fig. 5.5a. The measurement at Q-band was performed under illumination from a halogen lamp in order to achieve the same intensity ratio between the resonances at g_{CE} and g_{e} for both mw frequencies. (b) Spectra measured over a larger magnetic field range. Note that the abscissa in this plot (ΔB_0) denotes the deviation of the magnetic field from the centre of the spectrum. The dashed vertical lines denote the positions of two satellite lines with their centre-of-gravity at $g_{\mathrm{P}} = 2.003$. Note that the splitting is independent of the mw frequency.

the line width of the central resonances in the X-band spectrum is similar to the width in the Q-band spectrum can be attributed to the high mw power used in the experiment. The resulting strong pulses are on the one hand helpful in emphasizing the broad satellite lines but on the other hand lead to significant power broadening and therefore deteriorate the true line shape.

5.4.3. Identification of defect states

In the following, we will assign the resonance positions to defect states in the samples based on findings from previous EDMR and EPR studies on thin films as well as powder samples.

Intrinsic µc-Si:H

In intrinsic and n-doped µc-Si:H an EPR resonance at $g = 1.997 - 1.998$ is reported in various studies which is associated with shallow localized states in energetic proximity to the conduction band, typically referred to as CE states [150, 151, 152, 145, 79, 153]. It was demonstrated by cw- and pEDMR measurements on µc-Si:H films that these states are involved in hopping transport at low temperatures as well as in tunnelling recombination between CE and dangling bond states [79, 146]. Hence, we assign the signal at $g_{\mathrm{CE}} = 1.9975(5)$, that was observed in all samples, to originate from CE states in the intrinsic microcrystalline absorber layer.

n-doped a-Si:H

Both samples that contain an a-Si:H n-layer (samples A and C) show signals at $g_{\mathrm{e}} = 2.0049(5)$ and $g_{\mathrm{P}} \approx 2.003$, which are absent in samples B and D. This is a strong indication that these resonances are related to localized states in n-a-Si:H. In the case of the line at g_{P} (in the following referred to as 'P signal'), this interpretation is supported by the fact that the EDMR signal consists of a pair of Gaussian lines with equal intensity that are split by 25 mT. This splitting is well known to arise from hyperfine (hf) interaction between phosphorus electron and nuclear spins in amorphous silicon [154] and was shown to also exist in the cw- and pEDMR spectra of phosphorus-doped a-Si:H [136, 131]. It is worthwhile noting here that phosphorus is only incorporated in the thin n-doped layer and that for phosphorus-doped µc-Si:H neither the 4.2 mT hyperfine splitting known from c-Si nor the above-mentioned 25 mT split hf lines are observed [145, 139]. This is consistent with our observations. Moreover, the Q-band measurements performed on sample A unambiguously show that the splitting arises from a field-independent interaction. The signal at g_{e} is presumably associated with conduction band tail states in the n-a-Si:H layer and is also observed in n-a-Si:H/c-Si solar cells [131]. EDMR investigations at temperatures between 100 and 150 K have revealed that a signal at $g = 2.0044$ may be associated with hopping of electrons among band tail states in a-Si:H (known as 'e signal') [135,136]. However, light-induced EPR measurements have shown an increase of the g value with decreasing temperature [155]. Thus, the discrepancy between $g = 2.0044$ and $g_{\mathrm{e}} = 2.0049(5)$ — as it was found in our measurements at $T = 10$ K — might be explained by the temperature difference. This is also in line with low-temperature pEDMR results for hopping via a-Si:H tail states in a-Si:H/c-Si solar cells [131, 62].

p-doped a-Si:H

Analogous to electron hopping described before, hopping of holes via valence band tail states in boron-doped a-Si:H can also contribute to the photocurrent. The corresponding resonance (‘h signal’) has been investigated in the past using EDMR [77, 135, 136] and optically detected magnetic resonance (ODMR) revealing $g = 2.011$ to 2.013 [156, 157, 158]. In the solar cells C and D (a-Si:H p-layer) we found a signal at $g_{\mathrm{h}} = 2.011$ which we assign to valence band tail states in a-Si:H. No evidence of boron acceptor states could be found.

The CH signal

In the pEDMR spectra of samples B and D (µc-Si:H n-layer) the 25 mT splitting of the phosphorous signal is absent. Further inspection of these spectra unravels an asymmetric signal of different shape (see Fig. 5.4). Fig. 5.7a gives an enlarged view of the pEDMR spectrum of sample B with a range covering the first 10% of the ordinate range of the plot in Fig. 5.4. The line shape of the resonance resembles the powder pattern of an asymmetric g tensor. The dashed curve in Fig. 5.7a depicts the results of a simulation (simulation program EasySpin [99], simulation parameters: $g_{\parallel} = 2.15$, $g_{\perp} = 1.995$, field-dependent inhomogeneous broadening $\Delta g_{\parallel} = 0.2$, $\Delta g_{\perp} = 0.01$). Note that field-dependent inhomogeneous broadening has been reported in many cases concerning disorder in amorphous silicon [159, 101, 160]. Asymmetric broad lines in echo-detected field-sweep spectra obtained by pulsed EPR have been reported in literature to be associated with holes in localized valence band tail states (referred to as CH signal) in undoped and boron doped µc-Si:H [139]. Therefore, it seems to be justified to assign the asymmetric signal described above to CH states in the intrinsic absorber layer which is present in all samples. The CH signal is indeed visible in the spectra of all samples, however, in samples A and C it is almost completely hidden underneath the high-field hf-satellite which has a higher intensity. We can exclude that this line originates from the a-Si:H layers because the EPR signature from valence band tail states in a-Si:H is different (cf. h signal described before) [77]. It should be noted that it is complicated to resolve broad lines in cwEDMR. In pulsed EPR and EDMR, however, one benefits from a flat baseline which facilitates the observation of broad spectral components.

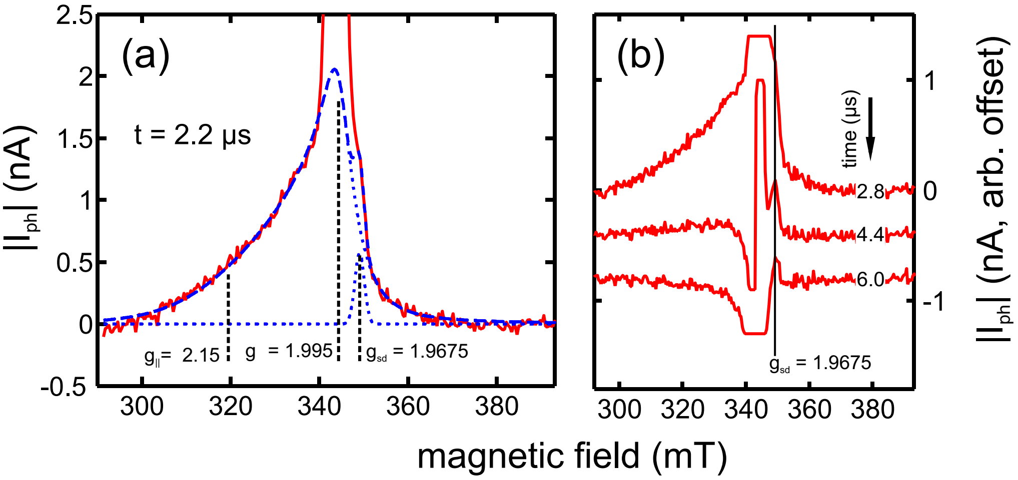

Figure 5.7.: Asymmetric line that was found in samples B and D (µc-Si:H n-layer). (a) Enlarged view of the pEDMR spectrum ($\Delta|I_{\mathrm{ph}}|$) of sample B as shown in Fig. 5.4 with an ordinate range covering the first 10% of the maximum signal amplitude (solid line: experiment; dashed line: results of a simulation consisting of an inhomogeneously broadened line with parameters given in the text and a symmetric Gaussian line at $g_{\mathrm{sd}} = 1.9675(5)$; dotted lines: both spectral components separately). (b) pEDMR spectra of sample B for several delays after the mw excitation. The solid vertical line serves as a g value marker. Note that the time behaviour of the asymmetric line and the sd resonance is considerably different.

The sd signal

Further examination of Fig. 5.7a reveals an additional spectral component with Gaussian line shape at $g_{\mathrm{sd}} = 1.9675(5)$ (FWHM = 2.5 mT) which is represented by a dotted curve in Fig. 5.7a. The fact that this line (referred to as 'sd signal') is not part of the asymmetric resonance becomes clear when evaluating the time evolution of the pEDMR spectra. This is illustrated in Fig. 5.7b where three spectra taken between 2.8 and 6.0 µs after the mw excitation are shown. The position of g_{sd} is marked by a solid vertical line. The central lines have been cut in order to facilitate the analysis of the weaker signals. The plot unambiguously shows that the sd signal has a distinctively different time dependence as compared to the asymmetric line, indicating that both signals arise from different paramagnetic centres and microscopic processes. While the asymmetric line resulting from CH states was found in all four samples, the sd signal could exclusively be observed in sample B.

To the best of our knowledge, no EPR or EDMR signals caused by paramagnetic states at $g_{\mathrm{sd}} = 1.9675(5)$ have been reported for either a-Si:H or µc-Si:H. However, resonances at similar g values were obtained from shallow donors in ZnO [161, 162]. Here, the observed g value critically depends on the morphology (crystallite size) of the respective ZnO material. The photogenerated charge in all solar cells investigated traverses the ZnO layers on both sides of the pin structure which are both degenerately doped with aluminium. We therefore assign the sd signal to originate from either of the ZnO layers. Its g value and the fact that this resonance is only observed in sample B suggests that it is connected to a shallow donor state resulting from Al incorporated in the ZnO layer on the p-µc-Si:H side or at the interface between these two layers. From this argumentation, the sd resonance should also appear in sample A, but here the line may be buried below the broad and rather intensive hf satellites. We can exclude that the resonance is connected to transport at or through the ZnO/n-µc-Si:H interface since the sd signal is not visible in the spectrum of sample D.

In summary, the line parameters of the individual signals and the associated paramagnetic defects in the respective layers are listed in table 5.2.

Table 5.2.: g values, line shapes and line widths obtained from least-square fits to the pEDMR spectra with narrow and wide magnetic field range (see Fig. 5.4). Details are given in the text.

		sample A	sample B	sample C	sample D	paramagnetic state
CE	g_{CE} (Lorentzian)	1.9975(5)	1.9977(5)	1.9974(5)	1.9977(5)	cond. band tail
	$\mathrm{FWHM}_{\mathrm{CE}}$ (mT)	1.8(1)	1.8(1)	1.8(1)	1.9(1)	µc-Si:H
e	g_{e} (Lorentzian)	2.0049(5)		2.0049(5)		cond. band tail
	$\mathrm{FWHM}_{\mathrm{e}}$ (mT)	2.3(1)		1.8(1)		a-Si:H
h	g_{h} (Gaussian)			2.011	2.011	val. band tail
	$\mathrm{FWHM}_{\mathrm{h}}$ (mT)			2.9	2.9	a-Si:H
P	g_{P} (Gaussian)	2.003 hf split.: 25 mT		2.003 hf split.: 25 mT		phosph. donor a-Si:H
	$\mathrm{FWHM}_{\mathrm{P}}$ (mT)	11.3		11.3		
sd	g_{sd} (Gaussian)		1.9675(5)			shallow
	$\mathrm{FWHM}_{\mathrm{sd}}$ (mT)		2.5			donor ZnO
db	g_{db} (Lorentzian)		2.0045(5)			dangling bond
	$\mathrm{FWHM}_{\mathrm{db}}$ (mT)		1.3(1)			µc-Si:H
CH	g_{CH} (asym.)		$g_{\parallel} = 2.15$ $g_{\perp} = 1.995$			val. band tail µc-Si:H
	$\mathrm{FWHM}_{\mathrm{CH}}$ (mT)		5 (Lorentz.) $\Delta g_{\parallel} = 0.2$ $\Delta g_{\perp} = 0.01$			

5.4.4. Assignment to microscopic transport and recombination mechanisms

In order to fully describe the involvement of different defect states in charge transport processes, information obtained from line shape analyses have to be combined with the information extractable from pEDMR transients and Rabi oscillations.

In general, EDMR signals result from changes in the probability for spin-dependent transitions between paramagnetic states. All signals observed in this study can be explained within the framework of a spin pair model in which the transition probability depends on the relative spin orientation of both spin partners of the pair [44, 58, 34]. Upon application of a strong mw pulse which is in resonance with either of the participating states, the transition probability generally increases, leading to an increase of the corresponding transition rate. However, this rate change of a microscopic process can influence the macroscopic photocurrent of a pin µc-Si:H solar cell in different ways, depending in a complicated way on the microscopic mechanism, the device physics, and, in the particular case of pin solar cells, on the bias voltage applied to the sample [163, 164].

In the present case all experimental data have been obtained in the reverse bias regime ($U = -1$ V) where the photocurrent is negative. In this situation, the pEDMR transient exhibits a relative enhancement of the photocurrent ($\Delta|I_{\mathrm{ph}}| > 0$) immediately after the mw pulse for a spin-dependent hopping process (cf. Section 2.3.1.3), implying an improvement of carrier extraction due to the selective mw excitation. The resonant mw pulse leads to an increase of the hopping rate and thus can be considered to enhance the mobility in the hopping transport path. It has been shown that mobility modulations in thin-film silicon solar cells can strongly affect the conductivity, in particular at low temperatures [165, 166]. In contrast to that, one would expect an initial quenching of the photocurrent ($\Delta|I_{\mathrm{ph}}| < 0$) for spin-dependent recombination or trapping (cf. Section 2.3.1.1). In this case, the conductivity is altered by a spin-resonant change of the charge carrier concentrations. Note that the above-mentioned spin-dependent processes can be connected to other charge extraction limitations such as transport over energy barriers at contacts, recombination in a space charge region, space charge limited currents or trap assisted tunnelling through barriers. In such a case it is difficult to predict the sign of the photocurrent change since these processes can coexist and influence the current response of the device in a rather complex manner. However, irrespective of the spin-dependent transport limitation, theory predicts that the pEDMR transient shows a sign reversal when non-vanishing triplet transition probabilities are present [34, 35]. To discriminate between various mechanisms, additional information is needed which we may obtain from the dynamics of the pEDMR signals as well as from coherent spin motion experiments.

5.4.4.1. Analysis of pEDMR transients

To evaluate in which way the different signals affect the charge transport in the device, we deconvoluted the pEDMR signals in time domain by taking the line parameters from the spectra shown in Fig. 5.4 (cf. table 5.2) as fixed parameters and their relative intensities as fit parameters. Thus, we were able to independently study the time behaviour of the spectrally overlapping signals. In this way we obtained the integrated peak intensities, A_{peak}, of all resonances. In order to cross-check the validity of the spectral fits (see Fig. 5.4), the three lines at g_{CE} (FWHM $= 1.8$ mT), g_{e} (FWHM $= 1.8$ mT) and g_{h} (FWHM $=$ 2.9 mT) were taken into account for all samples.

Fig. 5.8 depicts the time evolution of A_{peak} for samples A to D. From the time traces shown it is obvious that the three pEDMR signals CE, e and h exhibit different dynamics. This indicates that none of the paramagnetic states associated with these resonances belong to the same spin-dependent process. In this case one would expect that both peak intensity and dynamics of two lines are correlated. Beside the different rise and fall times, all three signals show the same behaviour with respect to the observed sign of the mw induced effect (enhancing signal), except for the line at g_{e} in sample B which shows a photocurrent decrease after the mw excitation (quenching signal). The small dip at short times ($t <$ 3 µs) of this quenching signal is a measurement and data processing artefact. Although the g value of the quenching signal in sample B (see Fig. 5.4) seems indistinguishable from the g value of signals at g_e in sample A and C, we ascribe this quenching signal to a different paramagnetic state, namely dangling bond states in the intrinsic absorber layer. This argumentation is supported by the fact that we are able to resolve a small g value shift between the enhancing lines of samples A and C as compared to the quenching signal in sample B. In addition, the quenching signal exhibits different dynamics and can easily be separated from the CE line in sample B by evaluating the time evolution of the spectra. Fig. 5.9 shows a comparison between two spectra recorded at $t = 2.2$ and 4 µs after the mw pulse excitation. One can clearly observe the quenching contribution at $t = 4$ µs which can easily be fitted separately. From this analysis we find $g_{\mathrm{db}} = 2.0045(5)$ which slightly differs from g_{e} as it was found for samples A and C. Within the experimental uncertainty this agrees with the g values reported for Si dangling bonds in µc-Si:H ($g =$

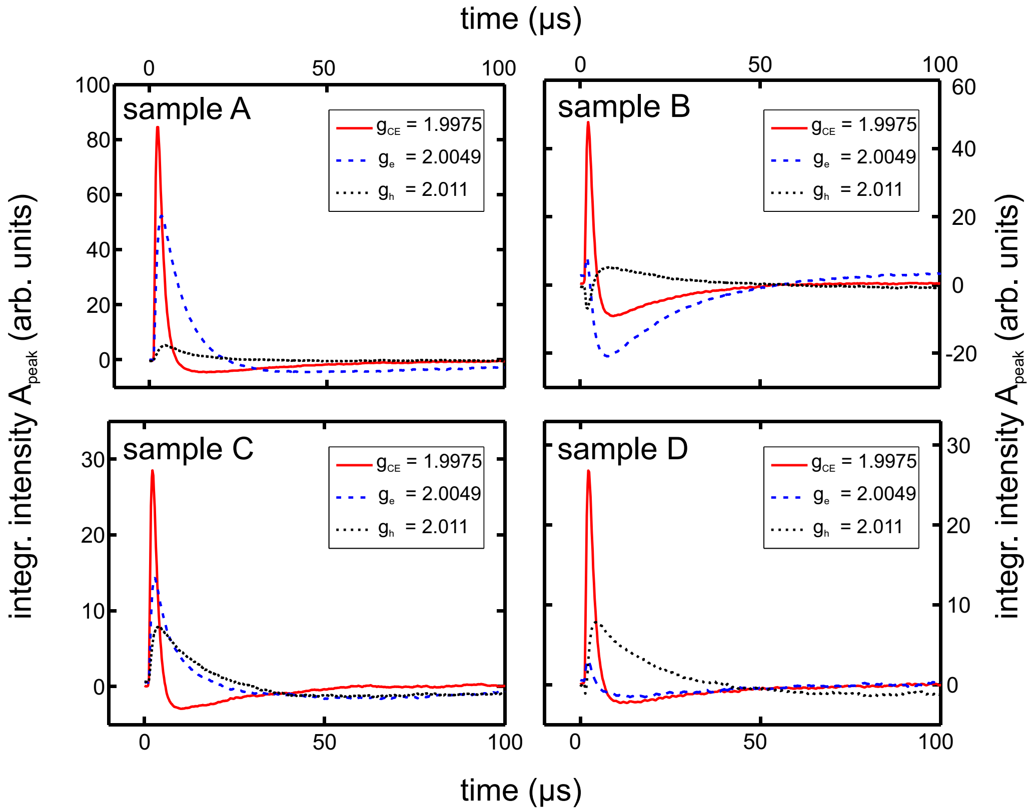

Figure 5.8.: Time-dependent integrated peak intensities, A_{peak}, of the deconvoluted pEDMR signals of samples A to D. The deconvolution procedure was applied to the experimental data obtained with narrow magnetic field range (cf. Fig. 5.4). The g values and line widths were assumed to be identical for all samples. Details of the deconvolution procedure are described in the text.

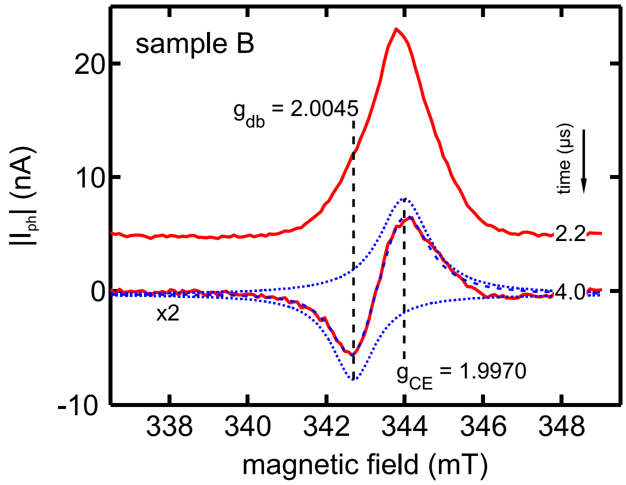

Figure 5.9.: pEDMR spectrum ($\Delta|I_{ph}|$) of sample B recorded 4.0 µs after the mw pulse. Two lines with different g values and opposite signs can clearly be distinguished (solid line: experiment; dashed line: result of a fit with two Lorentzian lines; dotted lines: both separate contributions to the fit). Note that the spectrum has been multiplied by a factor of two to allow for a better comparison with the spectrum recorded at 2.2 µs which is also included in the plot.

2.0042–2.0058 depending on the deposition conditions) [140, 167]. Further on, this is in line with a simulation assuming dangling bonds which are oriented perpendicular to the c-Si columns as shown in Fig. 4.11 in Section 4.2.4. This is in agreement with the assumption that recombination mainly takes place at defects located at grain boundaries. Note that in spite of the difference between g_{db} and g_e, the temporal evolution of the quenching signal (Fig. 5.8) is reflected by the line at $g_e = 2.0049$ (deduced from the enhancing signal found in samples A and C, cf. Fig. 5.4). At present it is not clear why this quenching signal is not also observed in samples A, C and D. Either this signal is associated with the specific interface of the intrinsic and the doped layers or the signal is simply masked by the strong signals related to the doped a-Si:H layers.

To evaluate the dynamics of the 25 mT hf split lines that show up in the spectra of samples A and C, the deconvolution procedure on these samples was additionally carried out using the pEDMR datasets with broad magnetic field range. Here, we assumed the same parameters as described before for the CE and e signals but, for the sake of simplicity, omitted the line at g_h. The P signal was taken into account by assuming a pair of symmetric Gaussian lines with equal intensity that are split by 25 mT and have their centre-of-gravity at $g_P = 2.003$. Fig. 5.10 shows the results of this analysis.

While the time dependence of the CE and e signals resembles that given in Fig. 5.8, we observe a clear correlation between the rise and fall times of the lines at g_e and g_P for both samples. For this to occur, both centres must either be involved in the same microscopic process or two different processes involving the two paramagnetic centres separately, but influence I_{ph} in a similar way [168]. Based on the experimental results

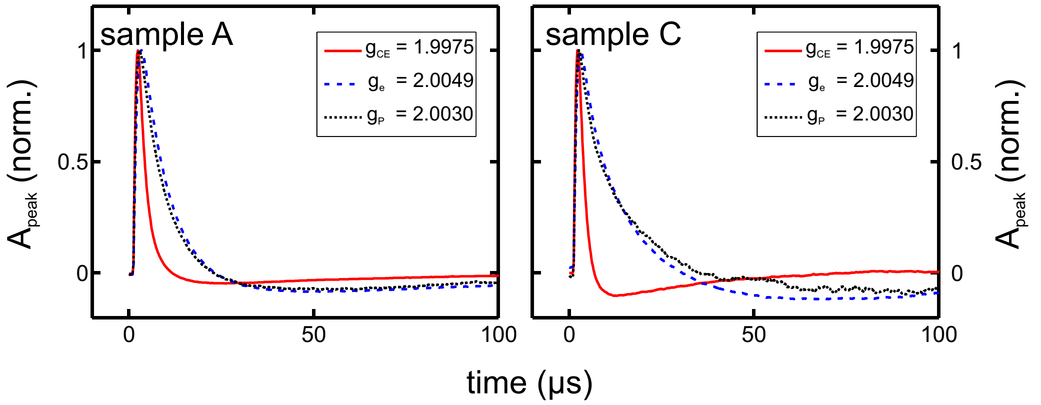

Figure 5.10.: Integrated peak intensities (A_{peak}) for samples A and C (cells with a-Si:H n-layer). The deconvolution procedure was performed using the two-dimensional pEDMR datasets with wide magnetic field range (cf. main plots in Fig. 5.4). The hyperfine signal that is visible in the respective spectra was taken into account by assuming a pair of Gaussian lines that are symmetric to $g_P = 2.003$. Note that the ordinate scale is normalized to 1 to facilitate the comparison of the dynamics.

we cannot unambiguously discriminate between both possibilities, but in any case the correlation between the pEDMR transients supports the interpretation that both signals stem from spin-dependent processes in the n-a-Si:H layer.

5.4.4.2. Coherent spin motion

Further information about charge transport mechanisms and the involvement of the defects assigned above may be obtained by analysing Rabi oscillations of the observer spins localized at the respective defect states. In particular, one can distinguish a spin-dependent transition (recombination or tunnelling) that involves only one paramagnetic centre — like direct capture recombination at silicon dangling bonds or a hopping process among tail states — from a process in which the spin-dependent transition takes place between two centres having different g values [44, 58, 168]. In the latter case, one can address the spins of the charge carriers in both states separately by choosing the resonance condition according to the g value of the respective spin. The frequency of the coherent spin motion is given by the Rabi frequency of the paramagnetic centre which is in resonance, provided that the driving field γB_1 (B_1 denotes the amplitude of the mw magnetic field and γ is the gyromagnetic ratio) is small compared to the Larmor separation $\Delta\omega = (\omega_a - \omega_b)$ of the two respective centres [36, 37]. Here, ω_a and ω_b are the Larmor frequencies of the two centres *a* and *b*, respectively. On the contrary, when the Larmor separation of two participating centres is smaller than the driving field ($\Delta\omega \ll \gamma B_1$), theory predicts a Rabi frequency that is higher by a factor of two (cf. Section 2.5) [103, 95, 34].

To observe Rabi oscillations in pEDMR, the charge $Q(\tau)$ resulting from the integration of $\Delta|I_{\mathrm{ph}}|$ over several microseconds after the mw excitation is recorded as a function of the pulse length τ as described in detail in Section 3.1 [11]. Fig. 5.11 illustrates the charge response $Q(\tau)$ obtained on two different spectral positions (indicated by the g values as given in the legend) for each sample. The insets show Fast Fourier Transformations (FFT) of $Q(\tau)$ clearly indicating similar Rabi frequencies ($\Omega/2\pi = 12$–15 MHz) for all signals. Under the experimental conditions used in the experiment this corresponds to the Rabi frequencies we expect for a spin-dependent transition between weakly coupled spins that can be resolved in the pEDMR spectrum ($\Delta\omega \gg \gamma B_1$). It should be stressed that, unfortunately, the weak peak intensities of the broad lines (hf and CH) do not allow us to determine their Rabi frequencies.

Assuming that all EDMR signals found in this study can be explained by the spin pair model [44], in which the relative spin orientation of both partners of a spin pair determines a microscopic transition rate, two spectrally distinguishable paramagnetic states are involved in each spin-dependent transition such as recombination or hopping process. When the spectral positions and/or line widths of these resonances differ significantly, which is true for the signals e and P in samples A and C, the frequency measured in the coherent spin motion experiment reflects the Rabi oscillation of the centre which is in resonance (e signal in this case) [34]. In the opposite case, when the spin pair consists of two paramagnetic centres with similar g values and homogeneous broadening, only one line appears in the pEDMR spectrum. However, in this case it is impossible to manipulate only one spin partner without influencing the other (referred to as spin-locking behaviour, cf. Section 2.5.1) [36, 37], and thus, one measures a Rabi frequency which is predicted to be higher by a factor of two as compared to the case before [103, 95, 34]. Only if the lines of both spins are strongly inhomogeneously broadened, the spectral overlap between individual spin packets of both lines may be small enough to form a weakly coupled spin pair.

All Rabi measurements presented here indicate spin-dependent transitions between paramagnetic centres which do not overlap in the EDMR spectra. This, however, raises the question which EDMR resonance line represents the respective recombination or hopping partner. For the EDMR signals which could be assigned to the n-a-Si:H layer, this puzzle may be answered referring to the transients of the EDMR signals shown in Fig.

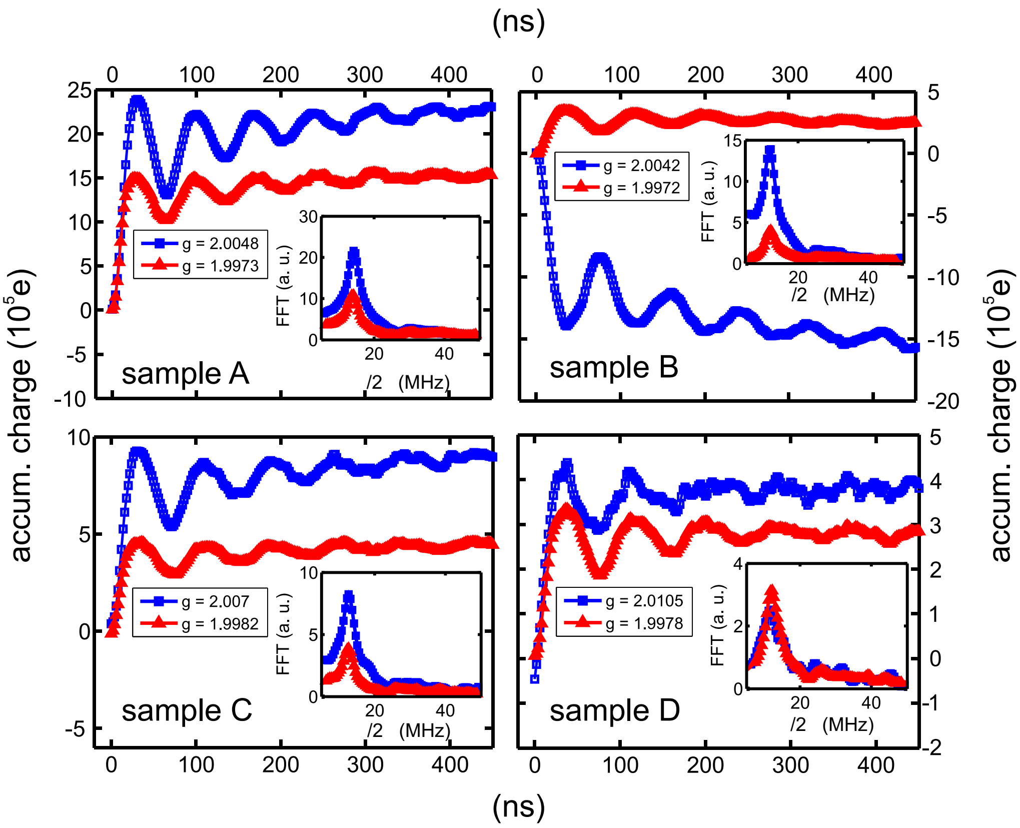

Figure 5.11.: Results of pEDMR measurements of coherent spin motion carried out at two spectral positions for each sample A to D. The mw pulse length was varied from 0 to 450 ns with an increment of 2 ns. The oscillations reflect the coherent spin motion of the spin pair ensemble during the mw pulse. Fast Fourier Transformations of the data are depicted in the insets. The oscillation frequencies $\Omega/2\pi$ lie in the range from 12 to 15 MHz which corresponds to the Rabi frequency of a spin $1/2$ under the conditions used in the experiment.

5.8. Both signals e and P, which originate from conduction band tail states and phosphorus donor states in the amorphous n-layer, have the same dynamics and their resonances in the pEDMR spectrum are clearly separated. Hence, they may constitute a weakly coupled spin pair, where the spin partners may be excited independently by the microwave pulse, resulting in the observed Rabi frequencies. This indicates a spin-dependent process between the two respective centres. Following the previous interpretation of the centres, we assign the spin-dependent process to hopping between band tail and phosphorous states in a-Si:H [168].

For the signals related to the µc-Si:H absorber layer this question remains an obstacle because the transients depicted in Fig. 5.8 exhibit completely different time constants. At present it is not clear how these paramagnetic centres are related to microscopic transport or recombination processes. A straightforward explanation of the observed Rabi behaviour can only be delivered if we assume that in the case of the signals CE, CH and db the respective pair partners are not visible in the pEDMR spectra due to the fact that their lines are strongly inhomogeneously broadened or that the signals arise from a microscopic process involving more than two spins (cf. Section 2.4).

The paramagnetic centres that were identified by the pEDMR analyses described above are summarized in Fig. 5.12.

5.5. Coherent pEDMR at room temperature

All pEDMR measurements presented so far were performed at $T = 10$ K in order to benefit form the enhanced signal-to-noise ratio at low temperatures. This is particularly helpful for pinpointing the defect states that contribute to the spin-dependent signals and to identify the underlying microscopic processes. However, the performance-limiting processes at normal solar cell operating conditions clearly differ from the processes that prevail at 10 K. Hence, from the viewpoint of solar cell characterization, the preceding measurements have solely set the stage for further studies at 300 K.

In general, EDMR measurements are not restricted to the low-temperature regime. On the contrary, many early cwEDMR experiments were carried out at room temperature [8, 42]. It thus seems conceivable to also perform pulsed EDMR measurements at 300 K. The fact that there are — to the best of the author's knowledge — no reports about EDMR on silicon-based devices available to date is primarily attributed to the limited sensitivity,

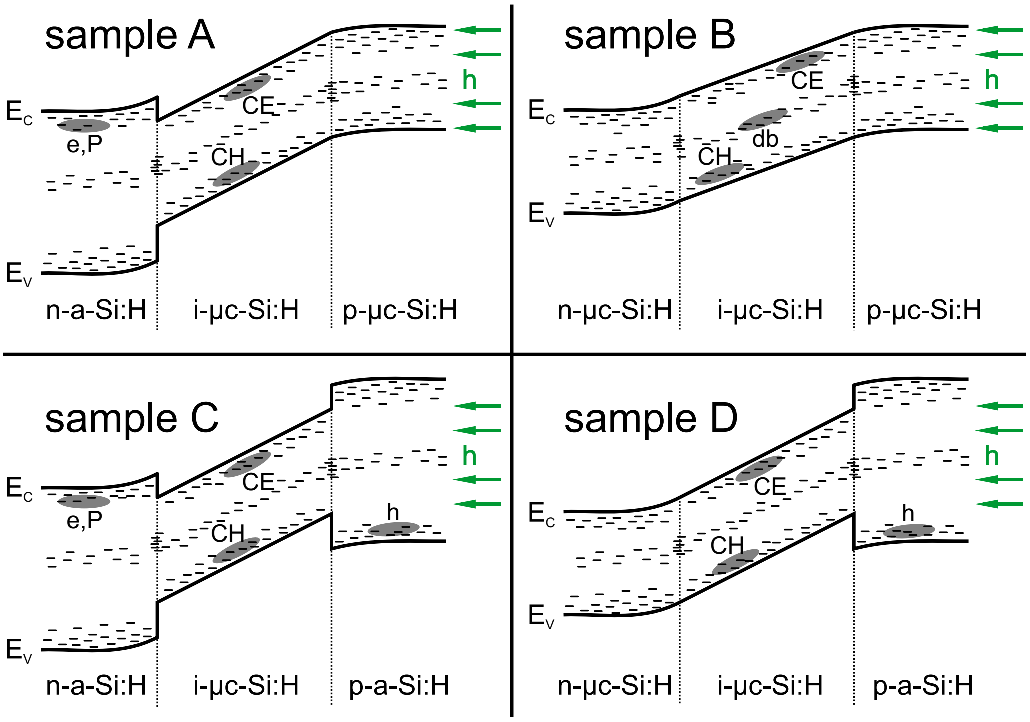

Figure 5.12.: Sketch of energy-band diagrams at room temperature without illumination for samples A to D. The paramagnetic centres that were found to be involved in spin-dependent processes in the respective samples are shown schematically. Details can be found in the text.

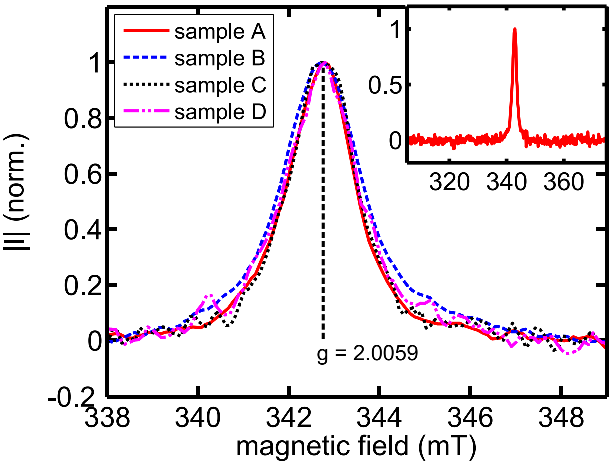

Figure 5.13.: Room-temperature pEDMR spectra ($\Delta|I|$ normalized to 1) taken at $t = 2.0$ µs after a 320 ns long mw pulse for samples A to D (see Table 5.1). The measurements were performed without illumination in the forward bias regime ($U = 0.26 - 0.48$ V, $I = 9 - 20$ µA). All spectra are normalized to allow for a comparison of the line shapes. The inset shows a spectrum of sample A on a larger magnetic field range.

which is still significantly lower than for cwEDMR with phase-sensitive detection. For different materials, namely C_{60} films and organic solar cells based on zinc-phthalocyanine, pEDMR was recently applied to observe coherent spin effects at $T = 300$ K [169, 170]. This raises the question whether coherent spin motion can equally be measured in silicon-based devices or whether short spin relaxation times in silicon prevent the observation of coherent effects at room temperature. Due to instrumental improvements carried out in this work (see Chapter 3), we were able to perform pEDMR measurements at 300 K on the µc-Si:H solar cells described in Section 5.2. In the following, we will show that coherent effects can also be observed.

5.5.1. pEDMR spectra

Fig. 5.13 shows room-temperature pEDMR spectra of the µc-Si:H based solar cell structures A to D (cf. table 5.1) at $t = 2.0$ µs after a 320 ns long mw pulse. The measurements were carried out without illumination in the charge carrier injection regime, i.e. a positive bias voltage between 0.26 and 0.48 V was applied which corresponds to a current density[3] between 0.9 and $2\,\mathrm{mA\,cm^{-2}}$. The pEDMR signal intensities are normalized in order to ensure comparability. While the low-temperature measurements that were performed on the same specimens revealed that the spectral features are distinctively different for the samples A to D (see Fig. 5.4), the spectra at 295 K are dominated by an asymmetric resonance line at $g = 2.0059(5)$ which is similar for all four samples. Although the g value

---

[3] The values vary from sample to sample because the current-voltage characteristics depend on the morphology of the doped layers.

significantly differs from the g value of dangling bonds in microcrystalline silicon, the fact that the same spectrum is observed for all four samples strongly indicates that the signal originates from defect states in the intrinsic µc-Si:H layer. If the doped layers contributed to the spectra, one would expect to observe pronounced differences for samples A to D. The negligible influence of the doped layers on the spin-dependent transport at room temperatures is consistent with the general change of the transport mechanisms in a-Si:H and µc-Si:H. While at 10 K hopping transport — which may be spin-dependent — among localized band tail states prevails, the conductivity at 300 K is dominated by transport which takes place above the mobility edge and does not exhibit spin-dependence [24]. These arguments support the assumption that the pEDMR signal indeed originates from recombination of electrically injected electrons and holes via db states in the i-µc-Si:H layer. This is in agreement with previous cwEDMR measurements and simulations on µc-Si:H pin solar cells [163, 164]. However, based on the pEDMR spectra alone it is impossible to elucidate the underlying microscopic mechanism of this spin-dependent process.

The inset of Fig. 5.13 shows the spectrum of sample A on a broader magnetic field range. It was measured under the same experimental conditions except for a mw power increased by 9 dB to enhance possible broad spectral components. As excepted, we observe no contributions from phosphorus in the n-a-Si:H or any other hyperfine satellites. This provides further evidence for the above-mentioned interpretation that resonance at $g = 2.0059$ originates from the intrinsic layer.

We will now discuss the deviation of the $g = 2.0059$ from the commonly observed g value of dangling bonds in microcrystalline silicon (g_{db}, refer to Section 5.4.4.1). As can be seen from Fig. 5.13, the resonance signals exhibit an asymmetric shape, indicating that different defect states contribute to the signal. In fact, best fits to the experimental data can be obtained when assuming two Lorentzian lines with different g values and line widths. Fig. 5.14a demonstrates this for the spectrum of sample A. The same fitting procedure was applied to the spectra of samples B to D. The resulting g values of both lines are shown in Fig. 5.14b. It is obvious that the g values scatter significantly[4], which can only partly be attributed to the limited signal-to-noise ratio at room-temperature. It rather is anticipated that the spectral features vary from sample to sample because the electric field distributions depend on the morphology of the doped layers which is different for samples A to D. However, based on the presented results we cannot assign the origin of the strong variation of g_2.

---

[4] The errorbars in Fig. 5.14b indicate only the errors with respect to the particular sample.

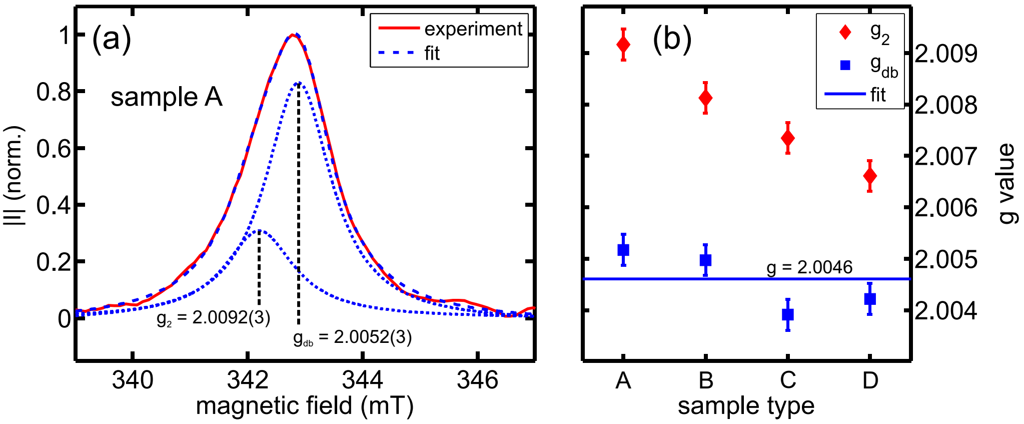

Figure 5.14.: (a) Room-temperature pEDMR spectrum ($\Delta|I|$ normalized to 1) of sample A along with the results from a fit to the experimental data (solid line: experimental data; dashed line: fit results consisting of two Lorentzian lines; dotted lines: both lines separately). (b) g values obtained from fits to the room-temperature spectra of samples A to D. Note that the lower g value (average value 2.0046) is within the range that is associated with db states in μc-Si:H, whereas the higher g value markedly shifts from samples A to D.

Common to all spectra is that the lower g value is within the range which is attributed to dangling bonds in microcrystalline silicon ($g_{\mathrm{db}} = 2.0042$–2.0058 [140, 167]). The observation of an additional resonance besides the signal from db states is in accordance with earlier cwEDMR studies on amorphous silicon [171]. Here, Brandt *et al.* found a systematic shift of the resonance position towards higher g values upon decreasing the photon energy of the illumination for db-related recombination. This was attributed to the hopping of holes in the valence band tail which was identified as the rate-limiting process at low photon energies. With increasing contribution from valence band tail states, the g value approaches the average value between g_{dB} and g_{h} [77] and the resonance line becomes asymmetric. The same trend was observed by Lips *et al.* in a-Si:H based pin solar cells but interpreted in a different way [91]. They ascribed the change of the EDMR spectrum to the inhomogeneous light absorption and the concomitant inhomogeneous recombination profile. Following the former interpretation by Brandt *et al.* we can consistently explain the spectra in Figs. 5.13 and 5.14a when we assume that situation for db-related recombination in a-Si:H and μc-Si:H is comparable and that the quasi-Fermi levels of holes are similar in the case of electrical charge carrier injection and under illumination with sub- or near-band gap light.

5.5.2. Spin-Rabi nutations at room temperature

Since the intensities of both resonances at g_{db} and g_2 differ significantly, the spin-dependent transition between dangling bonds and valence band tail states (db-CH recombination) is certainly not the only recombination process that contributes to the pEDMR spectra. Consequently, the question arises whether a process that solely involves the db states might be responsible for the strong spectral component at g_{db}. A *direct capture process* is in principle capable of explaining the existence of only one resonance line in the spectrum [79, 11]. Here, the spin-manipulation takes place in an excited state consisting of two electrons in a db centre. To check whether a direct capture process has to be considered, we utilize the fact that both electrons at a db site can only be manipulated simultaneously by the mw pulse since their g values are indistinguishable. Thus, electrically detected spin-Rabi nutations are expected to exhibit spin-locking behaviour as explained in Section 2.5.1, i.e. an oscillation at the frequency 2Ω. In the case of recombination between two separate states with ‘invisible’ recombination partner or a three particle process as suggested in Section 2.4, the Rabi frequency Ω for selective excitation is supposed to prevail.

An essential prerequisite for the electrical detection of coherent spin motion is that the spin relaxation times of both constituents of a recombining spin pair are sufficiently long compared to the spin manipulation time. There is no experimental data on spin relaxation times available for µc-Si:H at room temperature, but it is anticipated that the longitudinal spin-relaxation time, T_1, and the transverse spin-relaxation time, T_2, of dangling bonds are of the same order of magnitude in µc-Si:H and a-Si:H. Previous measurement of the spin-lattice relaxation time via the adiabatic-passage technique revealed $T_1 \approx 10$ µs for db states in a-Si:H at room temperature [172]. Recent measurements employing pulsed EPR yielded both T_1 and T_2 to be approximately 5 µs [173]. Thus, with regard to spin relaxation, coherent pEDMR measurements with spin manipulation times of a few 100 ns seem feasible and can indeed be carried out as we will demonstrate in the following.

Fig. 5.15a shows electrically detected spin-Rabi nutations that were measured at the centre of the resonance line at $g = 2.0059$ (see Fig. 5.13) with a procedure described in Section 3.1. The different curves were obtained using several mw attenuation levels, A. The oscillations do not show clear evidence of two distinct Rabi frequencies. It rather seems that the oscillations for all values of A are dominated by the Rabi frequency of spin pairs in either the selective excitation or the spin-locking regime. To unequivocally discriminate between the Ω and 2Ω components, we attached a small reference sample consisting of

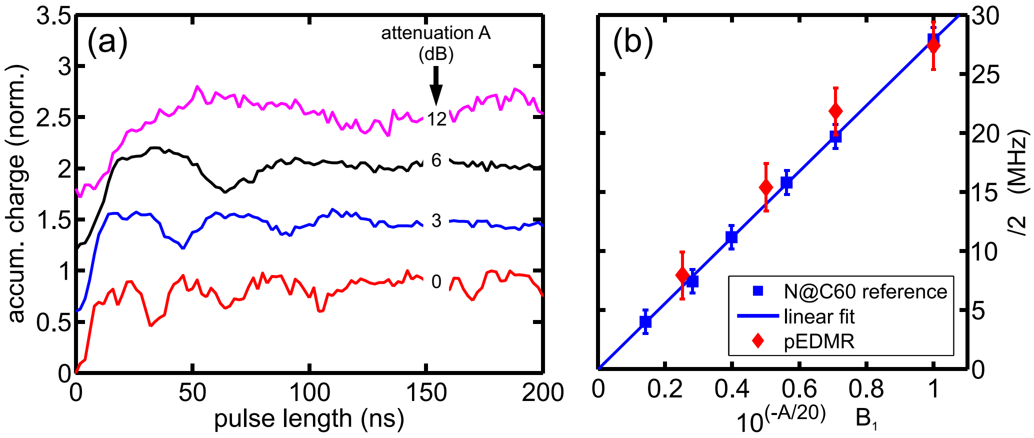

Figure 5.15.: (a) Electrically detected spin-Rabi nutations at the centre of the resonance line at $g = 2.0059$ (sample A) for several mw attenuation levels, A, as indicated in the plot. A bias voltage of 0.3 V (forward bias) was applied to the cell. (b) Rabi frequencies for a N@C$_{60}$ reference sample obtained by pulsed EPR (squares) and linear fit (solid line). The diamonds represent the Rabi frequencies obtained from the pEDMR measurements in (a). Details are given in the text.

N@C$_{60}$ powder to EDMR sample with the distance between solar cell and N@C$_{60}$ being smaller than 1 mm. Hence, we were able to perform spin-Rabi nutation measurements of the nitrogen electron spin using conventional EPR and the previously shown pEDMR measurements under identical experimental conditions. For the EPR measurements we employed the pulse sequence $\left(t_1 - T - \frac{\pi}{2} - \tau - \pi - \tau - \text{echo}\right)$ to obtain the longitudinal magnetization after a nutation pulse of varying length t_1 via echo-detection [174]. Fig. 5.15b shows the resulting Rabi frequencies for the N@C$_{60}$ reference sample (EPR) along with a linear fit and the spin-dependent signal from the solar cell (EDMR) as a function of $10^{(-A/20)}$ which is proportional to B_1. The fact that the Rabi frequencies from EPR and EDMR measurements coincide within the experimental errors indicates that the spin-nutations shown in Fig. 5.15a are dominated by the frequency Ω, i.e. the Rabi frequency of spin pairs under selective excitation conditions. This result rules out the direct capture mechanism to be responsible for the EDMR signal at g_{db} because the oscillations lack a significant contribution of the 2Ω (spin-locking) component.

5.6. Conclusion

The preceding pEDMR study demonstrates that an identification of paramagnetic defect states and charge transport processes can be obtained in completely processed pin solar cells. The complexity of the problem to assign the defect states to materials and interfaces in a multi-layer solar cell made a systematic alternation of the morphology of the highly doped n- and p-layers mandatory. We could show that by combining the information obtained from low-temperature pEDMR spectra and from the time evolution of the spin-dependent photocurrent transients the spectral resolution may be significantly enhanced. As a result, valuable additional information about transport mechanisms could be obtained as compared to conventional EPR and EDMR investigations.

Thereby we succeeded in identifying electron hopping processes between conduction band tail states and phosphorus donor states in the n-a-Si:H layer. The identity of the latter could unequivocally be assigned by comparing X- and Q-band pEDMR spectra. Similarly, spin-dependent processes involving holes in valence band tail states in the p-a-Si:H layer could be observed. Presumably, these states are involved in a hopping or tunnelling process, however, the details of these mechanisms are at present unclear. Paramagnetic states in the intrinsic µc-Si:H absorber, which was present in all samples, give rise to pronounced resonances. A strong signal related to localized electrons in the conduction band tail (CE) was observed in the i-µc-Si:H layer. In addition, we found a signal which we assign to holes localized in the valence band tail (CH). These states give rise to an asymmetric and broad line that could be simulated assuming a strongly asymmetric g tensor and asymmetric line broadening. Signals related to dangling bonds in the µc-Si:H absorber could only be observed for the sample with microcrystalline n- and p-layers.

Besides this, we were able to detect a pEDMR signal at $g = 1.9675(5)$ in the µc-Si:H pin solar cell with p- and n-doped µc-Si:H layers which we associate with shallow donor states in the Al-doped ZnO. Here, more work is needed on thin ZnO layers and devices, in which the ZnO is replaced by other transparent conducting oxides, to further investigate the microscopic nature of this resonance.

Coherent spin motion measurements at 10 K in X- and Q-band revealed the signature of spin-dependent transitions in which both spins of the respective spin pair can be addressed separately. In the case of the hopping signals originating from the n-a-Si:H layer, this is in agreement with the pEDMR spectra, provided that we indeed observe a hopping process from a phosphorus donor state to a band tail state or vice versa. In the case of the resonances that stem from the p-a-Si:H and i-μc-Si:H layers, no such correlation between two signals could be found in the pEDMR spectra and transients. This indicates that either the missing spin partners cannot be observed in the spectra or that the spin pair model cannot account for the underlying microscopic mechanisms (cf. Section 2.4). Due to its strong inhomogeneity, spin-dependent processes through the CH states could serve as the missing link in the interpretation of the Rabi oscillations. To connect the CH states to a specific process, the dynamic behaviour of this line has to be studied in greater detail which, however, is difficult in view of the relatively small signal amplitude.

The identification of defect states and transport mechanisms at low temperatures constitutes the basis for studies focusing spin-dependent processes under normal solar cell operating conditions. Benefiting from instrumental improvements we succeeded in performing pEDMR measurements (photocurrent relaxation as well as coherent experiments) at room temperature. In contrast to the low-temperature measurements, the pEDMR spectra at 300 K exhibit no contribution from the highly doped layers. The spectra of all samples are dominated by recombination via dangling bonds in the intrinsic absorber layer. Measurements of coherent spin motion at room temperature indicate that a direct capture process which involves only db states cannot account for the observed signals.

6. Polaron pair recombination in organic solar cells

Based on the instrumental and methodological achievements described in the previous chapters, we now extend the application of pEDMR to a new class of materials, namely organic compounds embedded in organic PV devices. Among them in particular MEH-PPV:PCBM has led to impressive improvements with respect to efficiency and long term stability, which motivated us to dedicate the present study to solar cells based on this blend. However, similar to other organic solar cells the performance of MEH-PPV:PCBM solar cells is still far beyond optimum. Major limitations originate from electron hole recombination processes in the material. Similar to the case of solar cells based on silicon materials, recombination in organic solar cells frequently involves paramagnetic species which can be studied by EDMR. However, recent studies on MEH-PPV:PCBM making use of cw EDMR only were not able to unambiguously assign the origin of the observed EDMR signatures. In order to identify and describe the underlying mechanisms at room temperature, we employed different EDMR detection schemes capable of identifying the paramagnetic species dominating the spin-dependent recombination processes as well as the character of the recombination process itself. cwEDMR was employed to precisely determine the spectral position as well as the line shape and width of the resonance signal. In order to clarify the question whether one or two resonance signals contribute to the EDMR signal and further elucidate the underlying spin-dependent transport mechanism, we employed pEDMR under spin-locking conditions. We found that the experimental results can be consistently explained within the framework of polaron pair recombination and address the implications for solar cell operation.

6.1. Introduction

Understanding the transport mechanisms in solar cell devices is one of the prerequisites for the design of novel solar concepts with improved efficiency. This is especially true for future solar cells based on organic materials where the efficiency of the device is determined by the rates of forward charge separation via organic radicals which compete with the rates of backward recombination pathways.

The basic principle of the organic solar cell investigated here is as follows: Light is absorbed in the polymer MEH-PPV and creates an exciton which can either recombine or dissociate into two separate charge carriers (‘polarons’) [29]. In order to promote the separation of charge carriers and thus prevent the recombination of excitons, the solar cell consists of an interpenetrating phase separated network of an electron donor (MEH-PPV) and an electron acceptor (PCBM). If an exciton is created close to a donor/acceptor interface, electron transfer from the photoexcited polymer to the acceptor occurs with high quantum yield [29]. In this way a spatial separation between the opposite charges is accomplished and thus the charge carriers are unlikely to recombine again. Similar like in an inorganic solar cell consisting of a classical pn junction, it is energetically favourable for the separated negative charges to percolate through the PCBM phase towards the metal electrode. Analogously, the positive charges will move towards the ITO through the polymer [175]. Thus, both types of charge carriers contribute to the current which can be extracted from the solar cell.

Provided that the primary excitation results in two separated polarons, the performance of the solar cell is determined by the chance of the polarons to reach the respective electrodes. Two different processes can prevent the polarons from being extracted, namely (i) polaron pair recombination and (ii) bipolaron formation. (i) If two oppositely charged polarons encounter, they may form a polaron pair and recombine [97]. Since the recombination probability depends on the spin state of the polaron pair, this process is spin-dependent. Each recombination process annihilates two current-carrying charge carriers and is therefore detrimental for the solar cell performance — analogously to electron-hole recombination in inorganic solar cells. (ii) The importance of bipolaron formation for the charge carrier transport results from the fact that conduction in disordered materials occurs via hopping of polarons among localized states. In principle, these localized states can be occupied by a bipolaron consisting of two like-charged polarons [98]. Since large on-site exchange effects lead to energies which are much higher for triplet bipolarons than for singlet bipolarons, we only consider bipolarons in the singlet state. Thus, a polaron cannot make a transition to a previously singly occupied state when both spins are parallel ('spin-blocking') [98]. Consequently, the formation of a bipolaron — which is involved in the transport path — is spin-dependent as well.

Since the spin states of polarons can be manipulated by EPR, the resonant changes of polaron pair recombination and bipolaron formation rates can be probed in an EDMR experiment. The EPR signatures can be extracted from the cwEDMR spectrum. Although the g values of positive and negative polarons in MEH-PPV are almost identical [176], the line widths are different and can therefore be used to identify both species. This was demonstrated in an EDMR study on organic light-emitting diodes consisting of MEH-PPV [177]. However, the unambiguous discrimination between different spin-dependent processes involving the same paramagnetic species (in particular formation of positive and negative bipolarons vs. polaron pair recombination) based on the cwEDMR spectrum alone is not possible. The aim of the experiments presented here was to identify the paramagnetic species influencing the charge transport and to conclude on the underlying recombination mechanisms in the material. For this purpose we performed coherent spin motion measurements and comparative simulations (cf. Section 2.6). This allowed us to discriminate between different transport and recombination processes which are indistinguishable in cwEDMR.

6.2. Materials and methods

6.2.1. Solar cell preparation

The organic bulk heterojunction solar cells for pEDMR investigations were fabricated at the University of St. Andrews by Elizabeth A. Thomsen and Ajay K. Pandey. Details about the sample structures can be found in Ref. [178]. A summary of the processing steps is given in the following.

The EDMR samples were fabricated on indium tin oxide (ITO) coated glass substrates. The ITO layer was patterned using a wet chemical etching process in order to achieve a contacting scheme similar to the geometry shown in Fig. 3.5b. After cleaning the ITO electrodes in several steps (see Ref. [178] for details), the substrates were transferred to a N_2-filled glove box for further processing. A single layer consisting of the semiconducting polymer poly(2-methoxy-5-(2'-ethyl)-hexoxy-p-phenylene) vinylene (referred to

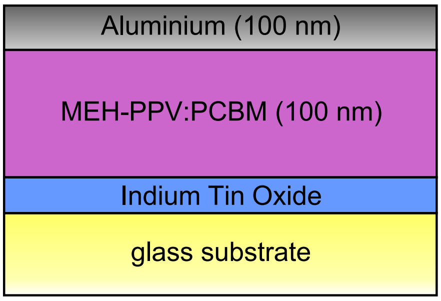

Figure 6.1.: Structure of the organic bulk heterojunction solar cell for EDMR measurements.

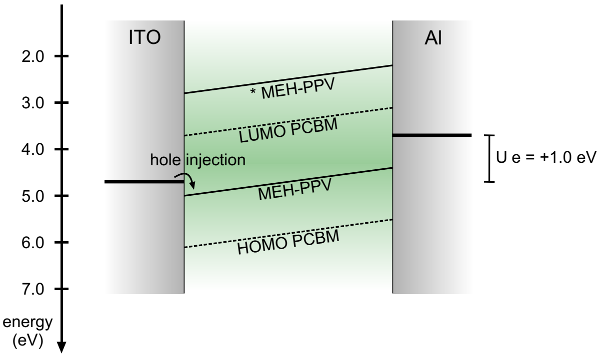

Figure 6.2.: Schematic energy-level diagram for the MEH-PPV:PCBM solar cell under forward bias conditions ($U = 1.0$ V) neglecting any interfacial effects at the contact layers.

as MEH-PPV) and [6,6]-phenyl C_{61}-butyric acid methyl ester (referred to as PCBM) was spin coated from a previously prepared blend solution of MEH-PPV and PCBM dissolved in chlorobenzene in the ratio of 1:4 (by wt %). A 100 nm thick Al layer was then deposited through a shadow mask resulting in an active device area of 5 mm^2. The final device configuration as shown in Fig. 6.1 is glass substrate/ITO/100 nm MEH-PPV:PCBM/100 nm Al.

6.2.2. Experimental conditions

In order to study the influence of polaron pair recombination on the charge transport in organic solar cells, we injected charge carriers into the MEH-PPV:PCBM blend electrically by applying a positive bias voltage. Operating the device in this ‘LED-mode’ proved beneficial because the EDMR measurements can be performed in the dark. In this way it is possible to even investigate non-encapsulated devices, which suffer from fast degradation under illumination in ambient air. The energy-level diagram under forward bias conditions is shown schematically in Fig. 6.2. Due to the fact that the injection barrier for holes from the ITO electrode into the highest occupied molecular orbitals (HOMO, π orbitals) of the MEH-PPV is about 0.2 eV and thus relatively low [179], whereas the barrier for electron

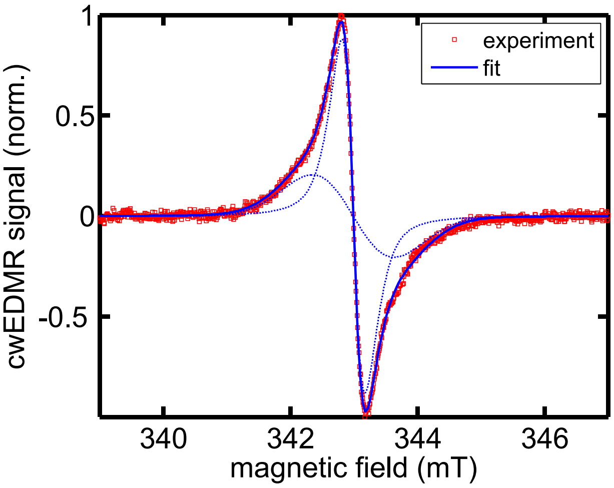

Figure 6.3.: cwEDMR spectrum normalized to 1 obtained at room temperature without illumination. The sample was biased at $U = +1.0$ V (forward bias) leading to a current of 18.7 µA. The mw power used was 20 mW. The solid line represents the fit results assuming two resonance lines with equal doubly integrated intensities and g values but different line shapes and line widths. The dotted lines show the individual fit components.

injection from the Al electrode into the lowest unoccupied molecular orbitals (LUMO) of the PCBM is significantly higher (≈ 0.6 eV [29]), we assume that the charge transport in the forward bias regime is dominated by positive charge carriers in the MEH-PPV.

6.3. Results and discussion

In the present study three different EDMR detection schemes were employed to investigate the spin-dependent transport mechanisms involving paramagnetic species in organic bulk heterojunction solar cells: cwEDMR, pEDMR and electrically detected Rabi oscillations. These detection schemes are described in detail in Sections 3.1 and 3.2. In the following, we will present the results obtained from these measurements.

6.3.1. cwEDMR

Fig. 6.3 shows the cwEDMR spectrum of the bulk heterojunction solar cell obtained at room temperature in the dark under constant forward bias injection condition ($U = 1.0$ V, $I = 18.7$ µA). We observe a relative increase of the current under resonance conditions, i.e. at $g = 2.0028(3)$. The signal has neither a clear Gaussian nor Lorentzian shape, indicating the influence of at least two different paramagnetic centres. Best fits to the data, as shown in Fig. 6.3, are obtained by assuming one narrow resonance with a Pseudo-Voigtian line shape with strong Lorentzian character (rel. Lorentzian intensity: 0.9, rel. Gaussian intensity: 0.1, $g = 2.0028(3)$, FWHM $= 0.6(1)$ mT) and a wider component having Gaussian shape

($g = 2.0028(3)$, FWHM $= 1.5(1)$ mT) and having identical doubly integrated intensity as compared to the narrow line. Line widths and g values are consistent with earlier EDMR as well as light-induced EPR measurements and are generally attributed to positive polarons (radical cations) as well as negative polarons (radical anions) in MEH-PPV [176].

Polaron pairs consisting of negative and positive polarons [97, 180] as well as bipolarons [177, 181] comprising like-charged pairs of polarons, are known to be a source of EDMR signals at $g \approx 2.0028$ when they influence transport by either spin-dependent recombination or hopping. Discriminating between both mechanisms (polaron pair recombination and bipolaron-formation) is of fundamental scientific interest, not only because polaron pairs and bipolarons influence charge transport in organic solar cells and organic light emitting diodes (OLEDs), but also because they play an important role in the recently discovered organic magnetoresistance (OMAR) effect [182]. Here, polaron pair recombination [183] and bipolaron formation [98, 184] can lead to the same experimental observations (i.e. a the change of the sample conductivity as a function of an external magnetic field).

The cwEDMR spectrum does not allow us to unambiguously assign the underlying microscopic mechanism. In particular, reasonable fits could conceivably be achieved for a single type of paramagnetic centre with hyperfine interaction to a nearby nucleus or two exchange-coupled centres with different g values. However, the fact that the spectrum can be approximated when assuming two lines with identical doubly integrated intensities indicates that both lines might originate from one spin-dependent transition which involves both members of a polaron pair. This assumption is supported by the pEDMR measurements presented in the remainder of this chapter. It is important to add that the line shape of positive polarons in MEH-PPV is mainly attributed to unresolved hyperfine interactions with spin-carrying nuclei in close proximity to the polarons. This results in a Gaussian line shape which is indeed observed in light-induced EPR [185]. In EDMR and electroluminescence detected magnetic resonance (ELDMR), however, the resonance lines associated with positive polarons in PPV-derivatives exhibit Lorentzian line shapes as reported by various groups [180, 177, 181, 32, 186, 187]. This is in accordance with our observations and might be related to motional averaging of the anisotropic magnetic interaction parameters. A Lorentzian line shape might also arise when the polaron pair lifetime is limited by recombination or annihilation on a timescale shorter than spin relaxation times. From the spectral position of the resonance lines in the EDMR spectrum a significant contribu-

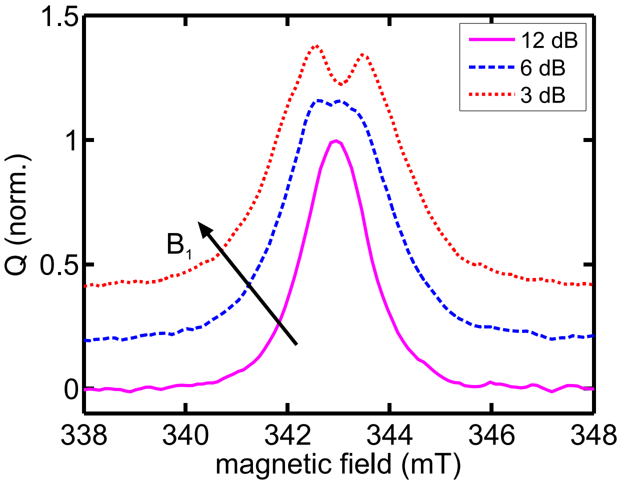

Figure 6.4.: Microwave power dependence of the pEDMR spectrum ($Q \equiv \int_0^{30\,\mu\mathrm{s}} \Delta I(t)\,dt$ normalized to 1). 3 dB attenuation corresponds to $P_\mathrm{mw} = 500$ W at the output of the mw amplifier. Upon increasing the mw power, the width of the resonance peak increases and a 'dip' emerges at the centre of the spectrum.

tion of PCBM anions ($g_x = 2.0003(1)$, $g_y = 2.0001(1)$, and $g_z = 1.9982(1)$ [188]) can be excluded.

6.3.2. pEDMR

A more detailed insight into the identification of the participating species in the EDMR signal results from the pEDMR measurements taken at room temperature under otherwise identical conditions as for the cwEDMR data. Fig. 6.4 shows pEDMR spectra that result from an integration of $\Delta I(t)$ over the first 30 µs after the mw pulse with a fixed length ($\tau = 160$ ns) recorded for different mw power levels, P_mw.

It is important to note that an analysis of the current relaxation dynamics, which was used to deconvolute spectrally overlapping signals in Section 5.4.4.1, revealed the same time behaviour for both spectral components. This indicates, but does not prove, that both paramagnetic centres are involved in the same spin-dependent process.

The different mw attenuation levels used for recording the spectra in Fig. 6.4 correspond to π-pulse lengths between 72 ns (12 dB) and 18 ns (0 dB). For attenuations above 12 dB obviously a single resonance line is observed. With increasing mw power this line broadens and above 6 dB a 'dip' emerges exactly in the middle of the resonance line. This spectral signature in combination with the information extracted from the pEDMR transient analysis provides strong evidence for the presence of two correlated spins coupled by the mw pulse. This effect, referred to as spin-locking behaviour (cf. Section 2.5), has decisive implications for electrically detected spin-Rabi nutations as explained in the following.

pEDMR under spin-locking conditions

pEDMR signals originating from overlapping resonance lines involved in the same transport mechanism with similar line width and spectral position are very sensitive to the applied microwave power. This is due to the fact that the respective spins may be locked by the magnetic component of the microwave field when the mw power is sufficiently high to excite both spins of the same spin pair as explained in Section 2.5.1. This implies that the total spin of the pair is not altered by the mw and thus the population is shifted between the three triplet sublevels (T_+, T_0, T_-) which are all characterized by the total spin $S = 1$. This effect was described theoretically [189] and observed experimentally for radical pairs by means of absorption detected magnetic resonance (ADMR) [103, 95, 96].

In EDMR, spin-locking influences both the shape of the pEDMR spectrum as well as the frequency spectrum of the pEDMR detected Spin Rabi oscillations. Under spin-locking conditions, the microwave has no direct effect on the EDMR observable, i.e. the current change ΔI depending on the deviations of the singlet and triplet populations from their respective steady-state values, since the total spin remains unchanged and the spin population is only altered between the sublevels (T_+, T_0, T_-) of the triplet manifold [34, 95]. However, this leads to a decrease of the microwave induced pEDMR signal to the steady state value, which may be observed as a dip in the centre of the spectrum [95, 96]. In addition, the frequency spectrum of the pEDMR detected Rabi oscillations may be altered due to intersystem crossing (ISC, cf. Section 2.5.2), a case that is frequently encountered in amorphous hydrocarbons at room temperature. In the presence of ISC, the oscillation frequency 2Ω is expected to be observed in electrically detected spin-Rabi nutations under spin-locking conditions.

6.3.3. Rabi oscillations

Fig. 6.5a shows the charge response $Q(\tau)$ ($0\text{ ns} < \tau < 500\text{ ns}$) measured on resonance at $g = 2.0028$ with a pulse increment time of 2 ns. The signal clearly exhibits oscillations which reflect coherent spin motion of the paramagnetic species during the mw pulse. For all mw power levels shown, ΔI initially increases with increasing τ. This is in line with the sign of the current change observed in the pEDMR spectra. The oscillation amplitude is

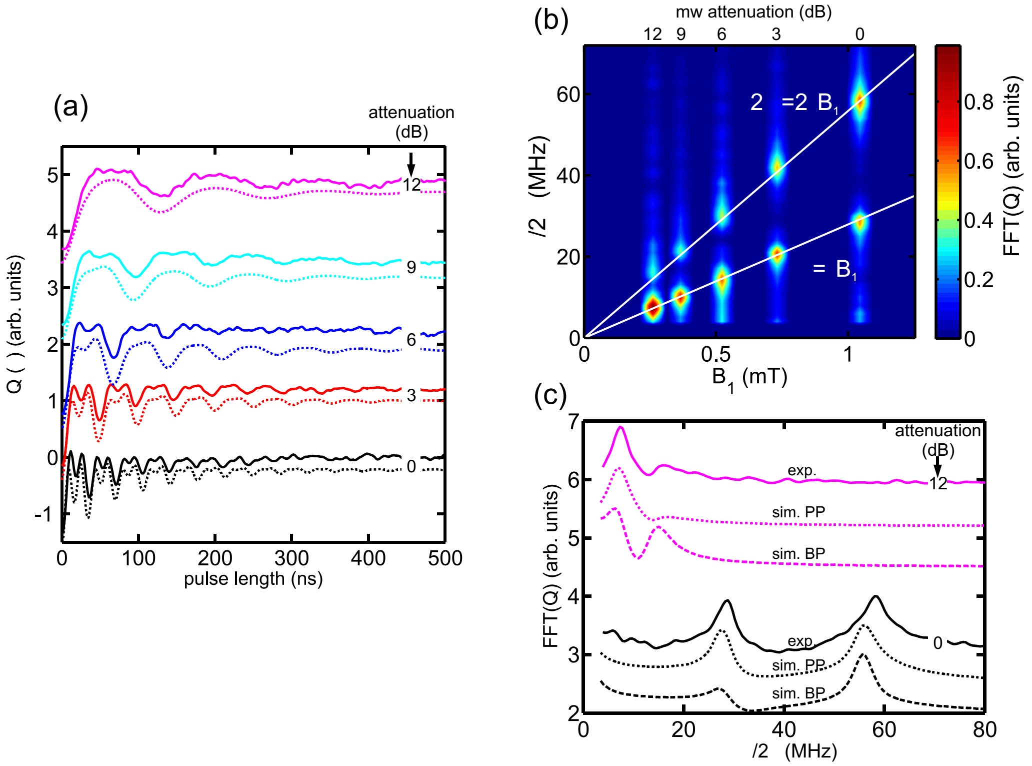

Figure 6.5.: Electrically detected spin-Rabi nutations obtained at room temperature. (a) Solid lines: integrated charge Q (cf. Fig. 3.1) as a function of the mw pulse length τ for several P_{mw} as indicated by the corresponding mw attenuations. Dotted lines: simulation results (combined population of product states $|\uparrow\downarrow\rangle$ and $|\downarrow\uparrow\rangle$ with mixed symmetry) for the polaron pair recombination model. Details can be found in the text. Experimental and simulation data are vertically offset for clarity. (b) Fast Fourier Transformations of the data shown in (a) yielding the respective Rabi frequencies. With increasing P_{mw} the intensity of the Ω component (represented by the colour code) decreases whereas the intensity of the double frequency component increases. Both frequencies are linearly dependent on the mw field amplitude B_1 ($\propto \sqrt{P_{\mathrm{mw}}}$). (c) FFTs for 12 and 0 dB attenuation of the measurement data (solid lines), the simulation results according to the polaron pair (PP) recombination model (dotted lines) and simulation results for the bipolaron (BP) model (dashed lines) as discussed in the text. The individual curves are offset vertically. Note that the relative intensities of the single and double frequency components are well reproduced by the simulation for polaron pairs.

damped with time constant ≈ 150 ns. The damping of the Rabi oscillations in pEDMR can be caused be several effects, among them spin relaxation of the individual partners of the contributing spin pair, pair dissociation and recombination or coherent dephasing effects due to inhomogeneities of the B_1 field (for a review see [35]). The effect of coherent dephasing can be analysed separately by a pEDMR echo experiment [113, 70], but this is not considered the subject of this study. As it is obvious from Fig. 6.5a, with increasing mw power a new Rabi frequency component becomes visible. In the case of low mw power (12 dB), the frequency of the oscillation ($\Omega/2\pi$) corresponds to the Rabi frequency of a species that is associated with a total spin $1/2$ (see the Fast Fourier Transformations (FFT) shown in Fig. 6.5b). Upon increasing the mw power, we observe an increase of the oscillation frequency according to Rabi's formula $\Omega = \gamma B_1$ with γ being the gyromagnetic ratio and B_1 the amplitude of the rotating magnetic field induced by the microwave. Besides this, a second frequency appears which is higher by a factor of two. The intensity of this component increases monotonically when raising the mw power until the amplitudes of both frequency components are similar at 0 dB. It should be noted that the power level at which the second frequency appears (≈ 9 dB, cf. Fig. 6.5a) roughly coincides with the change of the respective pEDMR spectra shown in Fig. 6.4. This observation can qualitatively be explained by the spin-locking model.

To quantitatively confirm this assumption, we calculated the spin pair evolution as a function of the mw pulse length numerically for the respective mw power levels with a procedure described in Appendix B. While polaron pair recombination as well as bipolaron formation can equally lead to spin-locking, the power dependence of the Rabi oscillations is different for both processes and can thus be used to discriminate between them.

To extract the correct g value distributions for the simulation, we have fitted the cwEDMR spectrum in Fig. 6.3 and find best results assuming two spectral components with equal intensity and g values but different line shapes as mentioned above. The strong Lorentzian character of the pseudo-Voigtian narrow line indicates that the width extracted from the fit is not the inhomogeneous line width determined by unresolved hyperfine interactions but rather arises from motional or lifetime effects. However, for the simulation of the spin nutation, only the inhomogeneous line width has to be considered. We therefore include the following Gaussian distribution in the simulation (cf. Section 2.6.1):

$$p(g_a) = \exp\left[-4\ln(2)\frac{(g_a-\bar{g}_a)^2}{\Delta g_a^2}\right] \qquad \text{with} \quad \bar{g}_a = 2.0028 \quad \text{and} \quad \Delta g_a = 0.002\,. \quad (6.1)$$

The width $\Delta g_a = 0.002$ of the distribution corresponds to an inhomogeneous line width of ≈ 0.3 mT. Although this value is only an estimate, it must necessarily be smaller than the line width extracted from the cwEDMR spectrum (FWHM $= 0.6(1)$ mT). The simulation is rather insensitive to the exact value as long as it is significantly smaller than the width of the broad line — which certainly is the case here.

The width of the broad spectral component (FWHM $= 1.5(1)$ mT) can analogously be expressed in terms of the same Gaussian g value distribution (6.1) except for a different width $\Delta g_b = 0.009$.

For 10^4 spin pairs with varying g values (taken from the distributions $p(g_a)$ and $p(g_b)$ consisting of 10^2 points each) we determined the population of the product states $|\uparrow\downarrow\rangle$ and $|\downarrow\uparrow\rangle$ with antiparallel spin alignment at the end of the pulse under the assumption that all spin pairs are initially ($\tau = 0$) in a configuration in which the spins are aligned parallel (triplet states). Note that the combined population of states $|\uparrow\downarrow\rangle$ and $|\downarrow\uparrow\rangle$ corresponds to the sum of the populations of the states $|S\rangle$ and $|T_0\rangle$ in the case of strong ISC. Thus, the 'observable' is independent of the chosen basis. Averaging over the contributions from all pairs yields the dotted curves shown in Fig. 6.5a for the mw power levels used in the experiment. It should be noted that no spin-spin interactions (neither exchange nor dipolar interaction) were taken into account. Also, we neglected any dephasing processes that are active only in the triplet manifold (triplet-triplet dephasing) as observed for micellized radical pairs [96] by means of ADMR. Such processes could possibly lead to different dephasing time constants for the single and double frequency components. Damping of the oscillations due to gradual loss of spin pairs during the excitation was accounted for by including exponential damping of the oscillation amplitude with a time constant of 150 ns. Damping due to coherently dephasing spin pairs is automatically incorporated in the simulation by including g value distributions. The results of the simulation are in good agreement with the experimental data. This confirms that the experimental results can consistently be explained within the framework of the spin-locking model.

In the simulation, the spin pairs are formed by taking one spin from the narrow distribution $p(g_a)$ and one spin from the broad distribution $p(g_b)$. This holds true for the polaron pair mechanism where all pairs consist of one positive and one negative polaron. In the bipolaron model, however, spin pairs comprise like-charged polarons. Thus, for modelling Rabi oscillations according to the bipolaron model, two types of spin pairs have to be considered, namely positive bipolarons (consisting of two spins both taken from $p(g_a)$) as well as negative bipolarons (consisting of two spins taken from $p(g_b)$). The general trend of the corresponding Rabi oscillations is similar to the behaviour found for the polaron model, namely the intensity of the 2Ω component increases upon increasing the mw power. However, the relative intensities of both frequency components differ markedly for both models. This can best be visualized by the respective FFTs of the oscillations which are shown in Fig. 6.5c along with the FFTs of the experimental data for 12 and 0 dB mw attenuation.

Two significant differences between the simulations for polaron pairs and bipolarons deserve some attention. First, due to the narrow width of distribution $p(g_a)$ positive bipolarons exhibit spin-locking behaviour already at relatively low mw power (12 dB attenuation). At this power level, almost no 2Ω component is visible for polaron pairs. Second, the oscillation at 2Ω at high mw power (0 dB attenuation) is clearly present in both cases. However, the gradual dephasing of this spin-locking component is much less pronounced for bipolarons than for polaron pairs, resulting in a stronger 2Ω component in the frequency spectrum. This can also be attributed to the relatively narrow g value distribution of the positive bipolarons and contradicts the experimental observation. In contrast to that, the simulated data according to the polaron pair model are in good agreement with the experiment. These findings strongly indicate that the polaron pair mechanism is responsible for the experimental results. Another observation that is at variance with the bipolaron model is based on the intensities found in the cwEDMR spectrum shown in Fig. 6.3. Although EDMR signals are neither directly proportional to the concentrations nor to the mobilities of either positive or negative polarons, one would not expect both components to have equal intensities as the mobilities of both types of charge carriers differs markedly in MEH-PPV. It would rather be anticipated that an imbalance between positive and negative bipolarons exists. In the case of polaron pair recombination, however, equal EDMR intensities for both spin pair constituents seem plausible.

Fig. 6.6 summarizes schematically how the EDMR signals are interpreted in the absence (left) and presence (right) of the spin-locking mechanism in the framework of the polaron pair model.

Intersystem crossing

The presented mw power dependence of the Rabi oscillations at room temperature varies from the recently observed behaviour for low-temperature ($T = 5$ K) polaron pair recombination in OLEDs made from MEH-PPV [187]. While we clearly observed a 2Ω component upon increasing the mw power without loss of signal-to-noise ratio, McCamey *et*

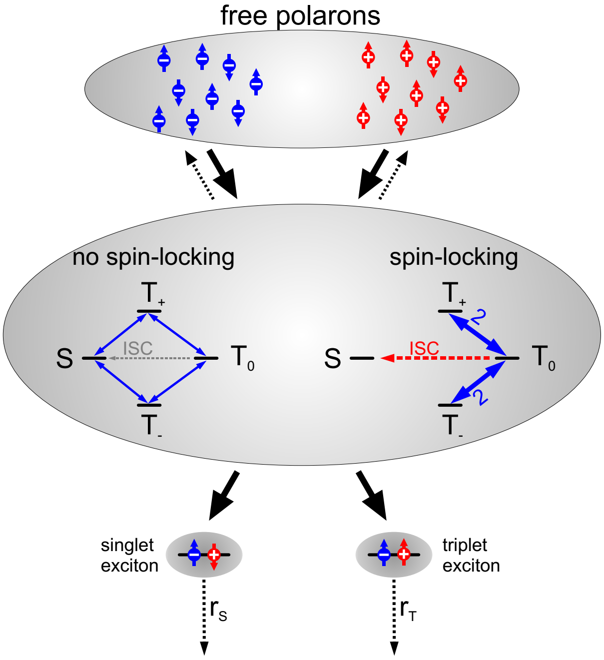

Figure 6.6.: Schematic illustration of PP recombination in the absence and presence of spin-locking. Polaron pairs are created by encounter of positive and negative free polarons. Resonant mw excitation alters the populations of the PP states. In the case of selective excitation (low microwave power, shown on the left side), the mw directly 'connects' singlet and triplet states (which are not necessarily eigenstates) at the Rabi frequency Ω. In the spin-locking case, the singlet state is decoupled from the triplet manifold. Hence, the shift of population is restricted to the three triplet states, and the frequency corresponds to 2Ω. Intersystem crossing (ISC) establishes a connection for population transfer from T_0 to the singlet state. After spin-manipulation, the polaron pairs recombine with rate coefficients r_S and r_T which are proportional to the singlet and triplet content, respectively.

al. [187] found a significant increase of the noise at high mw powers and did not observe a double frequency component. Both discrepancies can consistently be explained when the intersystem crossing rate changes with temperature.

Since both the mobility of the polarons as well as the movement of spin-carrying nuclei in the polymer usually exhibit a pronounced temperature dependence [190], the hyperfine interaction as a source of ISC is also expected to vary with temperature. Based on this model, the fact that a strong contribution of the frequency 2Ω is observed in the Rabi oscillations measured at room temperature (cf. Fig. 6.5) whereas this feature is missing at low temperature ($T = 5$ K) [187], can be attributed to the temperature dependence of the ISC rate. It should be noted that ISC is of minor importance for the Rabi oscillation at the single frequency Ω in the absence of spin-locking which occurs for low microwave powers. In this case only one spin of each polaron pair is manipulated by the microwave. For a π-pulse of length $\tau = \pi/\Omega$ (spin flip by 180°) the microwave drives transitions from the states $|T_+\rangle = |\uparrow\uparrow\rangle$ and $|T_-\rangle = |\downarrow\downarrow\rangle$ to the product states $|\uparrow\downarrow\rangle$ and $|\downarrow\uparrow\rangle$ and therefore directly affects the singlet and triplet populations without the need for an indirect process promoted by ISC. As a consequence, we expect this contribution of the Rabi oscillations to be rather temperature-independent, which is in accordance with the experimental observations at low temperatures [187].

The fact that the appearance of the second Rabi frequency at high mw powers is a consequence of intersystem crossing opens up the possibility to directly measure intersystem crossing rates in organic devices. In particular, the influence of the fluctuating hyperfine field felt by the polarons can quantitatively be evaluated as a function of temperature by means of pEDMR. This analysis is not restricted to solar cells but might also be relevant for studying the microscopic origin of magnetoresistance that was recently observed in a wide range of organic materials [191, 192, 193, 194].

6.4. Conclusion

All EDMR-based observations discussed above can consistently be described within the framework of the spin-locking model, provided that the spin-dependent conductivity changes arise from recombining polaron pairs each consisting of one positive and one negative polaron in the polymer. The cwEDMR signal can be fitted when assuming two resonance lines with equal intensities resembling the spectral shapes of oppositely charged polarons that were previously investigated by light-induced EPR and cwEDMR. Experiments performed at different mw power levels lead to spin-locking effects in pEDMR spectra as well as in electrically detected Rabi oscillations. Numerical simulations of spin Rabi nutations support the interpretation that polaron pairs are responsible for the observed spin-dependent signals under the particular experimental conditions. Nevertheless, it should be mentioned that changing the device composition or the experimental conditions (temperature or applied voltage) could dramatically influence the mechanism responsible for EDMR. In general, studying electrically detected Rabi oscillations for different mw power levels might provide a key experiment to distinguish between different competing models capable of explaining both loss mechanisms in organic solar cells as well as recently discovered organic magnetoresistance effects. Despite the presented arguments in favour of the polaron pair model we cannot fully exclude the bipolaron mechanism to explain our results. However, due to the difference between the mobilities of positive and negative polarons in MEH-PPV, we would expect to observe a strong imbalance between the EDMR components for the respective bipolarons in cwEDMR as well as in the electrically detected Rabi oscillations.

Implications for solar cell operation

The spin-dependent process involving polaron pairs clearly hinders solar cell operation because it reduces the concentration of free polarons carrying the current. We suggest that under the experimental conditions chosen in the present work (no illumination, forward bias) the charge transport is mainly governed by positive polarons in the MEH-PPV since their interchain mobility exceeds the mobility of negative polarons as it is the case for most conjugated polymers [29]. We further assume that the PCBM does not significantly contribute to the current because the injection barrier for electrons from the Al electrode towards the LUMO of the PCBM is quite high, and thus the PCBM is not accessible for electron injection. The applied forward bias of 1.0 V is not sufficient to overcome this energy barrier. Positive polarons drift in the electric field from the ITO side towards the Al electrode. We assume that there are negative polarons in the MEH-PPV close to the Al electrode as illustrated schematically in Fig. 6.7. Since their mobility is rather low, most negative polarons reside in that region. When positive polarons from the ITO electrode encounter negative polarons in the vicinity of the Al side, both charge carriers can form a polaron pair which can be annihilated either by recombination or dissociation. These pairs can be considered to block the current transport path which is provided by free polarons. When the recombination rate of such polaron pairs is enhanced by the resonant microwave,

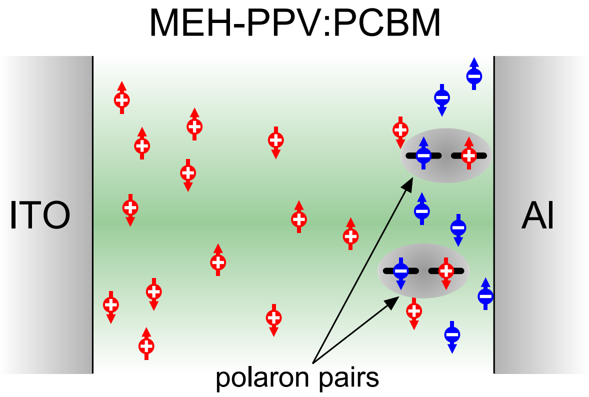

Figure 6.7.: Artist's view of the suggested polaron pair recombination process responsible for the pEDMR signals. Due to their low mobility, negative polarons in the MEH-PPV stay close to the Al electrode where they are injected. Positive polarons (with higher mobility) are injected from the ITO electrode and drift in the electric field provided by the bias voltage towards the Al electrode. When a positive polaron encounters a negative counterpart, polaron pairs are formed which hinder the charge transport. The recombination rate of these pairs is manipulated by the resonant mw excitation. Enhanced polaron pair recombination results in an increase of the conductivity.

the transport path is not blocked any more and thus a positive current change is observed. Note that the situation is similar to recombination in solar cells based on amorphous silicon under forward bias conditions without illumination, where also a positive EDMR signal due to enhanced recombination in the space charge region is observed [91]. The described recombination pathway will necessarily limit the efficiency of organic solar cells based on the blends investigated here, due to the following mechanism: The charge separation after photoexcitation in the MEH-PPV has been shown to be a fast and very efficient process [29, 195]. However, this holds true only for the case when a PCBM molecule is present in close proximity to the primary excitation. If this is not the case, then the exciton will either annihilate by recombination or dissociate into a negative and a positive free polaron. In the latter case, the hole will efficiently drift in the electric field towards the ITO electrode. Owing to its smaller mobility, the negative polaron stays close to its place of birth and can act as a recombination centre for (current-carrying) positive polarons. When recombination occurs, one free polaron is destroyed and therefore leads to a reduction of the device current. The underlying microscopic mechanism of this process is thus identical to the spin-dependent process close to the Al electrode which we observe in the pEDMR experiments performed under forward bias without illumination.

7. Conclusions and future work

Recent advances in PV production technologies resulted in impressive ongoing improvements of established solar cell concepts. However, the urge for even higher efficiencies and lower production costs requires novel concepts based on tailor made PV materials and redesigned cell structures. One prerequisite for this goal to achieve is the availability of advanced characterization methods capable of providing detailed information about the material properties with respect to transport and loss mechanisms in the cell. Among these techniques, magnetic resonance and EPR in particular provided key information on processes determining solar cell performance. However, the successful application of conventional EPR is often impossible because the defect concentrations in the different types of solar cells are usually well below the sensitivity of EPR. Thus, EDMR techniques providing higher detection sensitivity and the potential to discriminate resonance signals influencing the charge transport in the solar cell from background signals have to be employed.

In the framework of the present work pEDMR was utilized to study loss mechanisms in three different types of advanced solar cells. The devices under investigation were provided by the HZB (a-Si:H/c-Si heterojunction solar cells), the Forschungszentrum Jülich (µc-Si:H thin-film solar cells) as well as the University of St. Andrews (organic bulk heterojunction solar cells). In order to fully exploit the potential of pEDMR, a relatively recent spectroscopic technique developed in our lab, instrumental improvements to the EPR spectrometers at the HZB and the FU Berlin had to be carried out. These upgrades resulted in a significant gain in spectral resolution and detection sensitivity, now enabling pEDMR measurements from cryogenic to room temperatures, and paved the way for future multi-frequency pEDMR experiments. In order to definitely assign the observed pEDMR signals to the underlying defects and transport mechanisms, the existing theoretical body describing pEDMR experiments had to be extended with respect to disorder-related effects which significantly influence pEDMR signals in the sample structures investigated. Benefiting from these methodological improvements, novel pEDMR schemes came into reach, which allowed us to monitor spin-dependent transport processes in fully processed solar cells. The conclusive results are summarized in the following.

7.1. a-Si:H/c-Si heterojunction solar cells

In the a-Si:H/c-Si heterojunction solar cells investigated in Chapter 4, defects at the interface between a-Si:H and c-Si act as recombination centres for photogenerated charge carriers. Although a correlation between these interface defects and the device performance is well established, their influence has so far only been investigated indirectly because most characterization methods either lack the microscopic selectivity (like capacitance-voltages based methods) or the detection sensitivity (like conventional EPR).

By applying EDMR we were able to overcome these limitations and directly measure the effect of interface recombination on the charge transport. After studying spin-dependent processes at the interface between isotopically purified ^{28}Si and SiO_2 which serves as a model system and provides reference spectra with high resolution, we performed EDMR measurements on fully processed a-Si:H/c-Si solar cells. The discrimination between interface states and defects in the 'bulk' amorphous silicon could be achieved by exploiting the well-defined orientation of the c-Si surface dangling bonds which are oriented along the $[111]$ direction. The measurements revealed that the a-Si:H/c-Si interface defect coincides within experimental uncertainty with the well-known P_b centre at the Si/SiO_2 interface with respect to both the symmetry of the g tensor as well as its principal values. These findings indicate that either a thin SiO_x interlayer was present at the a-Si:H/c-Si interface or that the g tensors of the P_b centre and the a-Si:H/c-Si interface defect are identical. Following the former interpretation, the experimental results have important implications for the solar cells because they show that the c-Si surface clearly deviates from an ideal H-terminated surface prior to the a-Si:H deposition and that the oxide is not fully removed during the deposition process. An oxidized c-Si surface is known to exhibit a significantly higher density of surface states [15]. Note that the pretreatment of the c-Si wafer and the a-Si:H deposition conditions were the same for the EDMR samples and for high-efficiency heterojunction solar cells. Thus, there might be further room for improvement of the recently achieved maximum efficiencies at the HZB (n-a-Si:H/p-c-Si: 18.5% [111], p-a-Si:H/n-c-Si: 19.8% [109]). If the structures of the a-Si:H/c-Si interface defect and the P_b centre were indeed identical (following the second interpretation), the experimental results would be particularly helpful for the interpretation of spin-dependent recombination data obtained from µc-Si:H based solar cells which essentially consist of many disordered a-Si:H/c-Si interfaces. Prospective studies on a-Si:H/c-Si structures with and without a SiO_2 interlayer can shed light on the microscopic identity of the interface-related EDMR signals.

7.2. µc-Si:H thin-film solar cells

In µc-Si:H based thin-film solar cells, paramagnetic defects equally influence the charge transport. However, the situation is much more complicated because of two reasons. First, the structure of µc-Si:H itself is complex as it consists of small crystallites surrounded by amorphous material. Second, thin-film solar cells are usually realized in a pin configuration. This multi-layer structure impedes the identification of defects in the individual layers.

In Chapter 5 we demonstrated that the identification of paramagnetic states and their assignment to charge transport processes can nevertheless be accomplished in completely processed pin solar cells. To separate the EDMR signals from the respective layers — which is impossible based on the spectral information alone — we pursued two strategies: On the one hand we varied the morphology of the n- and p-doped layers from amorphous to microcrystalline to evaluate their influence on the EDMR spectra separately. On the other hand we developed a procedure to deconvolute spectrally overlapping signals in the time domain. This made an improvement of the detection electronics with particular emphasis on the achievable time resolution mandatory. A combination of both approaches yielded the identification of conduction band tail states as well as phosphorus donor states in samples with an amorphous n-layer and a resonance associated with valence band tail states in samples containing an amorphous p-layer. Comparative X- and Q-band analyses were utilized to distinguish between field-dependent and field-independent spectral components. In this way we could unequivocally assign EDMR signals to phosphorus donor states based on the field-independent hyperfine interaction between the donor electron spin and the ^{31}P nuclear spin. Moreover, conduction and valence band tail states in the intrinsic µc-Si:H absorber layer could be identified. At 10 K the tail states in the individual layers are involved in hopping or tunnelling processes which give rise to positive (current-enhancing) EDMR signals. Recombination via dangling bonds in the µc-Si:H layer could only be observed in the sample structure with microcrystalline n- and p-layers.

Benefiting from the instrumental improvements described in Chapter 3, we succeeded in performing pEDMR measurements on silicon solar cells at room temperature for the first time. This is indispensable for reliable and realistic solar cell characterization because performance-limiting processes at normal solar cell operating conditions clearly differ from the processes that prevail at 10 K. For all sample structures investigated we observed a resonance which we assigned to recombination via dangling bonds in the microcrystalline absorber layer which is known to be an important loss mechanism is this type of solar cells. In contrast to the pEDMR measurements that were performed at 10 K, we did not find any evidence of hopping signals resulting from the doped layers or the intrinsic absorber layer at 300 K. This result indicates that the transport processes involving tail states that were observed at 10 K are certainly not the processes that limit the solar cell efficiency. Nevertheless, pEDMR studies at low temperatures can be used to extract structural information about tail states which are known to critically influence the charge carrier mobilities in μc-Si:H solar cells also at room temperature.

7.3. Organic bulk heterojunction solar cells

The pEDMR measurements performed on organic heterojunction solar cells comprising MEH-PPV and PCBM served two particular purposes: On the one hand we were interested in the influence of spin-dependent processes on charge transport in the device itself. On the other hand we utilized the close analogy between polaron pairs in polymers and spin-correlated radical pairs to further improve our understanding of EDMR in inorganic devices.

The starting point of our investigation was a cwEDMR spectrum that exhibited signatures of positive as well as negative polarons in the MEH-PPV. However, the assignment of the underlying process based on cwEDMR alone inevitably remains speculative. Therefore, we employed pEDMR to reveal effects of spin-locking — a process frequently encountered in radical pair chemistry — in both transient EDMR measurements and electrically detected Rabi oscillations. A comparison with simulations revealed that two different microscopic processes that could possibly explain the cwEDMR results, namely polaron pair recombination and bipolaron hopping, can be distinguished in the spin-locking regime. Our experimental results can consistently be explained by polaron pair recombination, which constitutes a loss mechanism for photogenerated charge carriers in organic solar cells.

7.4. Outlook

The above-mentioned examples show that pEDMR is indeed capable of providing important pieces of information about defects determining loss mechanisms in state-of-the-art solar cells. Based on the methodological developments carried out in this work, the emerging field of pEDMR can be now applied to other pressing questions related to the properties of PV-relevant materials. In the following, we propose two pEDMR experiments which may outline a future research route:

Studying the light induced degradation in solar cells based on amorphous silicon

In order to improve the performance of solar cells containing a-Si:H layers, further insight into the phenomenon of light-induced degradation, usually referred to as the Staebler-Wronski effect (SWE) [25], is mandatory. To characterize the defect structures related to the SWE, advanced multifrequency EPR and electron nuclear double resonance (ENDOR) studies are on the way at HZB and FU Berlin (PhD project Matthias Fehr). Despite the detailed structural insight — in particular the hydrogen distribution in the vicinity of the light-induced dangling bonds — provided by these methods, their detection sensitivity is far below the number of defects encountered in state of the art solar cells. In order to close this gap, the superior detection sensitivity of pEDMR may be exploited. The fact that at 10 K recombination via dangling bonds in the absorber could only be observed for samples with microcrystalline n- and p-layers has important implications for prospective studies on the SWE. Our findings indicate that the strong EDMR signals, which originate from the highly doped layers, can be suppressed by the use of microcrystalline n- and p-layers. Thus, by combining an intrinsic a-Si:H absorber with doped µc-Si:H layers, the creation of new dangling bonds in a-Si:H based solar cells under illumination and their influence on the recombination properties may be studied in situ by pEDMR.

Loss mechanisms in poly-Si solar cells studied by multifrequency EDMR

In general, the defect identification that was performed in this work has set the stage for further investigations focussing on the structural properties of specific defects in Si materials by means of multi-frequency and multi-resonance pEDMR. The first pEDMR measurements at Q-band frequency, which were successfully performed in close collaboration with the AG Bittl at the FU Berlin, constitute the first step into this direction. In the near future, these studies will be extended towards even higher microwave frequencies like W-band and the high-field spectrometers at FU Berlin and HZB. The possibility to perform

EDMR measurements at different resonance frequencies turned out to be a powerful tool to discriminate overlapping signals exhibiting field-dependent and field-independent line broadening mechanisms — a case which is frequently encountered in silicon materials with modulated morphology like μc-Si:H or polycrystalline silicon (poly-Si). The present study on μc-Si:H showed that in order to get a complete picture about the spin-dependent transport processes, pEDMR measurements at different temperatures from cryogenic to room temperatures have to be carried out.

A. Rabi oscillations

In Section 2.5 we study the effect of resonant pulses on a spin (pair) ensemble. This appendix describes the underlying calculations in more detail. We utilize the matrix representation of rotation operators to consecutively study the influence of coherent pulses on an ensemble consisting of spin $1/2$ particles, spin pairs in which only one spin of each pair is excited by the pulse and finally spin pairs in which the pulse is resonant for both spins of each pair.

A.1. Rotations of single spins

In the most simple case the spin ensemble consists of $S = 1/2$ particles that are initially all in the $|\uparrow\rangle$ state. Thus, the initial density matrix representing this pure ensemble state is given by

$$\hat{\rho}^i = \begin{pmatrix} 1 & 0 \\ 0 & 0 \end{pmatrix} . \tag{A.1}$$

In general, the rotation operator describing a pulse with phase ϕ and flip angle β is represented by $\hat{R}_\phi(\beta)$ [196]. Neglecting spin relaxation during the pulse, its matrix representation for $S = 1/2$ takes the form [94]

$$\hat{R}_\phi(\beta) = \begin{pmatrix} \cos\frac{\beta}{2} & -i\sin\frac{\beta}{2}e^{-i\phi} \\ -i\sin\frac{\beta}{2}e^{+i\phi} & \cos\frac{\beta}{2} \end{pmatrix} . \tag{A.2}$$

The density operator is then transformed according to $\hat{\rho}^f = \hat{R}_\phi(\beta)\hat{\rho}_1\hat{R}_\phi(\beta)^\dagger$. For a mw pulse of length τ that rotates the magnetization around the x-axis ($\phi = 0$) at the frequency Ω, this transformation yields the density matrix for the final state

$$\hat{\rho}^f = \hat{R}_x(\Omega\tau)\hat{\rho}^i\hat{R}_x(-\Omega\tau) = \begin{pmatrix} c & -is \\ -is & c \end{pmatrix} \begin{pmatrix} 1 & 0 \\ 0 & 0 \end{pmatrix} \begin{pmatrix} c & is \\ is & c \end{pmatrix} = \begin{pmatrix} c^2 & isc \\ -isc & s^2 \end{pmatrix} \tag{A.3}$$

using the abbreviations $s = \sin\frac{\Omega\tau}{2}$ and $c = \cos\frac{\Omega\tau}{2}$. As expected, the population of the state $|\uparrow\rangle$ which is given by the $(1,1)$ element of $\hat{\rho}^f$,

$$\rho_{11}^f = \cos^2\frac{\Omega\tau}{2} = \frac{1}{2} + \frac{1}{2}\cos\Omega\tau\,, \tag{A.4}$$

oscillates between 0 and 1 at the Rabi frequency Ω.

A.2. Rotations of spin pairs — selective excitation

When the ensemble consists of weakly coupled (exchange or dipolar spin-spin coupling) spin pairs of which only one spin partner is excited by the mw pulse, the situation is similar to the case described in Appendix A.1. Assuming that all spin pairs start their evolution from the triplet states $|\uparrow\uparrow\rangle$ and $|\downarrow\downarrow\rangle$, the initial density matrix in the product base representation becomes

$$\hat{\rho}^i = \frac{1}{2}\begin{pmatrix} 1 & 0 & 0 & 0 \\ 0 & 0 & 0 & 0 \\ 0 & 0 & 0 & 0 \\ 0 & 0 & 0 & 1 \end{pmatrix}\,. \tag{A.5}$$

Accordingly, the rotation operator in (A.2) has to be expanded to the product space. When the pulse acts only on spin one, the 'rotation operator' for spin two can be substituted by the identity matrix. This yields the the product base rotation operator (again for a pulse with $\phi = 0$ and flip angle $\Omega\tau$)

$$\begin{aligned} \hat{R}_x(\Omega\tau) = \hat{R}_{1,x}(\Omega\tau)\mathbb{1}_{2\times 2} &= \begin{pmatrix} c & -is \\ -is & c \end{pmatrix} \otimes \begin{pmatrix} 1 & 0 \\ 0 & 1 \end{pmatrix} \\ &= \begin{pmatrix} c & 0 & -is & 0 \\ 0 & c & 0 & -is \\ -is & 0 & c & 0 \\ 0 & -is & 0 & c \end{pmatrix} \end{aligned} \tag{A.6}$$

with the same abbreviations like in (A.3). Following the argumentation from Appendix A.1, the final state density matrix is given by

$$\begin{aligned}
\hat{\rho}^f &= \hat{R}_x(\Omega\tau)\hat{\rho}^i\hat{R}_x(-\Omega\tau) \\
&= \begin{pmatrix} c & 0 & -is & 0 \\ 0 & c & 0 & -is \\ -is & 0 & c & 0 \\ 0 & -is & 0 & c \end{pmatrix} \frac{1}{2} \begin{pmatrix} 1 & 0 & 0 & 0 \\ 0 & 0 & 0 & 0 \\ 0 & 0 & 0 & 0 \\ 0 & 0 & 0 & 1 \end{pmatrix} \begin{pmatrix} c & 0 & is & 0 \\ 0 & c & 0 & is \\ is & 0 & c & 0 \\ 0 & is & 0 & c \end{pmatrix} \\
&= \frac{1}{2} \begin{pmatrix} c^2 & 0 & isc & 0 \\ 0 & s^2 & 0 & -isc \\ -isc & 0 & s^2 & 0 \\ 0 & isc & 0 & c^2 \end{pmatrix} . \qquad \text{(A.7)}
\end{aligned}$$

Hence, the population of the triplet states $|\uparrow\uparrow\rangle$ and $|\downarrow\downarrow\rangle$ behaves exactly like the population of the state $|\uparrow\rangle$ in the case of single $S = 1/2$ particles,

$$\rho^f_{11} + \rho^f_{44} = \cos^2\frac{\Omega\tau}{2} = \frac{1}{2} + \frac{1}{2}\cos\Omega\tau\,, \qquad \text{(A.8)}$$

namely it oscillates with the same Rabi frequency Ω between 0 and 1.

A.3. Rotations of spin pairs — non-selective excitation

We now consider the evolution of an ensemble of weakly coupled spin pairs under the influence of a non-selective mw pulse. In this case, both spins rotate around the x-axis simultaneously, leading to a qualitatively different behaviour as compared to the situation described before. Throughout this thesis, the case of non-selective spin-pair excitation is referred to as *spin-locking*. Elsewhere, the term *strong light-field coupling* [197, 36, 37] is used to describe the same effect.

We start from the same density matrix like in (A.5). However, in the present case the rotation operator acts on both spins, so it takes the form

$$\begin{aligned}\hat{R}_x(\Omega\tau) = \hat{R}_{1,x}(\Omega\tau)\hat{R}_{2,x}(\Omega\tau) &= \begin{pmatrix} c & -is \\ -is & c \end{pmatrix} \otimes \begin{pmatrix} c & -is \\ -is & c \end{pmatrix} \\ &= \begin{pmatrix} c^2 & -isc & -isc & -s^2 \\ -isc & c^2 & -s^2 & -isc \\ -isc & -s^2 & c^2 & -isc \\ -s^2 & -isc & -isc & c^2 \end{pmatrix} . \end{aligned} \tag{A.9}$$

Therefore, the final state density matrix becomes

$$\begin{aligned}\hat{\rho}^f &= \hat{R}_x(\Omega\tau)\hat{\rho}^i\hat{R}_x(-\Omega\tau) \\ &= \begin{pmatrix} c^2 & -isc & -isc & -s^2 \\ -isc & c^2 & -s^2 & -isc \\ -isc & -s^2 & c^2 & -isc \\ -s^2 & -isc & -isc & c^2 \end{pmatrix} \frac{1}{2}\begin{pmatrix} 1 & 0 & 0 & 0 \\ 0 & 0 & 0 & 0 \\ 0 & 0 & 0 & 0 \\ 0 & 0 & 0 & 1 \end{pmatrix} \begin{pmatrix} c^2 & isc & isc & -s^2 \\ isc & c^2 & -s^2 & isc \\ isc & -s^2 & c^2 & isc \\ -s^2 & isc & isc & c^2 \end{pmatrix} \\ &= \frac{1}{2}\begin{pmatrix} s^4+c^4 & isc^3-is^3c & isc^3-is^3c & -2s^2c^2 \\ -isc^3+is^3c & 2s^2c^2 & 2s^2c^2 & is^3c-isc^3 \\ -isc^3+is^3c & 2s^2c^2 & 2s^2c^2 & is^3c-isc^3 \\ -2s^2c^2 & -is^3c+isc^3 & -is^3c+isc^3 & s^4+c^4 \end{pmatrix} . \end{aligned} \tag{A.10}$$

It is apparent that the population changes induced by the mw pulse in the spin-locking regime are markedly different from the behaviour in the case of selective excitation. The triplet state populations of $|\uparrow\uparrow\rangle$ and $|\downarrow\downarrow\rangle$ oscillate according to

$$\begin{aligned}\rho^f_{11} + \rho^f_{44} &= \sin^4\frac{\Omega\tau}{2} + \cos^4\frac{\Omega\tau}{2} \\ &= \frac{1}{8}(\cos 2\Omega\tau - 4\cos\Omega\tau + 3) + \frac{1}{8}(\cos 2\Omega\tau + 4\cos\Omega\tau + 3) \\ &= \frac{3}{4} + \frac{1}{4}\cos 2\Omega\tau \end{aligned} \tag{A.11}$$

between 0.5 and 1. The oscillation frequency 2Ω corresponds to twice the value of the Rabi frequency Ω that was obtained for the rotation of single spins (cf. Appendix A.1) and spin pairs with selective mw excitation (cf. Appendix A.2). This behaviour is illustrated in Fig. A.1 for the Rabi frequency $\Omega/2\pi = 10$ MHz.

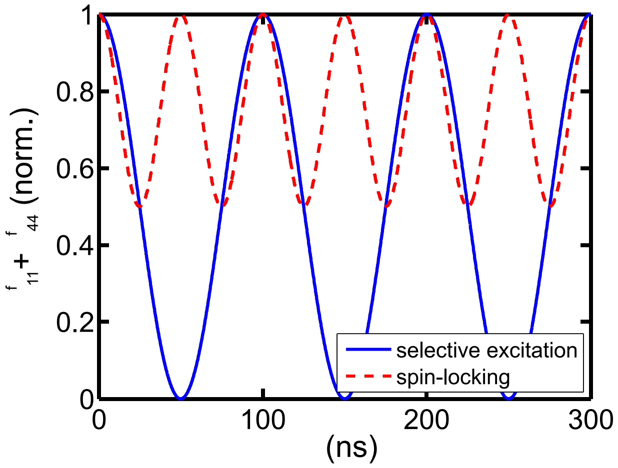

Figure A.1.: Population of the triplet states $|\uparrow\uparrow\rangle$ and $|\downarrow\downarrow\rangle$ for the case of selective excitation and spin-locking, respectively. The single spin Rabi frequency is $\Omega/2\pi = 10$ MHz in both cases.

A.4. The singlet content of a spin pair

The observable in EDMR, i.e. changes of the (photo-)current, is related to the singlet content of the spin pairs in the ensemble. When the density operator is given in the product base representation, the singlet content of the ensemble is determined by applying the singlet projection operator [94]

$$P_S = \frac{1}{2}\begin{pmatrix} 0 & 0 & 0 & 0 \\ 0 & 1 & -1 & 0 \\ 0 & -1 & 1 & 0 \\ 0 & 0 & 0 & 0 \end{pmatrix} \tag{A.12}$$

to the density matrix, i.e.

$$\mathrm{tr}\left(P_S\,\hat{\rho}\right) = \frac{1}{2}\left(\rho_{22} - \rho_{32} + \rho_{33} - \rho_{23}\right) . \tag{A.13}$$

Comparing this result with the final state density matrices given in (A.7) for selective excitation and in (A.10) for spin-locking, we see that the singlet content behaves differently in both cases. For selective excitation, the elements ρ^f_{23} and ρ^f_{32} are 0 and thus the singlet content is solely determined by the diagonal elements, yielding an oscillation of the singlet content between 0 and 1 at the Rabi frequency Ω. In contrast, in the spin-locking regime we have $\rho^f_{22} = \rho^f_{33} = \rho^f_{32} = \rho^f_{23}$. Consequently, the singlet content is 0 all the time and thus the transfer of population is restricted to the triplet manifold. Note that this is only valid under the assumption of non-vanishing coherences (ρ^f_{32} and ρ^f_{23}).

B. Numerical calculations

This appendix deals with time domain simulations of spin systems. After a general introduction into the formal description of spin dynamics, we will present an effective algorithm for the calculation of the density matrix evolution that was originally developed for NMR, harnessing the periodicity of the spin Hamiltonian.

Numerical calculations of coherent spin motion are used in Section 2.6 to study the influence of disorder on spin-Rabi nutations. This appendix contains a more detailed description of the mathematical framework.

B.1. Formal description of spin dynamics

All necessary information about the state of a spin ensemble is contained in the density operator $\hat{\rho}(t)$. Its temporal evolution is determined by the spin Hamiltonian and can be described by the Liouville-von Neumann equation [94]

$$\frac{d\hat{\rho}(t)}{dt} = -\frac{i}{\hbar}[H(t), \hat{\rho}(t)] \tag{B.1}$$

where $H(t)$ is the spin Hamiltonian which usually consists of a time-independent part H_0 and a time-dependent part $H_1(t)$. The solution if formally given by

$$\hat{\rho}(t) = U(t,0)\hat{\rho}(0)U^{\dagger}(t,0) \tag{B.2}$$

with the propagator

$$U(t,0) = \hat{T}\exp\left(-\frac{i}{\hbar}\int_0^t H(t')\,dt'\right) . \tag{B.3}$$

Note that $H(t')$ is different for each infinitesimal small time interval t'. Here, $\hat{T}$ is the time order operator which orders the individual time intervals chronologically [198].

Knowing $U(t,0)$ for each time t corresponds to knowing the state of the spin system at all times. Thus, simulating the evolution of the density operator boils down to determining the propagator in (B.3). However, this is only straightforward in the case of a time-independent Hamiltonian.

For ‘simple’ systems such as one spin $S = 1/2$ with isotropic g tensor and hyperfine and dipolar interactions being much smaller than the Zeeman energy, the evolution of the spin can be described in its rotating frame [174]. By a unitary transformation to the reference frame in which the electron spin is at rest, the pulse Hamiltonian becomes time-independent and (B.3) can directly be integrated. In more complicated systems there is no reference frame in which all time-dependent terms vanish. In this case, one can either use an interaction frame (where the time-dependent terms are small) [174] or directly integrate the propagators in the laboratory frame. Since the use of the interaction frame does not significantly reduce the computational cost [199], we will carry out all propagator calculations in the laboratory frame.

B.2. The effective Hamiltonian method

The Liouville-von Neumann equation (B.1) is a system of first-order differential equations. Thus, the time evolution of the density operator for an arbitrary spin system can numerically be calculated using any algorithm that discretizes the time interval of interest from 0 to T and calculates $\hat{\rho}(t)$ for each time step t. This *direct approach* was previously followed in order to simulate coherent EDMR signals from spin pairs with exchange coupling [37] and without spin-spin coupling in the presence of disorder [102]. Here, a standard Runge-Kutta algorithm was used. A reasonable length of the time step is determined by the length of one mw period $1/\nu_{mw}$ which has to be separated into at least a few 100 steps. Mw pulses are usually much longer than $1/\nu_{mw}$, resulting in a large amount of time steps. For instance, in [37] mw pulses up to 1.5 µs were calculated at a step size of 1 ps. This makes the computation lengthy and the output extremely inconvenient to handle.

These limitations can be overcome by taking advantage of the periodicity of the spin Hamiltonian in the presence of mw pulses. The procedure described here is based on the COMPUTE (*c*omputation over *o*ne *m*odulation *p*eriod *u*sing *t*ime *e*volution) algorithm that was originally developed for NMR [200]. A similar approach is implemented in the widely used Easyspin simulation package [99].

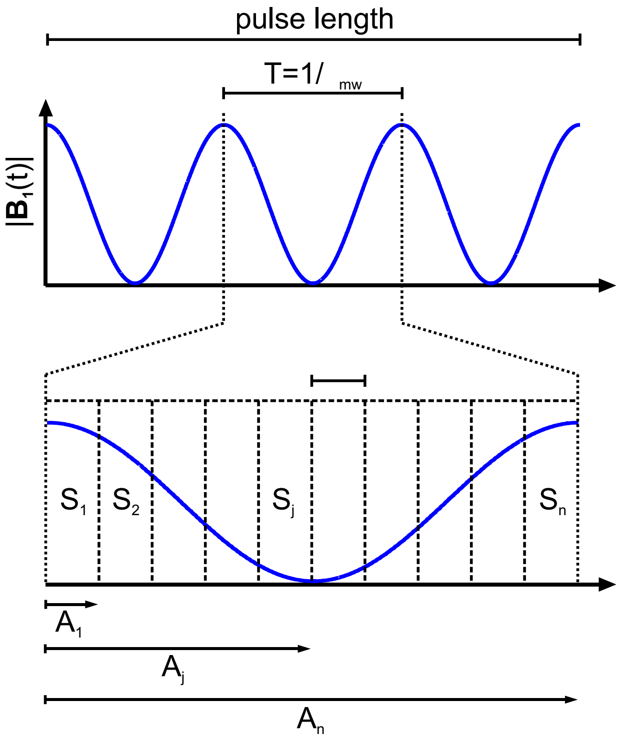

Figure B.1.: Calculation of the pulse propagator according to the COMPUTE algorithm [200]. The pulse is divided into modulation periods T, which are each separated into n intervals. Details can be found in the text.

The propagator for a mw pulse has a modulation period $T = 1/\nu_{mw}$. Therefore, its calculation can be be realized by determining the propagator for one modulation period,

$$U(T,0) = \exp\left(-\frac{i}{\hbar}\bar{H}T\right), \tag{B.4}$$

and then assembling the whole propagator by iteratively applying the same $U(T,0)$. Here, $\bar{H}$ is the time-independent *effective Hamiltonian* which applies to a single modulation period. This procedure is schematically shown in Fig. B.1. We consider only one modulation period (a small part of the mw pulse) and subdivide it into n intervals of length $\tau = T/n$. The propagator for segment j is denoted S_j, and the respective propagator that describes the evolution from time 0 to time $j\tau$ is denoted A_j. In this notation A_n corresponds to $U(T,0)$.

Each single segment propagator can be calculated in analogy to (B.4) [198] by evaluating the Hamiltonian at the time $t = (j-1)\tau + \tau/2$,

$$S_j = U\left(j\tau,(j-1)\tau\right) = \exp\left[-\frac{i}{\hbar}H\left((j-1)\tau+\tau/2\right)\tau\right] \qquad \text{for } 1 \leq j \leq n\,. \tag{B.5}$$

The corresponding accumulated propagators are given by [200]

$$A_j = \begin{cases} S_j A_{j-1} & \text{for } 1 \leq j \leq n \\ \mathbb{1}_{N\times N} & \text{for } j = 0\,, \end{cases} \tag{B.6}$$

finally yielding A_n for the whole modulation period T. When all intermediate propagators A_j are stored, pulse propagators of arbitrary length can easily be constructed later on.

B.3. Practical computation of pulse propagators

To calculate the evolution of a spin pair ensemble we determine the density matrix after a mw pulse according to (B.2). For this purpose we compute the pulse propagator $A_n = U(T,0)$ for one microwave period $T = 1/\nu_{mw}$ as described in the previous section. This propagator is then recursively applied to $\hat{\rho}(0)$ in order to yield the state of the density matrix at the time $m \cdot T$,

$$\hat{\rho}(t = m \cdot T) = [U(T,0)]^m\, \hat{\rho}(0)\, [U^\dagger(T,0)]^m\,, \tag{B.7}$$

where m is an integer. If the time interval T is too long for the respective purpose, e.g. when simulating spin-Rabi nutations at strong B_1, the intermediate propagators A_j as given in (B.6) may be used to obtain a time axis with smaller increment. The spin pair Hamiltonian that governs the spin motion consists of the time-independent part in (2.5) as well as the time-dependent part in (2.27).

As pointed out in Section 2.6, the ramifications of disorder can be taken into account by calculating the time evolution for several spin pairs comprising spins with different g values. Hence, the g values in the spin pair Hamiltonian have to be replaced by their respective distributions $p(g_a)$ and $p(g_b)$ which may be chosen arbitrarily. Both g distributions which are used for the simulations presented in this thesis typically consist of 100 individual g values. Thus, we have to calculate the time evolution of 10^4 spin pairs for each simulation. The software that was developed for this purpose (cf. Section 2.6) performs the computation for several spin pairs in parallel on multiprocessor-CPUs. It uses the routines provided by LAPACK[1].

---

[1] LAPACK (Linear Algebra PACKage) is written in Fortran90 and provides efficient routines for solving eigenvalue problems and other linear-algebra related tasks (see www.netlib.org/lapack/).

C. Spin pair generation

An experiment is presented which allows the observation of charge carrier pair formation that precedes electronic transitions such as spin-dependent recombination or spin-dependent transport. It is based on an electrically detected magnetic resonance induced rotary echo sequence. The experimental demonstration is performed on precursor (spin) pairs of electrons in the emitter layer of crystalline silicon/amorphous silicon heterostructures. Precursor pair generation rate coefficients extracted from these measurements are studied as a function of light intensity and are found to show only a minor dependence on the illumination level indicating that the pair generation is not determined by charge carrier densities.

C.1. Introduction

Transitions of charge carriers through localized electronic states occur in various qualitatively and quantitatively different forms such as defect or excitonic recombination processes or hopping transport in disordered materials. Common to all these processes is that they take place through multiple electronic transitions which involve the formation of intermediate pairs in one or several localization steps before the final recombination or transport transitions occurs. Examples for such processes are defect recombination described by Shockley and Read [72] for which intermediate pairs are crucial to exist even though they can often be neglected for the statistical Shockley-Read-Hall description of recombination. Other examples include excitonic recombination for which the excitonic states represent intermediate pairs [201], excitonic recombination through additional precursor states as observed in many organic semiconductor systems [202] or hopping transport in the low-temperature regime of disordered semiconductors [35] where precursor pairs are constituted by nearest-neighbour arrangements. The influence of the precursor states for macroscopic electrical or optical properties is oftentimes negligible, yet there are some exceptions where the nature of the precursor pairs and their formation profoundly affect transport or recombination. For these systems, the ability to experimentally access precursor pair generation rates becomes crucial for the understanding of their microscopic nature. Examples for this often involve spin-dependent transitions that can be found in weakly spin-orbital-coupled materials (e.g. in any known silicon morphology [35] or organic semiconductors [202, 187]) since the precursor pair formation determines for these cases macroscopic material and device properties such as magnetoresistance [98] or device efficiency [203].

In the following, we present an experiment which allows the observation of the precursor pair formation for spin-dependent transport and recombination processes. This experiment is based on the observation of coherent spin motion of precursor pairs using a pulsed electrically detected magnetic resonance (pEDMR) induced rotary echo pulse sequence. EDMR measures changes in the (photo-) conductivity of a semiconductor material resulting from magnetic resonant alteration of transition rates of spin pairs. Independent of the specific type of microscopic transition process — either spin-dependent hopping, trapping or recombination — intermediate spin pairs [44, 9, 34] (precursor pairs) consisting of two charge carriers with spin $S = 1/2$ determine the observed signals. EDMR detected rotary echoes are produced by spin ensembles which are dephased from an initial eigenstate due to a resonantly induced inhomogeneous spin nutation (a so called pulse induced Rabi nutation) before they are rephased due to a second pulse with opposite phase [174].

Rotary echoes have been used in the past for the measurement of precursor pair coherence times as the decay of a rotary echo train poses a limit on the net decay rate caused by precursor pair recombination or dissociation [11]. However, it is difficult to distinguish experimentally between different possible influences that can affect the echo decay, among them (a) transitions that destroy spin pair coherence (either hopping, recombination or trapping), (b) spin relaxation, (c) dissociation and (d) precursor pair generation during the experiment. While the theoretical models describing pEDMR have been tested experimentally with regard to dissociation, hopping and recombination dynamics [34, 35, 75], the process of precursor pair generation is complicated to access experimentally. Usually, spin pair generation is assumed to be negligible during the mw excitation in a pEDMR experiment. This is certainly justified for the typical current relaxation and transient nutation experiments where only one short microwave pulse with a length of a few 100 ns is used. In contrast to that, spin pair generation can become important for more advanced (and much longer) pulse sequences. Furthermore, spin pair generation influences pEDMR signals on the timescale where current relaxation transients (the basis of all pEDMR experiments) are recorded [34]. Note that, however, neither the decay of the rotary echo nor the transient behaviour of the observed EDMR signals reveals information about the pair generation rate as precursor pair generation rates are only weakly dependent on the rate changes induced by magnetic resonance (see arguments made in Refs. [34, 36, 37]). Therefore, measuring the dynamics of precursor pair generation has remained elusive so far.

For the experiment presented the problem is solved by measuring the Rabi nutation around a rotary echo signal as a function of a separation time between dephasing and rephasing of the spin ensemble. It is shown that one can distinguish the pEDMR signals from precursor pairs which existed before the dephasing pulse from those generated after the pulse due to a 180° phase difference of the Rabi nutation signals which originate from the two ensembles. Thus, a disentanglement of true loss of coherence (effects (a) to (c) as mentioned before) and spin pair generation (d) can be achieved.

The demonstration of this experiment was conducted on a heterostructure solar cell consisting of a highly phosphorus doped hydrogenated amorphous silicon (a-Si:H) emitter layer and a crystalline silicon (c-Si) absorber. These heterostructures are known to exhibit a strong pEDMR signal resulting from hopping of electrons via localized conduction band tail and phosphorus states in the a-Si:H layer [131, 35]. Changes in the precursor pair generation rate caused by a light flux controlled change in the charge carrier generation rate are investigated. While pEDMR was used for the experiments presented here, it shall be stressed that this experiment could conceivably be carried out in an equal way (using the same magnetic resonance pulse sequence) for the investigation of optically detected spin-dependent transitions using photoluminescent or electroluminescent processes [204, 205].

C.2. Electrically detected rotary echo

The experiment is started from the steady state where all electronic transition rates are constant. Therefore, precursor pairs are constantly generated and their influence on an observed rate (referred to as I_{ph} since we use a photocurrent for the experiments presented) is balanced by the annihilation of spin pairs through processes such as dissociation, hopping or recombination. In the steady state, the number of pairs, and therefore I_{ph}, are constant in time. When applying a resonant mw pulse, the spin pairs will begin a coherent nutation

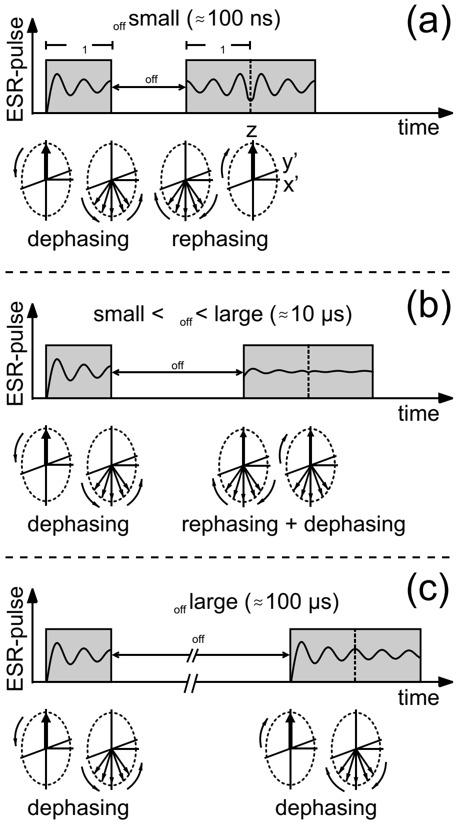

Figure C.1.: Sketch of the rotary echo experiment that can be used to study precursor pair generation. The pulse sequence consists of two microwave pulses with opposite phase and an interpulse waiting time, τ_{off}. The sketch illustrates three cases: (a) for τ_{off} much shorter than the pair generation time, (b) for τ_{off} of the order of the generation time and (c) for τ_{off} much longer than the pair generation time. The time-traces are drawn along with the dephasing states of the spin ensemble at the beginning and the end of each pulse. The Rabi oscillation of the spins reflected by the pEDMR signal $Q(\tau_{1,2})$, as plotted for the gray shaded time interval during the pulses, is phase inverted for pairs generated during the interpulse time in comparison to pairs generated before the pulse sequence begins. Hence, the deconvolution of the Rabi oscillation into phase inverted and non-phase inverted oscillation components allows a relative quantification of newly generated pairs and preexistent pairs. For details see text.

(a Rabi oscillation) and their phase coherence will be lost gradually due to spin relaxation, spin-dependent electronic pair decay and inhomogeneous magnetic fields. When further spin pairs are formed during the application of this pulse, these spin pairs will be generated in eigenstates and thus, due to their random time of generation, they will be at random phase to the already existing spin pair ensemble. Thus, spin pair generation will influence the signal in a similar way like any other source of decoherence. This can be studied by utilizing the pulse sequence illustrated in Fig. C.1 which consists of two subsequent pulses with opposite (180°) phase relation. During the first pulse, the spin ensemble carries out a gradually dephasing Rabi nutation which can be observed with pEDMR by measurement of the integrated charge $Q(\tau)$ after the pulse as a function of the applied pulse length τ (Ref. [35]). $Q(\tau)$, which is obtained by integrating the current transient after the mw excitation, represents a projection of the spin state of the precursor pair at the end of the pulse. For the pulse sequence in Fig. C.1, the length of the first pulse is kept at constant length τ_1 and $Q(\tau_2)$ is measured as a function of the length τ_2 of the second pulse which now represents initially (for $\tau_2 < \tau_1$) a dephased Rabi oscillation that gradually recovers to the rotary echo at $\tau_2 = \tau_1$ before it dephases again at $\tau_2 > \tau_1$. Note that this detection scheme for rotary echoes was used for the first electrical detection of spin coherence [11] and has since then been applied to various studies on decay processes of precursor pairs [206, 207, 204]. It shall be noted that rotary echoes are always observed at a time $\tau_2 = \tau_1$, independently of the length τ_1 of the initial dephasing pulse.

For the observation of the generation of precursor pairs we now set the length τ_1 to a value so that the corresponding flip angle of the spin ensemble is $(2n+1)\pi$ with n being an integer number (the flip angle is 5π in the sketched experiment) and we also introduce an interpulse waiting time, τ_{off}, between the two pulses during which the dephased spin ensemble remains completely unchanged in a rotating Bloch sphere representation, as long as no pairs decay and no new pairs are generated. The length τ_2 of the second pulse is again incremented gradually so that the integrated sample current $Q(\tau_2)$ measured after the two pulses as a function of τ_2 reflects the rephasing Rabi oscillation due to the rotary echo.

The expected pEDMR signal $Q(\tau_2)$ is depicted inside the grey shaded pulse intervals in Fig. C.1 for three different interpulse waiting times: (a) for a short τ_{off} almost all spins that have dephased during pulse 1 can be refocused during the second pulse. The echo signal corresponds to a (local) minimum of $Q(\tau_2)$ for $\tau_2 = \tau_1$. (b) For larger values of τ_{off} the spin pairs that are generated between the two mw pulses significantly influence $Q(\tau_2)$ in addition to spin pairs that are lost during τ_{off} due to annihilation (dissociation or recombination). While the surviving spin pairs that are refocused during pulse 2 again result in a minimum signal, the newly generated spin pairs give rise to a maximum at $\tau_2 = \tau_1$ as the flip angle of the newly generated spins is $(2n+1)\pi$. Thus, the measured signal is a combination of two 180° phase shifted oscillations. When the ensemble of newly generated pairs equals the ensemble of previously generated pairs, the two signals compensate each other at the time of the echo. c) When τ_{off} is sufficiently long so that the coherent information generated during the first pulse is lost due to spin pair annihilation, the signal measured is completely determined by spin pairs that have been generated during τ_{off}. Hence, the signal is the same like the signal obtained in a Rabi oscillation measurement without the first pulse, and therefore it exhibits a clear maximum at $\tau_2 = \tau_1$.

By fitting model functions to the experimental results of $Q(\tau_2)$ for various τ_{off}, the relative magnitudes of the ensemble sizes of the newly and previously generated precursor pairs can be obtained as a function of τ_{off}, and these dependencies represent both the generation and decay dynamics of the precursor pairs, respectively. This procedure is demonstrated in Section C.5 using experimentally obtained pEDMR rotary echo signals.

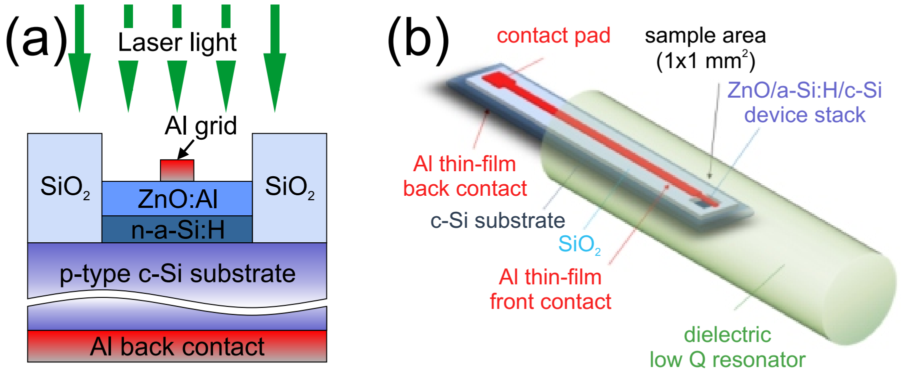

Figure C.2.: (a) Cross section of the heterostructure solar cell and (b) geometrical sketch of the entire pEDMR sample. The sample consists of 2×50 mm^2 of a boron doped crystalline silicon wafer which provides the absorber of the cell. The phosphorus doped amorphous silicon (emitter layer) and the ZnO (transparent conducting oxide) cover only a square of 1×1 mm^2. A window of the same size was etched out of the SiO_2 before the deposition. The front contact (Al grid finger) is connected to a thin-film strip line that extends to the opposite side of the substrate. Electrical isolation from the crystalline silicon is accomplished by the SiO_2. Structuring of the sample was done using standard optical lithography. For the pEDMR experiments the sample is illuminated through the a-Si:H side.

It shall be mentioned that the magnitude of the rotary echo is always affected by the distribution of Larmor frequencies which will result in a dephasing contribution that cannot be rephased with the method presented here. This ‘lost’ part of the spin pair ensemble is always equal for a given experiment and it will therefore always superimpose the $Q(\tau_2)$. It is therefore not relevant for the evaluation of decay times from the observed echo amplitude dependence of τ_{off}. It shall be noted though that Larmor rephasing is possible by means of a pEDMR Hahn echo experiment [113].

C.3. Experimental details

Fig. C.2 shows sketches of the a-Si:H/c-Si heterostructure used for the experiments in this study. Technologically, this device represents a solar cell. A 220 µm thick boron doped c-Si substrate with (100) surface orientation was used as absorber. The emitter layer, consisting of 20 nm phosphorous doped a-Si:H, was deposited on top of the c-Si substrate using plasma enhanced chemical vapor deposition. 80 nm of highly Al doped ZnO serves as transparent conducting oxide and is connected to a 100 µm wide and 200 nm thick Al front contact finger. A 200 nm thick Al back contact layer was deposited on the opposite side of the c-Si substrate. The active area of the solar cell was confined to 1 mm^2 resulting from the size of a window that was etched out of approx. 500 nm thermally grown SiO_2 covering the c-Si. The Al back contact as well as the Al front contact finger, which is electrically isolated from the c-Si by SiO_2, extend to the end of the substrate (size 50×2 mm^2). This thin-film wiring is indispensable in order to minimize artefacts induced by strong mw bursts used in the experiment and in order to not perturb the eigenmodes of the dielectric microwave resonator by the electrical circuitry. Several sample structures were processed on one wafer in parallel. They were cut into the appropriate size after the last processing step. Solar cells deposited in a similar manner were shown to reach efficiencies above 17% (cf. Ref. [128]) for a solar cell area of 1 cm^2.

All measurements were carried out in a Bruker E580 X-band EPR spectrometer. The sample was held at $T = 10$ K using a continuous flow helium cryostat. In order to facilitate a current which is sufficiently high for a pEDMR experiment, excess charge carriers were created optically by monochromatic light ($\lambda = 514$ nm) from an Argon-ion laser. The generation rate of free charge carriers in the sample could be changed by adjusting the optical output power of the laser. The light was fed through an optical fibre ending above the active sample area. A constant current source (Keithley 220PCS) was used to establish a constant photocurrent, $I_{\mathrm{ph}} = -1$ µA, corresponding to a current density of -0.1 mA cm^{-2} (reverse bias regime of the solar cell). Hence, optically generated electrons and holes in both the a-Si:H layer and the c-Si wafer are extracted through the Al contacts. The applied voltage which is required for $I_{\mathrm{ph}} = -1$ µA depends on the photon flux and amounts to values between 0.04 V and 0.27 V for the conditions used in the experiments. The response of the current source was slow compared to the time scale on which the pEDMR experiments were carried out, so that the EPR-induced current change, ΔI_{ph}, was not compensated.

In a pEDMR experiment the current transients after a mw excitation are recorded for several hundred microseconds for different values of the static magnetic field, B_0. Therefore, by analysing ΔI_{ph} as function of time, t, after a mw pulse at fixed B_0 (in the following referred to as pEDMR transients), one can gain insight into the dynamics of spin-dependent processes, whereas ΔI_{ph} at fixed t (pEDMR spectrum) contains the spectral information which is also accessible by the well established continuous wave (cw) EDMR technique [7,8].

C.4. pEDMR on a-Si:H/c-Si solar cells

Fig. C.3a shows the pEDMR spectrum measured $t = 10$ µs after excitation with a 320 ns long mw pulse. The relaxation of the photocurrent was recorded for 200 µs with a temporal resolution of 0.2 µs and averaging 5×10^4 transients for each value of B_0. The best fit to the pEDMR spectrum could be obtained by assuming a single Lorentzian line at $g = 2.0048(5)$. This is in accordance with earlier measurements on the same type of samples [131]. The underlying process is associated with electron hopping via conduction band tail states in a-Si:H [9, 146, 73] which also explains that directly after the mw pulse a positive change ΔI_{ph} is observed (see Fig. C.3b). The pEDMR spectrum is superimposed by two 25 mT split satellites that result from neutral phosphorus donor states, which lie in the same energy range as the conduction band tail states. The phosphorus hyperfine splitting of 25 mT in amorphous silicon, which significantly differs from the 4.2 mT splitting known from crystalline silicon [124], was originally determined by EPR [154] and later also observed in EDMR [135, 131]. The satellites cannot be observed in Fig. C.3a because of the limited magnetic field range used in the experiment.

Besides the spectral information, which alternatively could have been extracted from a cwEDMR experiment [132], pEDMR allows to study the time dependence of the resonance signal. The dynamics of pEDMR transients, i.e. the relaxation of I_{ph} back into the steady state after a resonant mw pulse excitation, is influenced by the spin pair recombination or hopping rates as well as precursor pair generation [35]. Fig. C.3b shows two pEDMR transients measured under different illumination conditions using a photon flux of $\phi_0 = 1 \times 10^{17}\,\mathrm{cm}^{-2}\,\mathrm{s}^{-1}$ and $\phi = 8 \times 10^{17}\,\mathrm{cm}^{-2}\,\mathrm{s}^{-1}$. The applied voltage was adjusted to yield $I_{\mathrm{ph}} = -1$ µA in both cases (corresponding to 0.21 and 0.27 V, respectively). It should be noted that the small adjustment of the bias voltage did not change the charge carrier extraction mechanism. The shape of the transients can be fitted when assuming a combination of two single exponential functions (one with positive and one with negative amplitude) for each transient as inferred from theory (see dashed line in Fig. C.3b) [34]. The fits yield the time constants $\tau_a \approx 40$ µs, $\tau_b \approx 300$ µs and $\tau_a^* \approx 8$ µs, $\tau_b^* \approx 50$ µs for ϕ_0 and $8 \times \phi_0$, respectively. It is tempting to associate the change of the two time constants upon increasing the photon flux with a rate change of the underlying microscopic mechanisms. However, although it is apparent that the photon flux certainly has a dramatic impact on the time constants, its interpretation with regard to spin-dependent transitions or precursor pair generation rate coefficients is not straightforward as the shape of pEDMR

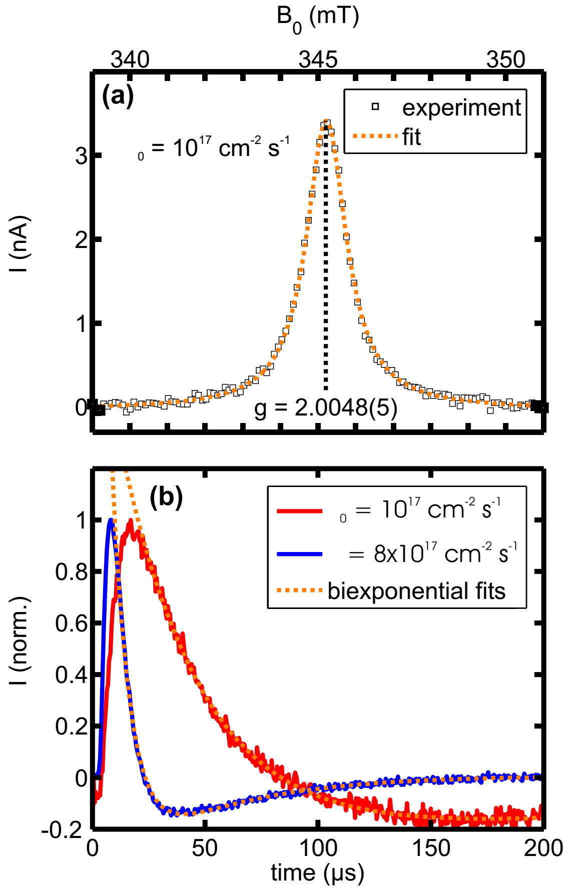

Figure C.3.: Results of a pEDMR experiment carried out at $T = 10$ K using a photocurrent of $I_{\text{ph}} = -1$ μA. (a) Current change at $t = 10$ μs after a 320 ns long mw pulse (pEDMR spectrum). The spectrum reveals a single Lorentzian line at $g = 2.0048(5)$ (dashed line) which in accordance with the g value of conduction band tail states in amorphous silicon. The line width is dominated by power broadening resulting from the high mw power ($B_1 \approx 70$ μT) used in the experiment. (b) Current relaxation as a function of time after the mw excitation (pEDMR transient) on the resonance position at $g = 2.0048(5)$ measured at two different light intensity levels as indicated in the legend. The dashed lines represent fits to the experimental data assuming a combination of two exponential functions for each transient. The respective time constants are given in the text.

transients can also be affected by RC time constants of the detection electronics or the dielectric relaxation times of sample (for a more detailed analysis see Ref. [208]).

An elegant way to study microscopic processes in pEDMR without any influences of RC time constants or other artefacts is to investigate the coherent spin motion during the mw excitation using a pulse length dependent measurement [34]. Fig. C.4a shows the charge response $Q(\tau) = \int_{3\,\mu\mathrm{s}}^{19\,\mu\mathrm{s}} \Delta I_{\mathrm{ph}}\, dt$ determined at $g = 2.0048$, i.e. at the maximum position of the resonance line shown in Fig. C.3a. These oscillations originate from spin Rabi oscillations of charge carriers that are involved in the spin-dependent hopping via localized conduction band tail and phosphorus states in a-Si:H [206].

A Fourier transformation of $Q(\tau)$ yields the associated Rabi frequencies. The inset of Fig. C.4a displays the frequencies determined at four different amplitudes, B_1, of the mw magnetic field. The B_1 axis has been scaled according to Rabi's formula $\Omega = \gamma B_1$, where $\Omega/2\pi$ is the Rabi frequency and $\gamma = g\mu_B/\hbar$ is the gyromagnetic ratio, i.e. the ratio between g value, the Bohr magneton, μ_B, and the Planck's constant, $\hbar$. The solid line represents a linear fit through the origin. From the Rabi frequencies it can be inferred that the oscillations shown in Fig. C.4a correspond to the Rabi frequency of individual $S = 1/2$ particles and therefore originate from spin pairs with weak spin-spin (exchange and dipolar) coupling [34, 36, 37]. In other words, the mw pulse manipulates only one spin of the precursor pair. The two constituents of the associated spin pair are assigned to neutral phosphorus and conduction band tail states.

To evaluate the decay of the Rabi oscillations, Fig. C.4b shows a horizontal cut through the dataset along the dashed line in Fig. C.4a. Maxima and minima of the oscillation were fitted with two exponential functions each. Fig. C.4c shows the difference of these fits as a function of the mw pulse length τ which represents the oscillation decay (in the following referred to as Rabi decay). This behaviour can be well described by a single exponential function with a decay time constant $\tau_{\mathrm{dec}} \approx 100$ ns and an additional constant offset (≈ 0.05). The effects (a) to (d) (as mentioned in the introduction) that determine pEDMR echo decay also influence the Rabi decay observed here. In addition, coherent dephasing caused by a distribution of Rabi frequencies can also contribute to the Rabi decay. Discriminating between these effects is the aim of the rotary echo experiment described in the following section.

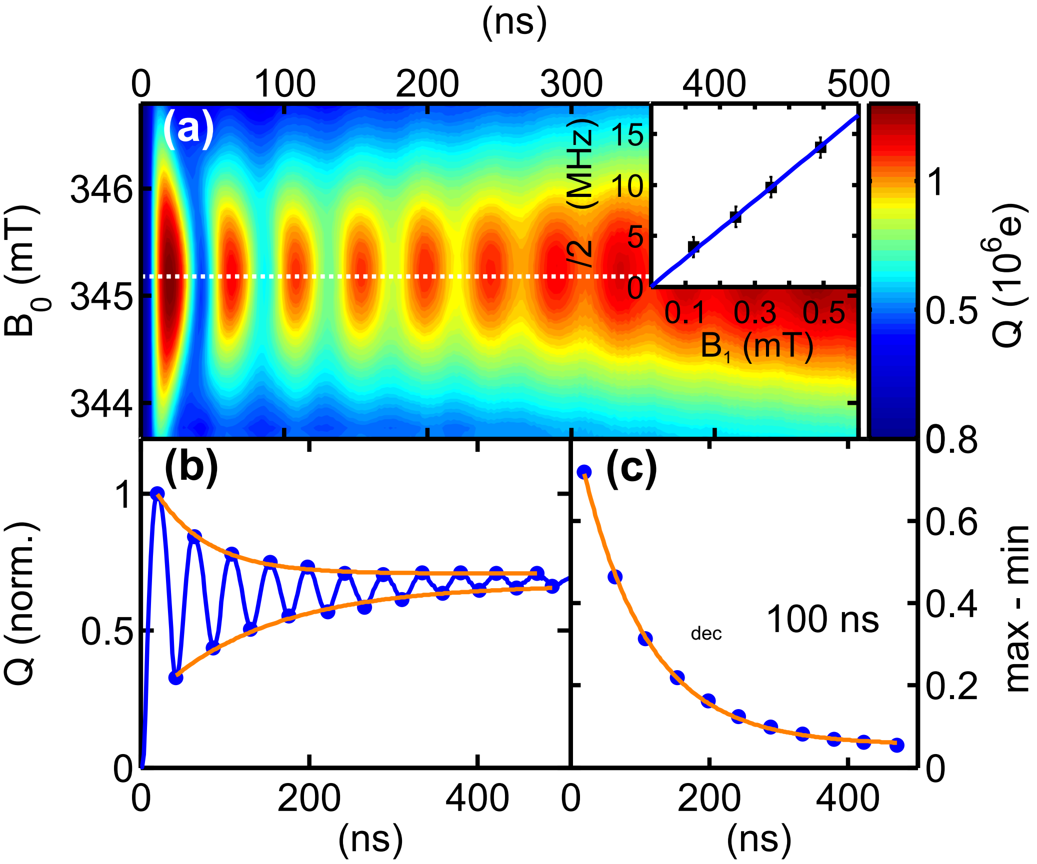

Figure C.4.: Observation of spin-Rabi nutation performed at a steady-state photocurrent of $I_{\text{ph}} = -1\ \mu\text{A}$ at $T = 10$ K. (a) Change of the photocurrent integrated from 3 to 19 µs after a mw excitation for 32 magnetic field values. The mw pulse length was varied from 0 to 510 ns with an increment of 2 ns. The oscillations reflect the coherent spin nutation of the spin pair ensemble during the mw pulse. The oscillation frequency $\Omega/2\pi$ is 23(2) MHz which corresponds to the Rabi frequency of a spin 1/2 under the conditions used in the experiment. The inset shows the Rabi frequencies determined by Fourier transformation of the coherent oscillations for several mw power levels. The solid line represents a linear fit through the origin. (b) Cut through the data displayed in (a) along the dashed line corrected for a linear baseline. To evaluate the Rabi decay quantitatively, the maxima and minima of the oscillations (marked by the bullets) were fitted with two exponential functions each (solid lines). (c) Difference between maxima and minima in plot (b) versus τ. The solid line shows a fit to the experimental data assuming a single exponential decay (time constant $\tau_{\text{dec}} \approx 100$ ns) and a constant offset (≈ 0.05).

C.5. Experimental observation of rotary echoes

Using identical experimental conditions as before (see Fig. C.3 and C.4), a rotary echo experiment as described in Section C.2 was performed. For this purpose, $Q(\tau_2)$ was recorded for τ_{off} varying between 0 and 200 µs. The length of pulse 1 was fixed at $\tau_1 = 136$ ns which corresponds to a flip angle of $\phi = \Omega \cdot \tau_1 = 5\pi$. The length of pulse 2 was increased from $\tau_2 = 0$ to 254 ns with an increment of 2 ns. Fig. C.5a shows the signal $Q(\tau_2)$ that was obtained by integrating ΔI_{ph} in the interval from 3 to 19 µs after pulse 2 has ended. The maximum echo signal occurs, as expected, when both pulses have the same length, i.e. for $\tau_2 = \tau_1$. With increasing waiting time we clearly observe in Fig. C.5a that the maximum due to the echo signal changes into a minimum at $\tau_{\text{off}} \approx 10$ µs.

The signal at $\tau_{\text{off}} = 0$ (uppermost curve in Fig. C.5a) can approximately be described by an oscillation that is symmetrical to $\tau_2 - \tau_1 = 0$. It represents the echo decay contribution to the EDMR signal, Q_{ed}, that arises from refocused spin pairs. This contribution decreases with increasing τ_{off} due to annihilation of spin pairs between both pulses. Since there is no delay between both pulses here ($\tau_{\text{off}} = 0$), we can neglect spin-dependent generation. By assuming an exponential damping of the amplitude, the model function can be written as

$$Q_{ed} = A_{ed} - B_{ed} \cos\left(\omega \cdot |\tau_2 - \tau_1| + \phi_{ed}\right) \cdot e^{-\frac{|\tau_2 - \tau_1|}{d_{ed}}} \tag{C.1}$$

with B_{ed} being the amplitude of the oscillation, ω the Rabi frequency and ϕ_{ed} an additional phase factor. d_{ed} denotes the time constant of the exponential damping and A_{ed} is a constant offset. All these parameters are determined by a least square fit. The only parameter that depends on τ_{off} is the amplitude B_{ed}.

Similarly, the signal Q_{np} that originates from new pairs generated during $\tau_{\text{off}} = 200$ µs (lowermost curve in Fig. C.5a), can approximately be described by

$$Q_{np} = A_{np} + B_{np} \sin\left(\omega \cdot \tau_2 + \phi_{np}\right) \cdot e^{-\frac{\tau_2}{d_{np}}} . \tag{C.2}$$

This expression ignores refocused spin pairs (Q_{ed}) and therefore, B_{np} denotes the amplitude of the damped Rabi oscillation carried out by spin pairs that were generated during τ_{off}. The meaning of the parameters A_{np}, ω, ϕ_{np} and d_{np} is analogous to the corresponding echo decay parameters defined above.

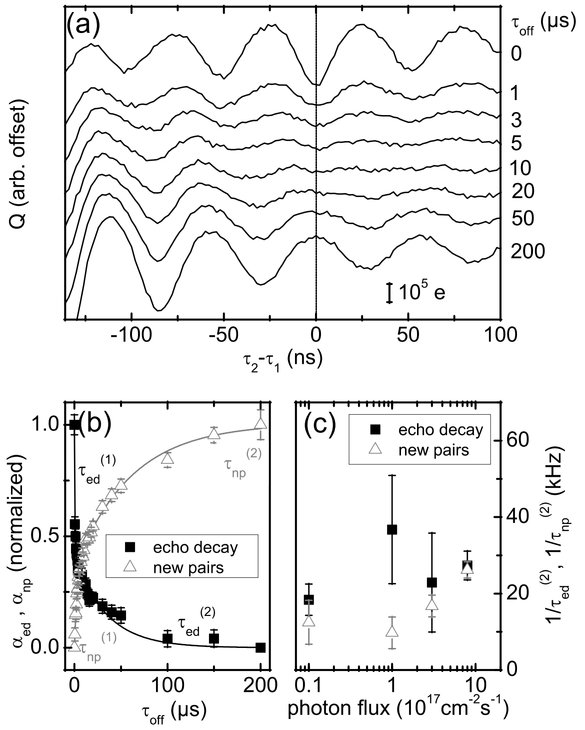

Figure C.5.: Results of the pEDMR rotary echo experiment. The experimental conditions are the same like for the previously shown pEDMR results. (a) Charge Q resulting from the integration of the current change between 3 and 19 µs after the second mw pulse as a function of the length of pulse 2. The individual curves correspond to different values of τ_{off} as indicated on the right side of the plot. The sensitivity of the measurement can be estimated from the bar that represents the charge of 10^5 electrons. The condition where the maximum refocusing of the spins occurs ($\tau_1 = \tau_2$) is marked by the dotted vertical line. (b) Coefficients α_{ed} and α_{np} representing the contributions to the signal due to echo decay and during τ_{off} generated precursor pairs, respectively. These coefficients were extracted from the data displayed in (a) with a procedure described in the text. The solid lines show best fits using two biexponential functions for the description of the echo decay as well as the signal caused by new spin pairs as a function of τ_{off}. For the four time constants as displayed next to the fit curves we obtain $\tau_{ed}^{(1)} = (0.46 \pm 0.06)$ µs, $\tau_{ed}^{(2)} = (35 \pm 3)$ µs, $\tau_{np}^{(1)} = (2.9 \pm 0.3)$ µs and $\tau_{np}^{(2)} = (60 \pm 6)$ µs. (c) Rate coefficients (inverse of the slow time constants $\tau_{ed}^{(2)}$ and $\tau_{np}^{(2)}$) for several light intensity levels. To obtain these data points, the laser power was varied between 5 and 400 mW corresponding to a photon flux between approx. 10^{16} and $8 \times 10^{17}\,\mathrm{cm}^{-2}\,\mathrm{s}^{-1}$.

After determining these parameters by a least square fit, $Q(\tau_2)$ for each value of τ_{off} can be interpreted as a superposition of both contributions Q_{ed} and Q_{np}. Using this phenomenological approach, the EDMR echo signal for each τ_{off} can be described by

$$Q(\tau_2) = \alpha_{ed} \cdot Q_{ed} + \alpha_{np} \cdot Q_{np} + C \tag{C.3}$$

with Q_{ed} and Q_{np} being the contributions that arise from echo decay and new spin pairs which are given by the expressions in equations C.1 and C.2. The parameters α_{ed} (echo decay determined by spin pair annihilation) and α_{np} (signal caused by generation of new pairs) are the respective prefactors that weight the two contributions. C is an additional constant offset.

Thus, by determining the parameters α_{ed} and α_{np} from a fit to the experimentally obtained data for τ_{off} between 0 and 200 µs, a disentanglement of the contributions of spin pair annihilation and precursor pair generation can be achieved. Fig. C.5b displays these values as a function of τ_{off}. The solid lines represent fits with functions describing a biexponential decay and increase with time constants $\tau_{ed}^{(1)}$, $\tau_{ed}^{(2)}$ and $\tau_{np}^{(1)}$, $\tau_{np}^{(2)}$, respectively. For the light intensity used in this experiment we find $\tau_{ed}^{(1)} = (0.46 \pm 0.06)$ µs, $\tau_{ed}^{(2)} = (35 \pm 3)$ µs, $\tau_{np}^{(1)} = (2.9 \pm 0.3)$ µs and $\tau_{np}^{(2)} = (60 \pm 6)$ µs.

Note that the equations for $Q(\tau_2)$ as given above represent only a phenomenological description of the echo signal which is valid for small spin couplings. A more precise expression taking into account the coupling of the spin pairs can be found in Ref. [34]. Note further that the good agreement between the biexponential fits and the experimentally found dependence of α_{ed} and α_{np} on τ_{off} does not exclude other models which can correctly describe the experimental data. Reasonably good fits can also be achieved when assuming a distribution of spin pair annihilation and formation rates which results in a stretched exponential behaviour. This is anticipated since stretched exponentials are convolutions of more than two exponentials used for the fit with a biexponential decay.

Fig. C.5c shows the inverse of the slow time constants, namely the rate coefficients $r_{ed}^{(2)} = 1/\tau_{ed}^{(2)}$ and $r_{np}^{(2)} = 1/\tau_{np}^{(2)}$, obtained from similar measurements carried out at different light intensities. Changing of the photon flux was accomplished by adjusting the laser power. Thereby, the generation rate of free charge carriers (not necessarily the precursor pair generation rate) could be varied. Surprisingly, we observe that neither the time constant related to the generation process, nor the time constant describing the echo decay change significantly, although the photon flux was varied over almost two orders of magnitude (see

Fig. C.5c). We have restricted this analysis to the slow time constants (with upper index 2) because the smallest value of τ_{off} used in this study was 500 ns and thus too long to deduce reliable values for the fast time constants $\tau_{ed}^{(1)}$ and $\tau_{np}^{(1)}$ which are indispensable for a thorough analysis. Note that the observation of only weak light intensity dependence and therefore only weak charge carrier density dependence can be understood by pair formation at defect sites (following Shockley, Read and Hall) when the charge carrier generation rate is high enough to saturate almost all defects in the steady state. As the pair generation rate will approach the pair decay rate under these conditions, the carrier density will only slightly influence the carrier capture and thus the pair formation.

C.6. Discussion and conclusion

The Rabi oscillations shown in Fig. C.4 decay exponentially with a time constant of approximately 100 ns. That is significantly smaller than $\tau_{ed}^{(1)} = (0.46 \pm 0.06)$ µs, i.e. the fastest time constant describing the echo decay. This is in accordance with the finding from a previous study [35] that the damping of the oscillations is mainly caused by Rabi dephasing due to a distribution of g values or B_1, whereas the effect of annihilation of spin pairs plays only a minor role on the timescale of the mw pulse (the maximum pulse length for the data shown in Fig. C.4 was approx. 500 ns). Hence, refocusing of spins with an echo experiment is possible and thus, the requirement for the application of the presented rotary echo experiment is fulfilled.

The contributions to the echo signal caused by refocused spin pairs (given by α_{ed}) and during τ_{off} generated pairs (given by α_{np}) can clearly be separated by taking advantage of the phase difference between the corresponding pEDMR signals. The dependence of both parameters on τ_{off} can be approximated when assuming two biexponential functions, which might indicate that both spin pair annihilation and generation are determined by at least two different processes each. In the case of τ_{ed}, two time constants appear if the annihilation rate out of pure triplet states $|\uparrow\uparrow\rangle$ and $|\downarrow\downarrow\rangle$ is different from the rate out of states $|\uparrow\downarrow\rangle$ and $|\downarrow\uparrow\rangle$ with mixed symmetry [34]. These rates are the same that enter the expressions for the pEDMR transients. However, as indicated in Fig. C.3b, the shape of pEDMR transients can be affected by spin-independent influences such as RC constants of the detection electronics or the sample itself, even when there is no change in the dynamics of the spin-dependent processes. While the time constants extracted from pEDMR transients show a strong dependence on the photon flux (see Fig. C.3b), the time constants deduced from the echo experiment are only slightly affected (cf. Fig. C.5c) although the laser power was varied over almost two orders of magnitude. Taking into account that the concentration of electrons in the conduction band of the amorphous silicon is approximately proportional to the photon flux [209], the pEDMR signal shows no pronounced dependence on the the concentration of conduction electrons. For a quantitative analysis of the fast echo decay, a more detailed study of the signal at small waiting times ($\tau_{\mathrm{off}} < 500$ ns) is needed, particularly to evaluate the influence of Larmor dephasing and to distinguish between different models (biexponential increase/decay or stretched exponential) that could explain echo decay and spin pair generation in accordance with the presented experimental results. It shall be pointed out that the independence of the precursor pair generation and decay times could indicate that both rates are density of state limited processes in contrast to a charge carrier density limited processes.

The above interpretation of the experimental results is based on the assumption that the signal Q_{np} is solely determined by spin pairs that were indeed generated during τ_{off}. This assumption is clearly justified when the first pulse is strong enough to excite the whole resonance line. However, due to experimental constraints we were not able to excite the whole line when using a flip angle of $\Omega\tau_1 = 5\pi$ as we did in the experiment. In our case, we used $\tau_1 = 136$ ns for the first pulse. The 'natural' line width of the EDMR resonance, i.e. the line width one obtains without artificial power broadening (at low B_1) is ≈ 1.1 mT. From a comparison of this value with the excitation width that results from τ_1 it is apparent that only $\approx 38\%$ of the resonance line is excited. Consequently, spin pairs from the part of the spectrum which is not in resonance during the first pulse might become resonant during τ_{off} by spectral diffusion [174] and thus also contribute to Q_{np}. Hence, spins that are excited can change the local field (through dipolar interaction) at the position of an initially not excited spin. Since dipolar interaction strongly depends on the distance between the respective spins, we would expect this effect to exhibit a strong dependence on the spin concentration in the tail states which in turn depends on the light intensity. This is not observed in the experiments. Other forms of spectral or instantaneous diffusion could, in principle, influence the the echo decay signal (Q_{ed}), but not Q_{np}. Moreover, we want to emphasize that spectral diffusion does only marginally influence spin lattice relaxation and as the detected rotary echo decay is spin-lattice relaxation dependent [34], we anticipate that spectral diffusion does not affect the generation rates extracted from the echo experiment.

The connection between experimentally observed EDMR signals and their microscopic origin is not always apparent because different processes such as spin-dependent recombination, hopping transport and scattering can provoke similar signals [131, 9, 210] if they involve paramagnetic centers with identical or similar g values. Independent of the microscopic mechanism, the echo experiment opens the possibility to study spin pair generation provided that the change in conductivity is indeed influenced by spin pairs. This is especially relevant for organic semiconductors, where fundamentally different models for the formation of polaron (spin) pairs exist [97, 211]. It has recently been demonstrated that pEDMR can successfully applied to organic light-emitting diodes [187] to measure Rabi oscillations, which is the basis for the rotary echo experiment.

For the quantitative description of pEDMR transients, spin pair generation is usually taken into account in the form of a constant rate that is equal for all four eigenstates of the spin pair [34, 35]. However, there are indications that, at least in some systems, the generation rate could be different for the pure triplet states and the states with mixed symmetry [212]. Thus, the rotary echo experiment could be used to test the validity of this general assumption.

C.7. Summary

In summary, we have demonstrated an electrically detected rotary echo experiment which allows the observation of precursor pair formation of spin-dependent electronic transitions through localized states in semiconductors. We have applied the rotary echo experiment to a heterostructure solar cell in order to analyse the influence of spin pair generation on the pEDMR signal. No significant influence of the spin pair generation rate on the light intensity was found for the case of a hopping process via conduction band tail and phosphorus states in a 20 nm thick layer of amorphous silicon.

Bibliography

[1] CHAPIN, D. M. ; FULLER, C. S. ; PEARSON, G. L.: A New Silicon P-N Junction Photocell for Converting Solar Radiation into Electrical Power. In: *J. Appl. Phys.* 25 (1954), no. 5, p. 676–677

[2] GREEN, M. A. ; EMERY, K. ; HISHIKAWA, Y. ; WARTA, W.: Solar cell efficiency tables (Version 34). In: *Prog. Photovol.: Res. Appl.* 17 (2009), no. 5, p. 320–326

[3] ZHAO, J. H. ; WANG, A. H. ; GREEN, M. A. ; FERRAZZA, F.: 19.8% efficient "honeycomb" textured multicrystalline and 24.4% monocrystalline silicon solar cells. In: *Appl. Phys. Lett.* 73 (1998), no. 14, p. 1991–1993

[4] SPAETH, J.-M. ; OVERHOF, H.: *Point defects in semiconductors and insulators : determination of atomic and electronic structure from paramagnetic hyperfine interactions*. Berlin ; New York : Springer, 2003

[5] HONIG, A.: Neutral-Impurity Scattering and Impurity Zeeman Spectroscopy in Semiconductors Using Highly Spin-Polarized Carriers. In: *Phys. Rev. Lett.* 17 (1966), no. 4, p. 186–188

[6] MAXWELL, R. ; HONIG, A.: Neutral-Impurity Scattering Experiments in Silicon with Highly Spin-Polarized Electrons. In: *Phys. Rev. Lett.* 17 (1966), no. 4, p. 188–190

[7] SCHMIDT, J. ; SOLOMON, I.: Modulation De La Photoconductivite Dans Le Silicium a Basse Temperature Par Resonance Magnetique Electronique Des Impuretes Peu Profondes. In: *Compt. Rend. Acad. Sci. B* 263 (1966), no. 2, p. 169–172

[8] LEPINE, D. J.: Spin-Dependent Recombination on Silicon Surface. In: *Phys. Rev. B* 6 (1972), no. 2, p. 436–441

[9] STUTZMANN, M. ; BRANDT, M. S. ; BAYERL, M. W.: Spin-dependent processes in amorphous and microcrystalline silicon: a survey. In: *J. Non-Cryst. Solids* 266-269 (2000), p. 1–22

[10] Boehme, C. ; Lips, K.: Time domain measurement of spin-dependent recombination. In: *Appl. Phys. Lett.* 79 (2001), no. 26, p. 4363–4365

[11] Boehme, C. ; Lips, K.: Electrical detection of spin coherence in silicon. In: *Phys. Rev. Lett.* 91 (2003), no. 24, p. 246603

[12] Shockley, W. ; Queisser, H. J.: Detailed Balance Limit of Efficiency of P-N Junction Solar Cells. In: *J. Appl. Phys.* 32 (1961), no. 3, p. 510–519

[13] Swanson, R. M.: Approaching the 29% limit efficiency of silicon solar cells. In: *31st IEEE Photovoltaic Specialists Conference*. Lake Buena Vista, FL : IEEE, 2005, p. 889–894

[14] Maruyama, E. ; Terakawa, A. ; Taguchi, M. ; Yoshimine, Y. ; Ide, D. ; Baba, T. ; Shima, M. ; Sakata, H. ; Tanaka, M.: Sanyo's challenges to the development of high-efficiency HIT solar cells and the expansion of HIT business. In: *Conference Record of the 2006 IEEE 4th World Conference on Photovoltaic Energy Conversion, Vols 1 and 2* (2006), p. 1455–1460

[15] Angermann, H. ; Henrion, W. ; Rebien, M. ; Roseler, A.: Wet-chemical preparation and spectroscopic characterization of Si interfaces. In: *Applied Surface Science* 235 (2004), no. 3, p. 322–339

[16] Das, U. K. ; Burrows, M. Z. ; Lu, M. ; Bowden, S. ; Birkmire, R. W.: Surface passivation and heterojunction cells on Si (100) and (111) wafers using dc and rf plasma deposited Si:H thin films. In: *Appl. Phys. Lett.* 92 (2008), p. 063504

[17] De Wolf, S. ; Kondo, M.: Boron-doped a-Si:H/c-Si interface passivation: Degradation mechanism. In: *Appl. Phys. Lett.* 91 (2007), p. 112109

[18] De Wolf, S. ; Olibet, S. ; Ballif, C.: Stretched-exponential a-Si:H/c-Si interface recombination decay. In: *Appl. Phys. Lett.* 93 (2008), p. 032101

[19] Schmidt, M. ; Schoepke, A. ; Korte, L. ; Milch, O. ; Fuhs, W.: Density distribution of gap states in extremely thin a-Si:H layers on crystalline silicon wafers. In: *J. Non-Cryst. Solids* 338-40 (2004), p. 211–214

[20] Korte, L. ; Laades, A. ; Schmidt, M.: Electronic states in a-Si:H/c-Si heterostructures. In: *J. Non-Cryst. Solids* 352 (2006), no. 9-20, p. 1217–1220

[21] Lang, D. V. ; Cohen, J. D. ; Harbison, J. P.: Measurement of the Density of Gap States in Hydrogenated Amorphous-Silicon by Space-Charge Spectroscopy. In: *Phys. Rev. B* 25 (1982), no. 8, p. 5285–5320

[22] GUDOVSKIKH, A. S. ; KLEIDER, J. P. ; DAMON-LACOSTE, J. ; CABARROCAS, P. R. I. ; VESCHETTI, Y. ; MULLER, J. C. ; RIBEYRON, P. J. ; ROLLAND, E.: Interface properties of a-Si:H/c-Si heterojunction solar cells from admittance spectroscopy. In: *Thin Solid Films* 511 (2006), p. 385–389

[23] CARLSON, D. E. ; WRONSKI, C. R.: Amorphous Silicon Solar Cell. In: *Appl. Phys. Lett.* 28 (1976), no. 11, p. 671–673

[24] STREET, R. A.: *Hydrogenated amorphous silicon*. Cambridge ; New York : Cambridge University Press, 1991

[25] STAEBLER, D. L. ; WRONSKI, C. R.: Reversible Conductivity Changes in Discharge-Produced Amorphous Si. In: *Appl. Phys. Lett.* 31 (1977), no. 4, p. 292–294

[26] SHAH, A. ; MEIER, J. ; VALLAT-SAUVAIN, E. ; WYRSCH, N. ; KROLL, U. ; DROZ, C. ; GRAF, U.: Material and solar cell research in microcrystalline silicon. In: *Sol. Energy Mat. Sol. Cells* 78 (2003), no. 1-4, p. 469–491

[27] RECH, B. ; ROSCHEK, T. ; REPMANN, T. ; MÜLLER, J. ; SCHMITZ, R. ; APPENZELLER, W.: Microcrystalline silicon for large area thin film solar cells. In: *Thin Solid Films* 427 (2003), no. 1-2, p. 157–165

[28] TZOLOV, M. ; FINGER, F. ; CARIUS, R. ; HAPKE, P.: Optical and transport studies on thin microcrystalline silicon films prepared by very high frequency glow discharge for solar cell applications. In: *J. Appl. Phys.* 81 (1997), no. 11, p. 7376–7385

[29] BRABEC, C. J. ; SARICIFTCI, N. S. ; HUMMELEN, J. C.: Plastic solar cells. In: *Adv. Funct. Mater.* 11 (2001), no. 1, p. 15–26

[30] JANSSEN, R. A. J. ; HUMMELEN, J. C. ; SARICIFTI, N. S.: Polymer-fullerene bulk heterojunction solar cells. In: *MRS Bulletin* 30 (2005), no. 1, p. 33–36

[31] SCHARBER, M. C.: *Magnetic Resonance Studies on Conjugated Polymers and Conjugated Polymer Fullerene Mixtures*, Universität Linz, Diss., 2002

[32] SCHARBER, M. C. ; SCHULTZ, N. A. ; SARICIFTCI, N. S. ; BRABEC, C. J.: Optical- and photocurrent-detected magnetic resonance studies on conjugated polymer/fullerene composites. In: *Phys. Rev. B* 67 (2003), no. 8, p. 085202

[33] BÖHME, C.: *Dynamics of spin-dependent charger carrier recombination*, Philipps Universität Marburg, Diss., 2002

[34] Boehme, C. ; Lips, K.: Theory of time-domain measurement of spin-dependent recombination with pulsed electrically detected magnetic resonance. In: *Phys. Rev. B* 68 (2003), no. 24, p. 245105

[35] Boehme, C. ; Lips, K.: The investigation of charge carrier recombination and hopping transport with pulsed electrically detected magnetic resonance techniques. In: Baranovski, S. (Ed.): *Charge transport in disordered solids with applications in electronics*. Chichester, England ; Hoboken, NJ : Wiley, 2006, p. 179–219

[36] Rajevac, V. ; Boehme, C. ; Michel, C. ; Gliesche, A. ; Lips, K. ; Baranovskii, S. D. ; Thomas, P.: Transport and recombination through weakly coupled localized spin pairs in semiconductors during coherent spin excitation. In: *Phys. Rev. B* 74 (2006), no. 24, p. 245206

[37] Gliesche, A. ; Michel, C. ; Rajevac, V. ; Lips, K. ; Baranovskii, S. D. ; Gebhard, F. ; Boehme, C.: Effect of exchange coupling on coherently controlled spin-dependent transition rates. In: *Phys. Rev. B* 77 (2008), no. 24, p. 245206

[38] Kishimoto, N. ; Morigaki, K. ; Murakami, K.: Conductivity Change Due to Electron-Spin Resonance in Amorphous Si-Au System. In: *J. Phys. Soc. Jpn.* 50 (1981), no. 6, p. 1970–1977

[39] Solomon, I. ; Biegelsen, D. ; Knights, J. C.: Spin-Dependent Photoconductivity in N-Type and P-Type Amorphous Silicon. In: *Solid State Commun.* 22 (1977), no. 8, p. 505–508

[40] Schiff, E. A.: Spin polarization effects in the photoconductivity of a-Si:H. In: *AIP Conf. Proc.* 73 (1981), no. 1, p. 233–237

[41] Street, R. A.: Spin-Dependent Photoconductivity in Undoped a-Si:H. In: *Philos. Mag. B* 46 (1982), no. 3, p. 273–278

[42] Solomon, I.: Spin-Dependent Recombination in a Silicon Para-Normal Junction. In: *Solid State Commun.* 20 (1976), no. 3, p. 215–217

[43] Rong, F. C. ; Gerardi, G. J. ; Buchwald, W. R. ; Poindexter, E. H. ; Umlor, M. T. ; Keeble, D. J. ; Warren, W. L.: Electrically Detected Magnetic-Resonance of a Transition-Metal Related Recombination Center in Si P-N Diodes. In: *Appl. Phys. Lett.* 60 (1992), no. 5, p. 610–612

[44] KAPLAN, D. ; SOLOMON, I. ; MOTT, N. F.: Explanation of Large Spin-Dependent Recombination Effect in Semiconductors. In: *Journ. de Phys. Lettr.* 39 (1978), no. 4, p. L51–L54

[45] ATHERTON, N. M.: *Principles of electron spin resonance*. New York : Ellis Horwood : PTR Prentice Hall, 1993

[46] ABRAGAM, A. ; BLEANEY, B.: *Electron paramagnetic resonance of transition ions*. Oxford : Clarendon P., 1970

[47] FREED, J. H. ; PEDERSEN, J. B.: The Theory of Chemically Induced Dynamic Spin Polarization. In: *Adv. Magn. Reson.* 8 (1976), p. 1–84

[48] TANG, J. ; NORRIS, J. R.: Theoretical Calculations of Microwave Effects on the Triplet Yield in Photosynthetic Reaction Centers. In: *Chem. Phys. Lett.* 94 (1983), no. 1, p. 77–80

[49] BUCKLEY, C. D. ; HUNTER, D. A. ; HORE, P. J. ; MCLAUCHLAN, K. A.: Electron-Spin-Resonance of Spin-Correlated Radical Pairs. In: *Chem. Phys. Lett.* 135 (1987), no. 3, p. 307–312

[50] BITTL, R. ; KOTHE, G.: Transient Epr of Radical Pairs in Photosynthetic Reaction Centers - Prediction of Quantum Beats. In: *Chem. Phys. Lett.* 177 (1991), no. 6, p. 547–553

[51] KUBAREV, S. J. ; PSHENICHNOV, E. A.: The effect of high frequency magnetic fields on the recombination of radicals. In: *Chem. Phys. Lett.* 28 (1974), no. 1, p. 66–67

[52] HABERKORN, R. ; DIETZ, W.: Theory of Spin-Dependent Recombination in Semiconductors. In: *Solid State Commun.* 35 (1980), no. 6, p. 505–508

[53] HOFF, A. J.: *Advanced EPR : applications in biology and biochemistry*. Amsterdam ; New York, NY, U.S.A. : Elsevier, 1989

[54] EICKELKAMP, T. ; ROTH, S. ; MEHRING, M.: Electrically detected magnetic resonance in photoexcited fullerenes. In: *Mol. Phys.* 95 (1998), no. 5, p. 967–972

[55] HOEHNE, F.: *Multi-Frequency Spectroscopy of Phosphorus Donors at the Si/SiO*$_2$*-Interface*, Technische Universität München, Diplomarbeit, 2007

[56] HUEBL, H.-G.: *Coherent manipulation and electrical detection of phosphorus donor spins in silicon*, Technische Universität München, Diss., 2007

[57] MOVAGHAR, B. ; RIES, B. ; SCHWEITZER, L.: Theory of the Resonant and Non-Resonant Photoconductivity Changes in Amorphous-Silicon. In: *Philos. Mag. B* 41 (1980), no. 2, p. 159–167

[58] RONG, F. C. ; BUCHWALD, W. R. ; POINDEXTER, E. H. ; WARREN, W. L. ; KEEBLE, D. J.: Spin-Dependent Shockley-Read Recombination of Electrons and Holes in Indirect-Band-Gap Semiconductor P-N-Junction Diodes. In: *Solid-State Electron.* 34 (1991), no. 8, p. 835–841

[59] XIONG, Z. ; MILLER, D. J.: General Expression for the Electrically Detected Magnetic-Resonance Signal from Semiconductors. In: *Appl. Phys. Lett.* 63 (1993), no. 3, p. 352–354

[60] LIPS, K. ; LERNER, C. ; FUHS, W.: Semiclassical model of electrically detected magnetic resonance in undoped a-Si:H. In: *J. Non-Cryst. Solids* 200 (1996), p. 267–270

[61] BARABANOV, A. V. ; LVOV, V. A. ; TRETYAK, O. V.: About the mechanisms of spin-dependent recombination in semiconductors. In: *phys. stat. sol. (b)* 207 (1998), no. 2, p. 419–427

[62] BEHRENDS, J. ; LIPS, K. ; BOEHME, C.: Observation of precursor pair formation of recombining charge carriers. In: *Phys. Rev. B* 80 (2009), p. 045207

[63] KUROBE, A. ; KAMIMURA, H.: Correlation-Effects on Variable Range Hopping Conduction and the Magnetoresistance. In: *J. Phys. Soc. Jpn.* 51 (1982), no. 6, p. 1904–1913

[64] MOVAGHAR, B. ; SCHWEITZER, L.: Model for Anomalous Magnetoresistance in Amorphous-Semiconductors. In: *J. Phys. C* 11 (1978), no. 1, p. 125–135

[65] KUROBE, A. ; KAMIMURA, H.: Theory of Magnetoresistance in Amorphous-Semiconductors. In: *J. Non-Cryst. Solids* 59-60 (1983), p. 41–44

[66] KAMIMURA, H. ; AOKI, H.: *The physics of interacting electrons in disordered systems*. Oxford New York : Clarendon Press ; Oxford University Press, 1989

[67] EPHRON, D. ; BEASLEY, M. R. ; BAHLOULI, H. ; MATVEEV, K. A.: Correlated Hopping through Thin Disordered Insulators. In: *Phys. Rev. B* 49 (1994), no. 4, p. 2989–2992

[68] STUKE, J.: Recent Results on Hydrogenated Amorphous-Silicon. In: *Ann. Rev. Mat. Sci.* 15 (1985), p. 79–102

[69] McCamey, D. R. ; Morley, G. W. ; Seipel, H. A. ; Brunel, L. C. ; van Tol, J. ; Boehme, C.: Spin-dependent processes at the crystalline Si-SiO$_2$ interface at high magnetic fields. In: *Phys. Rev. B* 78 (2008), no. 4, p. 045303

[70] Morley, G. W. ; McCamey, D. R. ; Seipel, H. A. ; Brunel, L. C. ; van Tol, J. ; Boehme, C.: Long-Lived Spin Coherence in Silicon with an Electrical Spin Trap Readout. In: *Phys. Rev. Lett.* 101 (2008), no. 20, p. 207602

[71] McCamey, D. R. ; van Tol, J. ; Morley, G. W. ; Boehme, C.: Fast Nuclear Spin Hyperpolarization of Phosphorus in Silicon. In: *Phys. Rev. Lett.* 102 (2009), no. 2, p. 027601

[72] Shockley, W. ; Read, W. T.: Statistics of the Recombinations of Holes and Electrons. In: *Phys. Rev.* 87 (1952), no. 5, p. 835–842

[73] Behrends, J. ; Schnegg, A. ; Boehme, C. ; Haas, S. ; Stiebig, H. ; Finger, F. ; Rech, B. ; Lips, K.: Recombination and transport in microcrystalline pin solar cells studied with pulsed electrically detected magnetic resonance. In: *J. Non-Cryst. Solids* 354 (2008), no. 19-25, p. 2411–2415

[74] Stich, B. ; Greulich-Weber, S. ; Spaeth, J. M.: Electrical Detection of Electron-Paramagnetic-Resonance - New Possibilities for the Study of Point-Defects. In: *J. Appl. Phys.* 77 (1995), no. 4, p. 1546–1553

[75] Stegner, A. R. ; Boehme, C. ; Huebl, H. ; Stutzmann, M. ; Lips, K. ; Brandt, M. S.: Electrical detection of coherent ^{31}P spin quantum states. In: *Nature Phys.* 2 (2006), no. 12, p. 835–838

[76] Galler, B.: *Charge Transport and Spin-Dependent Recombination at the Si/SiO$_2$-Interface*, Technische Universität München, Diplomarbeit, 2008

[77] Dersch, H. ; Schweitzer, L. ; Stuke, J.: Recombination Processes in a-Si:H: Spin-Dependent Photoconductivity. In: *Phys. Rev. B* 28 (1983), no. 8, p. 4678–4684

[78] Herring, T. W. ; Lee, S. Y. ; McCamey, D. R. ; Taylor, P. C. ; Lips, K. ; Hu, J. ; Zhu, F. ; Madan, A. ; Boehme, C.: Experimental discrimination of geminate and non-geminate recombination in a-Si:H. In: *Phys. Rev. B* 79 (2009), no. 19, p. 195205

[79] Kanschat, P. ; Lips, K. ; Fuhs, W.: Identification of non-radiative recombination paths in microcrystalline silicon (μc-Si:H). In: *J. Non-Cryst. Solids* 266 (2000), p. 524–528

[80] VRANCH, R. L. ; HENDERSON, B. ; PEPPER, M.: Spin-Dependent Pair Generation at Si/SiO_2 Interfaces. In: *Appl. Phys. Lett.* 53 (1988), no. 14, p. 1299–1301

[81] DEPINNA, S. P. ; CAVENETT, B. C. ; SUSSMANN, R.: Odmr Investigation of Recombination Processes in a-Si_xC_{1-x}:H. In: *Philos. Mag. B* 47 (1983), no. 5, p. L51–L55

[82] MORIGAKI, K.: Recombination Mechanisms in Amorphous-Semiconductors Deduced from Resonance Measurements. In: *J. Non-Cryst. Solids* 77-8 (1985), p. 583–592

[83] YOSHIDA, M. ; MORIGAKI, K.: Triplet Exciton Recombination in a-Si:H as Elucidated by Optically Detected Magnetic-Resonance Experiments. In: *Philos. Mag. B* 54 (1986), no. 2, p. L63–L66

[84] SINGH, J. ; SHIMAKAWA, K.: *Advances in amorphous semiconductors*. London ; New York : Taylor & Francis, 2003

[85] AOKI, T. ; SHIMIZU, T. ; KOMEDOORI, S. ; KOBAYASHI, S. ; SHIMAKAWA, K.: Coexistence of geminate and non-geminate recombination in a-Si:H and a-Ge:H observed by quadrature frequency resolved spectroscopy. In: *J. Non-Cryst. Solids* 338-40 (2004), p. 456–459

[86] REHM, W. ; FISCHER, R.: Fast Radiationless Recombination in Amorphous Silicon. In: *phys. stat. sol. (b)* 94 (1979), no. 2, p. 595–602

[87] STREET, R. A.: Recombination in a-Si:H - Auger Effects and Non-Geminate Recombination. In: *Phys. Rev. B* 23 (1981), no. 2, p. 861–868

[88] STREET, R. A.: Luminescence and Recombination in Hydrogenated Amorphous Silicon. In: *Adv. in Phys.* 30 (1981), no. 5, p. 593–676

[89] AMBROS, S. ; CARIUS, R. ; WAGNER, H.: Lifetime Distribution in a-Si:H - Geminate-Process, Nongeminate-Process and Auger-Process. In: *J. Non-Cryst. Solids* 137 (1991), p. 555–558

[90] SCHMID, W.: Auger Lifetimes for Excitons Bound to Neutral Donors and Acceptors in Si. In: *phys. stat. sol. (b)* 84 (1977), no. 2, p. 529–540

[91] LIPS, K. ; FUHS, W.: Transport and Recombination in Amorphous P-I-N-Type Solar-Cells Studied by Electrically Detected Magnetic-Resonance. In: *J. Appl. Phys.* 74 (1993), no. 6, p. 3993–3999

[92] YANG, A. ; STEGER, M. ; KARAISKAJ, D. ; THEWALT, M. L. W. ; CARDONA, M. ; ITOH, K. M. ; RIEMANN, H. ; ABROSIMOV, N. V. ; CHURBANOV, M. F. ; GUSEV, A. V. ; BULANOV, A. D. ; KALITEEVSKII, A. K. ; GODISOV, O. N. ; BECKER, P. ; POHL, H. J. ; AGER, J. W. ; HALLER, E. E.: Optical detection and ionization of donors in specific electronic and nuclear spin states. In: *Phys. Rev. Lett.* 97 (2006), no. 22, p. 227401

[93] STEGNER, A. R. ; PEREIRA, R. N. ; KLEIN, K. ; LECHNER, R. ; DIETMUELLER, R. ; BRANDT, M. S. ; STUTZMANN, M. ; WIGGERS, H.: Electronic transport in phosphorus-doped silicon nanocrystal networks. In: *Phys. Rev. Lett.* 100 (2008), no. 2, p. 026803

[94] SAKURAI, J. J. ; TUAN, S. F.: *Modern quantum mechanics*. Rev. Reading, Mass. : Addison-Wesley Pub., 1994

[95] ARAKI, Y. ; MAEDA, K. ; MURAI, H.: Observation of two-spin controlling of a radical pair by pulsed irradiation of microwave monitored by absorption detected magnetic resonance. In: *Chem. Phys. Lett.* 332 (2000), no. 5-6, p. 515–520

[96] GORELIK, V. R. ; MAEDA, K. ; YASHIRO, H. ; MURAI, H.: Microwave-induced quantum beats in micellized radical pairs under spin-locking conditions. In: *J. Phys. Chem. A* 105 (2001), no. 34, p. 8011–8017

[97] FRANKEVICH, E. L. ; LYMAREV, A. A. ; SOKOLIK, I. ; KARASZ, F. E. ; BLUMSTENGEL, S. ; BAUGHMAN, R. H. ; HORHOLD, H. H.: Polaron-Pair Generation in Poly(Phenylene Vinylenes). In: *Phys. Rev. B* 46 (1992), no. 15, p. 9320–9324

[98] BOBBERT, P. A. ; NGUYEN, T. D. ; OOST, F. W. A. ; KOOPMANS, B. ; WOHLGENANNT, M.: Bipolaron mechanism for organic magnetoresistance. In: *Phys. Rev. Lett.* 99 (2007), no. 21, p. 216801

[99] STOLL, S. ; SCHWEIGER, A.: EasySpin, a comprehensive software package for spectral simulation and analysis in EPR. In: *J. Magn. Reson.* 178 (2006), no. 1, p. 42–55

[100] THOMSEN, E. A. ; KEEBLE, D. J. ; LOCHAB, B. ; BURN, P. L. ; EL-MKAMI, H. ; SAMUEL, I. D. W.: Photoinduced charge separation in poly(1,4-phenylenevinylene) derivatives studied by electron paramagnetic resonance. In: *Org. Electron.* 9 (2008), no. 5, p. 809–815

[101] UMEDA, T. ; YAMASAKI, S. ; ISOYA, J. ; TANAKA, K.: Electron-spin-resonance center of dangling bonds in undoped a-Si:H. In: *Phys. Rev. B* 59 (1999), no. 7, p. 4849–4857

[102] MICHEL, C. ; GLIESCHE, A. ; BARANOVSKII, S. D. ; LIPS, K. ; GEBHARD, F. ; BOEHME, C.: Influence of disorder on electrically and optically detected electron spin nutation. In: *Phys. Rev. B* 79 (2009), no. 5, p. 052201

[103] TADJIKOV, B. M. ; ASTASHKIN, A. V. ; SAKAGUCHI, Y.: Quantum beats of the reaction yield induced by a pulsed microwave field. In: *Chem. Phys. Lett.* 283 (1998), no. 3-4, p. 179–186

[104] LANGHANKI, B.: *Electron Paramagnetic Resonance of Process-Induced Defects in Silicon*, Universität Paderborn, Diss., 2001

[105] WEGER, M.: Passage Effects in Paramagnetic Resonance Experiments. In: *Bell Syst. Tech. J.* 39 (1960), no. 4, p. 1013–1112

[106] POOLE, C. P.: *Electron spin resonance : a comprehensive treatise on experimental techniques*. 2nd. New York : Wiley, 1983

[107] HAAS, S. ; GORDIJN, A. ; STIEBIG, H.: High speed laser processing for monolithical series connection of silicon thin-film modules. In: *Prog. Photovol.: Res. Appl.* 16 (2008), no. 3, p. 195–203

[108] TANAKA, M. ; TAGUCHI, M. ; MATSUYAMA, T. ; SAWADA, T. ; TSUDA, S. ; NAKANO, S. ; HANAFUSA, H. ; KUWANO, Y.: Development of New a-Si/c-Si Heterojunction Solar-Cells: ACJ-HIT (Artificially Constructed Junction-Heterojunction with Intrinsic Thin-Layer). In: *Jap. J. Appl. Phys. Part 1* 31 (1992), no. 11, p. 3518–3522

[109] SCHMIDT, M. ; ANGERMANN, H. ; CONRAD, E. ; KORTE, L. ; LAADES, A. ; VON MAYDELL, K. ; SCHUBERT, C. ; STANGL, R.: Physical and technological aspects of a-Si:H/c-Si hetero-junction solar cells. In: *Conference Record of the 2006 IEEE 4th World Conference on Photovoltaic Energy Conversion, Vols 1 and 2* (2006), p. 1433–1438 2568

[110] STANGL, R. ; KRIEGEL, M. ; SCHMIDT, M.: AFORS-HET, version 2.2, a numerical computer program for simulation of heterojunction solar cells and measurements. In: *Conference Record of the 2006 IEEE 4th World Conference on Photovoltaic Energy Conversion, Vols 1 and 2* (2006), p. 1350–1353 2568

[111] Korte, L. ; Conrad, E. ; Angermann, H. ; Stangl, R. ; Schmidt, M.: Advances in a-Si:H/c-Si heterojunction solar cell fabrication and characterization. In: *Sol. Energy Mat. Sol. Cells* 93 (2009), no. 6-7, p. 905–910

[112] McCamey, D. R. ; Huebl, H. ; Brandt, M. S. ; Hutchison, W. D. ; McCallum, J. C. ; Clark, R. G. ; Hamilton, A. R.: Electrically detected magnetic resonance in ion-implanted Si:P nanostructures. In: *Appl. Phys. Lett.* 89 (2006), no. 18, p. 182115

[113] Huebl, H. ; Hoehne, F. ; Grolik, B. ; Stegner, A. R. ; Stutzmann, M. ; Brandt, M. S.: Spin echoes in the charge transport through phosphorus donors in silicon. In: *Phys. Rev. Lett.* 100 (2008), no. 17, p. 177602

[114] Kane, B. E.: A silicon-based nuclear spin quantum computer. In: *Nature* 393 (1998), no. 6681, p. 133–137

[115] Stesmans, A. ; Afanas'ev, V. V.: Electron spin resonance features of interface defects in thermal (100)Si/SiO$_2$. In: *J. Appl. Phys.* 83 (1998), no. 5, p. 2449–2457

[116] Nishi, Y.: Study of Silicon-Silicon Dioxide Structure by Electron Spin Resonance .1. In: *Japanese Journal of Applied Physics* 10 (1971), no. 1, p. 52–62

[117] Caplan, P. J. ; Poindexter, E. H. ; Deal, B. E. ; Razouk, R. R.: ESR Centers, Interface States, and Oxide Fixed Charge in Thermally Oxidized Silicon Wafers. In: *J. Appl. Phys.* 50 (1979), no. 9, p. 5847–5854

[118] Brower, K. L.: ^{29}Si Hyperfine-Structure of Unpaired Spins at the Si/SiO$_2$ Interface. In: *Appl. Phys. Lett.* 43 (1983), no. 12, p. 1111–1113

[119] Stesmans, A.: Structural Relaxation of P$_b$ Defects at the (111)Si/SiO$_2$ Interface as a Function of Oxidation Temperature - the P$_b$-Generation-Stress Relationship. In: *Phys. Rev. B* 48 (1993), no. 4, p. 2418–2435

[120] Poindexter, E. H. ; Caplan, P. J. ; Deal, B. E. ; Razouk, R. R.: Interface States and Electron-Spin Resonance Centers in Thermally Oxidized (111) and (100) Silicon-Wafers. In: *J. Appl. Phys.* 52 (1981), no. 2, p. 879–884

[121] Kohn, W.: Shallow Impurity States in Silicon and Germanium. In: Seitz, F. (Ed.) ; Turnbull, D. (Ed.): *Solid State Physics* Bd. 5. New York : Academic Press, 1957, p. 257–320

[122] FEHER, G.: Electron Spin Resonance Experiments on Donors in Silicon .1. Electronic Structure of Donors by the Electron Nuclear Double Resonance Technique. In: *Phys. Rev.* 114 (1959), no. 5, p. 1219–1244

[123] ABE, E. ; FUJIMOTO, A. ; ISOYA, J. ; YAMASAKI, S. ; ITOH, K. M.: Line Broadening and Decoherence of Electron Spins in Phosphorus-Doped Silicon Due to Environmental ^{29}Si Nuclear Spins. In: *arXiv:cond-mat/0512404v1* (2005)

[124] FLETCHER, R. C. ; YAGER, W. A. ; PEARSON, G. L. ; HOLDEN, A. N. ; READ, W. T. ; MERRITT, F. R.: Spin Resonance of Donors in Silicon. In: *Phys. Rev.* 94 (1954), no. 5, p. 1392–1393

[125] STEGNER, A.: *Spin properties of phosphorus donors in silicon epilayers*, Technische Universität München, Diplomarbeit, 2005

[126] TYRYSHKIN, A. M. ; LYON, S. A. ; ASTASHKIN, A. V. ; RAITSIMRING, A. M.: Electron spin relaxation times of phosphorus donors in silicon. In: *Phys. Rev. B* 68 (2003), no. 19, p. 193207

[127] LANGHANKI, B. ; GREULICH-WEBER, S. ; SPAETH, J. M. ; MICHEL, J.: Detection of two dangling bond centers with trigonal symmetry at and below a (100) Si/SiO$_2$ interface. In: *Appl. Phys. Lett.* 78 (2001), no. 23, p. 3633–3635

[128] VON MAYDELL, K. ; CONRAD, E. ; SCHMIDT, M.: Efficient silicon heterojunction solar cells based on p- and n-type substrates processed at temperatures < 220 degrees C. In: *Prog. Photovol.: Res. Appl.* 14 (2006), no. 4, p. 289–295

[129] FROITZHEIM, A. M.: *Hetero-Solarzellen aus amorphem und kristallinem Silizium*, Universität Marburg, Diss., 2003

[130] BEHRENDS, J.: *Spinabhängiger Transport und Rekombination in Silizium-Heterodioden*, Universität Oldenburg, Diplomarbeit, 2006

[131] BOEHME, C. ; BEHRENDS, J. ; VON MAYDELL, K. ; SCHMIDT, M. ; LIPS, K.: Investigation of hopping transport in n-a-Si:H/c-Si solar cells with pulsed electrically detected magnetic resonance. In: *J. Non-Cryst. Solids* 352 (2006), no. 9-20, p. 1113–1116

[132] MÜLLER, R. ; KANSCHAT, P. ; AICHBERGER, S. von ; LIPS, K. ; FUHS, W.: Identification of transport and recombination paths in homo and heterojunction silicon solar cells by electrically detected magnetic resonance. In: *J. Non-Cryst. Solids* 266-269 (2000), p. 1124–1128

[133] SCHULZE, T. F.: *private communication*. 2009

[134] TAGUCHI, M. ; SAKATA, H. ; YOSHIMINE, Y. ; MARUYAMA, E. ; TERAKAWA, A. ; TANAKA, M. ; KIYAMA, S.: An approach for the higher efficiency in the HIT cells. In: *Conference Record of the Thirty-First IEEE Photovoltaic Specialists Conference - 2005* (2005), p. 866–871 1822

[135] BRANDT, M. S. ; STUTZMANN, M.: Spin-Dependent Conductivity in Amorphous Hydrogenated Silicon. In: *Phys. Rev. B* 43 (1991), no. 6, p. 5184–5187

[136] LIPS, K. ; SCHÜTTE, S. ; FUHS, W.: Microwave-Induced Resonant Changes in Transport and Recombination in Hydrogenated Amorphous Silicon. In: *Philos. Mag. B* 65 (1992), no. 5, p. 945–959

[137] YOUNG, C. F. ; POINDEXTER, E. H. ; GERARDI, G. J. ; WARREN, W. L. ; KEEBLE, D. J.: Electron paramagnetic resonance of conduction-band electrons in silicon. In: *Phys. Rev. B* 55 (1997), no. 24, p. 16245–16248

[138] KLEIDER, J. P. ; SORO, Y. M. ; CHOUFFOT, R. ; GUDOVSKIKH, A. S. ; CABARROCAS, P. R. I. ; DAMON-LACOSTE, J. ; EON, D. ; RIBEYRON, P. J.: High interfacial conductivity at amorphous silicon/crystalline silicon heterojunctions. In: *J. Non-Cryst. Solids* 354 (2008), no. 19-25, p. 2641–2645

[139] LIPS, K. ; KANSCHAT, P. ; FUHS, W.: Defects and recombination in microcrystalline silicon. In: *Sol. Energy Mat. Sol. Cells* 78 (2003), no. 1-4, p. 513–541

[140] FINGER, F. ; NETO, L. B. ; CARIUS, R. ; DYLLA, T. ; KLEIN, S.: Paramagnetic defects in undoped microcrystalline silicon. In: *phys. stat. sol. (c)* 1 (2004), no. 5, p. 1248–1254

[141] KONDO, M. ; YAMASAKI, S. ; MATSUDA, A.: Microscopic structure of defects in microcrystalline silicon. In: *J. Non-Cryst. Solids* 266 (2000), p. 544–547

[142] STESMANS, A. ; AFANAS'EV, V. V.: Electron spin resonance observation of Si dangling-bond-type defects at the interface of (100) Si with ultrathin layers of SiO_x, Al_2O_3 and ZrO_2. In: *Journal of Physics-Condensed Matter* 13 (2001), no. 28, p. L673–L680

[143] STESMANS, A. ; AFANAS'EV, V. V.: Si dangling-bond-type defects at the interface of (100)Si with ultrathin HfO_2. In: *Appl. Phys. Lett.* 82 (2003), no. 23, p. 4074–4076

[144] KANG, A. Y. ; LENAHAN, P. M. ; CONLEY, J. F. ; SOLANKI, R.: Electron spin resonance study of interface defects in atomic layer deposited hafnium oxide on Si. In: *Appl. Phys. Lett.* 81 (2002), no. 6, p. 1128–1130

[145] MÜLLER, J. ; FINGER, F. ; CARIUS, R. ; WAGNER, H.: Electron spin resonance investigation of electronic states in hydrogenated microcrystalline silicon. In: *Phys. Rev. B* 60 (1999), no. 16, p. 11666–11677

[146] FUHS, W.: Recombination and transport through localized states in hydrogenated amorphous and microcrystalline silicon. In: *J. Non-Cryst. Solids* 354 (2008), no. 19-25, p. 2067–2078

[147] MAI, Y. ; KLEIN, S. ; CARIUS, R. ; STIEBIG, H. ; GENG, X. ; FINGER, F.: Open circuit voltage improvement of high-deposition-rate microcrystalline silicon solar cells by hot wire interface layers. In: *Appl. Phys. Lett.* 87 (2005), no. 7, p. 073503

[148] MEIER, C.: *Aufbau einer Multifrequenz-EDMR zur Untersuchung spinabhängiger Prozesse in Silizium-Dünnschichtsolarzellen*, Freien Universität Berlin, Diplomarbeit, 2009

[149] CARIUS, R. ; FINGER, F. ; BACKHAUSEN, U. ; LUYSBERG, M. ; HAPKE, P. ; HOUBEN, L. ; OTTE, M. ; OVERHOF, H.: Electronic properties of microcrystalline silicon. In: *Amorphous and Microcrystalline Silicon Technology - 1997* 467 (1997), p. 283–294

[150] HASEGAWA, S. ; NARIKAWA, S. ; KURATA, Y.: Electron-Spin-Resonance and Electrical-Properties of P-Doped Microcrystalline Si. In: *Philos. Mag. B* 48 (1983), no. 5, p. 431–447

[151] FINGER, F. ; MÜLLER, J. ; MALTEN, C. ; WAGNER, H.: Electronic states in hydrogenated microcrystalline silicon. In: *Philos. Mag. B* 77 (1998), no. 3, p. 805–830

[152] KONDO, M. ; NISHIMIYA, T. ; SAITO, K. ; MATSUDA, A.: Light induced phenomena in microcrystalline silicon. In: *J. Non-Cryst. Solids* 230 (1998), p. 1031–1035

[153] DE LIMA, M. M. ; TAYLOR, P. C. ; MORRISON, S. ; LEGEUNE, A. ; MARQUES, F. C.: ESR observations of paramagnetic centers in intrinsic hydrogenated microcrystalline silicon. In: *Phys. Rev. B* 65 (2002), no. 23, p. 235324

[154] STUTZMANN, M. ; STREET, R. A.: Donor States in Hydrogenated Amorphous-Silicon and Germanium. In: *Phys. Rev. Lett.* 54 (1985), no. 16, p. 1836–1839

[155] DERSCH, H. ; STUKE, J. ; BEICHLER, J.: Temperature-Dependence of Electron-Spin-Resonance Spectra of Doped a-Si:H. In: *phys. stat. sol. (b)* 107 (1981), no. 1, p. 307–317

[156] MORIGAKI, K. ; DUNSTAN, D. J. ; CAVENETT, B. C. ; DAWSON, P. ; NICHOLLS, J. E. ; NITTA, S. ; SHIMAKAWA, K.: Optically Detected Electron-Spin Resonance in Amorphous Silicon. In: *Solid State Commun.* 26 (1978), no. 12, p. 981–985

[157] DEPINNA, S. ; CAVENETT, B. C. ; AUSTIN, I. G. ; SEARLE, T. M. ; THOMPSON, M. J. ; ALLISON, J. ; LECOMBER, P. G.: Characterization of Radiative Recombination in Amorphous-Silicon by Optically Detected Magnetic-Resonance: Part 1. In: *Philos. Mag. B* 46 (1982), no. 5, p. 473–500

[158] BOULITROP, F.: Recombination Processes in a-Si:H - a Study by Optically Detected Magnetic-Resonance. In: *Phys. Rev. B* 28 (1983), no. 11, p. 6192–6208

[159] STUTZMANN, M. ; BIEGELSEN, D. K. ; STREET, R. A.: Detailed Investigation of Doping in Hydrogenated Amorphous-Silicon and Germanium. In: *Phys. Rev. B* 35 (1987), no. 11, p. 5666–5701

[160] UMEDA, T. ; YAMASAKI, S. ; ISOYA, J. ; TANAKA, K.: Microscopic origin of light-induced ESR centers in undoped hydrogenated amorphous silicon. In: *Phys. Rev. B* 62 (2000), no. 23, p. 15702–15710

[161] ORLINSKII, S. B. ; SCHMIDT, J. ; BARANOV, P. G. ; LORRMANN, V. ; RIEDEL, I. ; RAUH, D. ; DYAKONOV, V.: Identification of shallow Al donors in Al-doped ZnO nanocrystals: EPR and ENDOR spectroscopy. In: *Phys. Rev. B* 77 (2008), no. 11, p. 115334

[162] HOFMANN, D. M. ; HOFSTAETTER, A. ; LEITER, F. ; ZHOU, H. J. ; HENECKER, F. ; MEYER, B. K. ; ORLINSKII, S. B. ; SCHMIDT, J. ; BARANOV, P. G.: Hydrogen: A relevant shallow donor in zinc oxide. In: *Phys. Rev. Lett.* 88 (2002), no. 4, p. 045504

[163] LIPS, K. ; BOEHME, C. ; FUHS, W.: Recombination in silicon thin-film solar cells: a study of electrically detected magnetic resonance. In: *IEE Proc. - Circ. Dev. Syst.* 150 (2003), no. 4, p. 309–315

[164] BRAMMER, T. ; STIEBIG, H. ; LIPS, K.: Numerical analysis of the spin-dependent dark current in microcrystalline silicon solar cells. In: *Appl. Phys. Lett.* 85 (2004), no. 9, p. 1625–1626

[165] Schiff, E. A.: Low-mobility solar cells: a device physics primer with application to amorphous silicon. In: *Sol. Energy Mat. Sol. Cells* 78 (2003), no. 1-4, p. 567–595

[166] Liang, J. J. ; Schiff, E. A. ; Guha, S. ; Yan, B. J. ; Yang, J.: Hole-mobility limit of amorphous silicon solar cells. In: *Appl. Phys. Lett.* 88 (2006), no. 6, p. 063512

[167] Astakhov, O. ; Carius, R. ; Petrusenko, Y. ; Borysenk, V. ; Barankov, D. ; Finger, F.: Defects in thin film silicon at the transition from amorphous to microcrystalline structure. In: *phys. stat. sol. (RRL)* 1 (2007), no. 2, p. R77–R79

[168] Boehme, C. ; Lips, K.: A pulsed EDMR study of hydrogenated microcrystalline silicon at low temperatures. In: *phys. stat. sol. (c)* 1 (2004), no. 5, p. 1255–1274

[169] Harneit, W. ; Boehme, C. ; Schaefer, S. ; Huebener, K. ; Fostiropoulos, K. ; Lips, K.: Room temperature electrical detection of spin coherence in C_{60}. In: *Phys. Rev. Lett.* 98 (2007), no. 21, p. 216601

[170] Schaefer, S. ; Saremi, S. ; Fostiropoulos, K. ; Behrends, J. ; Lips, K. ; Harneit, W.: Electrical detection of coherent spin pair oscillations in ZnPc devices. In: *phys. stat. sol. (b)* 245 (2008), no. 10, p. 2120–2123

[171] Brandt, M. S. ; Stutzmann, M.: Spin-Dependent Photoconductivity as a Function of Wavelength - a Test for the Constant Photocurrent Method in a-Si:H. In: *J. Non-Cryst. Solids* 166 (1993), p. 547–550

[172] Stutzmann, M. ; Biegelsen, D. K.: Electron-Spin-Lattice Relaxation in Amorphous-Silicon and Germanium. In: *Phys. Rev. B* 28 (1983), no. 11, p. 6256–6261

[173] Fehr, M.: *private communication*. 2009

[174] Schweiger, A. ; Jeschke, G.: *Principles of pulse electron paramagnetic resonance*. Oxford, UK ; New York : Oxford University Press, 2001

[175] Brütting, W.: *Physics of organic semiconductors*. Weinheim : Wiley-VCH, 2005

[176] Zezin, A. A. ; Feldman, V. I. ; Warman, J. M. ; Wildeman, J. ; Hadziioannou, G.: EPR study of positive holes on phenylene vinylene chains: from dimer to polymer. In: *Chem. Phys. Lett.* 389 (2004), no. 1-3, p. 108–112

[177] Silva, G. B. ; Santos, L. F. ; Faria, R. M. ; Graeff, C. F. O.: EDMR of MEH-PPV LEDs. In: *Physica B* 308 (2001), p. 1078–1080

[178] THOMSEN, E. A.: *Characterisation of Materials for Organic Photovoltaics*, University of St. Andrews, Diss., 2008

[179] BROWN, A. R. ; BRADLEY, D. D. C. ; BURROUGHES, J. H. ; FRIEND, R. H. ; GREENHAM, N. C. ; BURN, P. L. ; HOLMES, A. B. ; KRAFT, A.: Poly(P-Phenylenevinylene) Light-Emitting-Diodes - Enhanced Electroluminescent Efficiency through Charge Carrier Confinement. In: *Appl. Phys. Lett.* 61 (1992), no. 23, p. 2793–2795

[180] DYAKONOV, V. ; FRANKEVICH, E.: On the role played by polaron pairs in photophysical processes in semiconducting polymers. In: *Chem. Phys.* 227 (1998), no. 1-2, p. 203–217

[181] CASTRO, F. A. ; SILVA, G. B. ; SANTOS, L. F. ; FARIA, R. M. ; NUESCH, F. ; ZUPPIROLI, L. ; GRAEFF, C. F. O.: Electrically detected magnetic resonance of organic and polymeric light emitting diodes. In: *J. Non-Cryst. Solids* 338-40 (2004), p. 622–625

[182] MERMER, O. ; VEERARAGHAVAN, G. ; FRANCIS, T. L. ; SHENG, Y. ; NGUYEN, D. T. ; WOHLGENANNT, M. ; KOHLER, A. ; AL-SUTI, M. K. ; KHAN, M. S.: Large magnetoresistance in nonmagnetic pi-conjugated semiconductor thin film devices. In: *Phys. Rev. B* 72 (2005), no. 20, p. 205202

[183] HU, B. ; WU, Y.: Tuning magnetoresistance between positive and negative values in organic semiconductors. In: *Nature Mater.* 6 (2007), no. 12, p. 985–991

[184] BLOOM, F. L. ; WAGEMANS, W. ; KEMERINK, M. ; KOOPMANS, B.: Correspondence of the sign change in organic magnetoresistance with the onset of bipolar charge transport. In: *Appl. Phys. Lett.* 93 (2008), no. 26, p. 263302

[185] KURODA, S. ; MARUMOTO, K. ; ITO, H. ; GREENHAM, N. C. ; FRIEND, R. H. ; SHIMOI, Y. ; ABE, S.: Spin distributions and excitation spectra of optically generated polarons in poly(phenylenevinylene) derivatives. In: *Chem. Phys. Lett.* 325 (2000), no. 1-3, p. 183–188

[186] YANG, C. G. ; EHRENFREUND, E. ; WANG, F. ; DRORI, T. ; VARDENY, Z. V.: Spin-dependent kinetics of polaron pairs in organic light-emitting diodes studied by electroluminescence detected magnetic resonance dynamics. In: *Phys. Rev. B* 78 (2008), no. 20, p. 205312

[187] McCamey, D. R. ; Seipel, H. A. ; Paik, S. Y. ; Walter, M. J. ; Borys, N. J. ; Lupton, J. M. ; Boehme, C.: Spin Rabi flopping in the photocurrent of a polymer light-emitting diode. In: *Nature Mater.* 7 (2008), no. 9, p. 723–728

[188] De Ceuster, J. ; Goovaerts, E. ; Bouwen, A. ; Hummelen, J. C. ; Dyakonov, V.: High-frequency (95 GHz) electron paramagnetic resonance study of the photoinduced charge transfer in conjugated polymer-fullerene composites. In: *Phys. Rev. B* 64 (2001), no. 19, p. 195206

[189] Salikhov, K. M. ; Molin, Y. N.: Some Peculiarities of Spin Dynamics of Geminate Radical Pairs under Microwave Pumping. In: *J. Phys. Chem.* 97 (1993), no. 50, p. 13259–13266

[190] Kumar, A. ; Bhatnagar, P. K. ; Mathur, P. C. ; Husain, M. ; Sengupta, S. ; Kumar, J.: Temperature and electric-field dependences of hole mobility in light-emitting diodes based on poly [2-methoxy-5-(2-ethylhexoxy)-1,4-phenylene vinylene]. In: *J. Appl. Phys.* 98 (2005), no. 2, p. 024502

[191] Francis, T. L. ; Mermer, O. ; Veeraraghavan, G. ; Wohlgenannt, M.: Large magnetoresistance at room temperature in semiconducting polymer sandwich devices. In: *New Journal of Physics* 6 (2004), p. 1–8

[192] Odaka, H. ; Okimoto, Y. ; Yamada, T. ; Okamoto, H. ; Kawasaki, M. ; Tokura, Y.: Control of magnetic-field effect on electroluminescence in Alq_3-based organic light emitting diodes. In: *Appl. Phys. Lett.* 88 (2006), no. 12, p. 123501

[193] Prigodin, V. N. ; Bergeson, J. D. ; Lincoln, D. M. ; Epstein, A. J.: Anomalous room temperature magnetoresistance in organic semiconductors. In: *Synth. Met.* 156 (2006), no. 9-10, p. 757–761

[194] Bloom, F. L. ; Wagemans, W. ; Kemerink, M. ; Koopmans, B.: Separating positive and negative magnetoresistance in organic semiconductor devices. In: *Phys. Rev. Lett.* 99 (2007), no. 25, p. 257201

[195] Wei, X. ; Vardeny, Z. V. ; Sariciftci, N. S. ; Heeger, A. J.: Absorption-detected magnetic-resonance studies of photoexcitations in conjugated-polymer/C_{60} composites. In: *Phys. Rev. B* 53 (1996), no. 5, p. 2187–2190

[196] Levitt, M. H.: *Spin dynamics : basics of nuclear magnetic resonance*. Chichester ; New York : John Wiley & Sons, 2001

[197] MICHEL, C.: *Theoretical studies of spin-dependent transport phenomena*, Philipps Universität Marburg, Diss., 2007

[198] CHARPENTIER, T. ; FERMON, C. ; VIRLET, J.: Efficient time propagation technique for MAS NMR simulation: Application to quadrupolar nuclei. In: *J. Magn. Reson.* 132 (1998), no. 2, p. 181–190

[199] STOLL, S.: *Spectral Simulations in Solid-State Electron Paramagnetic Resonance*, ETH Zürich, Diss., 2003

[200] EDEN, M. ; LEE, Y. K. ; LEVITT, M. H.: Efficient simulation of periodic problems in NMR. Application to decoupling and rotational resonance. In: *J. Magn. Reson., Ser. A* 120 (1996), no. 1, p. 56–71

[201] MOTT, N. F.: *Metal-insulator transitions*. 2nd. London ; New York : Taylor & Francis, 1990

[202] FRANKEVICH, E. L.: On mechanisms of population of spin substates of polaron pairs. In: *Chem. Phys.* 297 (2004), no. 1-3, p. 315–322

[203] REUFER, M. ; WALTER, M. J. ; LAGOUDAKIS, P. G. ; HUMMEL, B. ; KOLB, J. S. ; ROSKOS, H. G. ; SCHERF, U. ; LUPTON, J. M.: Spin-conserving carrier recombination in conjugated polymers. In: *Nature Mater.* 4 (2005), no. 4, p. 340–346

[204] LIPS, K. ; BOEHME, C. ; EHARA, T.: The impact of the electron spin on charge carrier recombination - The example of amorphous silicon. In: *J. Optoelectron. Adv. Mats.* 7 (2005), no. 1, p. 13–24

[205] BOEHME, C. ; LIPS, K.: Coherent defect spectroscopy with pulsed optically and electrically detected magnetic resonance. In: *J. Mater. Sci.: Mater. Electron.* 18 (2007), p. S285–S291

[206] BOEHME, C. ; LIPS, K.: The nature of dangling bond recombination in µc-Si:H. In: *J. Non-Cryst. Solids* 338-340 (2004), p. 434–439

[207] BOEHME, C. ; LIPS, K.: Investigation of electronic transitions in semiconductors with pulsed electrically detected magnetic resonance. In: *Appl. Magn. Res.* 27 (2004), no. 1-2, p. 109–122

[208] BEHRENDS, J. ; SCHNEGG, A. ; FEHR, M. ; LAMBERTZ, A. ; HAAS, S. ; FINGER, F. ; RECH, B. ; LIPS, K.: Electrical detection of electron spin resonance in

microcrystalline silicon pin solar cells. In: *Philos. Mag.* 89 (2009), no. 28, p. 2655 – 2676

[209] VOMVAS, A. ; FRITZSCHE, H.: The Temperature-Dependence of the Photoconductivity of N-Type a-Si:H and the Effect of Staebler-Wronski Defects. In: *J. Non-Cryst. Solids* 97-98 (1987), p. 823–826

[210] LO, C. C. ; BOKOR, J. ; SCHENKEL, T. ; TYRYSHKIN, A. M. ; LYON, S. A.: Spin-dependent scattering off neutral antimony donors in ^{28}Si field-effect transistors. In: *Appl. Phys. Lett.* 91 (2007), no. 24, p. 242106

[211] LIST, E. J. W. ; KIM, C. H. ; NAIK, A. K. ; SCHERF, U. ; LEISING, G. ; GRAUPNER, W. ; SHINAR, J.: Interaction of singlet excitons with polarons in wide band-gap organic semiconductors: A quantitative study. In: *Phys. Rev. B* 64 (2001), no. 15, p. 155204

[212] KOPPENS, F. H. L. ; BUIZERT, C. ; TIELROOIJ, K. J. ; VINK, I. T. ; NOWACK, K. C. ; MEUNIER, T. ; KOUWENHOVEN, L. P. ; VANDERSYPEN, L. M. K.: Driven coherent oscillations of a single electron spin in a quantum dot. In: *Nature* 442 (2006), no. 7104, p. 766–771

List of publications

1. C. Boehme, J. Behrends, K. von Maydell, M. Schmidt, K. Lips
   Investigation of hopping transport in n-a-Si:H/c-Si solar cells with pulsed electrically detected magnetic resonance
   J. Non-Cryst. Solids, **352**, 1113-1116 (2006)

2. R. Brüggemann, J. Behrends, S. Meier, S. Tardon
   Luminescence, quasi-Fermi levels and applied voltage in ideal and real semiconductor structures
   J. Optoelectron. Adv. Mats., **9**, 77-83 (2007)

3. S. Schaefer, K. Huebener, W. Harneit, C. Boehme, K. Fostiropoulos, H. Angermann, J. Rappich, J. Behrends, K. Lips
   Thin film engineering for N@C60 quantum computers: Spin detection and device patterning approaches
   Solid State Sciences, **10**, 1314-1321 (2008)

4. J. Behrends, A. Schnegg, C. Boehme, S. Haas, H. Stiebig, F. Finger, B. Rech, K. Lips
   Recombination and transport in microcrystalline pin solar cells studied with pulsed electrically detected magnetic resonance
   J. Non-Cryst. Solids, **354**, 2411-2415 (2008)

5. C. Becker, P. Dogan, B. Gorka, F. Ruske, T. Hänel, J. Behrends, F. Fenske, K. Lips, S. Gall, B. Rech
   Polycrystalline Silicon Thin-film Solar Cells on ZnO:Al Coated Glass
   Mat. Res. Soc. Symp. Proc., **1066**, 139-144 (2008)

6. J. Tribollet, J. Behrends, K. Lips
   Ultra long spin coherence time for Fe3+ in ZnO: A new spin qubit
   Europhysics Letters, **2**, 20009 (2008)

7. S. Schaefer, S. Saremi, K. Fostiropoulos, J. Behrends, K. Lips, W. Harneit
   Electrical detection of coherent spin pair oscillations in ZnPc devices
   phys. stat. sol. (b), **245**, 2120-2123 (2008)

8. J. Behrends, K. Lips, C. Boehme
   Observation of precursor pair formation of recombining charge carriers
   Phys. Rev. B, **80**, 045207 (2009) (selected as Physical Review Editors' Suggestion)

9. A. Schnegg, J. Behrends, K. Lips, R. Bittl, K. Holldack
   Frequency domain Fourier transform THz-EPR on single molecule magnets using coherent synchrotron radiation
   Phys. Chem. Chem. Phys., **11**, 6820-6825 (2009)

10. J. Behrends, A. Schnegg, M. Fehr, A. Lambertz, S. Haas, F. Finger, B. Rech, K. Lips
    Electrical Detection of Electron Spin Resonance in Microcrystalline Silicon pin Solar Cells
    Philos. Mag., **89**, 2655-2676 (2009)

11. J. Behrends, A. Schnegg, K. Lips, E.A. Thomsen, A.K. Pandey, I.D.W. Samuel, D.J. Keeble
    Bipolaron formation in organic solar cells observed by pulsed electrically detected magnetic resonance
    submitted

Danksagung

An dieser Stelle möchte ich allen danken, die mich beim Anfertigen dieser Arbeit auf unterschiedlichste Weise unterstützt haben:

Dr. Klaus Lips, der es mir ermöglicht hat, in seiner Gruppe dieses spannende Thema bearbeiten zu können. Ich danke ihm für die intensive Betreuung sowie die mir überlassenen Freiheiten. Außerdem gebührt ihm mein Dank für die unerlässliche Hilfe bei der Interpretation der Messergebnisse und den damit verbundenen Diskussionen.

Prof. Dr. Robert Bittl für die Möglichkeit, an der FU Berlin zu promovieren. Weiterhin danke ich ihm dafür, dass er die Spektrometer in seiner Arbeitsgruppe zur Untersuchung 'exotischer' EDMR-Proben zur Verfügung gestellt hat und für erhellende Diskussionen zur Spinphysik in Theorie und Praxis.

Prof. Dr. Bernd Rech für seine Bereitschaft, das Zweitgutachten zu übernehmen und sein Interesse an dem Thema. Auch danke ich ihm dafür, dass ich meine Doktorarbeit an seinem Institut überhaupt durchführen durfte.

Dr. Alexander Schnegg für die vielen wertvollen Diskussionen und dafür, dass ich sein unerschöpfliches Wissen über die 'echte' EPR anzapfen konnte. Die Tatsache, dass er maßgeblich die Brücke zur AG Bittl an der FU Berlin aufgebaut hat, war und ist eine sehr große Bereicherung für diese Arbeit und das EPR-Solar Projekt im Allgemeinen.

Prof. Dr. Christoph Böhme, dem Pionier der pEDMR, der mich in die Tücken des Spektrometers eingewiesen hat. Außerdem danke ich ihm für die Gastfreundschaft bei meinem Besuch in Utah.

Allen Mitarbeitern des Instituts für Silizium-Photovoltaik für die nette Arbeitsatmosphäre. Meinen Bürokollegen Matthias Fehr, Felice Friedrich und Marc-Andy Gluba sowie Dr. Norbert Nickel, Dr. Moshe Weizman, Lars-Peter Scheller, Dr. Jerome Tribollet, Dr. Yuri Ryabchikov und Benjamin Gorka für viele erleuchtende Diskussionen und sonstige Unterstützung. Der Mittwochs-Laufrunde für die nötige Abwechslung. Marion

Krusche für die Überwindung aller bürokratischer Hürden. Kerstin Jacob, Anja Scheu, Thomas Lußky, Thorsten Seefeldt und Andreas von Kozierowski für Hilfe in technischen Dingen. Dr. Manfred Schmidt, Dr. Rolf Stangl, Tim Schulze und Caspar Leendertz für die gemeinsame Arbeit an den a-Si:H/c-Si Zellen.

Allen Mitarbeitern der AG Bittl an der FU Berlin, die beim Aufbau der gepulsten Q-Band EDMR geholfen haben, insbesondere Dr. Christian Teutloff, Christoph Meier, Susanne Pudollek und Till Biskup. Weiterhin möchte ich mich bei den Mitarbeitern der AG Harneit für interessante gemeinsame Messungen bedanken. Mein besonderer Dank gilt Sebastian Schäfer für viele hilfreiche Diskussionen und die viel zu seltenen Rennradtouren.

Dr. Friedhelm Finger, Dr. Oleksandr Astakhov, Andreas Lambertz und Stefan Haas vom Forschungszentrum Jülich für die Herstellung der μc-Si:H Zellen für EDMR-Untersuchungen.

André Stegner, Konrad Klein, Dr. Hans Hübl und Felix Höhne vom Walter Schottky Institut für spannende Diskussionen und Messungen.

Dr. Elizabeth Thomsen und Dr. Ajay Pandey von der University of St. Andrews sowie Dr. David Keeble von der University of Dundee, die dafür gesorgt haben, dass ich über den Tellerrand hinaus einen Blick in die spannende Welt der Organik werfen konnte.

Dr. Karsten Holldack vom BESSY, der mir interessante Einblicke in die THz- und Synchrotron-Welt von ‘nebenan’ gewährt hat.

Prof. Dr. Gottfried Bauer von der Universität Oldenburg, der mir den Weg nach Berlin gewiesen hat.

Meinen Eltern, die mir ein sorgenfreies Studium ermöglicht und damit indirekt einen wesentlichen Beitrag zu dieser Arbeit geleistet haben. Meinem Bruder Arne danke ich für seine Unterstützung in jeglicher Hinsicht.

Nicht zuletzt danke ich Miriam für ihre Geduld und die schöne Zeit außerhalb von Institut und Uni.

Aus Datenschutzgründen ist der Lebenslauf nur in der gedruckten Version enthalten.